Connected Cruise Control Design in Mixed Traffic Flow Consisting of Human-Driven and Automated Vehicles

by

Jin Ge

A dissertation submitted in partial fulfillment
of the requirements for the degree of
Doctor of Philosophy
(Mechanical Engineering)
in the University of Michigan
2017

Doctoral Committee:

Assistant Professor Gabor Orosz, Co-Chair
Professor A. Galip Ulsoy, Co-Chair
Professor Alexandre M. Bayen, University of California
Professor Ilya Kolmanovsky

Jin Ge

gejin@umich.edu

ORCID iD: 0000-0001-6429-9337

To my parents and the many people who supported and encouraged me to walk on, to embrace the ever-increasing wonder and awe.

TABLE OF CONTENTS

LIST OF FIGURES

LIST OF APPENDICES

ABSTRACT

In this research we design connected cruise control algorithms based on vehicle-to-vehicle communication in order to improve both traffic efficiency and the performance of individual vehicles. We first model human car-following behavior using the optimal velocity model with driver reaction time delay and analyze the relationship between human parameters and traffic flow behavior. Then based on the human car-following model we provide a baseline design for connected automated vehicles. We propose an online estimation algorithm that is able to identify both human feedback gains and reaction time delay in real time using motion information received through wireless vehicle-to-vehicle (V2V) communication. For connected automated vehicle design in a V2V-sparse environment, we find that augmenting a human car-following model with acceleration feedback improves the head-to-tail string stability of the connected vehicle system, and acceleration signals from vehicles farther downstream should be used with larger delay time. For connected automated vehicle design in a V2V-rich environment, an optimal CCC controller is designed using linear quadratic regulation while considering driver reaction time delay. We show that when a CCC vehicle receives motion information from n vehicles ahead, the optimal feedback gains decrease for signals from vehicles farther away, and the CCC controller degrades gracefully when the communication links fail. This CCC controller is analytical, requires little computational load, and is able to provide certain levels of robustness against heterogeneous human parameters in the connected vehicle system. We also consider stochastic human parameters in the optimal CCC design when the mean dynamics of the connected vehicle system is represented with distributed time delay. We find that the optimal CCC controller maintains the same structure and performs well when tested with

experimental data. In the last part of this research, we include stochastic disturbances from the traffic flow and V2V communication in optimal CCC design, and introduce the probabilistic model checking method so that the CCC vehicle can perform well in more realistic traffic scenarios.

CHAPTER 1

Introduction

About one hundred years ago, the invention of the automobile and the construction of the highway system fundamentally changed road transportation in America. Today, the concept of connected automated vehicles (CAV) poses similar, if not more profound, impacts on how we travel. Automated driving is not merely replacing human eyes with cameras and lidar/radars. It liberates road transportation from unpredictable human mistakes and behaviors that cause many traffic problems; microscopically driving safety issues and macroscopically stop-and-go traffic jams. Moreover, with wireless vehicle-to-vehicle(V2V) and vehicle-to-infrastructure (V2I) communication, an automated vehicle is able to obtain traffic information beyond its line of sight, and navigate the traffic in a manner that benefits both its passengers and the traffic flow.

In this research, I pose and provide initial answers to some questions related to:

(1) how human driving behaviors may lead to certain unwanted traffic phenomena,

(2) how an automated car should behave when sharing the road with human-driven cars,

(3) how an automated car in such a mixed-driving scenario can benefit from the traffic information received through wireless connectivity.

This dissertation contains some initial answers from the perspective of longitudinal motion control, and the main ideas can be summarized as follows:

(1) Many unwanted traffic phenomena are related to speed and distance fluctuations propagating through the traffic flow as cars follow each other in each lane. We describe human car-following behaviors using the optimal velocity model (OVM) and show that most human-driven vehicles are unable to suppress speed fluctuations due to their large reaction time delay. As such fluctuations increase, stop-and-go traffic jams may form, and rear-end collisions may occur.

(2) To suppress speed fluctuations, a connected automated vehicle is equipped with vehicle-to-vehicle (V2V) communication and receives motion information from several cars ahead. Such motion information allows the vehicle to identify the preceding vehicles'

behavior and apply a connected cruise controller (CCC) that utilizes the information received via V2V communication. This approach has significant potential for performance improvement, allows an intuitive understanding of the controller design, and (for better user acceptance) maintains a similar behavior as human-driven vehicles.

(3) When a large number of V2V signals are available, an optimal CCC design can be used to tune the feedback gains systematically. We formulate this as a linear quadratic (LQ) optimization problem, so that the optimal controller allows heterogeneous and stochastic behaviors among preceding vehicles, while the computational load is kept low.

(4) More robust CCC controllers can be designed using probabilistic model checking, where CCC controllers from the LQ setup may serve as baselines for this dynamic feedback design.

This research is among the first steps to design connected automated vehicle systems from the viewpoint of a more efficient transportation system. It exploits V2V communication which makes available traffic information beyond the line of sight to compensate for the limited perception ability of on-board sensors. Such clairvoyance is not influenced by camera/lidar/radar failures, and the resulting connected automated vehicle becomes a smart agent in the traffic system "nudging" the traffic flow away from undesired behaviors. More importantly, such benefits come from connectivity but not enforced cooperation, i.e., the connected automated vehicles may not share common control objectives. This differs from many cooperative adaptive cruise control (CACC) research where a pre-organized platoon is established. As the automated vehicle is able to exchange information with nearby vehicles in an ad-hoc manner and co-exist with human-driven vehicles, it can be readily implemented in today's human-dominated traffic network and provide a path to the automation-dominated future.

1.1 Background

Research on automated driving dates back to the early 1990s. Facing the increasing demand to reduce traffic congestion, the California PATH program started to research automated vehicle and highway systems both experimentally and theoretically [8]. By 1997, there had been several public demonstrations on automated longitudinal control in close-formation platoons using radars and wireless LAN communication systems. Automatic lateral control was also experimentally tested using magnetic guidance and cameras. Even though the PATH automated highway project was terminated and an automated highway system did not materialize, the concepts formulated by PATH became the cornerstone for current automated driving research.

Meanwhile, industry is gradually adding partially automated features to passenger cars, such as adaptive cruise control (ACC) and lane-keeping systems. While ACC is often advertised as enhancing driver comfort, it can have significant benefits in terms of traffic flow behavior via better longitudinal control of equipped vehicles. Since human drivers have relatively large reaction times and limited perception abilities, they often perform poorly as longitudinal controllers. ACC may improve longitudinal control due to faster and more accurate sensing abilities and more sophisticated control strategies [9, 10]. However, ACC cannot overcome the limitation that only motion information of the vehicle immediately ahead can be obtained through range sensors.

Even as silicon valley and the automotive industry are trying to advance ACC and lane-keeping systems to a higher-level of driving autonomy, their perception systems mostly rely on on-board sensors like cameras, lidars, and radars. Thus the performance of these automated driving systems are severely limited by the available on-board sensors. For example, Nissan automated vehicles reported dozens of disengagements when their perception system failed to keep track of a vehicle entering/leaving its line of sight [11], and automated vehicles from Delphi were forced to disengage when the cameras failed to identify lane markings and traffic lights [12]. Even with a perfect on-board perception system, an automated vehicle is only able to obtain motion information of cars within its line of sight. Thus, without other information sources, an automated car is still limited when it comes to fuel economy, active safety, and passenger comfort. Also, due to the high cost in early implementation, the penetration rate of automated cars may be quite low in the near future. To produce observable benefits on traffic flow, automated cars have to obtain traffic information which on-board-sensors cannot provide.

In recent years wireless communication technology has seen tremendous improvements. In particular, the Federal Communications Commission allocated 75 MHz of bandwidth in the 5.9GHz spectrum to applications in intelligent transportation systems [13]. Later, this wireless communication channel was named dedicated short range communications (DSRC) and has been furnished with a full set of protocols and standards from IEEE and SAE [14], [15], [16]. DSRC enables 10-Hz ad-hoc communication between vehicles and the infrastructure, and among vehicles. Experimental research studies have been conducted where DSRC is used to monitor macroscopic traffic flow. As the cost of DSRC devices continues to decrease, new cars will be mandated to have DSRC by 2020 in the US. Thus, it is desired to incorporate information obtained via DSRC into motion control of individual vehicles.

While many intelligent transportation research studies focus on vehicle-to-infrastructure (V2I) communication based on DSRC [17], [18], this dissertation only focuses on vehicle-

to-vehicle (V2V) communication. In such a case, vehicles may be controlled while taking into account traffic flow conditions over a longer spatial horizon. This idea first took form in the PATH platooning project, where a fixed communication structure was assigned to a group of ACC vehicles, so that a platoon could run with relatively small headway, while velocity fluctuations were suppressed. Since then, a class of connectivity-based longitudinal controllers have been proposed under the name of cooperative adaptive cruise control (CACC) for various application scenarios [19–22], especially for designated-lane highway driving [23–25]. Some researchers also relaxed the rigid requirements on the communication topology for CACC, so that it may deal with more realistic multi-vehicle formations [26–28]. However, such cooperative systems often require a platoon of fully automated cars, while driving automation in its early implementation often will have to deal with a mixed traffic situation of human-driven and automated vehicles.

Therefore, in this dissertation, we propose a class of connected cruise control algorithms that are based on human car-following behavior and allow ad-hoc V2V communication with multiple vehicles. For each scenario under discussion, the controller is found to be computationally efficient while allowing certain levels of heterogeneity and stochasticity in the behavior of the preceding vehicles, and is able to maintain steady-state behavior similar to the nearby human drivers. For a more robust and dynamic response to the traffic, the framework is extended to design a connected cruise controller with dynamic feedback, where the CCC controller maintains its connectivity topology while the computational load varies.

1.2 Contributions

In Chapter 2, we describe human car-following behavior using the optimal velocity model with reaction time delay and investigate which human parameters may induce undesired traffic behaviors. Then by looking into the influence of delay time on the car-following model, we establish a baseline design for connected cruise control.

In Appendix In Chapter 3, based on experimental data, we identify the time-varying human parameters and reaction time using the sweeping least square method. This method can be implemented online and has reasonable computational load.

In Chapter 4, we propose and develop an acceleration-based CCC design in a V2V-sparse environment, where the CCC vehicle is able to suppress vehicle fluctuations propagating downstream.

In Chapter 5, we propose and develop an optimal CCC design based on headway and velocity in a V2V-rich environment. The optimal control problem is formulated as an LQ

problem, where the dynamics of preceding vehicles have nominal parameters and delay time. The resultant CCC controller has an analytic form and thus requires little computational effort. It allows certain levels of inaccuracy and heterogeneity in the model parameters of the preceding human-driven vehicles.

In Chapter 6, we consider stochastic variations in the parameters for the preceding vehicles. The LQ CCC design is extended based on the mean dynamics, and the benefits of the CCC controller remains.

In Chapter 7, we use probabilistic model checking to obtain an optimal CCC controller with performance guarantee. While the feedback gains in the controller require more numerical computation, the structure of the controller is maintained, and may facilitate further investigation regarding the influence of the CCC vehicle on the traffic system.

1.3 Publications

Results in this dissertation can be found in the following publications:

Journal Publications

[10] J. I. Ge and G. Orosz. Optimal connected vehicle design considering stochastic human car-following behavior. IEEE Transactions on Intelligent Transportation Systems, 2017. (in preperation)

[9] J. I. Ge and G. Orosz. Optimal control of connected vehicle systems with communication delay and driver reaction time. IEEE Transactions on Intelligent Transportation Systems, 2016. (published online)

[8] J. I. Ge and G. Orosz. Dynamics of connected vehicle systems with delayed acceleration feedback. Transportation Research Part C, 46:46-64, 2014.

Book Chapters

[7] J. I. Ge, G. Orosz, D. Hajdu, T. Insperger, and J. Moehlis. To delay or not to delay stability of connected cruise control. Time Delay Systems - Theory, Numerics, Applications and Experiments, Advances in Delays and Dynamics, T. Insperger, T. Ersal, and G. Orosz, Eds., vol. 7, pp. 263-282. Springer, 2017.

Conference Proceedings

[6] J. I. Ge and G. Orosz, Connected cruise control among human-driven vehicles: experiment-based parameter estimation and optimization, Conference on Decision and control, IEEE, 2017. (submitted)

[5] J. I. Ge and G. Orosz and R. M. Murray, Connected Cruise Control Design Using Probabilistic Model Checking, Proceedings of the American Control Conference, IEEE, 2017. (accepted)

[4] J. I. Ge and G. Orosz. Estimation of feedback gains and delays in connected vehicle systems. Proceedings of the American Control Conference, pp. 6000-6005, IEEE, 2016.

[3] J. I. Ge and G. Orosz. Optimal control of connected vehicle systems with delay. Proceedings of the 12th IFAC Workshop on Time Delay Systems, pp. 468-473, IFAC, 2015.

[2] J. I. Ge and G. Orosz. Optimal control of connected vehicle systems. Proceedings of the 53rd Conference on Decision and Control, pp. 4107-4112, IEEE, 2014.

[1] J. I. Ge, S. S. Avedisov, and G. Orosz. Stability of connected vehicle platoons with delayed acceleration feedback. Proceedings of the ASME Dynamic Systems and Control Conference, Paper no. DSCC2013-4040, pp. V002T30A006, ASME, 2013.

CHAPTER 2

Human-driven and automated car-following behavior

We consider the early implementation of automated driving when a connected automated vehicle needs to share the road with human-driven vehicles. While most vehicles on the road are not automated, some of them are equipped with wireless V2V communication devices such as DSRC, and the connected automated vehicle receives motion information from the DSRC-equipped vehicles. As the automated vehicle travels with the largely human-driven traffic flow, its behavior should bear a certain resemblance to a human-driven vehicle. For example, the automated car should follow a human-driven car with a similar distance as an average human driver would do. If it keeps a smaller distance, its passengers may feel uncomfortable. Moreover, the human driver ahead may not prefer being tailgated even if the automated car can brake faster. If the automated car keeps that distance larger than average, other human-driven vehicles may decide to cut in, which creates disturbances that may lead to safety hazards and negatively impact the traffic flow.

Since car-following behavior among all driving behaviors has the most recognized influence on traffic flow, we first model human car-following behavior, and then based on the human model propose a car-following model that can be used for automated cars.

2.1 Human car-following mechanism

In this section we model the car-following behavior of human drivers in non-emergency situations. For simplicity we only consider longitudinal motion control of vehicles in a single lane; see Fig. 2.1(a). Many human car-following models exist in the literature, as summarized in [29, 30]. These include continuous-time ones like the intelligent driver model (IDM) [31], the optimal velocity model (OVM) [32], the GM model [33, 34], the Pipes model [35], and the discrete-time ones like the Krauss model [36] and the Wiedemann

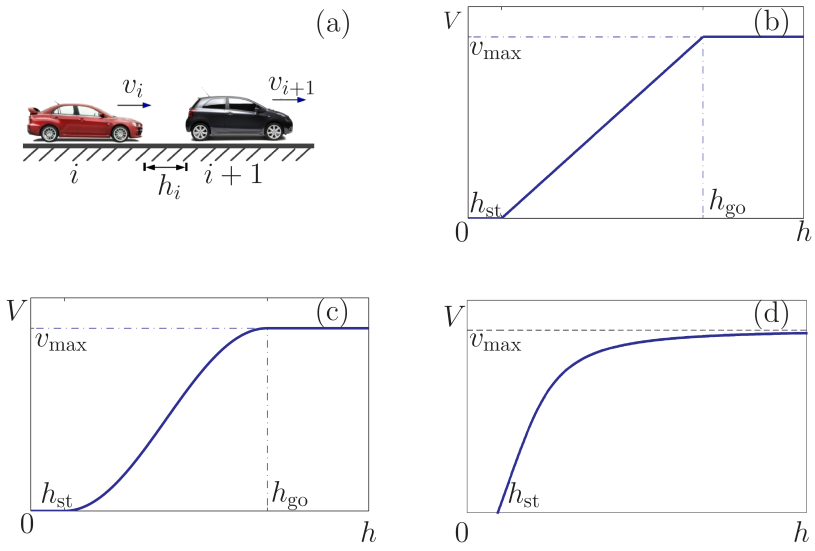

Figure 2.1: (a): Cars following each other on a single lane. (b): The range policy (2.3, 2.4) used in the literature, where $v_{\max}$ is the maximum velocity allowed for the vehicle, $h_{\rm st}$ is the smallest headway before the vehicle intends to stop, and $h_{\rm go}$ is the largest headway after which the vehicle intends to maintain $v_{\max}$. (c): The range policy (2.3, 2.5) used in this paper. (d): The range policy (2.8) implicitly contained in the IDM.

model [37]. Over the past decades many variations of these models have been developed in the efforts to reproduce a wide range of traffic phenomena by computer simulation [38, 39]. While models using a large number of parameters may be considered to be of higher fidelity, difficulties in parameter estimation through data fitting can negatively affect their accuracy [40, 41].

Thus we consider a class of continuous-time car-following models with relatively few parameters. These models (e.g., OVM, IDM, and GM model) can be written in the form

$$\begin{aligned} \dot{h}_i &= v_{i+1} - v_i \,, \\ \dot{v}_i &= F\big(h_i, \dot{h}_i, v_i\big) \,, \end{aligned} \tag{2.1}$$

to describe the car-following behavior of vehicle i. Here the dot stands for differentiation with respect to time t, h_i denotes the headway, i.e., the bumper-to-bumper distance between vehicle i and its predecessor, and v_i denotes the velocity of vehicle i; see Fig. 2.1(a).

Here we provide some details about the OVM and the IDM that are used very frequently in the literature. In case of the OVM [42], the vehicle acceleration is determined by the difference between the headway-dependent desired velocity and the actual velocity and by

the velocity difference between the vehicle and its predecessor, that is,

$$F(h, \dot{h}, v) = \alpha\big(V(h) - v\big) + \beta\dot{h}\,, \tag{2.2}$$

where the gains α and β are used by the human drivers to correct velocity errors. The desired velocity is determined by the headway using the continuous range policy

$$V(h) = \begin{cases} 0 & \text{if} \quad h \le h_{\rm st}\,, \\ f_{\rm v}(h) & \text{if} \quad h_{\rm st} < h < h_{\rm go}\,, \\ v_{\max} & \text{if} \quad h \ge h_{\rm go}\,, \end{cases} \tag{2.3}$$

i.e., the desired velocity is zero for small headways ($h \le h_{\rm st}$) and equal to the maximum speed $v_{\max}$ for large headways ($h \ge h_{\rm go}$). Between these, the desired velocity is given by $f_{\rm v}(h)$ which increases with the headway monotonically. There are many choices for the specific function $f_{\rm v}(h)$, but the qualitative dynamics remain similar if the above characteristics are kept [4, 42]. In [25] the function

$$f_{\rm v}(h) = v_{\max}\frac{h - h_{\rm st}}{h_{\rm go} - h_{\rm st}} \tag{2.4}$$

was used, which has constant slope $\kappa = v_{\max}/(h_{\rm go} - h_{\rm st})$, as shown in Fig. 2.1(b). However, the range policy (2.3, 2.4) is non-smooth at $h = h_{\rm st}$ and $h = h_{\rm go}$ and may generate a "jerky ride". Thus, here we use

$$f_{\rm v}(h) = \frac{v_{\max}}{2}\left(1 - \cos\left(\pi\frac{h - h_{\rm st}}{h_{\rm go} - h_{\rm st}}\right)\right) \tag{2.5}$$

as shown in Fig. 2.1(c). The range policy (2.3, 2.5) is smooth but has a changing slope.

We assume that human-driven vehicles try to maintain the equilibrium

$$h_i(t) \equiv h^*\,, \quad v_i(t) \equiv v^*\,, \tag{2.6}$$

given by $F(h^*, 0, v^*) = 0$, cf. (2.1), and the aggregate of such equilibria corresponds to the uniform traffic flow. Using (2.2) we find the equilibrium speed-headway relation of OVM given by its range policy function (2.3), i.e., $v^* = V(h^*)$.

On the other hand, the IDM [31] can be written in the form

$$F(h, \dot{h}, v) = a\left(1 - \left(\frac{v}{v_{\max}}\right)^4 - \left(\frac{h_{\rm st} + Tv - \dot{h}v/\sqrt{4ab}}{h}\right)^2\right), \tag{2.7}$$

where a is the maximum desired acceleration, T is a time constant, and b is the comfortable acceleration. While (2.7) does not contain a range policy function explicitly, the equilibrium speed-headway relation

$$h^* = V^{-1}(v^*) = \frac{h_{\rm st} + Tv^*}{\sqrt{1-(v^*/v_{\max})^4}}\,, \tag{2.8}$$

depicted in Fig. 2.1(d), describes qualitatively the same driving behavior as in Fig. 2.1(b,c). Notice that for $h^* < h_{\rm st}$, we have $v^* < 0$ in the IDM, which can be eliminated by requiring vehicle velocities to be non-negative.

As the parameters α and β in the OVM have clear physical meaning, we choose the OVM (2.2) as the representation of human car-following model and a basis for automated car-following design. We note that both the OVM (2.1, 2.2) and the IDM (2.1, 2.7) can be linearized into the same form [42]. Thus, at the linear level, the choice of OVM over IDM does not create structural changes to the automated vehicle design. Moreover, most results in this dissertation can be generalized for differentiable $F(h, \dot{h}, v)$.

2.2 Optimal velocity model with driver reaction time

One indispensable feature missing from the OVM (2.1, 2.2) is the human reaction time delay, which may include the lag time in the powertrain. Previous analysis has shown that the influence of time delay on traffic flow behavior cannot be ignored [43]. Thus, we add driver reaction time to the OVM:

$$\begin{aligned} \dot{h}_i(t) &= v_{i+1}(t) - v_i(t)\,, \\ \dot{v}_i(t) &= \alpha\big(V(h_i(t-\tau)) - v_i(t-\tau)\big) + \beta\big(v_{i+1}(t-\tau) - v_i(t-\tau)\big)\,, \end{aligned} \tag{2.9}$$

where τ is the human reaction time delay.

By assuming the system in the vicinity of the equilibrium (2.6) and defining the headway and velocity perturbations

$$\tilde{h}_i(t) = h_i(t) - h^*, \quad \tilde{v}_i(t) = v_i(t) - v^*\,, \tag{2.10}$$

we linearize (2.9) to obtain the linear delay differential equation (DDE)

$$\begin{aligned} \dot{\tilde{h}}_i(t) &= \tilde{v}_{i+1}(t) - \tilde{v}_i(t)\,, \\ \dot{\tilde{v}}_i(t) &= \alpha\big(\kappa\,\tilde{h}_i(t-\tau) - \tilde{v}_i(t-\tau)\big) + \beta\big(\tilde{v}_{i+1}(t-\tau) - \tilde{v}_i(t-\tau)\big)\,. \end{aligned} \tag{2.11}$$

Here $\kappa = V'(h^*)$ is the derivative of the range policy (2.3) at the equilibrium, and by abuse of terminology we denote the time headway $t_{\rm h} = 1/f_{\rm v}'(h^*) = 1/\kappa$ for $h_{\rm st} \leq h^* \leq h_{\rm go}$.

Controllers with a small time headway produce more aggressive car-following behaviors, which makes it more difficult to maintain uniform traffic flow [44]. In the extreme case of human car-following with zero time headway (constant headway distance for any velocity), the uniform traffic flow cannot be maintained in a group of such vehicles.

2.2.1 Linear stability analysis in human car-following model

Here we discuss the influence of human driving behavior (2.9) on the stability of uniform traffic flow, in particular the influence of driver reaction time τ. Based on highway traffic data [42], we set nominal values $v_{\max} = 30$ [m/s], $h_{\rm st} = 5$ [m], $h_{\rm go} = 35$ [m] in the range policy (2.3, 2.5). We evaluate the linear stability of (2.11) at the operating point $v^* = 15$ [m/s], $h^* = 20$ [m], where the range policy has the largest derivative $\kappa = \pi/2$ [1/s] and correspondingly the smallest time headway $t_{\rm h} \approx 0.64$ [s].

Since the uniform traffic flow corresponds to the trivial equilibrium (2.6) of the linearized car-following model (2.11), we can discuss plant stability and string stability in the vicinity of the equilibrium. A human-driven vehicle i is plant stable if the speed perturbation $\tilde{v}_i$ converges to zero with "zero input" $\tilde{v}_{i+1}(t) \equiv 0$. Plant stability describes the speed-regulation performance of individual vehicles regardless of the traffic. On the other hand, string stability, as a special case of bounded-input-bounded-output stability, is related to speed variations propagating along the vehicle chain. More specifically, string stability requires that velocity fluctuations are attenuated as they propagate upstream [44]. Therefore, to discuss the linear stability of uniform traffic flow with human-driven vehicles, we only need to discuss the plant stability of each vehicle, and the string stability in pairs of successive vehicles.

We consider the velocity perturbation $\tilde{v}_i$ of a human-driven vehicle as the output and the velocity perturbation $\tilde{v}_{i+1}$ of its preceding vehicle as the input. Taking the Laplace transform of the system (2.11) with zero initial conditions, we obtain the transfer function

$$\Gamma_i(s) = \frac{\tilde{V}_i(s)}{\tilde{V}_{i+1}(s)} = \frac{F(s)}{G(s)}\,, \tag{2.12}$$

where $\tilde{V}_i(s)$ and $\tilde{V}_{i+1}(s)$ denote the Laplace transform of $\tilde{v}_i(t)$ and $\tilde{v}_{i+1}(t)$, respectively,

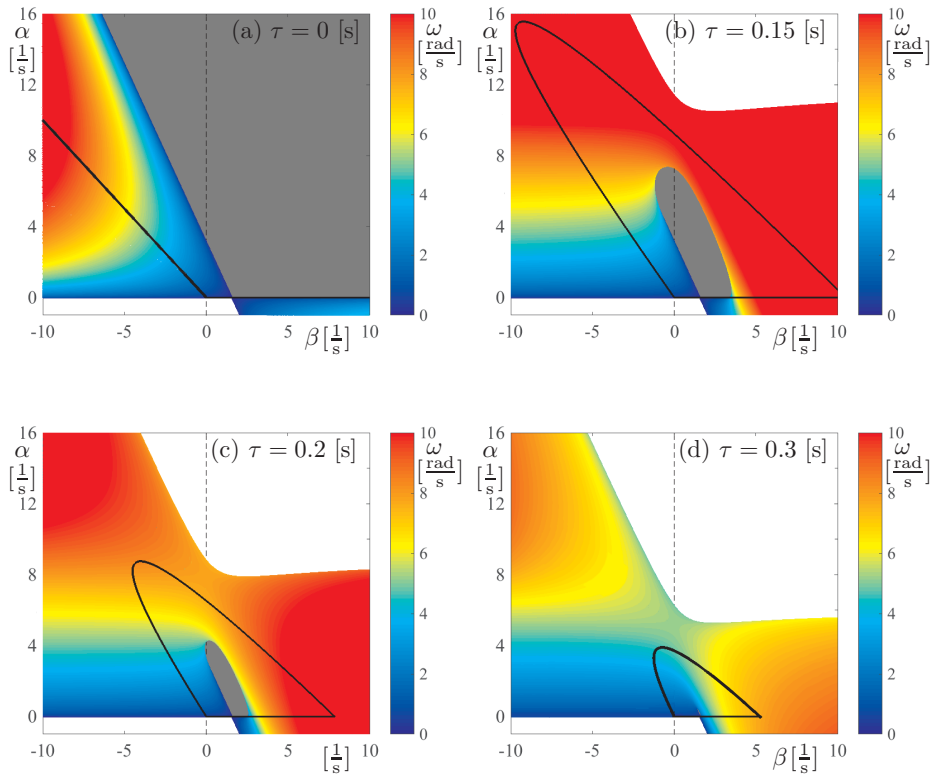

Figure 2.2: (a - d): Stability region of human-driven vehicles in (β, α)-plane for different τ values as indicated. The black curves are the plant stability boundaries. The dark gray areas are string stable. The color represents the highest frequency of string stability changes.

and

$$F(s) = \beta s + \alpha\kappa\,,$$
$$G(s) = s^2\,\mathrm{e}^{\tau s} + (\alpha+\beta)s + \alpha\kappa\,. \tag{2.13}$$

Plant stability is determined by the denominator $G(s)$ of the transfer function (2.12) and it is influenced only by the driver parameters α, β, and τ. The human-driven vehicle is linearly plant stable if and only if all solutions of the characteristic equation $G(s) = 0$ (also referred to as the poles) are located in the left half complex plane. By substituting $s = \mathrm{i}\Omega$, $\Omega \geq 0$ into the characteristic equation, we obtain the plant stability boundaries. When $\Omega = 0$, we have

$$\alpha = 0\,, \tag{2.14}$$

while for $\Omega > 0$ we obtain the plant stability boundary in parametric form:

$$\begin{aligned} \alpha &= \frac{\Omega^2}{\kappa}\cos(\Omega\tau)\,, \\ \beta &= \frac{\Omega}{\kappa}\big(\kappa\sin(\Omega\tau) - \Omega\cos(\Omega\tau)\big)\,. \end{aligned} \tag{2.15}$$

Note that the plant stability boundary (2.14) describes the stability loss corresponding to a real pole crossing the imaginary axis, while (2.15) describes a complex conjugate pair of poles crossing the imaginary axis. When $\tau = 0$ [s], (2.14) remains the same while (2.15) simplifies to $\beta = -\alpha$, as shown by the thick black line in Fig. 2.2(a). One may use the Routh-Hurwitz criteria to show that plant stability is achieved above the lines in the top right corner. For different values of $\tau > 0$ the curves (2.14) and (2.15) are shown as thick black curves in the (β, α)-plane in Fig. 2.2(b,c,d). One may apply Stépán's formulae [45] and show that stability is maintained inside the lobe-shaped domain. As the delay is increased the plant stable domain shrinks, and the size of the domain tends to zero as the delay approaches infinity. However, when the driver reaction time $\tau = 0.3$ [s], the human car-following model with realistic gains $\alpha, \beta \in (0,\ 2)$ is still plant stable, indicating that it is relatively easy for human drivers to ensure plant stability.

Since we can write perturbation signals using Fourier components using the superposition rule in linear systems, string stability is equivalent to that sinusoidal signals are attenuated between the preceding and the human-driven vehicles for all excitation frequencies. Therefore, at the linear level the necessary and sufficient condition for string stability is given by

$$|\Gamma_i(\,\mathrm{i}\omega)|^2 - 1 < 0\,, \quad \forall\omega > 0\,, \tag{2.16}$$

where $\Gamma_i(\,\mathrm{i}\omega)$ is as defined by (2.12). This condition may be rewritten as $\omega^2 P(\omega) > 0$ where

$$P(\omega) = \omega^2 + 2\alpha\beta + \alpha^2 - 2(\alpha+\beta)\omega\sin(\omega\tau) - 2\alpha\kappa\cos(\omega\tau)\,. \tag{2.17}$$

The stability boundaries can be identified corresponding to the minima of P becoming negative at $\omega_{\rm cr} > 0$ that is defined by

$$\begin{aligned} P(\omega_{\rm cr}) &= 0\,, \\ \frac{\partial P}{\partial\omega}(\omega_{\rm cr}) &= 0\,, \end{aligned} \tag{2.18}$$

while satisfying $\frac{\partial^2 P}{\partial\omega^2}(\omega_{\rm cr}) > 0$. Solving this for α and β one may obtain the string stability

boundaries parameterized by $\omega_{\rm cr}$ as

$$\begin{aligned}\alpha &= a \pm \sqrt{a^2+b}\,,\\ \beta &= \frac{\omega_{\rm cr}+\alpha\kappa\tau\sin(\omega_{\rm cr}\tau)}{\sin(\omega_{\rm cr}\tau)+\omega_{\rm cr}\tau\cos(\omega_{\rm cr}\tau)}-\alpha\,,\end{aligned} \tag{2.19}$$

where

$$\begin{aligned}a &= \frac{\omega_{\rm cr}(\kappa\tau-1)+\kappa\sin(\omega_{\rm cr}\tau)\cos(\omega_{\rm cr}\tau)}{(2\kappa\tau-1)\sin(\omega_{\rm cr}\tau)-\omega_{\rm cr}\tau\cos(\omega_{\rm cr}\tau)}\,,\\ b &= \frac{\omega_{\rm cr}^2(\sin(\omega_{\rm cr}\tau)-\omega_{\rm cr}\tau\cos(\omega_{\rm cr}\tau))}{(2\kappa\tau-1)\sin(\omega_{\rm cr}\tau)-\omega_{\rm cr}\tau\cos(\omega_{\rm cr}\tau)}\,.\end{aligned} \tag{2.20}$$

For $\omega_{\rm cr}=0$, the equalities $|\Gamma(0)|=1$ and $\frac{\partial|\Gamma|}{\partial\omega}(0)=0$ always hold. Thus, for string stability we need $\frac{\partial^2|\Gamma|}{\partial\omega^2}(0)<0$ which is equivalent to $P(0)=\alpha(\alpha+2\beta-2\kappa)>0$. That is, one of the boundaries is equivalent to the plant stability boundary (2.14) while the other is given by

$$\alpha = 2(\kappa-\beta)\,. \tag{2.21}$$

Notice that this zero-frequency boundary does not depend on the driver reaction time τ.

In the special case of $\tau=0$, only the sting stability boundaries (2.14) and (2.21) appear as shown by the straight lines bounding the gray string stable domain in Fig. 2.2(a). The coloring outside the string stable area corresponds to the solution of $P(\omega)=\omega^2+\alpha(\alpha+2\beta-2\kappa)=0$ for the frequency ω. The coloring indicates that string stability is lost for low frequencies. For different values of $\tau>0$ the stability boundaries (2.14, 2.19, 2.20, 2.21) enclose the grey-shaded string stability domain in the (β,α)-plane as depicted in Fig. 2.2(b,c,d). The coloring outside the string stable area corresponds to the solution of $P(\omega)=0$ for the frequency ω (cf. (2.17)). When there exist multiple solutions we use the largest ω value. The coloring indicates that when leaving the string stable area toward the left, string stability is still lost at low frequencies. On the other hand, leaving the area to the right, high-frequency string instability occurs.

One may observe that as the delay τ increases the string stable domain shrinks and for $\tau=0.3$ [s] it almost disappears. In fact, there exist a critical value of the delay such that for $\tau>\tau_{\rm cr}$ there exist no gain combinations that can ensure string stability. To calculate the critical delay one may use the L'Hospital rule to show that for $\omega_{\rm cr}\to 0$ formulae (2.19,

2.20) yield the points

$$
\begin{aligned}
(\alpha^+,\, \beta^+) &= \left(\frac{2\kappa\tau - 1}{\tau(\kappa\tau - 1)},\, \frac{2(\kappa\tau)^2 - 4\kappa\tau + 1}{2\tau(\kappa\tau - 1)} \right), \\
(\alpha^-,\, \beta^-) &= \left(0,\, \frac{1}{2\tau} \right).
\end{aligned}
\tag{2.22}
$$

which are located along the stability boundary around the yellow shading in Fig. 2.2(a). These points move closer to each other when the delay increases and coincide when the delay takes the value

$$
\tau_{\mathrm{cr}} = \frac{1}{2\kappa} = \frac{t_{\mathrm{h}}}{2} \approx 0.325\,[\mathrm{s}]. \tag{2.23}
$$

As human reaction time is generally larger than 0.3 [s], the optimal velocity model with time delay determines that human drivers mostly are unable to remain string stable. However, this problem can be solved by utilizing driving automation.

2.3 Two possibilities in eliminating delay time

Given the faster and more accurate sensing abilities of automated driving systems, an automated vehicle is able to eliminate delay time from the car-following model (2.9) in several different ways. In this section, we introduce each modification that may lead to a new car-following model for an automated car, and by comparing their string stability performance choose the most desirable one.

To start with, an automated vehicle may have the same car-following model as a human-driven vehicle (2.9), but with smaller delay time τ. However, an automated vehicle may use range sensors to measure the headway and relative velocity between the two cars in time, but instantaneously measure its own velocity v_i by on-board sensors. Assume the delay time to obtain those signals is σ, then the automated car-following model becomes

$$
\begin{aligned}
\dot{h}_i(t) &= v_{i+1}(t) - v_i(t)\,, \\
\dot{v}_i(t) &= \alpha\big(V(h_i(t-\sigma)) - v_i(t)\big) + \beta\big(v_{i+1}(t-\sigma) - v_i(t-\sigma)\big)\,.
\end{aligned}
\tag{2.24}
$$

This model still satisfies the equilibrium (2.6), but in the right hand side a mismatch in time is created by comparing the delayed value of desired velocity with the instantaneous value of the actual speed.

To further eliminate delays, one may consider obtaining the headway and the leading car's velocity via V2V communication while measuring its own velocity on board. In this

case, the automated car-following model becomes

$$\begin{aligned}\dot{h}_i(t) &= v_{i+1}(t) - v_i(t)\,,\\ \dot{v}_i(t) &= \alpha\big(V(h_i(t-\sigma)) - v_i(t)\big) + \beta\big(v_{i+1}(t-\sigma) - v_i(t)\big)\,,\end{aligned} \tag{2.25}$$

where both feedback terms in the second equation compare delayed values to instantaneous values. The model (2.25) also satisfies the equilibrium (2.6).

One may argue that when calculating the headway from vehicle positions, the GPS position of the automated vehicle itself does not have to be delayed. However, in this case the desired equilibrium (2.6) will vary depending on the delay time σ of the preceding car's GPS signal. In particular, the equilibrium headway becomes $V^{-1}(v^*) + v^*\sigma$ that may lead to safety hazards.

To investigate the advantages and disadvantages of the three models (2.9),(2.24) and (2.25) in terms of their linear stability around the equilibrium (2.6), we carry out the same string stability analysis as in Section 2.2.1, and plot stability charts for different values of the communication delay σ.

2.3.1 Linear stability analysis for one delay mismatch

Linearizing the model (2.24) about the equilibrium (2.6) yields

$$\begin{aligned}\dot{\tilde{h}}_i(t) &= \tilde{v}_{i+1}(t) - \tilde{v}_i(t)\,,\\ \dot{\tilde{v}}_i(t) &= \alpha\big(\kappa\tilde{h}_i(t-\sigma) - \tilde{v}_i(t)\big) + \beta\big(\tilde{v}_{i+1}(t-\sigma) - \tilde{v}_i(t-\sigma)\big)\,.\end{aligned} \tag{2.26}$$

Taking the Laplace transform with zero initial conditions we obtain the transfer function

$$\Gamma(s) = \frac{\tilde{V}(s)}{\tilde{V}_{\mathrm{L}}(s)} = \frac{\beta s + \alpha\kappa}{\mathrm{e}^{s\sigma}(s^2 + \alpha s) + \beta s + \alpha\kappa}\,. \tag{2.27}$$

The corresponding plant stability boundaries are given by (2.14) and

$$\begin{aligned}\alpha &= \frac{\Omega^2\cos(\Omega\sigma)}{\kappa - \Omega\sin(\Omega\sigma)}\,,\\ \beta &= \Omega\sin(\Omega\sigma) - \alpha\cos(\Omega\sigma)\,,\end{aligned} \tag{2.28}$$

that are shown as thick black curves in the (β, α)-plane in Fig. 2.3. Applying Stépán's formulae [45] shows that the system is plant stable when parameters are chosen from the region above the black curves. Again, increasing the delay leads to smaller plant stable domains.

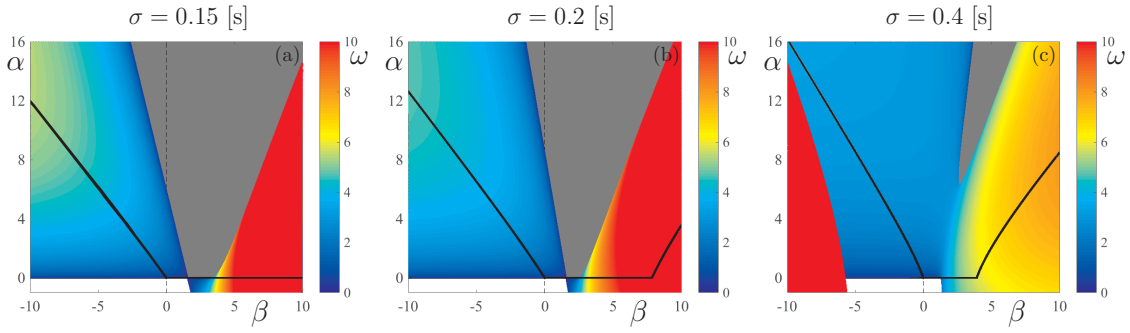

Figure 2.3: (a - c): Stability region of human-driven vehicles in (β, α)-plane for different σ values as indicated. The black curves are the plant stability boundaries. The dark gray areas are string stable. The color represents the highest frequency of string stability changes.

In this case the string stability condition can be rewritten as $\omega Q(\omega) > 0$ where

$$Q(\omega) = \omega^3 + \alpha^2\omega - 2(\alpha^2\kappa + \beta\omega^2)\sin(\omega\sigma) + 2(\alpha\beta - \alpha\kappa)\omega\cos(\omega\sigma)\,. \tag{2.29}$$

For $\omega_{\rm cr} > 0$ the string stability boundaries can be obtained by replacing P with Q in (2.18) which yields

$$\begin{aligned} &\sum_{p=0}^{3} a_p \alpha^p = 0\,, \\ &\beta = \frac{\omega_{\rm cr}^3 + \alpha^2\omega_{\rm cr} - 2\alpha\kappa\big(\alpha\sin(\omega_{\rm cr}\sigma) + \omega_{\rm cr}\cos(\omega_{\rm cr}\sigma)\big)}{2\omega_{\rm cr}\big(\omega_{\rm cr}\sin(\omega_{\rm cr}\sigma) - \alpha\cos(\omega_{\rm cr}\sigma)\big)}\,, \end{aligned} \tag{2.30}$$

where

$$\begin{aligned} a_0 &= \omega_{\rm cr}^4\cos(\omega_{\rm cr}\sigma)\big(-\sin(\omega_{\rm cr}\sigma) + \omega_{\rm cr}\sigma\cos(\omega_{\rm cr}\sigma)\big)\,, \\ a_1 &= \omega_{\rm cr}^2\cos(\omega_{\rm cr}\sigma)\big(\omega_{\rm cr}^2\sigma\sin(\omega_{\rm cr}\sigma) - 2\kappa\sin(\omega_{\rm cr}\sigma)\cos(\omega_{\rm cr}\sigma) + 2\omega_{\rm cr}\cos(\omega_{\rm cr}\sigma) - 2\kappa\omega_{\rm cr}\sigma\big)\,, \\ a_2 &= \omega_{\rm cr}\cos(\omega_{\rm cr}\sigma)\big(\omega_{\rm cr}\sin(\omega_{\rm cr}\sigma) - 4\kappa\sin^2(\omega_{\rm cr}\sigma) + \omega_{\rm cr}^2\sigma\cos(\omega_{\rm cr}\sigma)\big)\,, \\ a_3 &= \cos(\omega_{\rm cr}\sigma)\big(\omega_{\rm cr}^2\sigma\sin(\omega_{\rm cr}\sigma) + 2\kappa\sin(\omega_{\rm cr}\sigma)\cos(\omega_{\rm cr}\sigma) - 2\kappa\omega_{\rm cr}\sigma\big)\,. \end{aligned} \tag{2.31}$$

For $\omega_{\rm cr} = 0$, the inequality $\frac{\partial^2|\Gamma|}{\partial\omega^2}(0) < 0$ is equivalent to $\frac{\partial Q}{\partial\omega}(0) = \alpha\big((1-2\kappa\sigma)\alpha + 2\beta - 2\kappa\big) > 0$, that yields the boundaries (2.14) and

$$\alpha = \frac{2(\kappa - \beta)}{1 - 2\kappa\sigma}\,. \tag{2.32}$$

That is, in this case, the gradient of the zero-frequency boundary is influenced by the delay

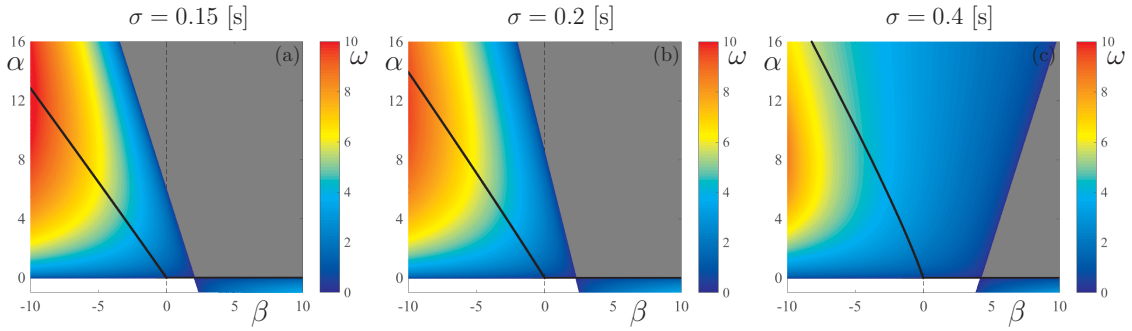

Figure 2.4: (a - c): Stability region of human-driven vehicles in (β, α)-plane for different σ values as indicated. The black curves are the plant stability boundaries. The dark gray areas are string stable. The color represents the highest frequency of string stability changes.

as shown by the boundary on the left of the gray string stable region in Fig. 2.2(a) and Fig. 2.3. Here the coloring corresponds to the solution of $Q(\omega) = 0$ for the frequency ω (cf. 2.29). Again, on the left string stability is lost at low frequencies while on the right high-frequency string instability occurs. The string stable domain is not closed from above but it still shrinks as the delay increases and it disappears when the delay exceeds

$$\sigma_{\mathrm{cr}} \approx \frac{0.785}{\kappa} = 0.785\, t_{\mathrm{h}}\,, \tag{2.33}$$

but this value cannot be calculated analytically.

When comparing Fig. 2.2 to Fig. 2.3 one may notice a trade-off. While the critical delay is significantly larger in the latter case, it also requires larger gains to make the systems string stable as the delay is increased. This may be difficult to achieve in practice due to the saturation of the actuators.

2.3.2 Linear stability analysis for two delay mismatches

Finally, the linearization of (2.25) about the equilibrium (2.6) takes the form

$$\begin{aligned} \dot{\tilde{h}}_i(t) &= \tilde{v}_{i+1}(t) - \tilde{v}_i(t)\,, \\ \dot{\tilde{v}}_i(t) &= \alpha\big(\kappa\tilde{h}_i(t-\sigma) - \tilde{v}_i(t)\big) + \beta\big(\tilde{v}_{i+1}(t-\sigma) - \tilde{v}_i(t)\big)\,, \end{aligned} \tag{2.34}$$

and the corresponding transfer function is given by

$$\Gamma(s) = \frac{\tilde{V}(s)}{\tilde{V}_{\mathrm{L}}(s)} = \frac{\beta s + \alpha\kappa}{\mathrm{e}^{s\sigma}\big(s^2 + (\alpha+\beta)s\big) + \alpha\kappa}\,. \tag{2.35}$$

Then the plant stability boundaries are given by (2.14) and

$$\begin{aligned} \alpha &= \frac{\Omega^2}{\kappa \cos(\Omega\sigma)}\,, \\ \beta &= \Omega \tan(\Omega\sigma) - \alpha\,, \end{aligned} \tag{2.36}$$

that are displayed as thick black curves in Fig. 2.4. According to Stépán's formulae [45] the system is plant stable above the curves and increasing the delay still deteriorates plant stability (though this effect is not so pronounced when comparing to the other two cases discussed above).

Again the string stability condition can be written as $\omega R(\omega) > 0$ where

$$R(\omega) = \omega^3 + \alpha^2\omega + 2\alpha\beta\omega - 2\alpha\kappa(\alpha+\beta)\sin(\omega\sigma) - 2\alpha\kappa\omega\cos(\omega\sigma)\,, \tag{2.37}$$

and substituting P with R in (2.18) results in the string stability boundaries

$$\begin{aligned} \alpha &= \hat{a} \pm \sqrt{\hat{a}^2 + \hat{b}}\,, \\ \beta &= \frac{\omega_{\mathrm{cr}}^3 + \alpha^2\omega_{\mathrm{cr}} - 2\alpha\kappa\big(\alpha\sin(\omega_{\mathrm{cr}}\sigma) + \omega_{\mathrm{cr}}\cos(\omega_{\mathrm{cr}}\sigma)\big)}{2\alpha\big(\kappa\sin(\omega_{\mathrm{cr}}\sigma) - \omega_{\mathrm{cr}}\big)}\,, \end{aligned} \tag{2.38}$$

where

$$\begin{aligned} \hat{a} &= \frac{-\omega_{\mathrm{cr}}^2\sigma\sin(\omega_{\mathrm{cr}}\sigma) - \kappa\sin(\omega_{\mathrm{cr}}\sigma)\cos(\omega_{\mathrm{cr}}\sigma) + \kappa\omega_{\mathrm{cr}}\sigma}{\sin(\omega_{\mathrm{cr}}\sigma) - \omega_{\mathrm{cr}}\sigma\cos(\omega_{\mathrm{cr}}\sigma)}\,, \\ \hat{b} &= \frac{\omega_{\mathrm{cr}}^2\big(3\kappa\sin(\omega_{\mathrm{cr}}\sigma) - \kappa\omega_{\mathrm{cr}}\sigma\cos(\omega_{\mathrm{cr}}\sigma) - 2\omega_{\mathrm{cr}}\big)}{\kappa\big(\sin(\omega_{\mathrm{cr}}\sigma) - \omega_{\mathrm{cr}}\sigma\cos(\omega_{\mathrm{cr}}\sigma)\big)}\,. \end{aligned} \tag{2.39}$$

However, we remark that these do not give stability boundaries in the physically realistic parameter ranges.

For $\omega_{\mathrm{cr}} = 0$, we obtain $\frac{\partial R}{\partial\omega}(0) = \alpha\big((1-2\kappa\sigma)\alpha + 2(1-\kappa\sigma)\beta - 2\kappa\big) > 0$, that yields the boundaries (2.14) and

$$\alpha = \frac{2\big(\kappa - (1-\kappa\sigma)\beta\big)}{1-2\kappa\sigma}\,. \tag{2.40}$$

That is, both the gradient and the position of the zero-frequency boundary is influenced by the delay which can be observed when looking at the left boundary in Fig. 2.2(a) and Fig. 2.3. As shown by the coloring, only low-frequency string instability occurs and the gray string stable domain is open from above and from the right. By investigating when the

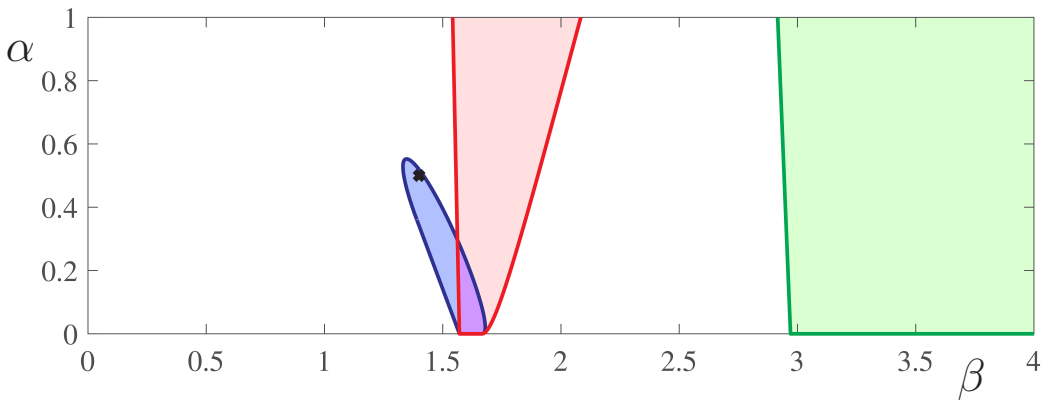

Figure 2.5: The blue, red, and green areas correspond to the string stability region for car-following model (2.9), (2.24), and (2.25), respectively. The driver reaction time is $\tau = 0.3$ [s] for (2.9) and $\sigma = 0.3$ [s] for (2.24) and (2.25). In all three cases, the range policy parameters are $h_{\text{st}} = 5$ [m], $h_{\text{go}} = 35$ [m], $v_{\max} = 30$ [m/s], and the range policy slope is $\kappa = \pi/2$ [1/s].

gradient of (2.40) becomes zero one can calculate the critical delay

$$\sigma_{\text{cr}} = \frac{1}{\kappa} = t_{\text{h}} \,, \tag{2.41}$$

above which the string stable domain disappears.

Again comparing Fig. 2.2, Fig. 2.3, and Fig. 2.4 one may notice that the critical delay increases but larger gains are required to make the system string stable which may not be possible due to the limitation of the actuators.

2.4 Car-following model for automated vehicles

Here we summarize the comparisons of the three car-following model candidates (2.9), (2.24), and (2.25), and explain why we prefer to select the exact human car-following model (2.9) in automated vehicle design.

To evaluate whether a car-following model can be used as a baseline in automated vehicle design, a main criterion is how the string stable region changes with delay time. By simply comparing the size of string stable areas (dark grey) in Fig. 2.2, Fig. 2.3, and Fig. 2.4, one may conclude that string stable regions in Fig. 2.4 occupy the largest areas and shrink slowest (cf. the critical delay (2.23), (2.33), (2.41)), and thus choose the car-following model with two delay mismatches (2.25) as the baseline design for an automated vehicle. However, the left string stability boundary (2.21) from the original car-following model is not influenced by delay time τ, i.e., small (α, β) values maintain string stability

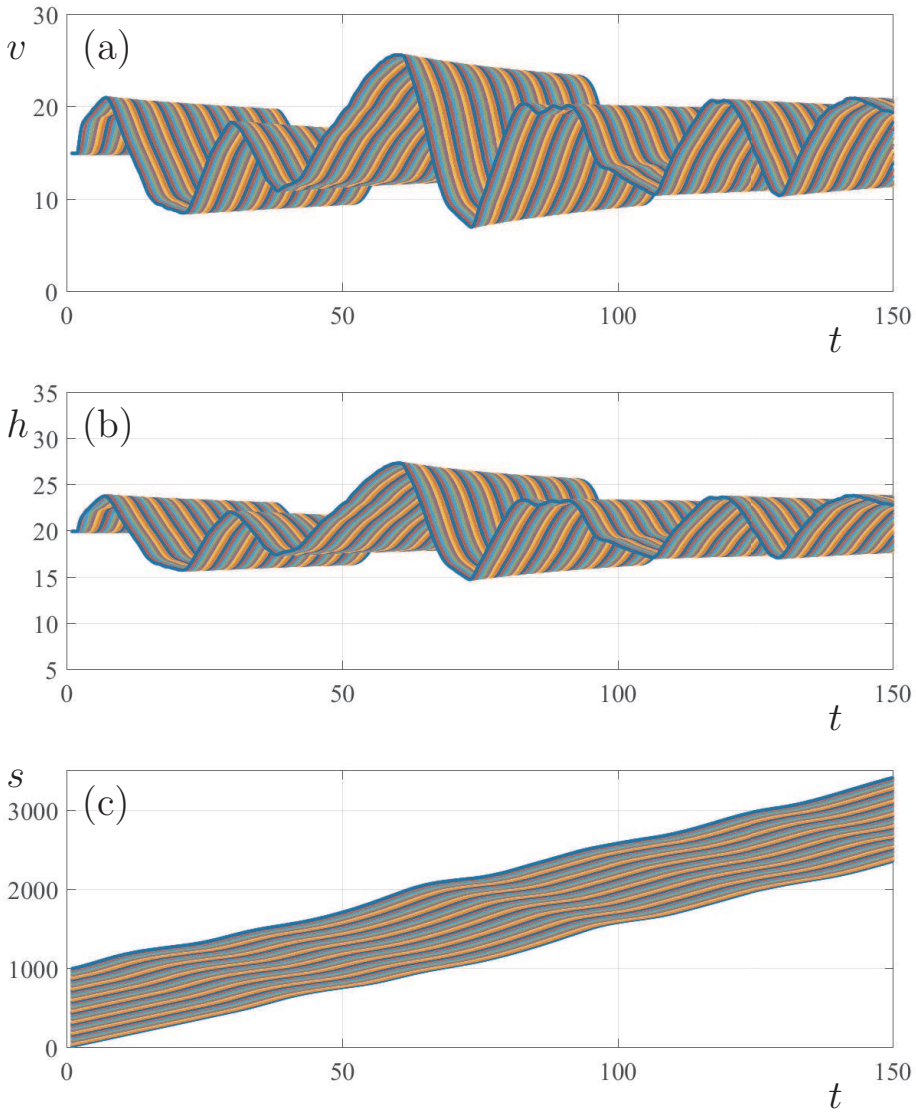

Figure 2.6: The velocity, headway, and position of a string of 50 vehicles with car-following model (2.3, 2.5, 2.9) under velocity disturbances in the traffic flow, where $\alpha = 0.5$ [1/s], $\beta = 1.4$ [1/s], $h_{\mathrm{st}} = 5$ [m], $h_{\mathrm{go}} = 35$ [m], $v_{\max} = 30$ [m/s], $\tau = 0.3$ [s]. Each colored curve corresponds to a vehicle trajectory.

as delay time increases. While the boundaries (2.32) and (2.40) from the modified models shift to the right as the delay time σ increases, which means that small $(\alpha,\ \beta)$ values are unable to maintain string stability. It is important to keep small $(\alpha,\ \beta)$ values string stable, for the engine/brake torque limits $(\alpha,\ \beta)$ to the lower left corner of the first quadrant. In Fig. 2.5 the string stable region for (2.9), (2.24) and (2.25) are shaded blue, red, and green, respectively. The delay time is $\tau = 0.3$ [s] for (2.9) and $\sigma = 0.3$ [s] for (2.24) and (2.25). While (2.25) has the largest stable area (green), it requires $\beta > 3$ [1/s], which will easily saturate the engine and brakes on average passenger cars. Similarly, even as the string stable area (red) from (2.24) is larger than the stable area (blue) from (2.9), the string stability is gained by increasing α and β, which might not be achievable on cars. In this sense, (2.9) is more suitable for implementation than (2.24) and (2.25).

To further demonstrate the benefits of the car-following model without delay mismatch (2.9) over the ones with mismatches (2.24) and (2.25), we simulate 50 cars in a string using each model and plot their velocity, headway, and position responses to speed fluctuations in the traffic flow. Fig. 2.6 shows the 50-car simulation using (2.3, 2.5, 2.9) with human gains $\alpha = 0.5$ [1/s], $\beta = 1.4$ [1/s], which is marked by the black cross in Fig. 2.5. (2.9) is string stable as shown in Fig. 2.5; cf. (2.21). Therefore, the headway and velocity fluctuations decrease as they propagate along the vehicle chain; see Fig. 2.6(a,b), and we see the traffic flow becoming smoother and no traffic jams are forming in Fig. 2.6(c).

Fig. 2.7 shows the 50-car simulation using (2.3, 2.5, 2.24) with the same human parameters as in Fig. 2.6. Note that in this case the car-following model is no longer string stable; cf. (2.32). Thus, in Fig. 2.7(a,b) the velocity and headway fluctuations are amplified through vehicles, and in Fig. 2.6(c) some "wrinkles" are forming, indicating possible stop-and-go traffic jams downstream.

Fig. 2.8 shows the 50-car simulation using (2.3, 2.5, 2.25) with the same human parameters as in Fig. 2.6. This car-following model is severely string unstable due to the delay mismatches; cf. (2.40). Therefore the velocity and headway fluctuations in Fig. 2.8(a,b) are significantly amplified along the vehicle chain, and the velocity of vehicles at the end of this chain varies between $v_{\max} = 30$ [m/s] and $v_{\min} = 0$ [m/s], indicating the formation of stop-and-go traffic jams. In Fig. 2.8(c) we can also see how the relatively mild disturbances to the head vehicle's motion lead to stop-and-go traffic jams, as the "wrinkles" grow deeper and propagate backwards along the traffic flow. This comparison of the macroscopic car-following behaviors shows that the car-following model without delay mismatch (2.9) should be favored over the ones with delay mismatch (2.24, 2.25) when designing automated vehicles.

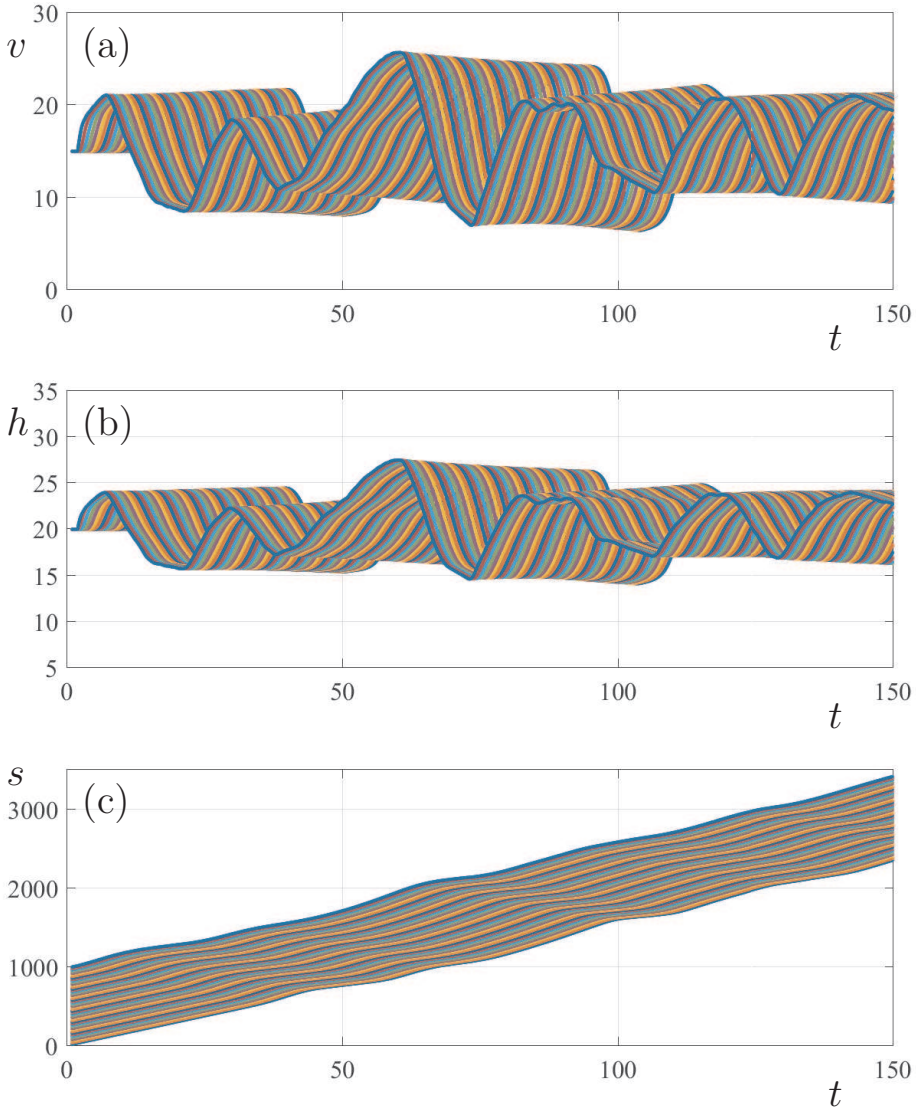

Figure 2.7: The velocity, headway, and position of a string of 50 vehicles with car-following model (2.3, 2.5, 2.24) under velocity disturbances in the traffic flow. The simulation parameters and notations are the same as in Fig. 2.6.

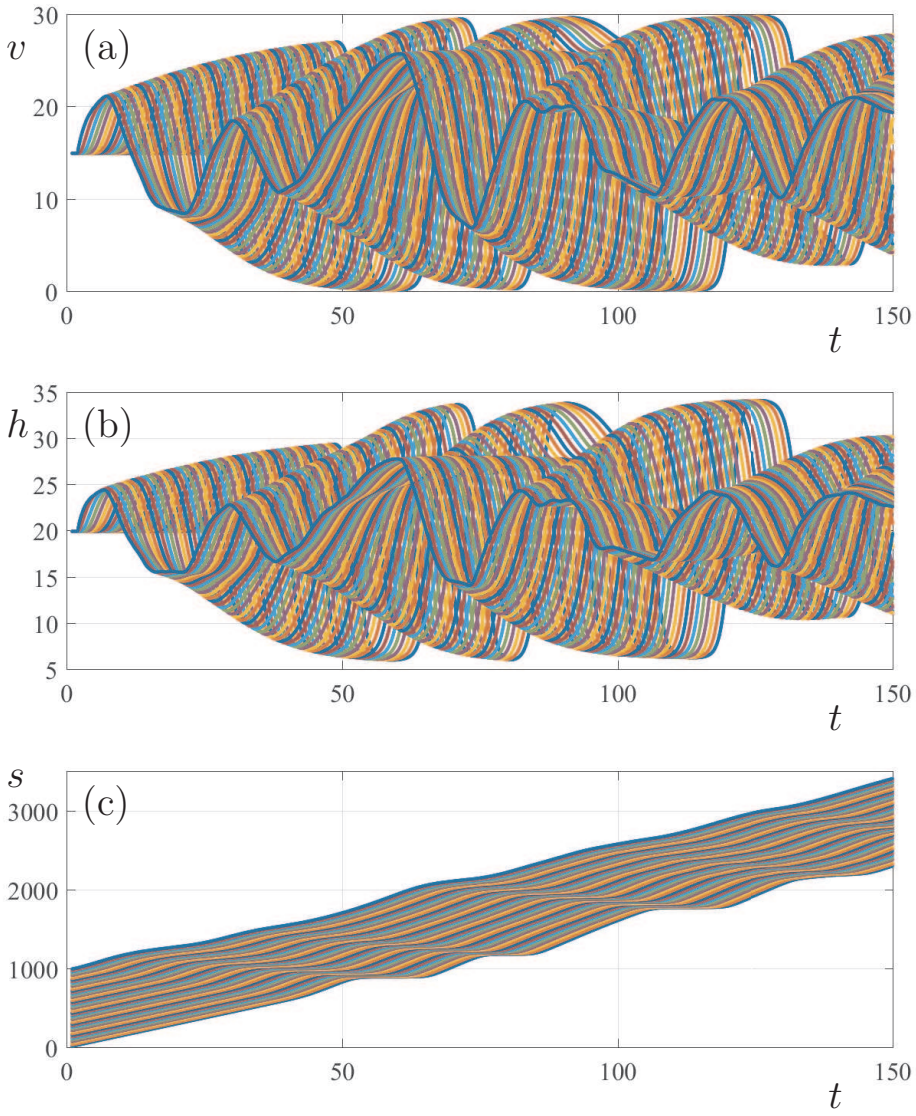

Figure 2.8: The velocity, headway, and position of a string of 50 vehicles with car-following model (2.3, 2.5, 2.25) under velocity disturbances in the traffic flow. The simulation parameters and notations are the same as in Fig. 2.6.

Thus, based on (2.9), the baseline car-following model for automated vehicle design is:

$$\begin{aligned} \dot{h}_i(t) &= v_{i+1}(t) - v_i(t)\,, \\ \dot{v}_i(t) &= \alpha\big(V(h_i(t-\tau)) - v_i(t-\tau)\big) + \beta\big(v_{i+1}(t-\tau) - v_i(t-\tau)\big)\,, \end{aligned} \tag{2.42}$$

where τ is the driver reaction time of the automated vehicle. In order to improve the string stability of (2.42) for $\tau > 0.3$ [s], in the following chapters, we will design connected cruise controllers based on V2V communication.

CHAPTER 3

Parameter identification in human car-following behavior

This chapter presents how to estimate parameters in the human car-following model (2.9) in real time as a connected automated vehicle receives headway and velocity data from preceding vehicles. The estimated parameters will then be used to design connected cruise controller for the automated vehicle in the forthcoming chapters.

Most existing connected automated vehicle design assume that the controller has a priori knowledge on the dynamics of the communicating vehicles [46], [47], [48]. While such an assumption may hold for CACC research where a platoon only contains automated vehicles [19], this assumption is invalid when the connected vehicle system contains human-driven vehicles, or when vehicles are allowed to join and leave the system. On the other hand, while the equilibrium (h^*, v^*) can be deduced from aggregated traffic data, no existing research has investigated the distribution and variation of α, β, κ, τ for individual drivers. Thus, it is necessary to consider online identification of car-following dynamics for preceding vehicles [49]. Although we assume that all non-CCC vehicles are human-driven for simplicity, the identification algorithms is able to deal with automated vehicles, as the latter is described by the same car-following model but with a smaller reaction time.

Since the driver reaction time has significant influence on the car-following dynamics (cf. Fig. 2.2), it is necessary to obtain both the human feedback gains α, β, range policy slope κ and the reaction time delay τ. Online parameter identification for problems without time delay has been well developed over the years [50]. While there also exist some results concerning parameter estimation in time delay systems [51], [52], estimating the delay time and feedback gains simultaneously is still challenging, as the convergence conditions are generally stringent [53], [54]. In Appendix B, an algorithm is proposed that requires a similar excitation condition as in non-delayed estimation problems and is able to converge simultaneously in both feedback gains and delay time with satisfactory speed. However, that estimator results in a system with state-dependent delay, and only local convergence

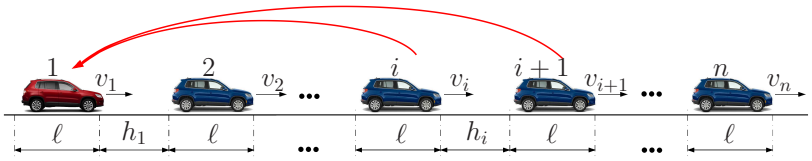

Figure 3.1: A string of n vehicles with a CCC vehicle at the tail receiving signals from human-driven vehicles ahead via wireless V2V communication. The red arrows denote information flow. The velocity of vehicle i is denoted by v_i. The bumper-to-bumper distance between vehicle i and vehicle $i+1$ is called the headway and denoted as h_i. The length of every vehicle is assumed to be l.

can be established. Thus, it may only be used to identify time-invariant parameters, and thus it is only applicable when identifying the parameters of automated vehicles.

Therefore, a connected automated vehicle needs a new online estimation algorithm to identify the car-following dynamics of human-driven vehicles from which it receives motion information. We propose a sweeping least squares method to simultaneously identify the feedback gains α, β, range policy slope κ, and driver reaction time τ in (2.11), based on the headway and velocity data collected via GPS and DSRC.

3.1 The sweeping least squares method

We consider the configuration in Fig. 3.1 where a group of vehicles travel on a single lane. We assume that vehicle 1 receives the motion information of two consecutive vehicles ahead through DSRC communication. By using signals from vehicles i and $i+1$, vehicle 1 is able to identify the dynamics of vehicle i and thus uses motion information of vehicle i for its longitudinal control. In this way, vehicle 1 can include feedback terms on the headway and velocity signals from multiple vehicles ahead, which we refer as connected cruise control.

The car-following dynamics of human-driven vehicle i can be described by (2.9) with range policy function $V_i(h_i) = \kappa_i h_i$, which is recalled here

$$\begin{aligned} \dot{h}_i(t) &= v_{i+1}(t) - v_i(t)\,, \\ \dot{v}_i(t) &= \alpha_i\big(\kappa_i h_i(t-\tau_i) - v_i(t-\tau_i)\big) + \beta_i\big(v_{i+1}(t-\tau_i) - v_i(t-\tau_i)\big)\,, \end{aligned} \tag{3.1}$$

by emphasizing the heterogeneity of drivers as the parameters α_i, β_i, τ_i and the range policy function $V_i(h)$ differ for each i. For simplicity we assume $h_{\mathrm{st},i} = 0$ [m] and $h < h_{\mathrm{go},i}$, so that this car-following model is truly linear. However, the least square method will remain valid without this assumption.

In order to identify the gains α_i, β_i, the range policy slope κ_i, and the reaction time τ_i, we assume that the GPS and speed data from vehicles i and $i+1$ are available via DSRC. We discretize the second equation in (3.1) using the explicit Euler method with time step Δt:

$$\frac{v_i[k+1]-v_i[k]}{\Delta t} = \alpha_i\big(\kappa_i h_i[k-m]-v_i[k-m]\big)+\beta_i\big(v_{i+1}[k-m]-v_i[k-m]\big)\,. \tag{3.2}$$

where $m=\mathrm{round}(\tau_i/\Delta t)$. Here $\Delta t = 0.1$ [s] as the communication frequency of DSRC is 10 Hz.

We consider N data points over a timespan of $N\Delta t$ and rewrite the unknown parameters α_i, β_i, κ_i in (3.2) as

$$a=-\alpha_i-\beta_i,\quad b=\alpha_i\kappa_i,\quad c=\beta_i\,. \tag{3.3}$$

We consider the possible range of driver reaction time $\tau_i\in[\tau_{\min},\tau_{\max}]$, and sample it such that $\tau_i=m\Delta t$. Then for each m, the least square estimation yields

$$\begin{bmatrix}a(m)\\ b(m)\\ c(m)\end{bmatrix} = (\mathbf{A}^{\mathrm{T}}\mathbf{A})^{-1}\mathbf{A}^{\mathrm{T}}\mathbf{B}(m), \tag{3.4}$$

where

$$\mathbf{A}=\begin{bmatrix}v_i[1] & h_i[1] & v_{i+1}[1]\\ \vdots & \vdots & \vdots\\ v_i[N] & h_i[N] & v_{i+1}[N]\end{bmatrix},\quad \mathbf{B}(m)=\frac{1}{\Delta t}\begin{bmatrix}v_i[m+2]-v_i[m+1]\\ \vdots\\ v_i[m+N+1]-v_i[m+N]\end{bmatrix}, \tag{3.5}$$

and the corresponding fitting error is

$$\mathbf{R}(m)=\mathbf{A}\begin{bmatrix}a(m)\\ b(m)\\ c(m)\end{bmatrix}-\mathbf{B}(m)\,. \tag{3.6}$$

Therefore, we obtain the estimated human reaction time as $\tilde{\tau}_i=\tilde{m}\Delta t$, where

$$\tilde{m}=\arg\,\min||\mathbf{R}(m)||_2\,. \tag{3.7}$$

Correspondingly the estimated human feedback gains are

$$\begin{aligned} \tilde{\alpha}_i &= -a(\tilde{m}) - c(\tilde{m})\,, \\ \tilde{\beta}_i &= c(\tilde{m})\,, \\ \tilde{\kappa}_i &= b(\tilde{m})/\tilde{\alpha}_i\,. \end{aligned} \tag{3.8}$$

Given reasonable N, each least square calculation (3.4, 3.5) exhibits a small computational load. Thus, the estimation algorithm (3.4, 3.5, 3.6, 3.7) can be implemented in real-time.

3.2 Data collection for algorithm validation

In order to identity the gains α_i, β_i, the range policy slope κ_i, and the reaction time τ_i in the optimal velocity model (3.1), we designed an experiment where a string of four human-driven vehicles run consecutively on a single-lane road; see Fig. 3.2. Each vehicle was equipped with a Commsignia on-board unit that provides GPS data and V2V communication based on DSRC. We record the vehicles' GPS coordinates (latitude ϕ, longitude λ, elevation r) and speed v every 0.1 [s]. Then the Haversine formula [55]

$$d_{ij} = 2\left(R + \frac{r_i + r_j}{2}\right) \arcsin \sqrt{\sin^2\left(\frac{\phi_i - \phi_j}{2}\right) + \cos\phi_i \cos\phi_j \sin^2\left(\frac{\lambda_i - \lambda_j}{2}\right)} \tag{3.9}$$

is used to calculate the great-circle distance d_{ij} between two GPS points (ϕ_i, λ_i, r_i) and (ϕ_j, λ_j, r_j). Here $R = 6371000$ [m] is the nominal radius of the earth.

Thus, the headway for vehicle i is

$$h_i = d_{i(i+1)} - l\,, \tag{3.10}$$

where l is the vehicle length. The headway and velocity profiles during one of the test runs are shown in Fig. 3.3. In Fig. 3.3(b) we can see that the velocity v_4 of the head vehicle (magenta curve) is almost constant before decreasing at $t \approx 125$ [s], while the velocities of following vehicles oscillate before 125 [s] and they also exhibit more severe deceleration (v_3 is the black curve, v_2 is the red curve, v_1 is the blue curve). This shows that human drivers amplify the velocity fluctuations propagating along the chain. Such amplifications may not only lead to stop-and-go traffic jams, but can also result in rear-end crashes in heavy traffic.

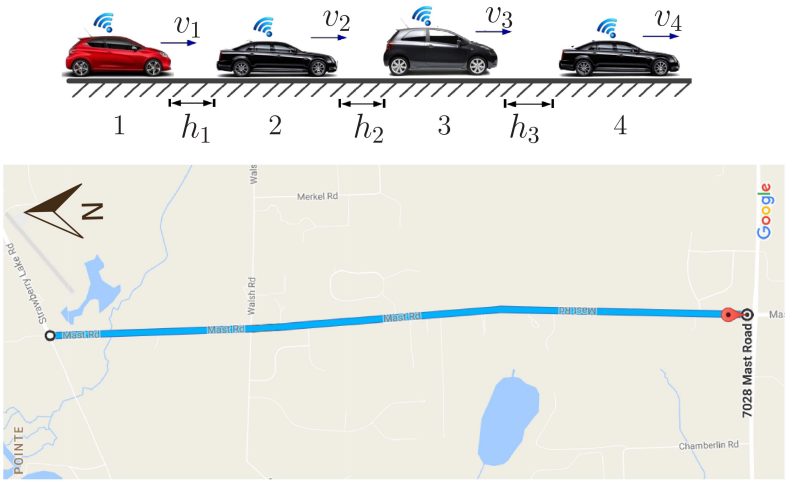

Figure 3.2: The experimental setup: a string of 4 vehicles on a single-lane road where all vehicles are equipped with GPS and DSRC devices. The test route is a 3-mile section of Mast Road near Dexter, MI.

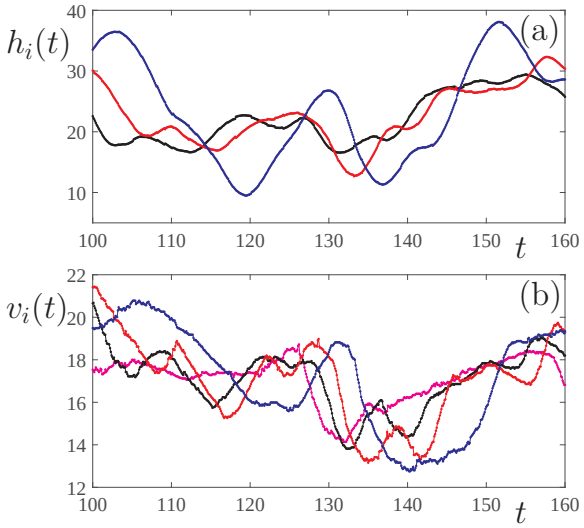

Figure 3.3: Headway and velocity profiles of the 4-vehicle string during one test run, where the black, red, and blue curves correspond to the headway and velocity of vehicles 3, 2, 1, respectively. The magenta curve in (b) is the velocity of the head vehicle 4.

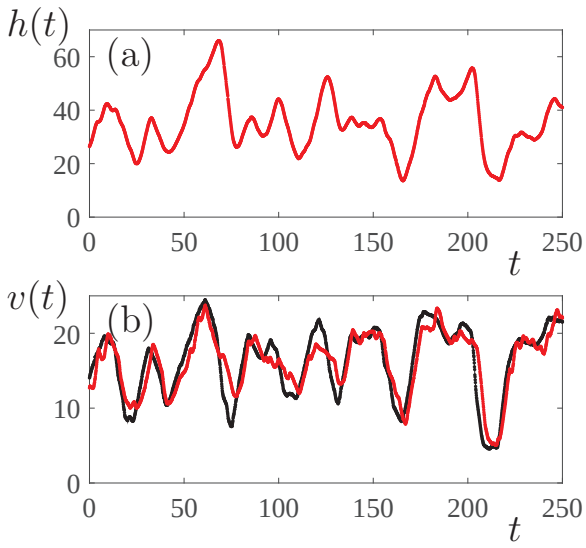

Figure 3.4: (a): Headway of vehicle 3 during one test run. (b): Velocity of vehicles 2 (black curve) and 3 (red curve) during one test run.

3.3 Variations of estimated driver parameters

The estimation algorithm (3.4, 3.5, 3.6, 3.7) produces the estimation $\tilde{\alpha}_i$, $\tilde{\beta}_i$, $\tilde{\kappa}_i$, $\tilde{\tau}_i$ for each data segment with size N. For example, at time stamp $t_0 = k_0\Delta t$ an estimation is obtained using the motion information $v_i[k]$, $h_i[k]$, and $v_{i+1}[k]$ for $k \in \{k_0 - N, \ldots, k_0 - 1\}$. As the car receives new motion information and the window shifts forward in time, the estimated values of $\tilde{\alpha}_i$, $\tilde{\beta}_i$, $\tilde{\kappa}_i$, and $\tilde{\tau}_i$ change. Thus, the estimated parameters will be time-varying.

As an example, we estimate the driver parameters α_3, β_3, κ_3, τ_3 for vehicle 3 using h_3, v_3, v_4. The headway h_3 is shown in Fig. 3.4(a), and the velocities v_3 and v_4 are shown in Fig. 3.4(b). We consider data length $N = 100$ and human reaction time $0 \leq \tau \leq 4$ [s], that is $m \in \{0, \ldots, 40\}$. The corresponding estimation starts at $t = 15$ [s], as shown in Fig. 3.5. As the data window moves forward in time, the estimated delay time $\tilde{\tau}$ varies between $\tau_{\max} = 2$ [s] and $\tau_{\min} = 0.2$ [s], and remains around 1 [s]. The estimated feedback gains $\tilde{\alpha}$ and $\tilde{\beta}$ are also time-varying. While they are significantly smaller than values previously assumed ($\alpha \approx 0.6$ [1/s], $\beta \approx 0.9$ [1/s]) based on macroscopic data [1], they remain positive for most of the time. Since the algorithm for $\tilde{\kappa}_i$ involves division (cf. (3.8)), we present $\tilde{\kappa}_i$ after filtering the noise using a third-order Savitzky-Golay filter with window size $N\Delta t/2 = 5$ [s]; see Fig. 3.5(d).

In Fig. 3.5, the human reaction time, feedback gains, and range policy slope exhibits stochastic variations. In the simplified case, a connected vehicle design can use their mean values, but it is desired to examine their distribution over a larger data set.

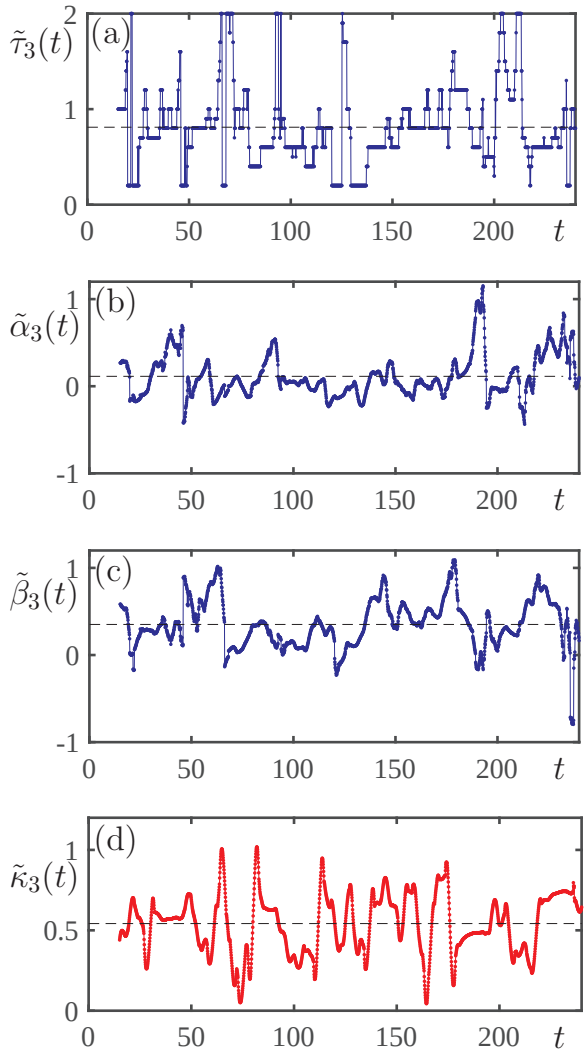

Figure 3.5: Estimated driver parameters of vehicle 3 starting from $t = 15$ [s] in a test run. The related headway and velocity information is shown in Fig. 3.4. (a): The time profile of estimated delay time $\tilde{\tau}_3$ with data window size $N = 100$, quantization step $\Delta t = 0.1$ [s], and the range of possible delay $\tau \in [0.2, 2]$ [s]. (b,c): The time profile of estimated feedback gains $\tilde{\alpha}_3$, $\tilde{\beta}_3$. (d): The time profile of estimated range policy slope $\tilde{\kappa}_3$. It is filtered by a third-order Savitzky-Golay filter with window size 5 [s]. The dashed black lines are the mean values.

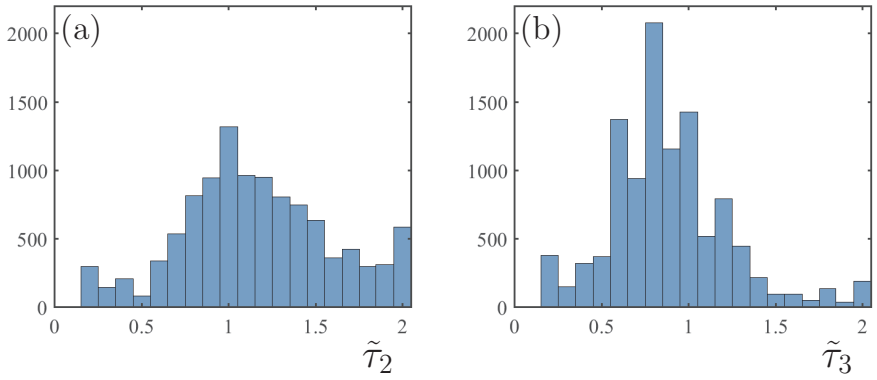

Figure 3.6: (a, b) Histogram of estimated driver reaction time for vehicles 2 and 3, respectively.

3.4 Distributions of estimated driver parameters

As we did four test runs on Mast Road and accumulated over 10000 estimates for every driver parameter in vehicles 2, 3, and 4, we are interested in the distribution of those parameters and the difference between the human drivers. In particular, we investigate the distribution of driver parameters for vehicles 2 and 3.

In Fig. 3.6(a,b) we show the histogram of estimated driver reaction time $\tilde{\tau}_2$ and $\tilde{\tau}_3$, respectively. Since it is infeasible to have driver reaction time smaller than 0.2 [s] in a human-driven vehicle, and there are few cases when the estimated delay is larger than 2 [s], we only consider the window $\tau \in [0.2, 2]$ [s]. It seems that a Gamma distribution is a suitable description for the reaction time. The mean and variance of the driver reaction time for car 2 is $(1.16, 0.19)$ [s], while for car 3 we have $(0.88, 0.12)$ [s].

It is noted that the driver for vehicle 2 has two years of driving experience while the driver for vehicle 3 has been driving for more than ten years. While a much larger sample is needed to establish the relation between driving proficiency and car-following parameters, the comparison between Fig. 3.6(a) and Fig. 3.6(b) provides some intuition on the variation between different drivers. Note that the experienced driver has smaller and more consistent reaction time, which may lead to a more reliable response to the traffic environment. However, the values of mean reaction time are not significantly different for the two drivers, which may be exploited in connected vehicle design.

In Fig. 3.7 we show the histograms of human feedback gains $\tilde{\alpha}_i$, $\tilde{\beta}_i$ and range policy slope $\tilde{\kappa}_i$ for vehicle 2 (panels (a,c,e)) and vehicle 3 (panels (b,d,f)). In each panel the histogram can be approximated by a Gaussian distribution with different mean and variance. By comparing Fig. 3.7(a,c,e) and Fig. 3.7(b,d,f) we can see that, while there exist some differences between the histograms, the human feedback gains $\tilde{\alpha}_i$, $\tilde{\beta}_i$ and range policy slope

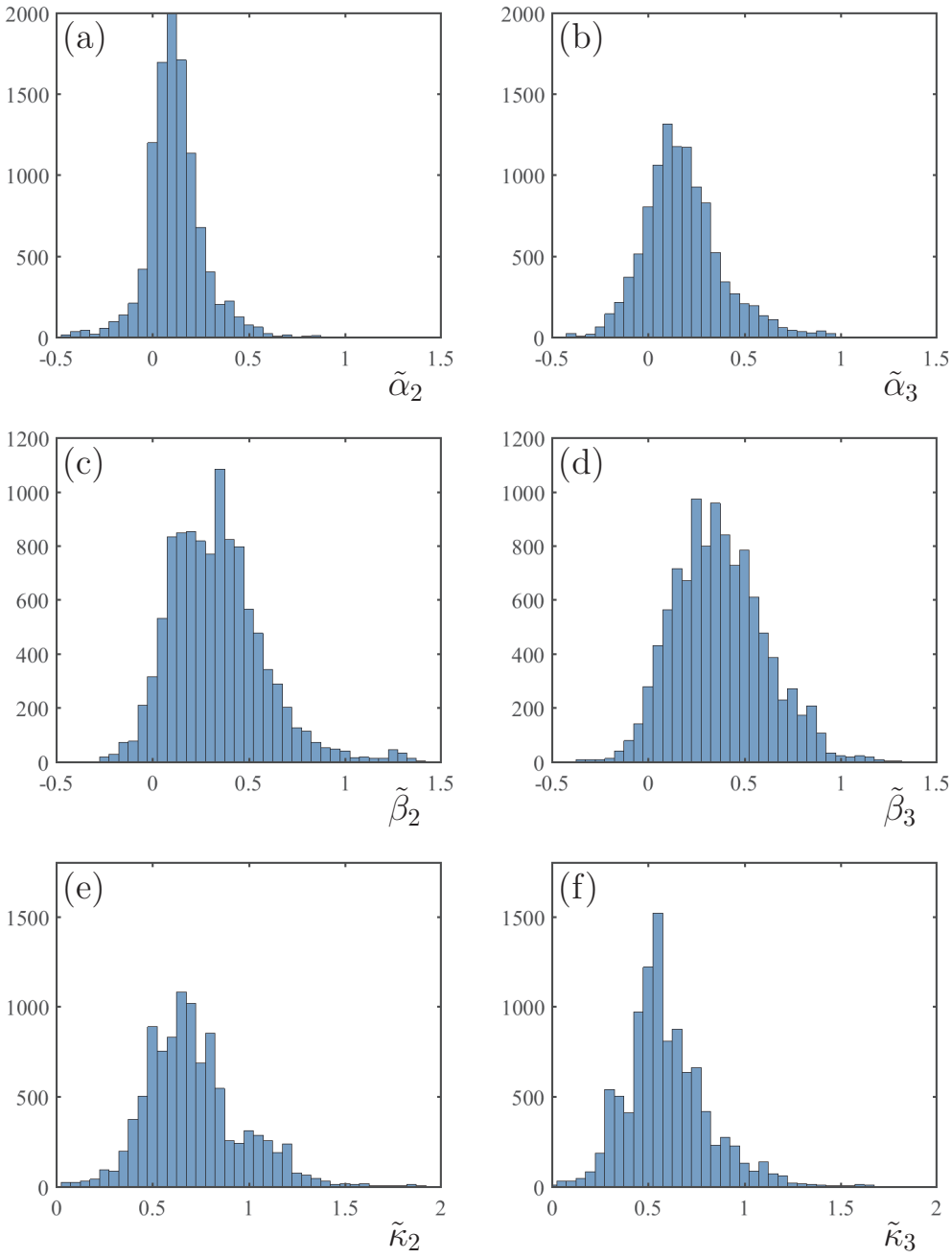

Figure 3.7: (a,c,e): Histogram of human feedback gains $\tilde{\alpha}_2$, $\tilde{\beta}_2$ and range policy slope $\tilde{\kappa}_2$ for vehicle 2. (b,d,f): Histogram of human feedback gains $\tilde{\alpha}_3$, $\tilde{\beta}_3$ and range policy slope $\tilde{\kappa}_3$ for vehicle 3.

$\tilde{\kappa}_i$ vary in the same range for the two drivers. Thus, it is feasible to use a nominal $\tilde{\alpha}$, $\tilde{\beta}$, $\tilde{\kappa}$ for both drivers in connected vehicle design.

3.5 Conclusion

In this chapter we designed an online algorithm for an automated vehicle to identify the dynamics of preceding vehicles via DSRC. This algorithm is able to obtain estimated parameters in real time, and is able to cope with time-varying human parameters. Both characteristics are crucial for application in connected vehicle system design.

From the four-car experiment we see that human parameters are time-varying, and appear to follow certain distributions. While the parameters vary between different drivers, their mean values can be considered as similar. Thus nominal values can be assumed when designing connected cruise control.

CHAPTER 4

Design of connected cruise control in a V2V-sparse environment

We consider connected automated vehicle design when there are only a few DSRC-equipped vehicles in the traffic flow. In order to have better longitudinal control than with the traditional adaptive cruise controller, the connected cruise controller has to take full advantage of the few motion signals it receives. In previous research [43, 46, 48, 56] headway and velocity information has been included in the connected cruise controller, but acceleration is seldom used since it requires taking derivatives of (noisy) velocity signals generated by the sensors. On the other hand, it has been shown that acceleration feedback can be effective in other applications involving human reaction time, e.g., human balancing [57]. Also, human drivers often use acceleration signals provided by the taillights, but they cannot determine the exact deceleration value, and can only observe the taillight of the vehicle immediately ahead. Using accurate acceleration information from multiple vehicles ahead may enable the host vehicle to better respond to traffic conditions.

In this chapter, we consider an acceleration-based CCC design, where the CCC controller receives acceleration information broadcasted by other vehicles and augments the human control commands based on the local headway and velocity information. We propose a control design where both the acceleration feedback gain and delay time are tuned as design parameters. We show that this design is robust against variations in human driver gains and reaction time, and we derive the ranges of feasible acceleration gains and delays that ensure overall string stability for the connected vehicle system. We note that this acceleration-based CCC design still applies for a connected and fully automated vehicle, where the local headway and velocity information will be monitored by sensors instead of human drivers.

The layout of this chapter is the following. In Section 4.1, we introduce the CCC controller with acceleration feedback. This model allows us to exploit the connectivity when only a few vehicles are providing their motion information through V2V communication.

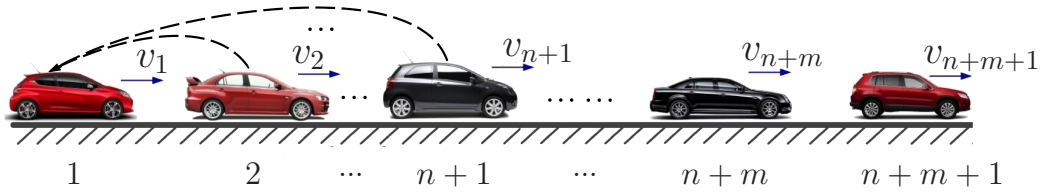

Figure 4.1: A heterogeneous string of $n+m+1$ vehicles with $n+m$ non-CCC vehicles and a CCC vehicle at the tail.

In Section 4.2, we linearize the system about the uniform flow equilibrium and analyze the head-to-tail string stability for different communication structures. The linear stability results are summarized using stability charts and the results are verified at the nonlinear level using numerical simulations. We conclude our results in Section 4.7.

4.1 Connected car-following models with acceleration feedback

We consider a string of $n+m+1$ vehicles traveling on a single lane as shown in Fig. 4.1. The preceding $n+m$ vehicles are not equipped with CCC and are assumed to be human-driven. The tail vehicle (the last vehicle in the string) implements acceleration-based CCC using acceleration signals received through V2V communication from n preceding vehicles. The car-following dynamics of the CCC vehicle is modeled by

$$\begin{aligned} \dot{h}_1(t) &= v_2(t) - v_1(t)\,, \\ \dot{v}_1(t) &= \alpha\big(V(h_1(t-\tau)) - v_1(t-\tau)\big) + \beta\big(v_2(t-\tau) - v_1(t-\tau)\big) + \sum_{k=2}^{n+1} \gamma_k\, \dot{v}_k(t-\sigma_k)\,, \end{aligned} \tag{4.1}$$

where τ represents the driver reaction time. The gains and the delays for the acceleration signals are denoted by γ_k and σ_k, $k = 2, \ldots, n+1$. Note that σ_k stands for the sum of communication delay and the delay in the controller when CCC is used to actuate the vehicle. Even though wireless V2V communication can be considered to be instantaneous, communication delay of magnitude 0.1 – 0.4 [s] is reported due to the intermittencies and packet drops [58], that shall be incorporated in the σ_k-s.

For simplicity, we consider that all human-driven vehicles are identical. Thus (4.1) and (2.9) contain the same range policy $V(h)$, headway gain α, relative velocity gain β, and

driver reaction time τ. To evaluate the robustness of our acceleration-based CCC design against uncertainties in driver parameters, we will investigate the dynamics for different values of α, β, and τ. On the other hand, the acceleration gains γ_k and delays σ_k will be used as design parameters. Indeed, these delays have minimal values as explained above, but we will show that they may be increased intentionally in order to obtain desired performance.

The longitudinal stability of a connected vehicle system also includes plant stability and string stability. The plant stability of the CCC vehicle is defined as for the human-driven vehicles: suppose that the vehicles whose signals are used by the CCC vehicle are driven at the same constant velocity, then the CCC vehicle is plant stable if its velocity approaches this constant velocity. Consequently, a connected vehicle system is said to be plant stable, if all vehicles approach the velocity of the head vehicle (the first vehicle in a string) when it is driven at a constant velocity.

However, string stability in a connected vehicle system cannot be discussed in a similar manner as in human-driven vehicle systems. A human-driven vehicle only reacts to the motion of the vehicle immediately ahead and a human-driven vehicle system can be decomposed into pairs of successive vehicles, while the control law of a CCC vehicle depends on several preceding vehicles in the system and the pair-wise decomposition is no longer valid. Moreover, many vehicles in the string can be purely human-driven, and their string stability cannot be ensured. Thus, the string stability of a heterogeneous system containing CCC and human-driven vehicles cannot be simplified to the string stability of pairs of successive vehicles. Here, we define the head-to-tail string stability and compare the velocity fluctuations of the head vehicle and the tail vehicle (that is assumed to be a CCC vehicle without loss of generality). This way, all the influences on the tail vehicle's motion are considered and we are able to compare the string stability of connected vehicle systems with different structures of connectivity that may include multiple CCC vehicles. Notice that this definition allows some following vehicles to amplify the velocity fluctuations of the leading vehicle, but fluctuations are attenuated when they reach the tail. In the remaining chapters of this dissertation, by abuse of terminology, we will refer to the head-to-tail string stability of a CCC vehicle as the string stability of a CCC vehicle.

4.2 Head-to-tail string stability for connected vehicle configurations

In this section, we focus on the dynamics of the connected vehicle system (2.9, 4.1) in the vicinity of an equilibrium that is achieved when all vehicles travel with the same constant velocity and maintain constant headways. While the equilibrium velocity v^* is determined by the head vehicle, the equilibrium headway h_i^* is obtained for each vehicle using the range policy $v^* = V_i(h_i^*)$. Since the range policies are assumed to be identical, we consider the uniform flow equilibrium (2.6) and the headway and velocity perturbations (2.10) for $i = 1, \dots, n+m+1$ and obtain the linearized dynamics of the CCC vehicle

$$\begin{aligned} \dot{\tilde{h}}_1(t) &= \tilde{v}_2(t) - \tilde{v}_1(t)\,, \\ \dot{\tilde{v}}_1(t) &= \alpha\big(\kappa\tilde{h}_1(t-\tau) - \tilde{v}_1(t-\tau)\big) + \beta\,\dot{\tilde{h}}_1(t-\tau) + \sum_{k=2}^{n+1} \gamma_k\ \dot{\tilde{v}}_k(t-\sigma_k)\,, \end{aligned} \tag{4.2}$$

while the linearized dynamics for human-driven vehicles $i = 2, \dots, n+m+1$ are given by (2.11).

We consider the velocity perturbation $\tilde{v}_{n+m+1}$ of the head vehicle as the input and the velocity perturbation $\tilde{v}_1$ of the tail vehicle as the output. Taking the Laplace transform of the system (4.2, 2.11) with zero initial conditions, and eliminating the velocities of the other vehicles and the headways, we obtain the head-to-tail transfer function

$$\Gamma(s) = \frac{\tilde{V}_1(s)}{\tilde{V}_{n+m+1}(s)} = \left(\frac{F(s)}{G(s)}\right)^{n+m} \left(1 + \sum_{k=2}^{n+1} \frac{F_k(s)\,(G(s))^{k-2}}{(F(s))^{k-1}}\right). \tag{4.3}$$

Here $\tilde{V}_1(s)$ and $\tilde{V}_{n+m+1}(s)$ denote the Laplace transform of $\tilde{v}_1(t)$ and $\tilde{v}_{n+m+1}(t)$, respectively, and we have

$$\begin{aligned} F(s) &= \beta s + \alpha\kappa\,, \\ F_k(s) &= \gamma_k s^2\, \mathrm{e}^{(\tau-\sigma_k)s}\,, \\ G(s) &= s^2\, \mathrm{e}^{\tau s} + (\alpha+\beta)s + \alpha\kappa\,. \end{aligned} \tag{4.4}$$

We remark that without V2V communication ($\gamma_k = 0 \;\Rightarrow\; F_k(s) = 0$, $k = 2, \dots, n+1$), the second term in (4.3) disappears and the transfer function degrades to $(F(s)/G(s))^{n+m}$, representing a string of human-driven vehicles.

Plant stability is determined by the denominator $G^{n+m}(s)$ of the transfer function (4.3),

that is, the acceleration feedback does not influence the plant stability inherited from the human driving model, and the plant stability of the connected vehicle system is also given by (2.15). In most cases, human car-following behavior is plant stable, and we can focus on ensuring head-to-tail string stability. In the following sections, we will depict this boundary using a circled curve when applicable.

At the linear level the necessary and sufficient condition for head-to-tail string stability is given by

$$P(\omega) = |\Gamma(\,\mathrm{i}\omega)|^2 - 1 < 0\,, \quad \forall \omega > 0\,, \tag{4.5}$$

where $\Gamma(\,\mathrm{i}\omega)$ is as defined by (4.3, 4.4). Since string stability is violated when the maximum of $P(\omega)$ is larger than 0, the stability boundary is given by the equations

$$\begin{aligned} P(\omega^{\mathrm{cr}}) &= 0\,, \\ \frac{\partial P(\omega^{\mathrm{cr}})}{\partial \omega} &= 0\,, \end{aligned} \tag{4.6}$$

subject to $\dfrac{\partial^2 P(\omega^{\mathrm{cr}})}{\partial \omega^2} < 0$, where ω^{cr} indicates the location of the maximum of $P(\omega)$. Note that $P(\omega)$ also depends on the system parameters $\alpha,\ \beta,\ \tau,\ \gamma_k,\ \sigma_k,\ k = 2, \ldots, n{+}1$, but they are not spelled out in (4.5, 4.6) for the sake of simplicity. To generate string stability boundaries in the (γ_k, α)-plane, we fix the other parameters and solve (4.6) for $(\gamma_k(\omega^{\mathrm{cr}}), \alpha(\omega^{\mathrm{cr}}))$. Since it is not possible to solve (4.6) analytically, we use the continuation package DDE-BIFTOOL [59] to obtain numerical solutions while varying the critical frequency ω^{cr}. In fact, we search for the equilibria of the mock differential equation

$$\begin{aligned} \dot{\gamma_k} &= P(\alpha, \gamma_k; \omega^{\mathrm{cr}})\,, \\ \dot{\alpha} &= \frac{\partial P(\alpha, \gamma_k; \omega^{\mathrm{cr}})}{\partial \omega}\,, \end{aligned} \tag{4.7}$$

that satisfy $\dfrac{\partial^2 P(\alpha, \gamma_k; \omega^{\mathrm{cr}})}{\partial \omega^2} < 0$. First, for a specific ω^{cr}, an initial guess for α and γ_k is corrected by the Newton-Raphson method. Then the obtained solution is used as initial guess for nearby values of ω^{cr}. This way the solution can be continued, and $\gamma(\omega^{\mathrm{cr}})$ and $\alpha(\omega^{\mathrm{cr}})$ can be obtained numerically.

Substituting $\omega^{\mathrm{cr}} = 0$ into equations (4.3), (4.4), and (4.6). We obtain $P(0) = 0$ and $\dfrac{\partial P(0)}{\partial \omega} = 0$. Thus, for zero frequency we require

$$\frac{\partial^2 P(0)}{\partial \omega^2} = -(n+m)(\alpha + 2\beta) + 2\kappa\Big(n + m - \sum_{k=2}^{n+1} \gamma_k\Big) < 0\,, \tag{4.8}$$

which is a necessary condition for string stability.

4.3 Monitoring the vehicle immediately ahead

We first consider the case when the CCC vehicle only receives acceleration signals from the vehicle immediately ahead, i.e., $n = 1$, $m = 0$ in (4.1, 2.11), cf. Fig.4.2(a). In this case, (4.3, 4.4) result in

$$\Gamma(s) = \frac{\tilde{V}_1(s)}{\tilde{V}_2(s)} = \frac{\gamma_2\, s^2\, \mathrm{e}^{(\tau-\sigma_2)s} + \beta s + \alpha\kappa}{s^2\, \mathrm{e}^{\tau s} + (\alpha+\beta)s + \alpha\kappa}\,, \tag{4.9}$$

and the string stability condition (4.5) can be written as

$$\begin{aligned} P(\omega) = (\gamma_2^2 - 1)\omega^4 + 2\Big((\alpha+\beta)\sin(\tau\omega) - \beta\gamma_2 \sin((\tau-\sigma_2)\omega)\Big)\omega^3 \\ - \alpha\Big(\alpha + 2\beta - 2\kappa\cos(\tau\omega) + 2\kappa\gamma_2\cos((\tau-\sigma_2)\omega)\Big)\omega^2 < 0\,. \end{aligned} \tag{4.10}$$

For $\omega^{\mathrm{cr}} > 0$ the corresponding boundaries are given by (4.6), while for $\omega^{\mathrm{cr}} \to 0$ (4.8) gives the conditions

$$\alpha > -2\beta + 2\kappa(1-\gamma_2)\,, \tag{4.11}$$

$$\alpha > 0\,. \tag{4.12}$$

As the acceleration gain γ_2 varies, the range of string stable parameters change for the gains α, β and the delays τ, σ_2. Here we fix the velocity gain $\beta = 0.9$ [1/s] and show this change using stability charts in the (γ_2, α)-plane for different values of the delays τ, σ_2 in Fig. 4.2. The string stability boundaries (4.6, 4.10), (4.11) and (4.12) are plotted as black curves enclosing the gray string stable area. The dashed lines in Fig. 4.2(c, e, g) show the sections of (4.11) that do not bound the string stable domains. Parameters outside the gray area result in that the transfer function (4.9) has magnitude larger than 1 at certain frequency ranges, which is represented by a color code: deep blue indicates low frequency and dark red indicates high frequency. More precisely, we solve (4.10) for frequencies $\omega_j^{\mathrm{P}} > 0$, $j = 1, 2, \ldots$ satisfying $P(\omega_j^{\mathrm{P}}) = |\Gamma(\,\mathrm{i}\omega_j^{\mathrm{P}})| - 1 = 0$ and color the points in the (γ_2, α)-plane according to the largest ω_j^{P}. In the vicinity of the string stability boundary, the color corresponds to the frequency at which string stability is lost.

Fig. 4.2(b, d, f) depicts the stability charts for $\tau = 0$, i.e., when the driver reaction time is omitted. In this case, for small values of γ_2, the string stability condition is given by (4.11), that is, string stability may be obtained by choosing sufficiently large α. When $\gamma_2 = 0$, we need $\alpha > 2(\kappa - \beta)$. As γ_2 increases, the required α decreases and becomes

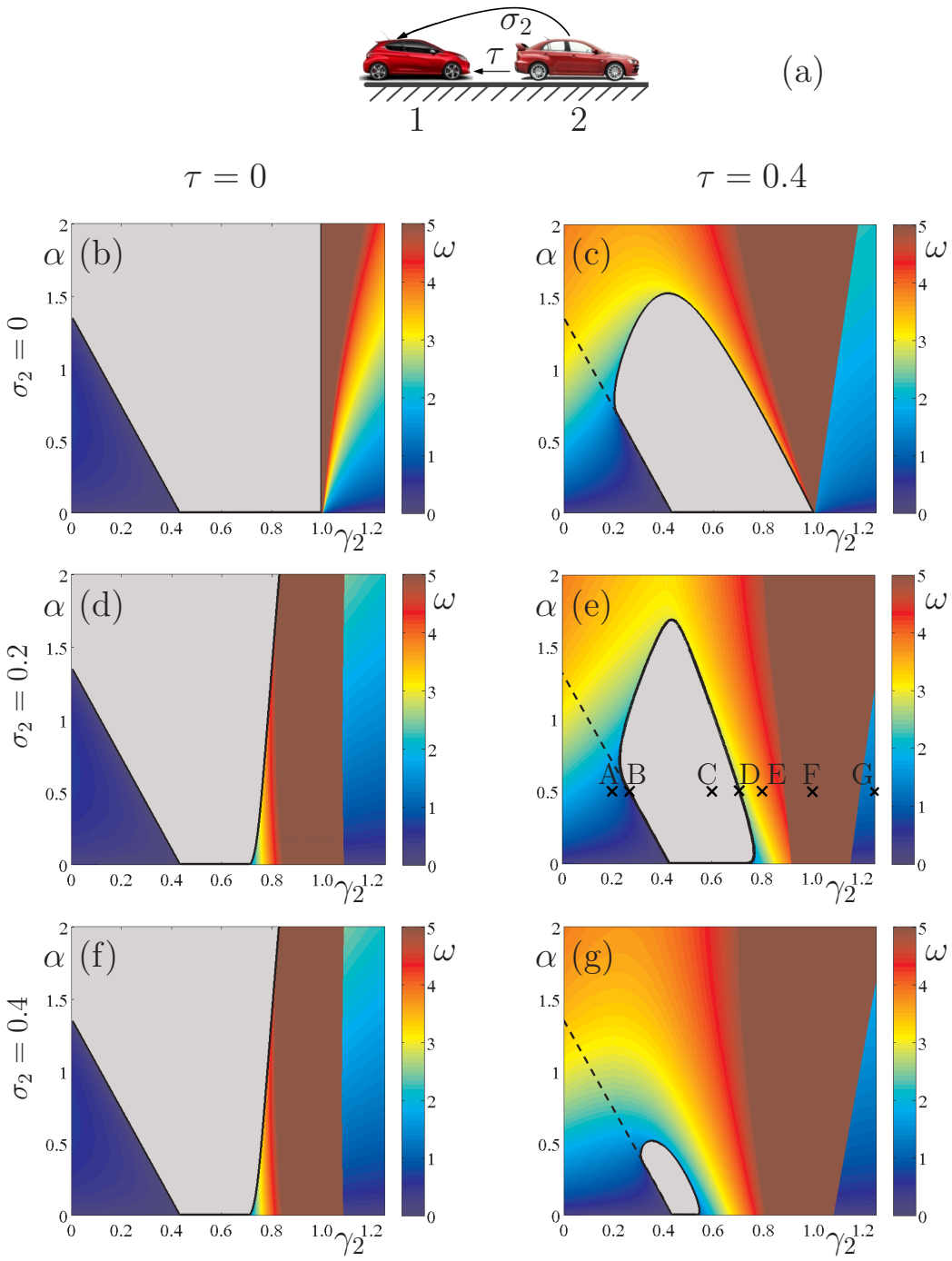

Figure 4.2: (a): Connectivity structure for a single-look-ahead vehicle system when a CCC vehicle monitors the car immediately ahead (i.e., $n = 1, m = 0$). The delays are indicated along the links. (b – g): String stability diagrams in the (γ_2, α)-plane for velocity gain $\beta = 0.9$ [1/s] and different driver reaction times τ and acceleration delays σ_2 as indicated. The gray areas are string stable. The color represents the highest frequency of string stability changes. The dashed lines in panels (b, d, f) represent the section of (4.11) that does not bound the string stable domain.

zero at $\gamma_2 = 1 - \beta/\kappa$. This boundary is independent of acceleration delay σ_2 as can be seen when comparing Fig. 4.2(b, d, f). In the vicinity of this boundary, deep blue color indicates that string stability is lost at low frequency $\omega^{\rm cr} \to 0$. On the other hand, large γ_2 results in string instability for high frequencies, as indicated by the dark red domains at the right side of Fig. 4.2(b, d, f). This boundary is at $\gamma_2 = 1$ when $\sigma_2 = 0$ (Fig. 4.2(b)), and it moves to the left decreasing the string stable domain as the acceleration delay σ_2 increases (Fig. 4.2(d, f)).

As shown in Fig. 4.2(c, e, g), the string stable area shrinks significantly when choosing realistic driver reaction time $\tau = 0.4$ [s]. In this case, the string stability can be maintained when choosing $\gamma_2 \approx 0.5$, but there is no string stable domain without acceleration feedback ($\gamma_2 = 0$). In fact, in the latter case the system is string unstable for all choices of human parameters α and β, since τ exceeds a critical delay time as will be discussed below. As the acceleration delay σ_2 increases, the string stability domain shrinks and disappears at $\sigma_2 \approx 0.55$ [s]. The critical frequencies of string stability loss are still low on the left and high on the right side, as can be seen from the coloring of the string unstable domains.

To illustrate the stability loss at different critical frequencies, we mark the points A–G in Fig. 4.2(e) and plot the magnitude of the transfer function $\Gamma(\,\mathrm{i}\omega)$ in Fig. 4.3 (cf. (4.9)). Comparing cases A, B and C, one can observe a string stability loss at low frequency ($\omega^{\rm cr} \to 0$). In case A, the system is string unstable for low frequencies $\omega < \omega^{\rm P} \approx 1.22$ [rad/s] (Fig. 4.3(a)), which corresponds to the blue color at A in Fig. 4.2(e). Point B is located at the string stability boundary (Fig. 4.3(b)), that is, $\dfrac{\partial^2 |\Gamma(0)|}{\partial \omega^2} = 0$ (cf. (5.53, 4.8)), while the system is string stable in case C as shown in Fig. 4.3(c). Comparing cases C, D and E, a string stability loss at higher frequency can be observed. Point D is located at the string stability boundary, that is, $\Gamma(\omega^{\rm cr}) = 1$, $\dfrac{\partial |\Gamma(\omega^{\rm cr})|}{\partial \omega} = 0$ (cf. (5.53, 5.54)) where $\omega^{\rm cr} \approx 2.34$ [rad/s]. In case E, the system is string unstable in the frequency domain $\omega_1^{\rm P} < \omega < \omega_2^{\rm P}$ (Fig. 4.3(e)) and the orange color at point E in Fig. 4.2(e) corresponds to the higher frequency $\omega_2^{\rm P} \approx 3.61$ [rad/s].

Notice that as $\omega \to \infty$, the magnitude of the transfer function approaches γ_2, i.e., $\lim_{\omega\to\infty} |\Gamma(\,\mathrm{i}\omega)| = \gamma_2$ (cf. (4.9)), which is indicated by the dotted horizontal lines in Fig. 4.3. Therefore, as $\gamma_2 \to 1^-$, string instabilities appear in higher frequency ranges. This is demonstrated in Fig. 4.3(f) where the system is string unstable for $\omega_1^{\rm P} < \omega < \omega_2^{\rm P}$ and $\omega_3^{\rm P} < \omega < \omega_4^{\rm P}$. The dark red color at point F in Fig. 4.2(e) corresponds to the highest frequency $\omega_4^{\rm P} \approx 22.97$ [rad/s]. Finally we remark that when $\gamma_2 > 1$ the system becomes unstable for almost all frequencies as demonstrated in Fig. 4.3(g), where the system is unstable for $\omega > \omega^{\rm P} \approx 1.18$ [rad/s], which corresponds to the coloring at G in Fig. 4.2(e).

Now we evaluate the robustness of the design against uncertainties of the human gains

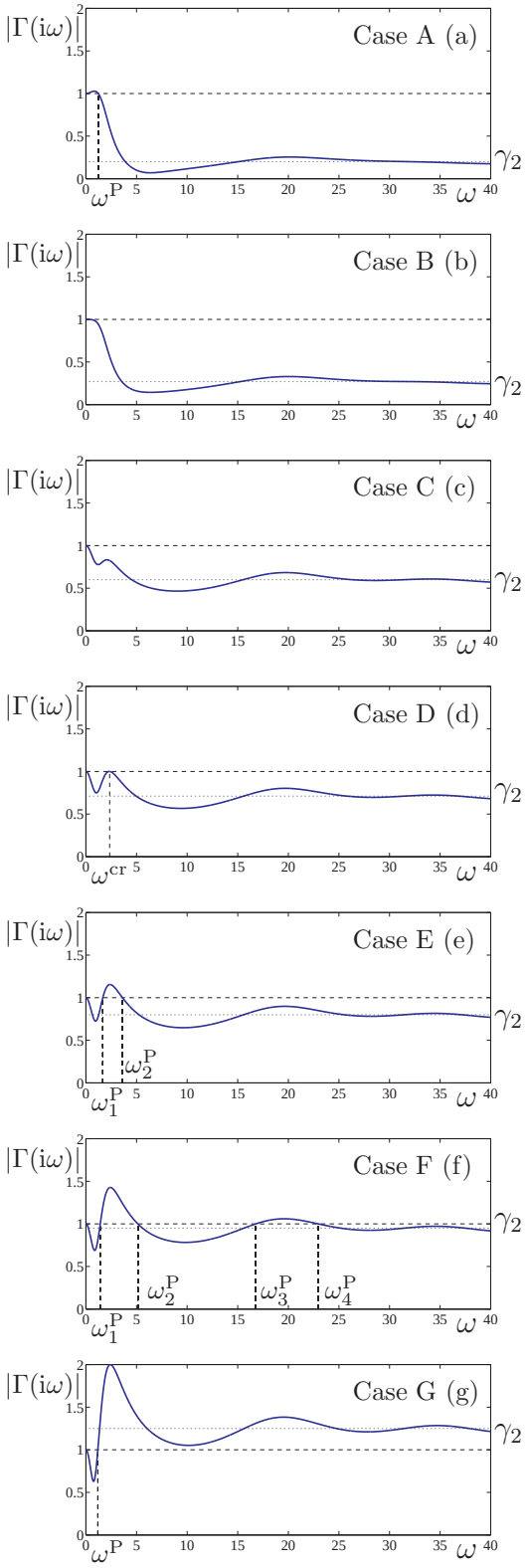

Figure 4.3: Magnitude of the transfer function when a CCC vehicle monitors the car immediately ahead (i.e., $n = 1, m = 0$) for the points marked (A–G) in Fig. 4.2(e). The horizontal dashed line at 1 indicates the threshold for string stability. The horizontal dotted line shows the magnitude of transfer function when the frequency approaches infinity.

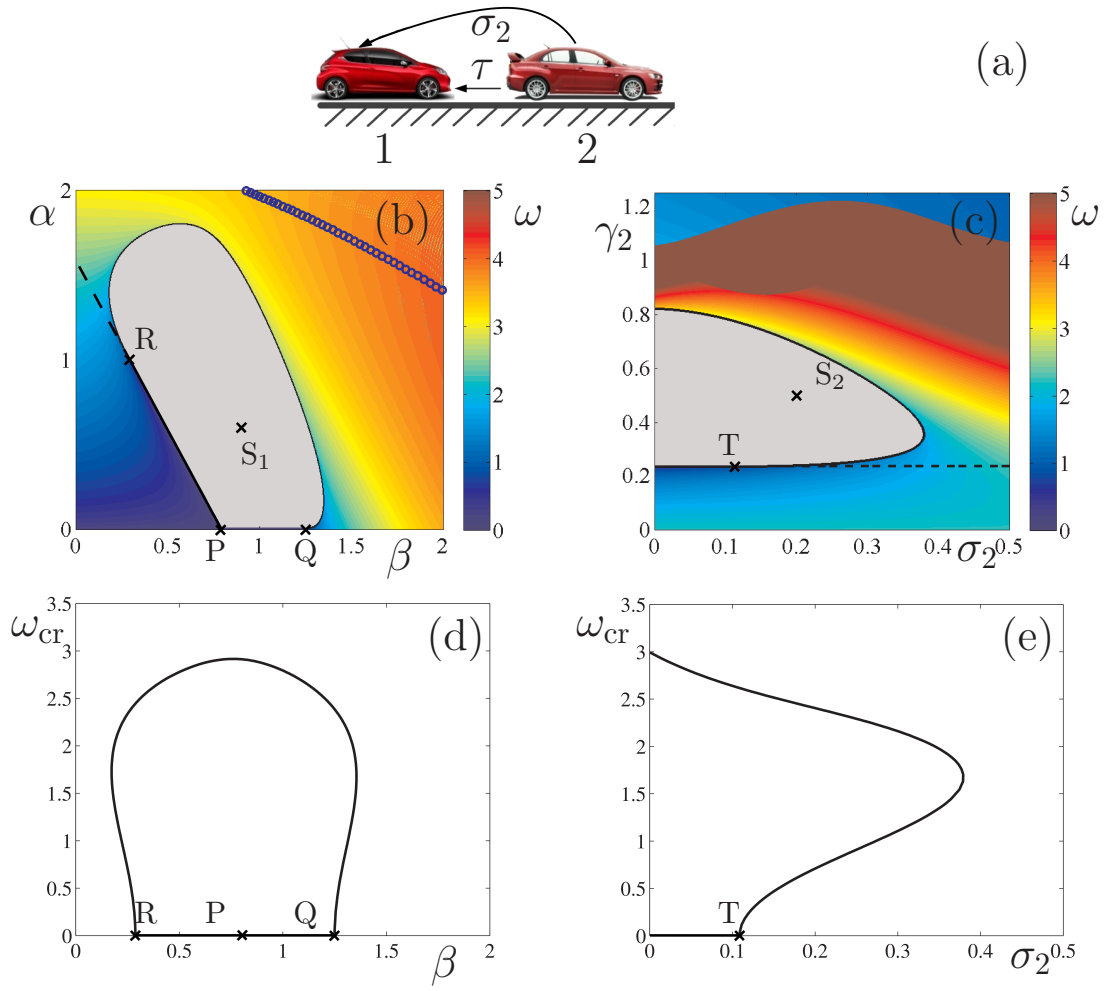

Figure 4.4: (a): Connectivity structure for a single-look-ahead vehicle system with delays indicated along the links. (b and c): String stability diagrams in the (β, α)-plane and (σ_2, γ_2)-plane for $\tau = 0.4$ [s]. In panel (b), points P, Q and R locate the intersections of (4.11), (4.12) and (5.54, 4.10), while S_1 is located at $(\alpha, \beta) = (0.6, 0.9)$ and corresponds to the parameters used in panel (c). In panel (c), point T locates the intersection between (4.11) and (5.54, 4.10), while S_2 is located at $(\sigma_2, \gamma_2) = (0.2, 0.5)$ and corresponds to the parameters used in panel (b). (d and e): The corresponding critical frequencies along the string stability boundaries. The same color coding is used as in Fig. 4.2.

α and β. In the right panels of Fig. 4.2, it can be observed that the stable regions cover the largest α interval for $\gamma_2 \approx 0.5$. Moreover, when every packet is delivered, DSRC communication has the average communication delay $\sigma_2 = 0.15$ [s], which goes up to $\sigma_2 = 0.2$ [s] when every second packet is lost [46, 60]. To evaluate the robustness, we use $\gamma_2 = 0.5$ and $\sigma_2 = 0.2$ [s]. Stability charts in the (β, α)-plane are shown in Fig. 4.4(b) for $\gamma_2 = 0.5$, $\sigma_2 = 0.2$ [s], $\tau = 0.4$ [s]. The circled line is the plant stability boundary (2.15), below which the parameters ensure plant stability. The gray string stable region (enveloped by the curves (5.54, 4.10), (4.11) and (4.12)) covers a large portion of realistic driver parameters α and β, showing the robustness of acceleration-based CCC design against variations in driver gains.

Now we investigate the robustness against the increase of the driver reaction time τ. The sections PR, PQ and QR of the string stability boundary in Fig. 4.4(b) are given by (4.11), (4.12), and (4.6, 4.10), respectively. The corresponding critical frequencies $\omega^{\rm cr}$ are shown in Fig. 4.4(d). Notice that at the codimension-two points P, Q and R the critical frequency is zero. When τ is increased, the string stable domain decreases, and the points P, Q and R move closer to each other. At the critical reaction time $\tau_{\rm cr}$, they collide at a codimension-three point, and for $\tau > \tau_{\rm cr}$ there exists no combination of gains α and β that can ensure string stability.

Using (4.6, 4.10), (4.11) and (4.12), we may obtain the location of P, Q, R as

$$\begin{aligned}
(\beta_{\rm P}, \alpha_{\rm P}) &= \big((1-\gamma_2)\kappa, 0\big)\,, \\
(\beta_{\rm Q}, \alpha_{\rm Q}) &= \left(\frac{\gamma_2^2 - 1}{2(\gamma_2(\tau-\sigma_2)-\tau)}, 0\right), \\
(\beta_{\rm R}, \alpha_{\rm R}) &= \left(\frac{r_1}{r_3}, \frac{r_2}{r_3}\right),
\end{aligned} \tag{4.13}$$

where

$$\begin{aligned}
r_1 &= (1-\gamma_2)\left(\gamma_2\left(1-2\kappa^2(\tau-\sigma_2)^2\right) + 2\kappa\tau(\kappa\tau-2)+1\right), \\
r_2 &= \big(2\kappa(\sigma_2-\tau)-1\big)\gamma_2^2 + 2\kappa(2\tau-\sigma_2)\gamma_2 - 2\kappa\tau + 1\,, \\
r_3 &= \gamma_2(\tau-\sigma_2)\big(\kappa(\tau-\sigma_2)+1\big) + \tau(1-\kappa\tau)\,.
\end{aligned} \tag{4.14}$$

For $r_2 = 0$, P, Q, and R coincide, which yields the critical driver reaction time

$$\tau_{\rm cr} = \frac{1}{2\kappa} + \frac{\gamma_2}{1-\gamma_2}\left(\frac{1}{\kappa} - \sigma_2\right) = \frac{t_{\rm h}}{2} + \frac{\gamma_2}{1-\gamma_2}\big(t_{\rm h} - \sigma_2\big)\,. \tag{4.15}$$

Without acceleration feedback ($\gamma_2 = 0$), $\tau_{\rm cr} = \dfrac{1}{2\kappa} = \dfrac{t_{\rm h}}{2}$, which means that human drivers can only maintain string stability when travelling at a time headway that is at least twice as long as their reaction time. This result also corresponds to the conclusion in [48, 61]. The second term is positive for the physically realistic parameters $0 < \gamma_2 < 1$ and $\sigma_2 < t_{\rm h}$ and thus the critical delay $\tau_{\rm cr}$ increases with γ_2. In particular, considering $\gamma_2 = 0.5$ without communication delay ($\sigma_2 = 0$ [s]), we have $\tau_{\rm cr} = 1.5 t_{\rm h}$, which is a three-fold increase. Even if the communication delay is as large as the human reaction time, we have $\tau_{\rm cr} = t_{\rm h}$, which is a two-fold increase. This demonstrates the benefits of acceleration-based driver assistance systems.

When $\gamma_2 > 1$, with $\sigma_2 < t_{\rm h}$, we can have $\tau_{\rm cr} < 0$ [s], as in Case G in Fig. 4.2(e). Finally, when $\gamma_2 \to 1^-$, $\tau_{\rm cr}$ approaches infinity. The cost of such a dramatic increase is the robustness of string stability: α and β both approach zero, resulting in a follower driving with its leader's acceleration (delayed by σ_2). In this case, the headway and velocity feedback terms are missing and thus the vehicle is unable to maintain a velocity-dependent headway.

The available values of the design parameters σ_2 and γ_2 are shown in Fig. 4.4(c) for human parameters $(\beta, \alpha) = (0.9, 0.6)$ (point $\rm S_1$ in panel (b)) while the corresponding critical frequencies $\omega^{\rm cr}$ are shown in Fig. 4.4(e). Since the plant stability is not influenced by acceleration feedback, the choice of human parameters ensures plant stability for all values of σ_2 and γ_2. The string stability boundaries (4.6, 4.10) and (4.11) envelope the gray string stable area, where the point $\rm S_2$ corresponds to the design parameters used in panel (b). Notice that γ_2 shall be chosen between 0.2 and 0.8 and σ_2 shall be smaller than 0.4 [s] to ensure string stability. According to the coloring, choosing smaller γ_2 leads to string instability at low frequencies, while larger γ_2 or longer σ_2 results in higher-frequency string instabilities.

Using $\gamma_2 \approx 0.5$ ensures robustness against the variations of the acceleration delay σ_2. In fact, we will show that $\gamma_2 \approx 0.5$ is a good choice for all other connectivity structures considered in the rest of this paper. Moreover, we will also demonstrate that this holds for all γ_k. While there is no formal proof why this value shall be chosen, this seems to be a compromise between using no acceleration feedback ($\gamma_k = 0$) and using excessive acceleration feedback ($\gamma_k > 1$) which typically leads to high-frequency instabilities.

Note that one may also use a ring configuration to obtain the results shown above, which gives analogous results and also provides insight into the pattern formation along the road as explained in Appendix C.1.

4.4 Monitoring two vehicles ahead

Since an advantage of connectivity is providing the host vehicle with non-local information, we consider larger vehicle systems and exploit the use of acceleration feedback from vehicles farther downstream. For simplicity, we start with the case where a CCC vehicle follows two other non-CCC vehicles and receives acceleration signals from the vehicle immediately ahead, as shown in Fig. 4.5(a). Therefore, using $n = 1$, $m = 1$ in (5.46) results in the transfer function

$$\Gamma(s) = \left(\frac{F(s)}{G(s)}\right)^2 \left(1 + \frac{F_2(s)}{F(s)}\right) . \tag{4.16}$$

The resulting stability charts are shown in the (β, α)-plane and (σ_2, γ_2)-plane in Fig. 4.5(b) and (c), respectively. The corresponding critical frequencies are plotted in Fig. 4.5(d) and (e). The same notation is used as in Fig. 4.4, but the color code is omitted for simplicity.

When comparing Fig. 4.4(b) and Fig. 4.5(b), it can be observed that when a CCC vehicle only monitors acceleration information of the vehicle immediately ahead, the longer link is more sensitive to uncertainties in the human parameters α and β. Moreover, comparing Fig. 4.4 (c) and Fig. 4.5(c) shows that, while the stable domain is still around $\gamma_2 \approx 0.5$, the domain of feasible control parameters decreases for the larger system, including the largest allowable acceleration delay. These results are not surprising: for the larger system the CCC vehicle needs to eliminate the perturbations that have been amplified by the human-driven vehicle 2, which is string unstable for $\tau = 0.4$ [s] (for any combination of α and β) since τ is larger than the critical time delay $\tau_{\rm cr} \approx 0.32$ [s], cf. (4.15) for $\gamma_2 = 0$.

Notice that there are points along the stability boundaries that correspond to multiple critical frequencies. Some of these codimension-two points corresponds to zero frequencies, but there are points where one or both critical frequencies are non-zero. In the latter case, when crossing the string stability boundary at these points (from stable to unstable), stability is lost in two distinct frequency domains and we obtain Bode plots that are qualitatively similar to the one in Fig. 4.3(f).

If the CCC vehicle receives acceleration feedback from the head vehicle as shown in Fig. 4.6(a), i.e., $n = 2$, $m = 0$ in (5.46), the transfer function becomes

$$\Gamma(s) = \left(\frac{F(s)}{G(s)}\right)^2 \left(1 + \frac{F_3(s)G(s)}{(F(s))^2}\right) . \tag{4.17}$$

Comparing the string stable areas in Fig. 4.5(b) and Fig. 4.6(b), one may observe that using longer acceleration link provides better robustness against uncertainties in the human parameters α and β. The comparison of Fig. 4.5(c) and Fig. 4.6(c) reveals that the accel-

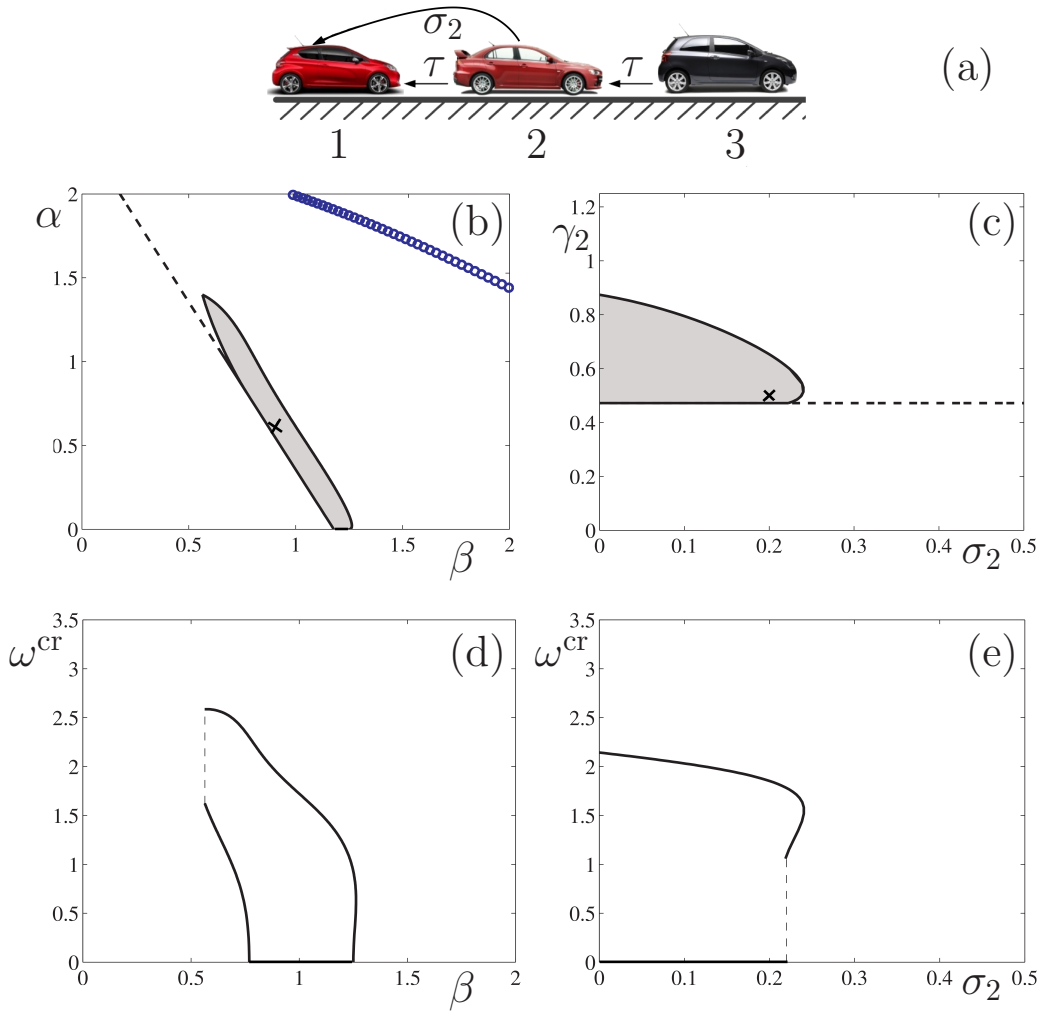

Figure 4.5: (a): Connectivity structure with the delays indicated along the links. (b and c): Stability diagrams in the (β, α)-plane and in the (σ_2, γ_2)-plane (the string stable domains are shaded). The cross in panel (b) is located at $(\beta, \alpha) = (0.9, 0.6)$ and corresponds to the parameters chosen in panel (c). Similarly, the cross in panel (c) is located at $(\sigma_2, \gamma_2) = (0.2, 0.5)$ and corresponds to the parameters chosen in panel (b). (d and e): Critical frequencies along the string stability boundaries. For all panels, $\tau = 0.4$ [s] is used. The notation is the same as in Fig. 4.4, except that the color code is omitted for simplicity.

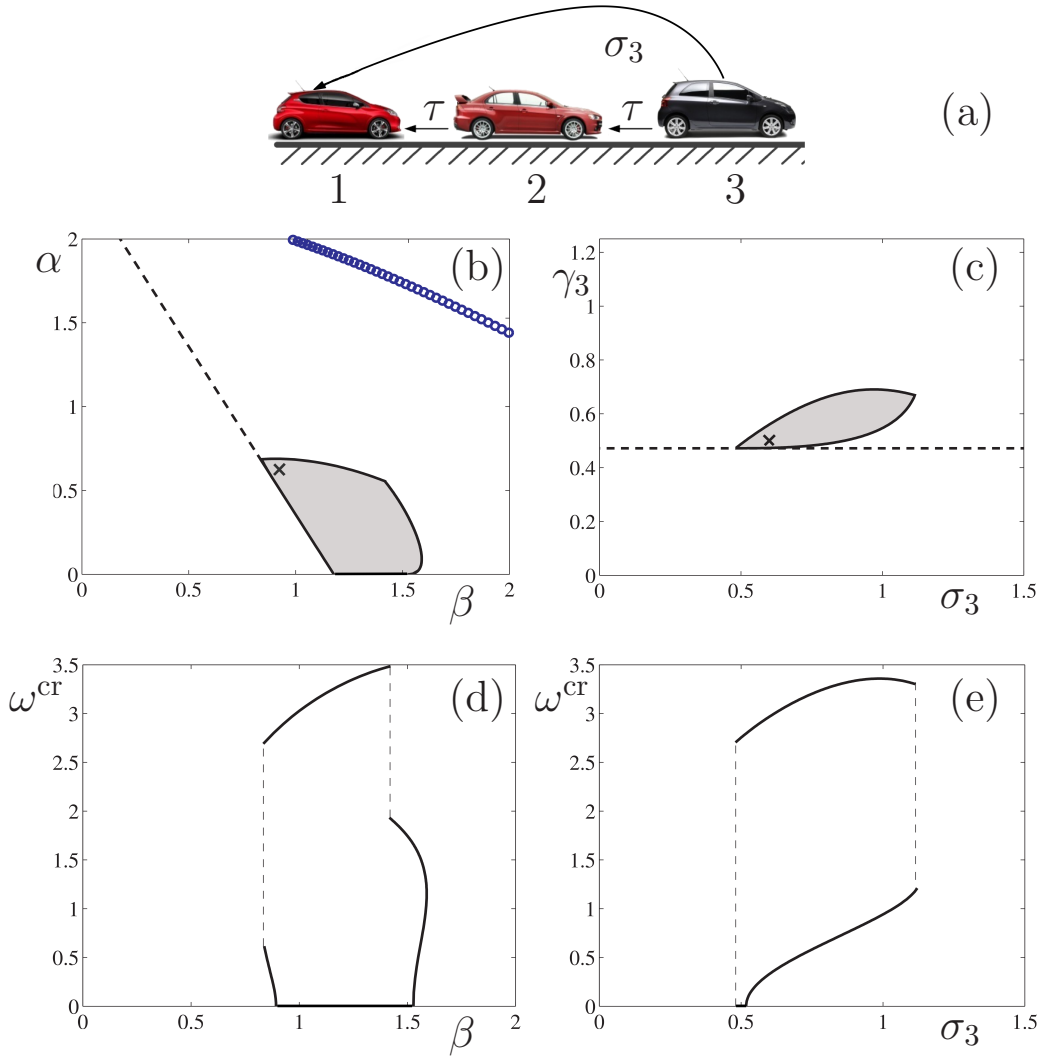

Figure 4.6: (a): Connectivity structure with the delays indicated along the links. (b and c): Stability diagram in (β, α)- plane and the (σ_2, γ_2)-plane (the string stable domain is shaded). The cross in panel (b) is located at $(\beta, \alpha) = (0.9, 0.6)$ and corresponds to the parameters chosen in panel (c). Similarly, the cross in panel (c) is located at $(\sigma_2, \gamma_2) = (0.6, 0.5)$ and corresponds to the parameters chosen in panel (b). (d and e): Critical frequencies along the string stability boundaries. For all panels $\tau = 0.4$ [s] is used and the notation is the same as in Fig. 4.5.

eration feedback gains γ_k, $k = 2, 3$, shall be kept around 0.5, independent of the source of acceleration signals. Surprisingly, for the longer communication links, the delay in the acceleration feedback loop must be larger than zero. This means that one must artificially increase the delay in order to maintain string stability. Therefore, it is not necessary to use higher communication rate, but instead the received packets shall be stored in buffers, so that they can be used at suitable times. The frequency plots shown in Fig. 4.6(d,e) are similar to Fig. 4.5(d,e), but there are multiple codimension-two points with non-zero critical frequencies.

4.5 Using multiple communication links for a CCC vehicle

Because the average broadcast range of DSRC is a few hundred meters, a CCC vehicle may acquire acceleration information from a car that is approximately four vehicles ahead when driving at highway speed. Thus, here we consider a string of five cars, place the CCC vehicle at the tail, and assume that it receives acceleration signals from two other vehicles downstream: the vehicle immediately ahead and another vehicle that is 2, 3, or 4 vehicles ahead; see Fig. 4.7(a) for the different configurations labelled A, B, and C. Considering these configurations in (4.3), we obtain the head-to-tail transfer functions

$$\Gamma_{\mathrm{A}}(s) = \left(\frac{F(s)}{G(s)}\right)^4 \left(1 + \frac{F_2(s)}{F(s)} + \frac{F_3(s)G(s)}{(F(s))^2}\right), \tag{4.18}$$

$$\Gamma_{\mathrm{B}}(s) = \left(\frac{F(s)}{G(s)}\right)^4 \left(1 + \frac{F_2(s)}{F(s)} + \frac{F_4(s)\,(G(s))^2}{(F(s))^3}\right), \tag{4.19}$$

$$\Gamma_{\mathrm{C}}(s) = \left(\frac{F(s)}{G(s)}\right)^4 \left(1 + \frac{F_2(s)}{F(s)} + \frac{F_5(s)\,(G(s))^3}{(F(s))^4}\right). \tag{4.20}$$

Figure 4.7(b,c) show the stability diagrams for $\alpha = 0.6$ [1/s], $\beta = 0.9$ [1/s], $\tau = 0.4$ [s]. Figure 4.7(b) depicts the stability charts in the (γ_k, σ_k)-plane for $k = 3, 4, 5$, when $\gamma_2 = 0.5$ and $\sigma_2 = 0.2$ [s]. The different configurations are distinguished by color. Notice again that while γ_k shall be kept around 0.5 for $k = 3, 4, 5$, σ_k shall increase with k to ensure string stability. That is, the controller has to delay acceleration signals coming from distant vehicles, and the longer the link is, the larger delays are needed. Similarly, Fig. 4.7(c) shows the stability charts in the (σ_k, σ_2)-plane when $\gamma_k = 0.5$ for $k = 2, 3, 4, 5$, using the same labeling and color scheme. While the range of σ_2 is not significantly in-

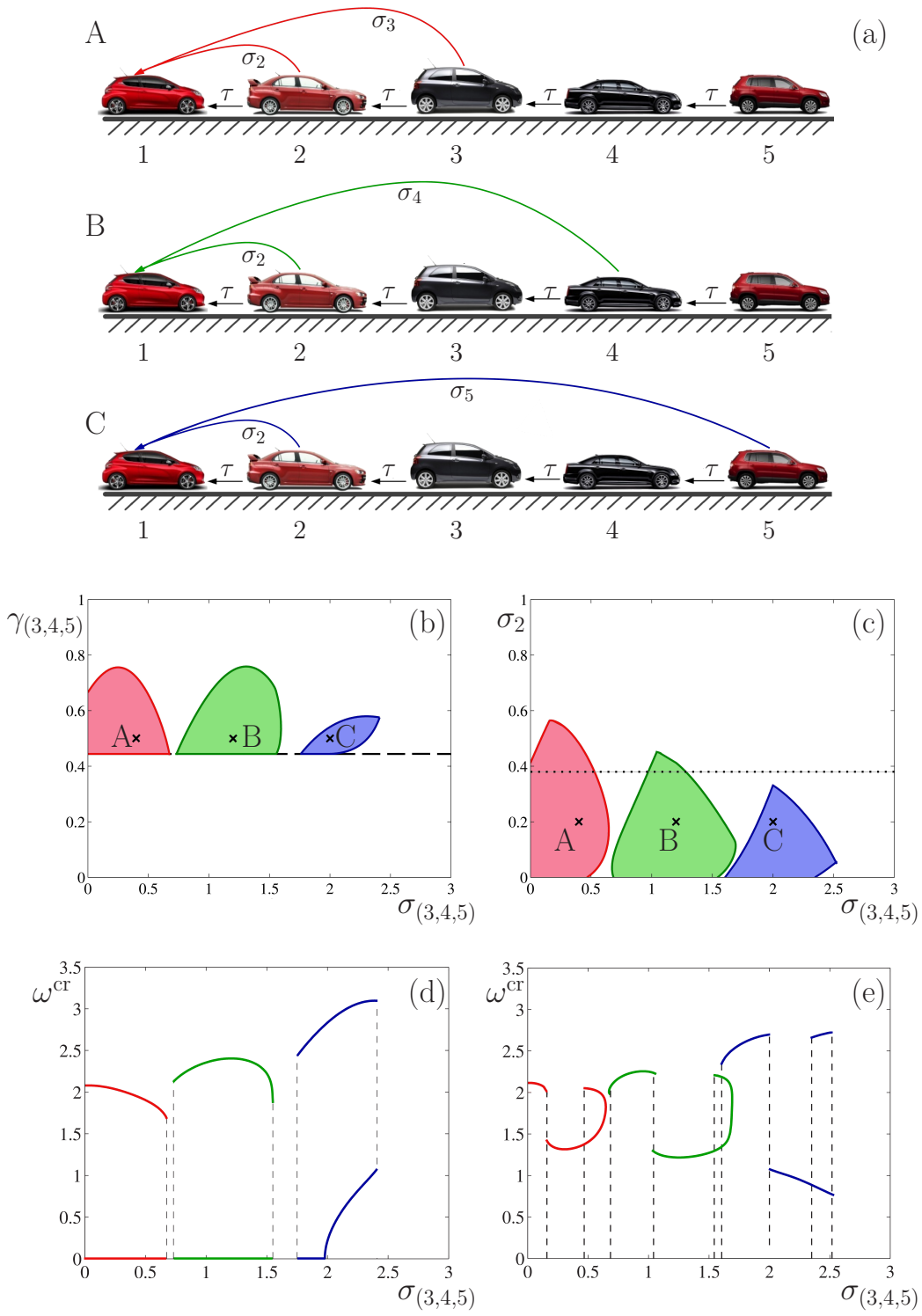

Figure 4.7: (a): Three connectivity configurations A, B and C for a five-car system with a CCC vehicle at the tail using two acceleration links. The delays are marked along the links. (b and c): String stability diagrams in the (σ_k, γ_k)-plane for $\sigma_2 = 0.2$ [s], $\gamma_2 = 0.5$, and in the (σ_k, σ_2)-plane for $\gamma_2 = \gamma_3 = \gamma_4 = \gamma_5 = 0.5$. The three configurations are indicated by labels and color. (d and e): The critical frequencies along the string stability boundaries. Color code is used to help identify the domains and the frequencies.

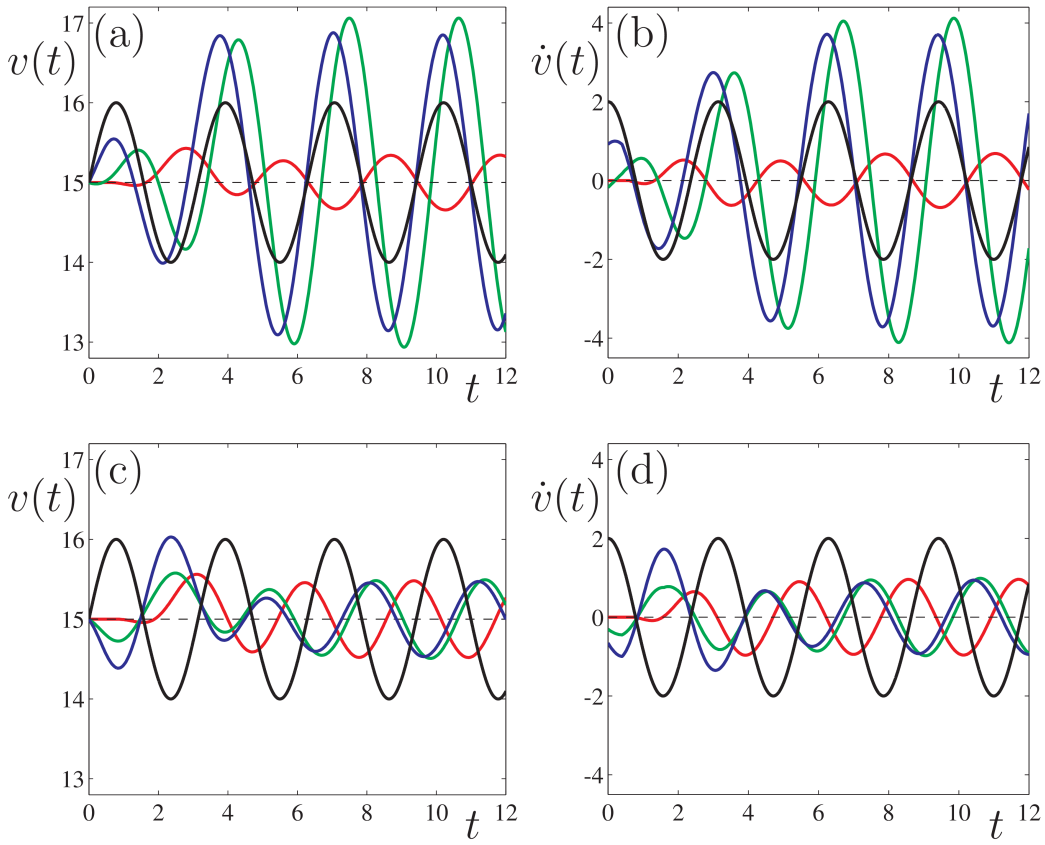

Figure 4.8: Velocity and acceleration responses of the CCC vehicle to a sinusoidal velocity perturbation of the head vehicle (black curves) for configurations A (red), B (green), and C (blue) shown in Fig. 4.7(a). The human parameters α, β, and τ are the same as in Fig. 4.7 and the acceleration gains are kept $\gamma_k = 0.5$ for all k-s. Panels (a, b) are for acceleration delays $\sigma_k = 0.2$ [s], $k = 2, 3, 4, 5$, while panels (c, d) are for delays $\sigma_2 = 0.2$ [s], $\sigma_3 = 0.4$ [s], $\sigma_4 = 1.2$ [s], $\sigma_5 = 2.0$ [s] (cf. the crosses A, B and C in Fig. 4.7(b, c)). The initial headways and velocities are set at the equilibrium where $h^* = 20$ [m], $v^* = 15$ [m/s] along the time interval $[-\max\{\sigma_k, \tau\}, 0]$ for all vehicles.

fluenced by the link length, longer links shall have larger delays to maintain string stability. Figure 4.7(d,e) give the critical frequencies along the string stability boundaries, showing multiple codimension-two points with two distinct frequencies. Notice that the codimension-two points in Fig. 4.7(d) have at least one critical frequency at zero, while all codimension-two points in Fig. 4.7(e) have only non-zero critical frequencies.

To illustrate the necessity of increasing the delay, we perform simulations for the three configurations A, B and C shown in Fig. 4.7(a) using the nonlinear model (4.1, 2.11). We use the same α, β and τ parameters as in Fig. 4.7. Figure 4.8 depicts the velocity and acceleration responses of the CCC vehicle when all cars start with equilibrium headway and velocity along the time interval $[-\max\{\sigma_k, \tau\}, 0]$. The head vehicle applies a periodic

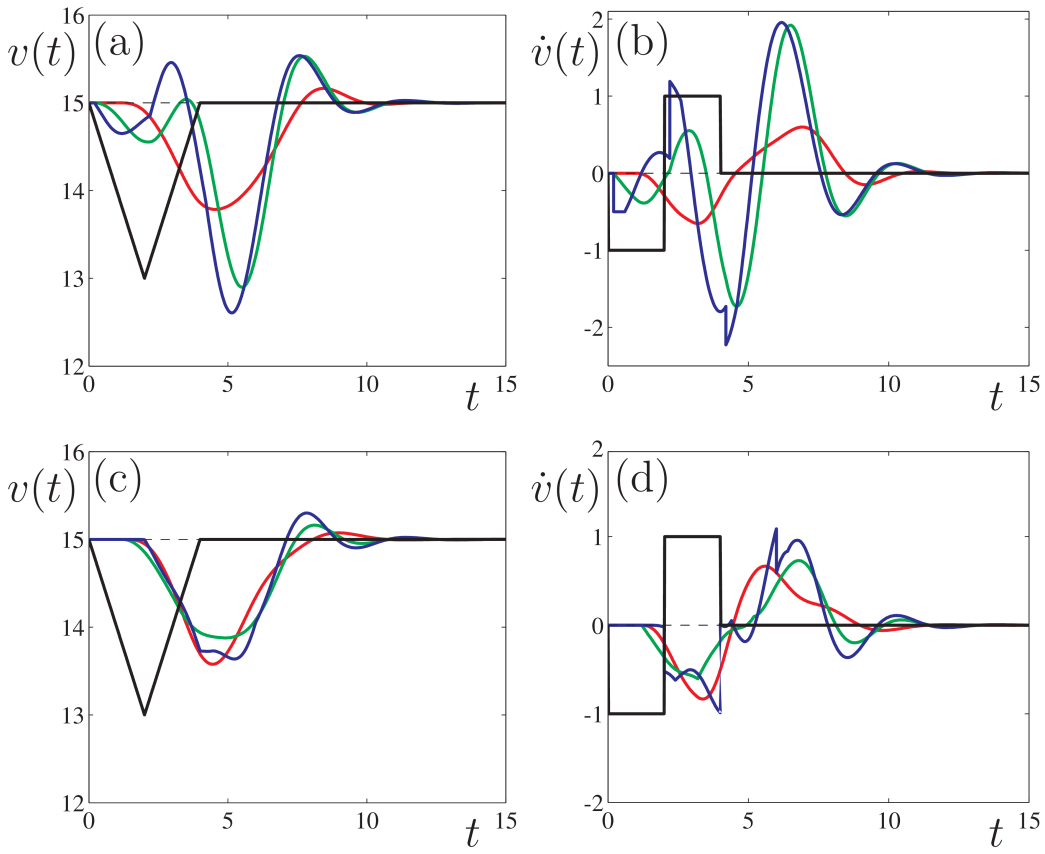

Figure 4.9: Velocity and acceleration responses of the CCC vehicle to a triangular velocity perturbation of the head vehicle (black curves) for configurations A (red), B (green), and C (blue) shown in Fig. 4.7(a). The parameters and initial conditions are the same as in Fig. 4.8.

perturbation with frequency $\omega = 2$ [rad/s] and amplitude $|\Delta v| = 1$ [m/s] (black curves in Fig. 4.8). This particular frequency is chosen based on the range of critical frequencies in Fig. 4.7(d, e). In Fig. 4.8(a, b), the acceleration delays are kept the same for all links, that is, $\sigma_k = 0.2$ [s], $\gamma_k = 0.5$, $k = 2, 3, 4, 5$. Case A (red curve) is string stable, i.e., the amplitude of the steady-state velocity response is smaller than the amplitude of the disturbance (black curve). However, cases B (green curve) and C (blue curve) are not string stable as the velocity disturbance is amplified. Figure 4.8(c, d) show the velocity and acceleration responses when the acceleration delays are increased with link length. In particular, we choose $\sigma_2 = 0.2$ [s], $\sigma_3 = 0.4$ [s], $\sigma_4 = 1.2$ [s], $\sigma_5 = 2.0$ [s] and $\gamma_k = 0.5$, $k = 2, 3, 4, 5$, corresponding to the crosses in Fig. 4.7(b, c). In this setting, all three configurations are string stable, i.e., the velocity perturbations for the red, green and blue curves are all smaller compared to the black curve. This is consistent with results of the linear analysis presented above.

To further emphasize this principle, Fig. 4.9 shows the velocity and acceleration responses when the head vehicle has a triangular velocity perturbation between $t \in [0, 4]$ [s] with perturbation size $|\Delta v| = 2$ [m/s] (black curves in Fig. 4.9). Since the triangular signal can be written as a sum of Fourier components, and is more common in real traffic than pure sinusoidal signals, the attenuation of triangular perturbation may be considered as an indication of string stability. In Fig. 4.9(a, b), we have $\sigma_k = 0.2$ [s], for $k = 2, 3, 4, 5$, and the perturbation is only attenuated in case A but amplified in cases B and C. On the other hand, panels (c, d) are for $\sigma_2 = 0.2$ [s], $\sigma_3 = 0.4$ [s], $\sigma_4 = 1.2$ [s], $\sigma_5 = 2.0$ [s], and the perturbation is attenuated in all cases. These simulation results demonstrate that near the equilibrium, the nonlinear model reproduces the predictions of the linear analysis.

4.6 Multiple CCC vehicles: effects of link intersections

As seen in the last section, multiple links may be used to improve string stability when there is only one CCC vehicle in the traffic flow. However, when more than one CCC vehicles appear, complicated connectivity structures may arise. In this section, we demonstrate that increasing the number of links may not always provide larger string stability domains.

Here we consider a five-car system and compare the head-to-tail string stability in configurations E–H depicted in Fig. 4.10(a). In each case, we use links that allow CCC vehicles to obtain acceleration information from a vehicle that is two vehicles ahead and choose the parameters for this acceleration link to be $\gamma_3 = 0.5$, $\sigma_3 = 0.6$ [s], cf. the cross in Fig. 4.6(c). Notice that the number of links increases when going from E to H. The corresponding (β, α) stability charts are shown in Fig. 4.10(b-e). Since we still consider $\tau = 0.4$ [s] as in

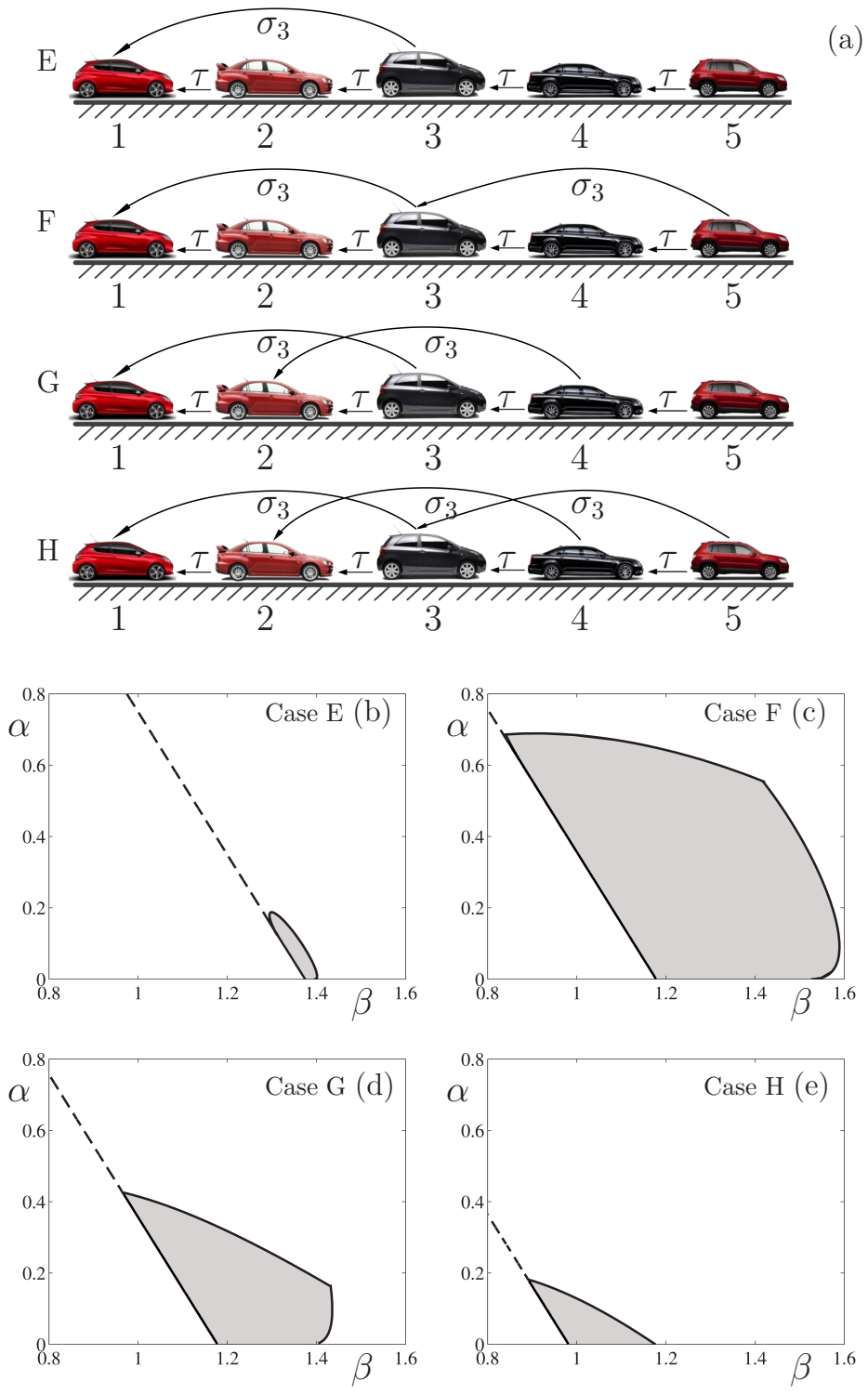

Figure 4.10: (a): Four connectivity configurations for a five-car system with multiple CCC vehicles and multiple acceleration links. The delays are shown along the links. (b, c, d, e): String stability diagrams in the (β, α)-plane for the different configurations while using $\tau = 0.4$ [s], $\gamma_3 = 0.5$, $\sigma_3 = 0.6$ [s]. The same notation is used as in Fig. 4.5.

Fig. 4.7, without acceleration feedback the connected vehicle system is string unstable. In case E, the CCC vehicle at the tail can make the system head-to-tail string stable, though the stable domain is fairly small as shown in Fig. 4.10(a). Case F is a cascade configuration with two CCC vehicles involved and the corresponding string stable domain is identical to the one in Fig. 4.6 (a). In case G, there are two CCC vehicles, but the two links intersect each other and the stability region shrinks significantly as shown in Fig. 4.10(d). This result indicates that intersection of acceleration links may deteriorate string stability. Finally, to investigate whether the stabilizing effect of acceleration links outweighs the destabilizing effect of link intersections, we consider three CCC vehicles with three acceleration links in case H. The corresponding stability plot in Fig. 4.10(e) shows that, surprisingly, the stable domain becomes much smaller. These results suggest that CCC vehicles shall use the available acceleration signals in a selective manner, to avoid link intersections which deteriorate string stability.

4.7 Conclusion

In this chapter, we present a connected vehicle design using acceleration signals of preceding vehicles received via V2V communication. We show that this design can improve the string stability of connected vehicle systems when most vehicles are human-driven and a few of them are equipped with DSRC. The improvement on string stability is robust against driver reaction time and communication delay. We observed that the critical driver reaction time increases significantly when using appropriately designed acceleration feedback. We also demonstrated that the gain of the acceleration feedback shall be kept around 0.5 for most circumstances discussed here. Having too low acceleration gains would lead to low-frequency oscillations (that are typical for human-driven vehicles), while too high acceleration gains lead to high-frequency string instabilities. As the acceleration signals come from vehicles farther downstream, the corresponding delay time shall also be increased, in order to maintain head-to-tail string stability. This indicates a necessity of designing the delay time when using acceleration feedback, instead of treating the delays as system limitations. Furthermore, we showed that string stability can be preserved when building larger connected vehicle systems, under the condition that the connectivity topology does not have intersecting links. In the next chapter, we will consider connected automated vehicle design in a V2V-rich environment, where a large portion of vehicles in the traffic flow are equipped with DSRC.

CHAPTER 5

Optimal design of connected cruise control in a V2V-rich environment

In this chapter, we consider the connected cruise control design in connected vehicle systems with high penetration of V2V devices. In this case, a CCC vehicle will receive motion signals from nearly every vehicle ahead within the range of V2V communication, and it is no longer feasible to directly tune the large number of corresponding feedback gains simultaneously. Instead, we design a multi-objective cost function including both velocity and headway fluctuations and acceleration efforts, and then use optimal control to generate the feedback law for the CCC controller.

Considering that algorithms such as rolling horizon optimal control [27] have relatively high computational cost and are only feasible among a small group of vehicles with specific communication structures, we would like to find optimization algorithms with low computational cost for general connectivity topologies. Therefore, we consider the linearized human car-following model (2.11) and design the optimal controller using linear quadratic regulation (LQR), where the time delay is considered so that the optimal design remains compatible with human driving behavior and communication delay.

While the LQR problem is formulated over a high-dimensional network, we show that the problem can be decomposed since the information flow is uni-directional in a connected vehicle system when vehicles only utilize motion information of vehicles ahead. Such decomposition allows us to obtain an analytical solution to the optimization problem recursively, and it allows graceful degradation of CCC performance when V2V communication deteriorates. We also show that the weights in the cost function can be chosen such that the velocity fluctuations of the CCC vehicle are attenuated compared with vehicles ahead (i.e., head-to-tail string stability can be achieved).

While the optimization is done at the linear level, we demonstrate that the controller performs well at the nonlinear level, and is robust against parameter variations and heterogeneities appearing in multi-vehicle systems. These findings allow us to fully exploit the

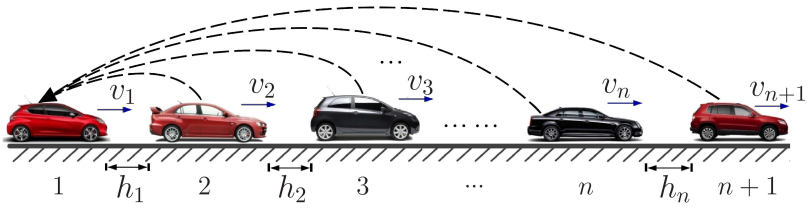

Figure 5.1: A string of $n+1$ vehicles in a single-lane scenario. The CCC vehicle at the tail receives signals from human-driven vehicles ahead via V2V communication. Dashed arrows indicate the flow of information in this connected vehicle system.

connectivity without increasing the complexity of gain-tuning.

The layout of this chapter is as follows. In Section 5.1 we build up the models for CCC design. In Section 5.2 we introduce the setup of the optimization problem and show that the solution of an infinite-dimensional Riccati equation can be used to design the CCC controller. The details for solving the optimization problem with time delay and the robustness of the proposed controller are provided in Appendix C.1 for interested readers. In Section 5.3 we present the stability analysis and summarize the impact of design parameters and robustness against variations in human parameters using stability charts. In Section 5.4 the application of the CCC controller is demonstrated at the nonlinear level using numerical simulations. Finally, we conclude the findings in Section 5.5.

5.1 Optimization problem setup

We now consider the single-lane configuration shown in Fig. 5.1 where the CCC vehicle at the tail receives motion information from the n non-CCC vehicles ahead through V2V communication (see dashed arrows from preceding vehicles to vehicle 1). Initially, we assume that all preceding vehicles are identical human-driven vehicles, but the effects of heterogeneous dynamics among preceding vehicles will be investigated in Appendix C.4.

We write the car-following dynamics of the CCC vehicle as

$$\begin{aligned} \dot{h}_1(t) &= v_2(t) - v_1(t)\,, \\ \dot{v}_1(t) &= u(t)\,, \end{aligned} \tag{5.1}$$

where $u(t)$ is the acceleration that will be designed using the motion information obtained via V2V communication. Communication delay is not included explicitly in the optimization, but will be added when analyzing the stability of CCC in Section 5.3.

We assume the CCC vehicle tries to maintain the same equilibrium as human-driven vehicles $i = 2, \ldots, n$, cf. (2.6). Using definition (2.10) we linearize (5.1) about the equi-

librium:

$$\begin{aligned} \dot{\tilde{h}}_1(t) &= \tilde{v}_2(t) - \tilde{v}_1(t)\,, \\ \dot{\tilde{v}}_1(t) &= u(t)\,. \end{aligned} \tag{5.2}$$

With the car-following dynamics of human-driven and CCC vehicles set up, we discuss how to use optimization to design $u(t)$.

In Chapter 4 we have seen that for CCC based on acceleration feedback we need to design both the feedback gains and delay time. Moreover, acceleration signals from vehicles farther downstream should be used with larger time delay, which is related to the wave speed in the traffic flow. While this finding bridges the microscopic and macroscopic description of traffic flow nicely, the time delay it introduces into the CCC controller is significant. For example, consider a CCC vehicle using the acceleration of vehicle 3 in Fig. 5.1

$$\begin{aligned} \dot{h}_1(t) &= v_2(t) - v_1(t)\,, \\ \dot{v}_1(t) &= \alpha\big(V(h_1(t-\tau)) - v_1(t-\tau)\big) + \beta\,\dot{h}_1(t-\tau) + \gamma_3\,\dot{v}_3(t-\sigma_3)\,, \end{aligned} \tag{5.3}$$

see (4.17) in Section 4.4. We can plug in the car-following model of vehicle 3 and write the acceleration in terms of headway and velocity. Then the dynamics of the connected vehicle system consisting of vehicles $1, 2, 3$ becomes

$$\begin{aligned} \dot{h}_1(t) &= v_2(t) - v_1(t)\,, \\ \dot{v}_1(t) &= \alpha\big(V(h_1(t-\tau)) - v_1(t-\tau)\big) + \beta(v_2(t-\tau) - v_1(t-\tau)) \\ &\quad + \gamma_3\left(\alpha\big(V(h_3(t-\tau-\sigma_3)) - v_3(t-\tau-\sigma_3)\big) + \beta(v_4(t-\tau-\sigma_3) - v_3(t-\tau-\sigma_3))\right), \\ \dot{h}_2(t) &= v_3(t) - v_2(t)\,, \\ \dot{v}_2(t) &= \alpha\big(V(h_2(t-\tau)) - v_2(t-\tau)\big) + \beta(v_3(t-\tau) - v_2(t-\tau))\,, \\ \dot{h}_3(t) &= v_4(t) - v_3(t)\,, \\ \dot{v}_3(t) &= \alpha\big(V(h_3(t-\tau)) - v_3(t-\tau)\big) + \beta(v_4(t-\tau) - v_3(t-\tau))\,. \end{aligned} \tag{5.4}$$

According to Fig. 4.6 of Section 4.4, $\sigma_3 > 0.5$ [s] is required for linear string stability when $\tau = 0.4$ [s], and thus a new delay of $\tau + \sigma_3$ is introduced into (5.4) with this acceleration feedback. While the large delay is proven to benefit the string stability of the connected vehicle system on the linear level, considerable caution should be exercised to guarantee stability and robustness on the nonlinear level as the delay time of a system doubles. Notice that the extra delay time σ_3 is introduced to "match the phase" of the perturbations

propagating through the string of vehicles. When motion signals from vehicle 2 through vehicle $n+1$ are available, we may be able to use a well-balanced combination of these signals without inserting large delay times. Since acceleration can be written in terms of headway and velocity using car-following models, we only use the headway and velocity of n preceding vehicles to design $u(t)$ (cf. (5.2)) in this chapter for simplicity.

5.2 Linear quadratic regulation with time delay

In this section, we present a systematic method for connected cruise control design while utilizing the linearized human car-following model (2.11). We formulate the CCC design as a linear quadratic (LQ) optimization problem with delay. Since the CCC vehicle would like to maintain constant velocity and headway without using large acceleration/deceleration, we minimize a cost function containing its headway and velocity fluctuations and its acceleration. The solution will give the gains for the CCC vehicle with respect to the current and delayed headways and velocities of the vehicles ahead.

In Section 5.2.1 we present the general solution of the optimization problem, while in Section 5.2.2 we show that the problem can be decomposed and solved analytically by exploiting the unidirectional information flow in the system. If the reader is not interested in these technical details, Sections 5.2.1 and 5.2.2 may be skipped. In Section 5.2.3 we obtain the CCC controller with full-state feedback and demonstrate that the gains decay exponentially as the number of vehicles between the source and the CCC vehicle increases. We also show that adding more vehicles downstream does not influence the existing design for the system. A brief discussion is provided in Appendix C.4 on the robustness of the controller against heterogeneities arising in the vehicle string.

Let us define

$$x_i = \begin{bmatrix} \kappa\tilde{h}_i - \tilde{v}_i \\ \tilde{v}_{i+1} - \tilde{v}_i \end{bmatrix}, \quad \phi_n = \begin{bmatrix} 0 \\ \dot{\tilde{v}}_{n+1} \end{bmatrix}. \tag{5.5}$$

Then we construct the vectors

$$X = \begin{bmatrix} x_1 \\ \vdots \\ x_n \end{bmatrix}, \quad \phi = \begin{bmatrix} 0 \\ \vdots \\ 0 \\ \phi_n \end{bmatrix}, \tag{5.6}$$

and rewrite (2.11, 5.2) as

$$\dot{X}(t) = \mathbf{A}X(t) + \mathbf{B}X(t-\tau) + \mathbf{D}u(t) + \phi(t)\,. \tag{5.7}$$

The coefficient matrices are given by

$$\mathbf{A} = \mathbf{I}_n \otimes \mathbf{A}_1, \quad \mathbf{B} = \begin{bmatrix} \mathbf{0} & \mathbf{B}_2 & & & \\ & \mathbf{B}_1 & \mathbf{B}_2 & & \\ & & \ddots & \ddots & \\ & & & \mathbf{B}_1 & \mathbf{B}_2 \\ & & & & \mathbf{B}_1 \end{bmatrix}, \quad \mathbf{D} = \begin{bmatrix} \mathbf{D}_1 \\ \mathbf{0} \\ \vdots \\ \mathbf{0} \\ \mathbf{0} \end{bmatrix}, \tag{5.8}$$

where $\otimes$ denotes the Kronecker product and the blocks are defined by

$$\mathbf{A}_1 = \begin{bmatrix} 0 & \kappa \\ 0 & 0 \end{bmatrix}, \ \mathbf{B}_1 = -\begin{bmatrix} \alpha & \beta \\ \alpha & \beta \end{bmatrix}, \ \mathbf{B}_2 = \begin{bmatrix} 0 & 0 \\ \alpha & \beta \end{bmatrix}, \ \mathbf{D}_1 = \begin{bmatrix} -1 \\ -1 \end{bmatrix}. \tag{5.9}$$

Note that $\mathbf{B}$ is upper block-triangular because vehicles only react to the motion of vehicles ahead. This topological structure of connectivity will allow us to greatly simplify the solution of the LQR problem.

We assume that the non-CCC vehicles are plant stable, i.e., they are able to maintain the uniform flow (2.6) when the vehicles ahead travel with constant speed v^*. Then the connected vehicle system (5.7, 5.8) is stabilizable, that is, uncontrollable part of the system is stable.

We define the multi-objective cost function based on the CCC vehicle's acceleration and deviations from the uniform flow as

$$J_{t_\mathrm{f}}(u, X) = \int_0^{t_\mathrm{f}} \left(\dot{\tilde{v}}_1^2 + \gamma_1 \big(\kappa \tilde{h}_1 - \tilde{v}_1\big)^2 + \gamma_2 \big(\tilde{v}_2 - \tilde{v}_1\big)^2 \right) \mathrm{d}t = \int_0^{t_\mathrm{f}} \left(u^2 + X^{\mathrm{T}} \mathbf{\Gamma} X \right) \mathrm{d}t\,, \tag{5.10}$$

where $\gamma_1 > 0$, $\gamma_2 > 0$ and

$$\mathbf{\Gamma} = \mathrm{diag}[\gamma_1, \gamma_2, 0, \ldots, 0] \in \mathbb{R}^{2n \times 2n}. \tag{5.11}$$

In (5.10) the first term is related with the fuel economy of the CCC vehicle, and the latter two terms account for the active safety and traffic efficiency. While more complicated cost functions can be used to consider more accurate powertrain dynamics [27, 62], the quadratic form of (5.10) will provide us with valuable insight about the upper-level control

of connected vehicle systems.

5.2.1 General solution of the LQ problem

In this section we lay out the general solution to the LQ problem in a time-delayed system with disturbance (5.7, 5.10). We will show that the disturbance has limited influence on the structure of the optimal controller. Thus, we design the optimal controller under zero disturbance. This setting allows us to exploit the uni-directional information flow to alleviate the high computational cost for optimal connected vehicle design. Readers not interested in the technical details may proceed to Section 5.2.3.

We define the augmented state $Y(t) = [X^{\mathrm{T}}(t) \;\; 1]^{\mathrm{T}}$ to place the disturbance term $\phi(t)$ in (5.7) into a time-variant coefficient matrix. This yields

$$\dot{Y}(t) = \tilde{\mathbf{A}}(t)Y(t) + \tilde{\mathbf{B}}Y(t-\tau) + \tilde{\mathbf{D}}u(t)\,, \tag{5.12}$$

where

$$\tilde{\mathbf{A}}(t) = \begin{bmatrix} \mathbf{A} & \phi(t) \\ 0 & 0 \end{bmatrix}, \quad \tilde{\mathbf{B}} = \begin{bmatrix} \mathbf{B} & 0 \\ 0 & 0 \end{bmatrix}, \quad \tilde{\mathbf{D}} = \begin{bmatrix} \mathbf{D} \\ 0 \end{bmatrix}. \tag{5.13}$$

The cost function (5.10) can be rewritten accordingly

$$J_{t_{\mathrm{f}}}(u, Y) = \int_0^{t_{\mathrm{f}}} \left(u^2 + Y^{\mathrm{T}} \tilde{\mathbf{\Gamma}} Y \right) \mathrm{d}t\,, \tag{5.14}$$

where $\tilde{\mathbf{\Gamma}} = \begin{bmatrix} \mathbf{\Gamma} & 0 \\ 0 & 0 \end{bmatrix}$.

The optimal control for (5.12, 5.14) is given by

$$u(t) = -\tilde{\mathbf{D}}^{\mathrm{T}} \left(\mathbf{P}(t)Y(t) + \int_{-\tau}^{0} \mathbf{Q}(t,\theta)Y(t+\theta)\,\mathrm{d}\theta \right), \tag{5.15}$$

see [63]. The matrices $\mathbf{P}(t)$ and $\mathbf{Q}(t,\theta)$ are obtained by solving the Riccati-type partial differential equation (PDE)

$$\begin{aligned} -\dot{\mathbf{P}}(t) &= \tilde{\mathbf{A}}^{\mathrm{T}}\mathbf{P}(t) + \mathbf{P}(t)\tilde{\mathbf{A}} - \mathbf{P}(t)\tilde{\mathbf{D}}\tilde{\mathbf{D}}^{\mathrm{T}}\mathbf{P}(t) + \mathbf{Q}(t,0) + \mathbf{Q}^{\mathrm{T}}(t,0) + \tilde{\mathbf{\Gamma}}\,, \\ (\partial_\theta - \partial_t)\mathbf{Q}(t,\theta) &= \left(\tilde{\mathbf{A}}^{\mathrm{T}} - \mathbf{P}\tilde{\mathbf{D}}\tilde{\mathbf{D}}^{\mathrm{T}}\right)\mathbf{Q}(t,\theta) + \mathbf{R}(t,0,\theta)\,, \\ (\partial_\xi + \partial_\theta - \partial_t)\mathbf{R}(t,\xi,\theta) &= -\mathbf{Q}^{\mathrm{T}}(t,\xi)\tilde{\mathbf{D}}\tilde{\mathbf{D}}^{\mathrm{T}}\mathbf{Q}(t,\theta)\,, \end{aligned} \tag{5.16}$$

with boundary conditions

$$\begin{aligned}
&\mathbf{P}(t_{\mathrm{f}}) = \mathbf{0}\,, \\
&\mathbf{Q}(t_{\mathrm{f}},\theta) = \mathbf{0}\,, \qquad \mathbf{Q}(t,-\tau) = \mathbf{P}^{\mathrm{T}}\tilde{\mathbf{B}}\,, \\
&\mathbf{R}(t_{\mathrm{f}},\xi,\theta) = \mathbf{0}\,, \quad \mathbf{R}(t,-\tau,\theta) = \tilde{\mathbf{B}}^{\mathrm{T}}\mathbf{Q}(t,\theta)\,,
\end{aligned} \tag{5.17}$$

where $\mathbf{P}(t)$ is symmetric and $\mathbf{R}^{\mathrm{T}}(t,\xi,\theta) = \mathbf{R}(t,\theta,\xi)$. Given the structure of coefficient matrices (5.13), the matrices $\mathbf{P}(t)$, $\mathbf{Q}(t,\theta)$ and $\mathbf{R}(t,\xi,\theta)$ can be constructed as

$$\mathbf{P} = \begin{bmatrix} \mathbf{P}_1 & \mathbf{P}_2 \\ \mathbf{P}_3 & \mathbf{P}_4 \end{bmatrix}, \quad \mathbf{Q} = \begin{bmatrix} \mathbf{Q}_1 & \mathbf{Q}_2 \\ \mathbf{Q}_3 & \mathbf{Q}_4 \end{bmatrix}, \quad \mathbf{R} = \begin{bmatrix} \mathbf{R}_1 & \mathbf{R}_2 \\ \mathbf{R}_3 & \mathbf{R}_4 \end{bmatrix}, \tag{5.18}$$

where $\mathbf{P}_1, \mathbf{Q}_1, \mathbf{R}_1 \in \mathbb{R}^{2n\times 2n}$, $\mathbf{P}_2, \mathbf{Q}_2, \mathbf{R}_2 \in \mathbb{R}^{2n\times 1}$, $\mathbf{P}_3, \mathbf{Q}_3, \mathbf{R}_3 \in \mathbb{R}^{1\times 2n}$, and $\mathbf{P}_4, \mathbf{Q}_4, \mathbf{R}_4$ are scalars. since $\mathbf{P}(t)$ is symmetric we have $\mathbf{P}_1(t) = \mathbf{P}_1^{\mathrm{T}}(t)$ and $\mathbf{P}_2(t) = \mathbf{P}_3^{\mathrm{T}}(t)$. Moreover, $\mathbf{R}(t,\xi,\theta) = \mathbf{R}^{\mathrm{T}}(t,\theta,\xi)$ yields $\mathbf{R}_1(t,\xi,\theta) = \mathbf{R}_1^{\mathrm{T}}(t,\theta,\xi)$ and $\mathbf{R}_2(t,\xi,\theta) = \mathbf{R}_3^{\mathrm{T}}(t,\theta,\xi)$.

Thus, the optimal controller (5.15) becomes

$$u(t) = -\mathbf{D}^{\mathrm{T}}\left(\mathbf{P}_1(t)X(t) + \int_{-\tau}^{0} \mathbf{Q}_1(t,\theta)X(t+\theta)\,\mathrm{d}\theta + \mathbf{P}_2(t) + \int_{-\tau}^{0} \mathbf{Q}_2(t,\theta)\,\mathrm{d}\theta\right). \tag{5.19}$$

By substituting (5.18) into (5.16, 5.17) we find that state-feedback-control gain matrices $\mathbf{P}_1, \mathbf{Q}_1$ in the optimal controller (5.19) are not influenced by the disturbance $\phi(t)$; see (C.1, C.3, C.5, C.7) in Appendix C.1. On the other hand, when including the disturbance in the optimization, (5.19) cannot be implemented in real time since $\phi(t)$ is not known a priori; cf. $\tilde{\mathbf{A}}(t)$ in (5.13, 5.16, 5.18). Therefore we first ignore the disturbance $\phi(t)$, but later in Section 5.3 we ensure that this zero-disturbance design can reject disturbances satisfyingly. Thus, we consider

$$\mathbf{P}_2(t) \equiv \mathbf{0}\,, \qquad \mathbf{Q}_2(t,\theta) \equiv \mathbf{0}\,, \tag{5.20}$$

which allows us to design the CCC controller analytically without impairing the stability of the multi-vehicle system.

Since $\mathbf{P}_1(t), \mathbf{Q}_1(t,\theta), \mathbf{R}_1(t,\xi,\theta)$ are given by (C.1), which is an initial value problem in backward time, we consider the steady-state solution

$$\mathbf{P}_1(t) \equiv \mathbf{P}_1, \quad \mathbf{Q}_1(t,\theta) \equiv \mathbf{Q}_1(\theta), \quad \mathbf{R}_1(t,\xi,\theta) \equiv \mathbf{R}_1(\xi,\theta), \tag{5.21}$$

which is equivalent to setting time horizon $t_{\mathrm{f}} \to \infty$ in the cost function (5.10); see [64].

Substituting (5.20, 5.21) into (5.19) leads to the simplified controller

$$u(t) = -\mathbf{D}^{\mathrm{T}}\left(\mathbf{P}_1 X(t) + \int_{-\tau}^{0} \mathbf{Q}_1(\theta) X(t+\theta)\,\mathrm{d}\theta\right), \tag{5.22}$$

where the matrices $\mathbf{P}_1,\ \mathbf{Q}_1(\theta)$ are given by

$$\begin{aligned}
&\mathbf{A}^{\mathrm{T}}\mathbf{P}_1 + \mathbf{P}_1\mathbf{A} - \mathbf{P}_1\mathbf{D}\mathbf{D}^{\mathrm{T}}\mathbf{P}_1 + \mathbf{Q}_1(0) + \mathbf{Q}_1^{\mathrm{T}}(0) + \mathbf{\Gamma} = \mathbf{0}\,,\\
&\partial_\theta \mathbf{Q}_1(\theta) = \left(\mathbf{A}^{\mathrm{T}} - \mathbf{P}_1\mathbf{D}\mathbf{D}^{\mathrm{T}}\right)\mathbf{Q}_1(\theta) + \mathbf{R}_1(0,\theta)\,,\\
&(\partial_\xi + \partial_\theta)\mathbf{R}_1(\xi,\theta) = -\mathbf{Q}_1^{\mathrm{T}}(\xi)\mathbf{D}\mathbf{D}^{\mathrm{T}}\mathbf{Q}_1(\theta)\,,
\end{aligned} \tag{5.23}$$

with boundary conditions

$$\mathbf{Q}_1(-\tau) = \mathbf{P}_1\mathbf{B}\,, \qquad \mathbf{R}_1(-\tau,\theta) = \mathbf{B}^{\mathrm{T}}\mathbf{Q}_1(\theta)\,, \tag{5.24}$$

which can be attained by setting $t_{\mathrm{f}} \to \infty$ in (C.1, C.2).

5.2.2 Decomposition of the solution

In this section, we exploit the uni-directional information flow and obtain the analytical solution to the delayed LQ problem (5.7, 5.10) with zero disturbance ($\phi(t) \equiv 0$) and infinite time horizon ($t_{\mathrm{f}} = \infty$), i.e., we solve the PDE (5.23, 5.24) analytically to obtain the controller (5.22).

While a numerical scheme for (5.23, 5.24) is given in [64] to obtain $\mathbf{P}_1$, $\mathbf{Q}_1(\theta)$ in (5.22), no closed-form solution exists with general $\mathbf{A}, \mathbf{B}, \mathbf{D}$ matrices. However, here only the first two rows of $\mathbf{P}_1, \mathbf{Q}_1(\theta)$ are used by the controller (5.22), since $\mathbf{D}$ is zero except its first two elements, cf. (5.8, 5.9). Thus we only need to obtain an analytical solution for the relevant parts in $\mathbf{P}_1$, $\mathbf{Q}_1(\theta)$, which is made possible by taking advantage of the upper-triangular block structure of $\mathbf{A}$ and $\mathbf{B}$.

We introduce the notation

$$\mathbf{P}_1 = \begin{bmatrix} \mathbf{P}_{11} & \cdots & \mathbf{P}_{1n} \\ \vdots & \ddots & \vdots \\ \mathbf{P}_{n1} & \cdots & \mathbf{P}_{nn} \end{bmatrix}, \quad \mathbf{Q}_1(\theta) = \begin{bmatrix} \mathbf{Q}_{11}(\theta) & \cdots & \mathbf{Q}_{1n}(\theta) \\ \vdots & \ddots & \vdots \\ \mathbf{Q}_{n1}(\theta) & \cdots & \mathbf{Q}_{nn}(\theta) \end{bmatrix}, \tag{5.25}$$

where $\mathbf{P}_{ij}, \mathbf{Q}_{ij}(\theta) \in \mathbb{R}^{2\times 2}$ for $i, j = 1, \ldots, n$, and rewrite (5.22) as

$$u(t) = -\mathbf{D}_1^{\mathrm{T}} \sum_{i=1}^{n} \left(\mathbf{P}_{1i} x_i(t) + \int_{-\tau}^{0} \mathbf{Q}_{1i}(\theta) x_i(t+\theta)\,\mathrm{d}\theta\right), \tag{5.26}$$

where $x_i(t)$ is given in (5.5). This shows that we only need to derive $\mathbf{P}_{1i}, \mathbf{Q}_{1i}(\theta)$ for $i = 1, \ldots, n$ to construct the controller. Substituting (5.25) into (5.23, 5.24), we obtain equations for each block $\mathbf{P}_{ij}, \mathbf{Q}_{ij}(\theta), \mathbf{R}_{ij}(\xi, \theta)$, $i, j = 1, \ldots, n$, which can be solved recursively. Specifically, $\mathbf{P}_{11}$ and $\mathbf{Q}_{11}(\theta)$ are given by

$$\begin{aligned}
&\hat{\mathbf{A}}_1 \mathbf{P}_{11} + \mathbf{P}_{11} \mathbf{A}_1 + \mathbf{Q}_{11}(0) + \mathbf{Q}_{11}^{\mathrm{T}}(0) + \mathrm{diag}[\gamma_1, \gamma_2] = \mathbf{0}\,, \\
&\partial_\theta \mathbf{Q}_{11}(\theta) = \hat{\mathbf{A}}_1 \mathbf{Q}_{11}(\theta) + \mathbf{R}_{11}(0, \theta)\,, \\
&(\partial_\xi + \partial_\theta) \mathbf{R}_{11}(\xi, \theta) = -\mathbf{Q}_{11}^{\mathrm{T}}(\xi) \mathbf{D} \mathbf{D}^{\mathrm{T}} \mathbf{Q}_{11}(\theta)\,,
\end{aligned} \tag{5.27}$$

with boundary conditions

$$\mathbf{Q}_{11}(-\tau) = \mathbf{0}\,, \qquad \mathbf{R}_{11}(-\tau, \theta) = \mathbf{0}\,, \tag{5.28}$$

where

$$\hat{\mathbf{A}}_1 = \mathbf{A}_1^{\mathrm{T}} - \mathbf{P}_{11} \mathbf{D}_1 \mathbf{D}_1^{\mathrm{T}}\,. \tag{5.29}$$

The solution of (5.27, 5.28) is given by

$$\mathbf{P}_{11} = \begin{bmatrix} p_{11} & p_{12} \\ p_{12} & p_{22} \end{bmatrix}, \quad \mathbf{Q}_{11}(\theta) \equiv \mathbf{0}, \quad \mathbf{R}_{11}(\xi, \theta) \equiv \mathbf{0}\,, \tag{5.30}$$

where

$$\begin{aligned}
p_{11} &= \frac{-\gamma_1 + \sqrt{\gamma_1}\sqrt{\gamma_1 + \gamma_2 + 2\kappa\sqrt{\gamma_1}}}{\kappa}\,, \\
p_{12} &= \sqrt{\gamma_1} - p_{11}\,, \\
p_{22} &= -2\sqrt{\gamma_1} + \sqrt{\gamma_1 + \gamma_2 + 2\kappa\sqrt{\gamma_1}} + p_{11}\,,
\end{aligned} \tag{5.31}$$

which is the only solution satisfying the condition $\mathbf{P}_{11} > \mathbf{0}$. Notice that the matrix $\mathbf{P}_{11}$ only depends on the weights γ_1, γ_2 and the CCC vehicle's range policy κ (cf. (2.3)).

Then, to obtain $\mathbf{P}_{1i}, \mathbf{Q}_{1i}(\theta), \mathbf{Q}_{i1}(\theta)$ for $i = 2, \ldots, n$, we need to solve

$$\begin{aligned}
&\hat{\mathbf{A}}_1 \mathbf{P}_{1i} + \mathbf{P}_{1i} \mathbf{A}_1 + \mathbf{Q}_{1i}(0) + \mathbf{Q}_{i1}^{\mathrm{T}}(0) = \mathbf{0}\,, \\
&\partial_\theta \mathbf{Q}_{1i}(\theta) = \hat{\mathbf{A}}_1 \mathbf{Q}_{1i}(\theta) + \mathbf{R}_{1i}(0, \theta)\,, \\
&\partial_\theta \mathbf{Q}_{i1}(\theta) = \mathbf{A}_1^{\mathrm{T}} \mathbf{Q}_{i1}(\theta) - \mathbf{P}_{1i}^{\mathrm{T}} \mathbf{D}_1 \mathbf{D}_1^{\mathrm{T}} \mathbf{Q}_{11}(\theta) + \mathbf{R}_{1i}^{\mathrm{T}}(\theta, 0)\,, \\
&(\partial_\xi + \partial_\theta) \mathbf{R}_{1i}(\xi, \theta) = -\mathbf{Q}_{11}^{\mathrm{T}}(\xi) \mathbf{D}_1 \mathbf{D}_1^{\mathrm{T}} \mathbf{Q}_{1i}(\theta)\,,
\end{aligned} \tag{5.32}$$

with boundary conditions

$$\begin{aligned}
&\mathbf{Q}_{1i}(-\tau) = \mathbf{P}_{1i}\mathbf{B}_1 + \mathbf{P}_{1(i-1)}\mathbf{B}_2\,,\\
&\mathbf{Q}_{i1}(-\tau) = \mathbf{0}\,,\\
&\mathbf{R}_{1i}(\theta,-\tau) = \mathbf{Q}_{i1}^{\mathrm{T}}(\theta)\mathbf{B}_1 + \mathbf{Q}_{(i-1)1}^{\mathrm{T}}(\theta)\mathbf{B}_2\,,\\
&\mathbf{R}_{1i}(-\tau,\theta) = \mathbf{0}\,.
\end{aligned} \tag{5.33}$$

Now (5.32, 5.33) give the solution

$$\mathbf{Q}_{i1}(\theta) \equiv \mathbf{0}, \quad \mathbf{R}_{1i}(\xi,\theta) \equiv \mathbf{0}\,, \tag{5.34}$$

while the equations for $\mathbf{Q}_{1i}(\theta)$ simplify to

$$\begin{aligned}
&\partial_\theta \mathbf{Q}_{1i}(\theta) = \hat{\mathbf{A}}_1\mathbf{Q}_{1i}(\theta),\\
&\mathbf{Q}_{1i}(-\tau) = \mathbf{P}_{1i}\mathbf{B}_1 + \mathbf{P}_{1(i-1)}\mathbf{B}_2\,,
\end{aligned} \tag{5.35}$$

yielding the solution

$$\mathbf{Q}_{1i}(\theta) = \mathrm{e}^{\hat{\mathbf{A}}_1(\theta+\tau)}(\mathbf{P}_{1i}\mathbf{B}_1 + \mathbf{P}_{1(i-1)}\mathbf{B}_2)\,, \tag{5.36}$$

for $i = 2,\dots,n$. Thus, the equation for $\mathbf{P}_{1i}$ becomes

$$\hat{\mathbf{A}}_1\mathbf{P}_{1i} + \mathbf{P}_{1i}\mathbf{A}_1 + \mathrm{e}^{\tau\hat{\mathbf{A}}_1}(\mathbf{P}_{1i}\mathbf{B}_1 + \mathbf{P}_{1(i-1)}\mathbf{B}_2) = \mathbf{0}\,, \tag{5.37}$$

yielding the solution

$$\mathrm{vec}(\mathbf{P}_{1i}) = \mathbf{M}^{i-1}\mathrm{vec}(\mathbf{P}_{11})\,, \tag{5.38}$$

for $i = 2,\dots,n$. Here $\mathrm{vec}(\cdot)$ gives a column vector by stacking the columns of the matrix on the top of each other, and $\mathbf{M} \in \mathbb{R}^{4\times 4}$ is given by

$$\mathbf{M} = -\big(\mathbf{I}\otimes\hat{\mathbf{A}}_1 + \mathbf{A}_1^{\mathrm{T}}\otimes\mathbf{I} + \mathbf{B}_1^{\mathrm{T}}\otimes\mathrm{e}^{\tau\hat{\mathbf{A}}_1}\big)^{-1}\big(\mathbf{B}_2^{\mathrm{T}}\otimes\mathrm{e}^{\tau\hat{\mathbf{A}}_1}\big)\,. \tag{5.39}$$

Consequently, $\mathbf{P}_{1i}$ and $\mathbf{Q}_{1i}(\theta)$ are obtained recursively using (5.30, 5.36, 5.38, 5.39). The recursive rules (5.36, 5.38) indicate that the feedback gains for signals coming from the j^{th} vehicle only depend on the dynamics of vehicles 2 to j and do not depend on the dynamics of vehicles in front of the j^{th} vehicle. On the other hand, since $\hat{\mathbf{A}}_1$ only depends on $\mathbf{P}_{11}$ (cf. (5.29, 5.30, 5.31)), the exponential term $\mathrm{e}^{\hat{\mathbf{A}}_1(\theta+\tau)}$ shared by every $\mathbf{Q}_{1i}(\theta)$ is independent from the dynamics of preceding vehicles but changes with the CCC vehicle's

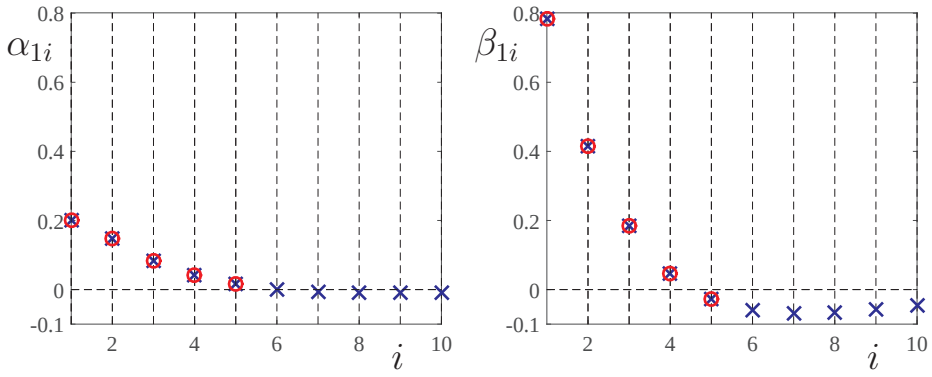

Figure 5.2: The optimized feedback gains $\alpha_{1i}, \beta_{1i}, i = 1, \ldots, n$ of the CCC vehicle in a string of $(n+1)$ vehicles for $n = 5$ (red circles) and for $n = 10$ (blue crosses). The human parameters are $\alpha = 0.6$ [1/s], $\beta = 0.9$ [1/s], $\kappa = \pi/2$ [1/s], $\tau = 0.4$ [s]. The design parameters are $\gamma_1 = 0.04\,[1/\mathrm{s}^2]$, $\gamma_2 = 0.30\,[1/\mathrm{s}^2]$.

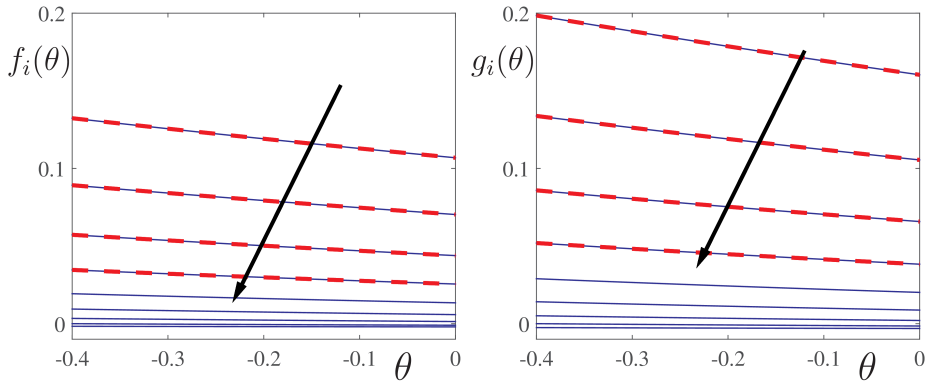

Figure 5.3: The optimized distribution kernels $f_i(\theta), g_i(\theta)$ for $i = 2, \ldots, n$ of the CCC vehicle for a $(n+1)$-car system with the same parameter as in Fig. 5.2. The red dashed curves correspond to $n = 5$, and the blue solid curves correspond to $n = 10$. The black arrows show the direction of increasing vehicle index i.

range policy κ and the optimization weights γ_1, γ_2.

5.2.3 Constructing the CCC controller

In (5.26) we move $\mathbf{D}_1$ (cf. (5.8)) into the integral and define

$$\begin{bmatrix} \alpha_{1i} & \beta_{1i} \end{bmatrix} = \begin{bmatrix} 1 & 1 \end{bmatrix} \mathbf{P}_{1i}, \quad \begin{bmatrix} f_i(\theta) & g_i(\theta) \end{bmatrix} = \begin{bmatrix} 1 & 1 \end{bmatrix} \mathbf{Q}_{1i}(\theta)\,. \tag{5.40}$$

Based on definitions (5.5, 5.40), the optimal controller (5.26) for the CCC vehicle is given by

$$u(t) = \sum_{i=1}^{n} \Big(\alpha_{1i} \big(\kappa \tilde{h}_i(t) - \tilde{v}_i(t) \big) + \beta_{1i} \big(\tilde{v}_{i+1}(t) - \tilde{v}_i(t) \big) \Big) + \sum_{i=1}^{n} \int_{-\tau}^{0} \Big(f_i(\theta) \big(\kappa \tilde{h}_i(t+\theta) - \tilde{v}_i(t+\theta) \big) + g_i(\theta) \big(\tilde{v}_{i+1}(t+\theta) - \tilde{v}_i(t+\theta) \big) \Big) \, \mathrm{d}\theta \,, \tag{5.41}$$

where the distribution kernels take the form

$$\begin{aligned} f_i(\theta) &= \big(a_{i0} + a_{i1}(\theta+\tau) \big) \, \mathrm{e}^{\lambda_1(\theta+\tau)} + a_{i2} \, \mathrm{e}^{\lambda_2(\theta+\tau)} \,, \\ g_i(\theta) &= \big(b_{i0} + b_{i1}(\theta+\tau) \big) \, \mathrm{e}^{\lambda_1(\theta+\tau)} + b_{i2} \, \mathrm{e}^{\lambda_2(\theta+\tau)} \,, \end{aligned} \tag{5.42}$$

for $i = 1, \ldots, n$, $\theta \in [-\tau, 0]$, where λ_1, λ_2 are the eigenvalues of $\hat{\mathbf{A}}_1$, and the expressions for λ_1, λ_2, a_{i0}, a_{i1}, a_{i2}, and b_{i0}, b_{i1}, b_{i2} are given in Appendix C.2.

From (5.30, 5.31, 5.40) we obtain that

$$\alpha_{11} = \sqrt{\gamma_1}, \quad \beta_{11} = -\sqrt{\gamma_1} + \sqrt{\gamma_1 + \gamma_2 + 2\kappa\sqrt{\gamma_1}} \,, \tag{5.43}$$

i.e., the gains on CCC vehicle's own headway and velocity do not depend on the dynamics of human-driven vehicles. Since $\mathbf{Q}_{11}(\theta) \equiv \mathbf{0}$, (5.40) yields

$$f_1(\theta) \equiv 0, \quad g_1(\theta) \equiv 0 \,, \tag{5.44}$$

i.e., the CCC vehicle does not have delayed feedback terms on its own headway and velocity. The rest of the gains α_{1i}, β_{1i} and the distribution kernels $f_i(\theta)$, $g_i(\theta)$ for $i = 2, \ldots, n$ in (5.40) can be obtained using (5.36, 5.38, 5.39).

In Appendix C.3 we show that the eigenvalues of $\mathbf{M}$ (cf. (5.39)) are inside the unit circle for realistic values of weights γ_1, γ_2, human gains α, β, and driver reaction time τ. Thus (5.38) is a contracting map. Since α_{1i}, β_{1i} are given in (5.40) as linear combinations of the components of $\mathbf{P}_{1i}$, they converge to zero as i increases.

Fig. 5.2 shows the corresponding exponential decay of α_{1i} and β_{1i} in a $(5+1)$ vehicle chain (red circles) and a $(10+1)$ vehicle chain (blue crosses) using the parameter values $\gamma_1 = 0.04\,[1/\mathrm{s}^2]$, $\gamma_2 = 0.30\,[1/\mathrm{s}]$, $\alpha = 0.6\,[1/\mathrm{s}]$, $\beta = 0.9\,[1/\mathrm{s}]$, $\kappa = \pi/2\,[1/\mathrm{s}]$ and $\tau = 0.4\,[\mathrm{s}]$. In this case, $\mathbf{M}$ has two zero eigenvalues and two non-zero eigenvalues $0.69 \pm 0.15i$. The exact match between the red circles and the blue crosses for vehicles 2 to 5 demonstrate that the existing optimized gains do not change when adding feedback terms on vehicles

farther away. This corresponds to the fact that the gains α_{11}, β_{11} are not influenced by the connectivity structure (cf. (5.30, 5.31, 5.40)), and that α_{1i}, β_{1i} are calculated recursively using (5.38). For the parameters considered above, we have the gains $\alpha_{11} \approx 0.20\,[1/\mathrm{s}]$, $\beta_{11} \approx 0.78\,[1/\mathrm{s}]$.

In Fig. 5.3 we plot the distribution kernels $f_i(\theta), g_i(\theta)$ for $i = 2, \ldots, n$ using the same parameters as in Fig. 5.2. The dashed red curves correspond to $n = 5$ and the blue solid curves correspond to $n = 10$. In both cases, the magnitude of $f_i(\theta)$ and $g_i(\theta)$ decreases with i. Indeed, for vehicles $i = 2, \ldots, 5$, the distribution kernels $f_i(\theta)$ and $g_i(\theta)$ are the same in both the $(5+1)$-car and the $(10+1)$-car systems.

Considering the similar feedback structure of the CCC controller (5.41) as in the conventional driving model (2.2), and the decay of feedback gains and distribution kernels shown in Fig. 5.2 and Fig. 5.3, we conclude that the proposed CCC controller will degrade gracefully under imperfect communication. More specifically, a CCC vehicle may experience severe packet drops from vehicles ahead, depending on the involved V2V communication devices, the physical distance between vehicles and the road environment [58]. When the communication channel with vehicle $i+1$ significantly deteriorates, we may set the feedback gains and distribution kernels corresponding to vehicle $i+1$ and vehicles farther ahead as zero, and only use motion signals up to vehicles i. Since motion signals from farther downstream vehicles are assigned with smaller gains, the switch to fewer signals will not induce a significant jump in control commands. Most importantly, since the gains for signals coming from vehicles 1–i do not depend on those from vehicles $i+1$ and beyond, the reduced CCC controller still remains optimal.

We note that the proposed CCC controller generates $2n$ feedback gains and distribution kernels with only 2 design parameters, while being robust against heterogeneity and connectivity structure changes among preceding vehicles, as discussed in detail in Appendix C.4.

5.3 Stability analysis of optimized connected vehicle systems

In this section, we analyze the linear stability of uniform traffic flow using the optimized controller for the CCC vehicle at the tail, to make sure that the arising connected vehicle system is able to maintain uniform traffic flow. Here we take into account the communication delay due to intermittency and packet loss in wireless communication. We analyze the plant stability and head-to-tail string stability and visualize the corresponding stability

areas using stability charts.

The intermittency in V2V communication with digital controllers results in an average communication delay of 0.15 [s]; see [43, 60]. However, packet losses may lead to significant increase of the delay. While the delay changes stochastically [46], here we approximate it with its average and study the dynamics while viewing the delay as a parameter. Then the linear dynamics (2.11, 5.2) becomes

$$\begin{aligned}
\dot{\tilde{h}}_1(t) &= \tilde{v}_2(t) - \tilde{v}_1(t)\,, \\
\dot{\tilde{v}}_1(t) &= u(t-\sigma)\,, \\
\dot{\tilde{h}}_i(t) &= \tilde{v}_{i+1}(t) - \tilde{v}_i(t)\,, \\
\dot{\tilde{v}}_i(t) &= \alpha\big(\kappa\tilde{h}_i(t-\tau) - \tilde{v}_i(t-\tau)\big) + \beta\big(\tilde{v}_{i+1}(t-\tau) - \tilde{v}_i(t-\tau)\big),
\end{aligned} \tag{5.45}$$

for $i = 2, \ldots, n$, where $u(t)$ is given by (5.41) and σ denotes the communication delay.

The plant stability of a CCC vehicle is given as follows: suppose that the vehicles whose signals are used by the CCC vehicle are driven at the same constant velocity, that is, $v_i(t) \equiv v^*$, $i = 2, \ldots, n+1$, then the velocity of the CCC vehicle approaches this constant velocity, i.e., $\lim_{t\to\infty} v_1(t) = v^*$. The plant stability of non-CCC vehicles is defined similarly: when the preceding vehicle is driven at constant velocity, the non-CCC vehicle should converge to the same velocity. In this paper we only consider plant stable non-CCC vehicles.

String stability characterizes the attenuation of velocity fluctuations as they propagate upstream [44]. For non-CCC vehicles it is required that the vehicle attenuates the velocity fluctuations arising from the preceding vehicle. For a CCC vehicle, one may compare its velocity fluctuations with any preceding vehicle whose signals is used by the CCC vehicle. The influence of a CCC vehicle on the traffic flow is evaluated the best by comparing its velocity fluctuations to that of the furthest vehicle ahead whose signal is received by the CCC vehicle (called the head vehicle). Thus, we define the head-to-tail string stability, which requires velocity fluctuations to be suppressed from the head vehicle to the tail. Since no control is placed upon the non-CCC vehicles, it is reasonable to allow amplification of velocity fluctuations among non-CCC vehicles. Still, the CCC vehicles may ensure head-to-tail string stability as demonstrated below.

While in the previous section the controller was designed for the zero disturbance case, here we consider the velocity perturbation $\tilde{v}_{n+1}$ of the head vehicle as the input and the velocity perturbation $\tilde{v}_1$ of the tail vehicle as the output in (5.45). Since perturbations of velocity can be represented using Fourier components and superposition holds for linear systems, the head-to-tail string stability can be ensured by attenuating sinusoidal signals for all

excitation frequencies. Thus, we consider the periodic excitation $\tilde{v}_{n+1}(t) = v_{n+1}^{\mathrm{amp}} \sin(\omega t)$ with frequency ω and amplitude v_{n+1}^{amp}. Then the steady state response of (5.45) with control (5.41) is $\tilde{v}_{1,\mathrm{ss}}(t) = v_1^{\mathrm{amp}} \sin(\omega t + \psi)$. In order to ensure head-to-tail string stability, we need the amplitude ratio $v_1^{\mathrm{amp}}/v_{n+1}^{\mathrm{amp}} < 1$ for all excitation frequencies $\omega > 0$, which can be obtained through transfer functions.

In particular, taking the Laplace transform of (5.45) with zero initial conditions and eliminating the velocities and headways of vehicles $i = 2, \ldots, n$, we obtain the head-to-tail transfer function

$$H(s) = \frac{\tilde{V}_1(s)}{\tilde{V}_{n+1}(s)} = \frac{\sum_{i=2}^{n} \big(F_{i-1}(s) - G_i(s)\big) \cdot \big(H_0(s)\big)^{n-i+1} + F_n(s)}{s^2 \mathrm{e}^{\sigma s} + G_1(s)} \,. \tag{5.46}$$

Here $\tilde{V}_1(s)$ and $\tilde{V}_{n+1}(s)$ denote the Laplace transform of $\tilde{v}_1(t)$ and $\tilde{v}_{n+1}(t)$, respectively, and

$$\begin{aligned}
H_0(s) &= \frac{F_0(s)}{G_0(s)} = \frac{\beta s + \alpha\kappa}{s^2 \mathrm{e}^{\tau s} + (\alpha+\beta)s + \alpha\kappa} \,, \\
F_i(s) &= \alpha_{1i}\kappa + \beta_{1i} s + (a_{i1}\kappa + b_{i1} s) h_1(s) + (a_{i0}\kappa + b_{i0} s) h_0(s) + (a_{i2}\kappa + b_{i2} s) h_2(s) \,, \\
G_i(s) &= F_i(s) + \alpha_{1i} s + s\big(a_{i0} h_0(s) + a_{i1} h_1(s) + a_{i2} h_2(s)\big) \,,
\end{aligned} \tag{5.47}$$

where $a_{i0}, a_{i1}, a_{i2}, b_{i0}, b_{i1}, b_{i2}$ are given in Appendix C.2 for $i = 1, \ldots, n$ and

$$\begin{aligned}
h_0(s) &= \frac{\mathrm{e}^{\tau\lambda_1} - \mathrm{e}^{-\tau s}}{s + \lambda_1} \,, \\
h_1(s) &= \frac{\tau \mathrm{e}^{-\tau s}}{s + \lambda_1} - \frac{\mathrm{e}^{\tau\lambda_1} - \mathrm{e}^{-\tau s}}{(s+\lambda_1)^2} \,, \\
h_2(s) &= \frac{\mathrm{e}^{\tau\lambda_2} - \mathrm{e}^{-\tau s}}{s + \lambda_2} \,.
\end{aligned} \tag{5.48}$$

Here $H_0(s)$ represents the transfer function between a non-CCC vehicle and its predecessor. Indeed, the amplitude ratio for frequency ω is given by $v_1^{\mathrm{amp}}/v_{n+1}^{\mathrm{amp}} = |H(\,\mathrm{i}\omega)|$, that is, the head-to-tail string stability is ensured when $|H(\,\mathrm{i}\omega)| < 1$ for all $\omega > 0$.

5.3.1 Plant stability

The plant stability for the linearized connected vehicle system (5.41, 5.45) requires that all its characteristic roots have negative real parts, i.e., the solutions of the characteristic

equation

$$G_0^{n-1}(s)\big(s^2\mathrm{e}^{\sigma s}+G_1(s)\big)=0\,. \tag{5.49}$$

stay in the left half complex plane.

Since $G_0(s)=0$ (see $H_0(s)$ in (5.47)) is the characteristic equation for linearized human car-following model (2.11), it is necessary that the human-driven vehicles are plant stable. This is a reasonable requirement as they should be able to maintain a desired speed with no disturbance from the traffic. By setting $s=\mathrm{i}\Omega$, $\Omega\geq 0$ in $G_0(s)=0$ we obtain the plant stability boundary for human-driven vehicles as

$$\begin{aligned}\alpha&=\frac{\Omega^2\cos(\tau\Omega)}{\kappa}\,,\\ \beta&=\Omega\sin(\tau\Omega)-\frac{\Omega^2\cos(\tau\Omega)}{\kappa}\,.\end{aligned} \tag{5.50}$$

And in the remainder of this paper we only consider human parameters α,β inside the plant stability region enclosed by (5.50) and $\alpha=0$ (given by $G(0)=0$); see the shading in Fig. 5.7.

For the remaining part of (5.49), we plug (C.9) in (5.47, 5.48) and obtain

$$s^2\mathrm{e}^{\sigma s}+(\alpha_{11}+\beta_{11})s+\alpha_{11}\kappa=0\,, \tag{5.51}$$

the characteristic equation for the CCC driving model. Due to the similarity between (5.51) and $G_0(s)=0$, the plant stability boundary is the same as (5.50) but with α_{11} instead of α, β_{11} instead of β, and σ instead of τ. However, it is more desirable to present it in the (γ_1,γ_2)-plane. Thus, we plug (5.43) into (5.51), consider $s=\mathrm{i}\Omega$, $\Omega\geq 0$, and obtain the plant stability boundary for the CCC vehicle as

$$\begin{aligned}\gamma_1&=\frac{\Omega^4\cos^2(\sigma\Omega)}{\kappa^2}\,,\\ \gamma_2&=\Omega^2\sin^2(\sigma\Omega)-\frac{\Omega^4\cos^2(\sigma\Omega)}{\kappa^2}-2\Omega^2\cos(\sigma\Omega)\,.\end{aligned} \tag{5.52}$$

Since the cost function (5.10) requires $\gamma_1>0,\gamma_2>0$, we only consider the first quadrant of the (γ_1,γ_2)-plane. In Fig. 5.4, the dashed curves represent plant stability boundaries, and the plant stability area is shaded as light gray for different values of communication delay as indicated. By comparing the two panels one may notice that as the communication delay increases the plant stable area shrinks, though it still covers a relatively large portion of the (γ_1,γ_2)-plane. Since the communication delay σ is seldom larger than human reaction time τ, panel (b) shows a quite conservative case.

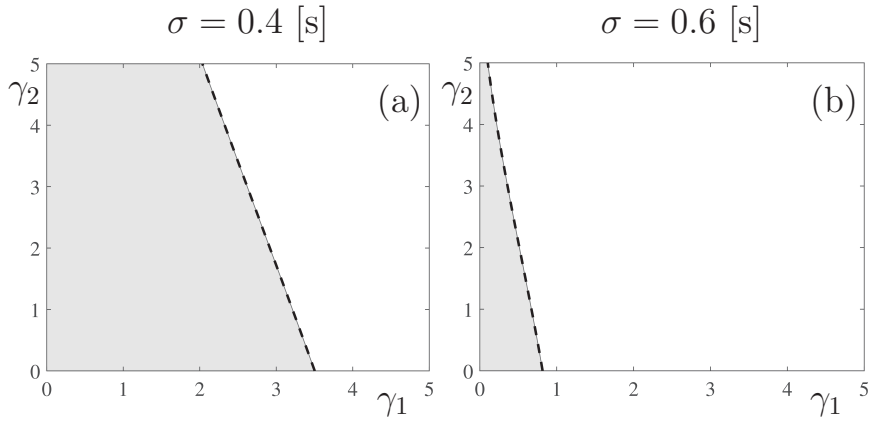

Figure 5.4: Plant stability charts in the (γ_1, γ_2)-plane with communication delay σ as indicated. The plant stability boundaries are denoted by dashed black curves. The plant stable domains are shaded light gray.

5.3.2 Head-to-tail string stability

At the linear level the necessary and sufficient condition of head-to-tail string stability is given by

$$L(\omega) = |H(\,\mathrm{i}\omega)|^2 - 1 < 0\,, \quad \forall \omega > 0\,, \tag{5.53}$$

where $H(\,\mathrm{i}\omega)$ is defined by (5.46, 5.47, 5.48). String stability is violated when the maximum of $L(\omega)$ is larger than 0, and thus, the string stability boundary is given by the equations

$$L(\omega^{\mathrm{cr}}) = 0\,, \quad \frac{\partial L(\omega^{\mathrm{cr}})}{\partial \omega} = 0\,, \tag{5.54}$$

subject to $\dfrac{\partial^2 L(\omega^{\mathrm{cr}})}{\partial \omega^2} \leq 0$, where ω^{cr} indicates the location of the maximum of $L(\omega)$. When $\omega^{\mathrm{cr}} = 0$, we always have $L(0) = 0$, $\dfrac{\partial L(0)}{\partial \omega} = 0$, and the boundary is given by

$$\frac{\partial^2 L(0)}{\partial \omega^2} = 0\,. \tag{5.55}$$

As demonstrated in the previous section, feedback gains for vehicles i, $i > 6$ are negligibly small. Therefore we consider a connected vehicle system with $n = 5$. To obtain string stability charts, we solve (5.54) numerically and plot the string stability boundaries in the (γ_1, γ_2)-plane and in the (β, α)-plane for different values of communication delay and human reaction time.

The charts in Fig. 5.5 allow us to choose the design parameters γ_1, γ_2 so that head-to-tail string stability is ensured, as indicated by the dark gray region bounded by solid colored curves. The human gains are chosen as $\alpha = 0.6$ [1/s], $\beta = 0.9$ [1/s], $\kappa = \pi/2$ [1/s] and

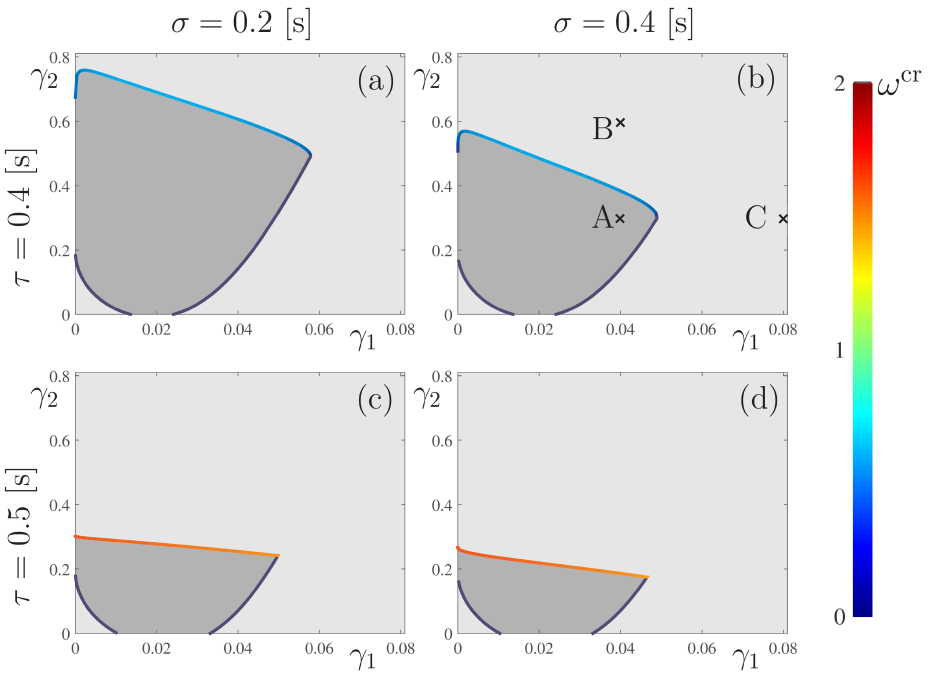

Figure 5.5: Stability charts of a $(5+1)$-car system in the (γ_1, γ_2)-plane for human parameters $\alpha = 0.6$ [1/s], $\beta = 0.9$ [1/s] and $\kappa = \pi/2$ [1/s]. The colored solid curves are the string stable boundaries. The coloring corresponds to the critical frequency at which string stability loss happens, as indicated by the colorbar on the right. Shading indicates plant stability while the string stable regions are shaded dark gray.

stability charts are shown for different values of human reaction time τ and communication delay σ. In the light gray region, only plant stability is satisfied. For the σ values considered here, all γ_1, γ_2 values in the windows shown ensure plant stability.

By comparing the size of the string stable region on the panels, we conclude that increasing the human reaction time and the communication delay both reduce string stability area, however, human reaction time affects the string stability more prominently. Notice that in order to achieve head-to-tail string stability, the weights γ_1, γ_2 have to be large enough. However, when either of these weights is exceedingly large, head-to-tail string stability will also be lost. The fact that both γ_1, γ_2 shall be below 1 to ensure string stability implies that penalties on velocity differences should be smaller than the penalty on the control effort (acceleration).

We remark that the human reaction time considered in Fig. 5.5 are larger than the critical reaction time $\tau_{\mathrm{cr}} \approx 0.325$ [s] and thus no string stability exists for any α, β combinations without V2V connectivity [48], but the system can be made head-to-tail string stable by using the connectivity in an appropriate way.

The coloring along the string stability boundaries shows the critical frequency where

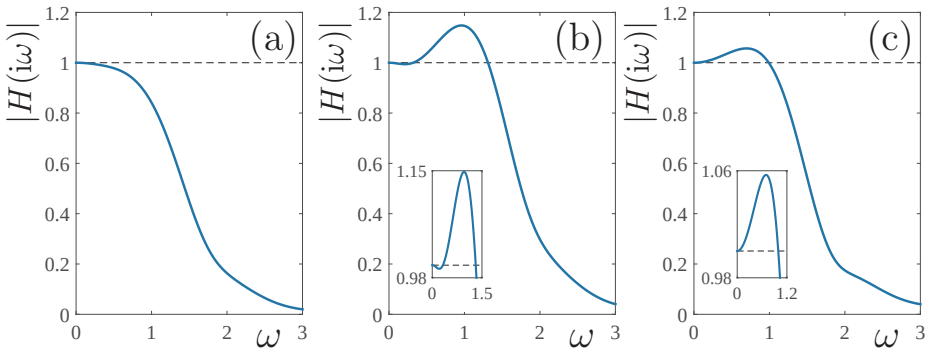

Figure 5.6: Magnitude of transfer function as a function of the excitation frequency. Panels (a–c) correspond to points marked A–C in Fig. 5.5(a).

string stability loss happens, as indicated by the colorbar on the right. Red corresponds to higher frequency and blue corresponds to lower frequency. Leaving the string stable region through the dark blue curves, zero-frequency stability loss happens, while leaving it through the colored curve at the top, the stability loss happens at non-zero frequency, indicating the consequence of improper connectivity design.

To demonstrate string instabilities at different frequencies, we mark three points A, B, and C in Fig. 5.5(b) and plot the corresponding Bode plots in Fig. 5.6. Case A is string stable, with amplitude of transfer function smaller than 1 for all positive frequencies, cf. (5.53). The corresponding feedback gains and distribution kernels are given in Figs. 5.2 and 5.3. Case B has string instability in higher frequency range, due to the non-zero-frequency string stability loss at the boundary between points A and B. Such phenomenon has also been observed when using acceleration feedback in Chapter 4. Case C is string unstable due to low-frequency instability, corresponding to the zero-frequency stability loss when crossing the boundary between points A and C.

The charts in Fig. 5.7 allows us to test the robustness of the CCC design for given design parameters with respect to different human parameters of the non-CCC vehicles. The same notations are used as in Figs. 5.4 and 5.5. The light gray areas bounded by black dashed curves given by (5.50) show the plant stable areas that shrink as human reaction time τ increases. The dark gray regions bounded by colored solid curves are string stable regions, with the color indicating the frequency at which the stability loss happens. The coloring along the string stability boundaries show that both zero-frequency and non-zero-frequency string stability loss exists for all cases. Note that although there may be string stability regions outside the plant stability region, the lack of plant stability prevents the connected vehicle system from maintaining uniform traffic flow, so those regions are not shown in Fig. 5.7.

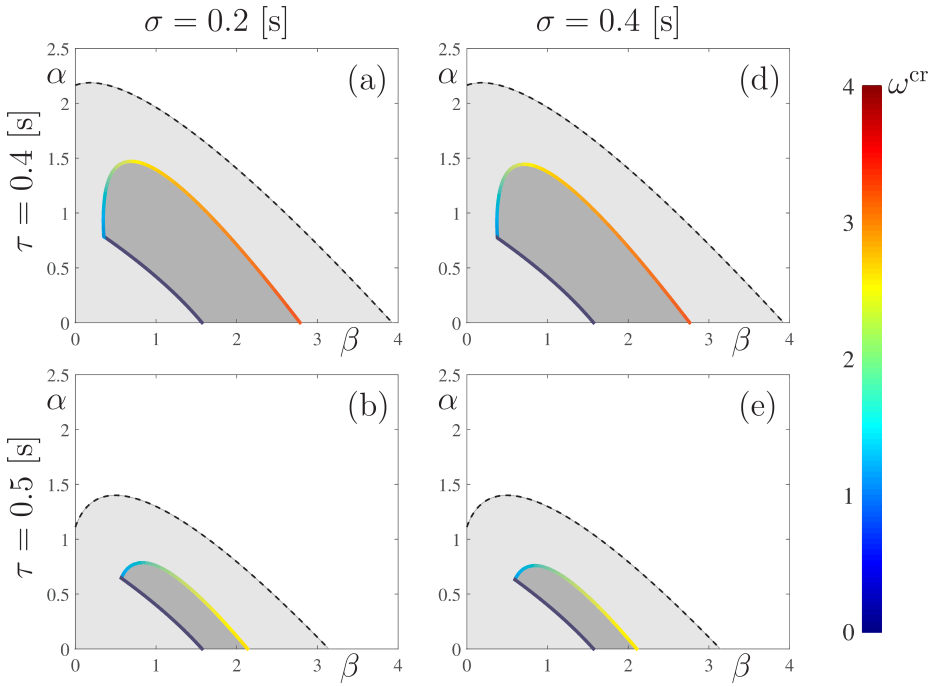

Figure 5.7: Stability charts of a $(5+1)$-car system in the (β, α)-plane for design parameters $\gamma_1 = 0.01\,[1/\mathrm{s}^2]$, $\gamma_2 = 0.10\,[1/\mathrm{s}^2]$. The notation is the same as in Figs. 5.4 and 5.5.

Comparing the different panels in Fig. 5.7, we find that increasing the human reaction time significantly decreases the string stable area, while the communication delay only slightly deteriorates string stability. In each panel, the string stable region requires $\beta > 0.5$ [1/s] but allows α to be infinitesimally small. This shows that the optimization-based CCC controller can stabilize the system even when there is little feedback on headway error.

5.4 Nonlinear simulations

While the CCC controller is obtained with little computational cost using a linearized model for non-CCC vehicles, the algorithm should be able to accommodate nonlinearities arising in the dynamics of non-CCC vehicles, especially the nonlinearity in the range policy (2.3). Here we show that this nonlinearity can be added to the CCC design (5.41, 5.45) by using

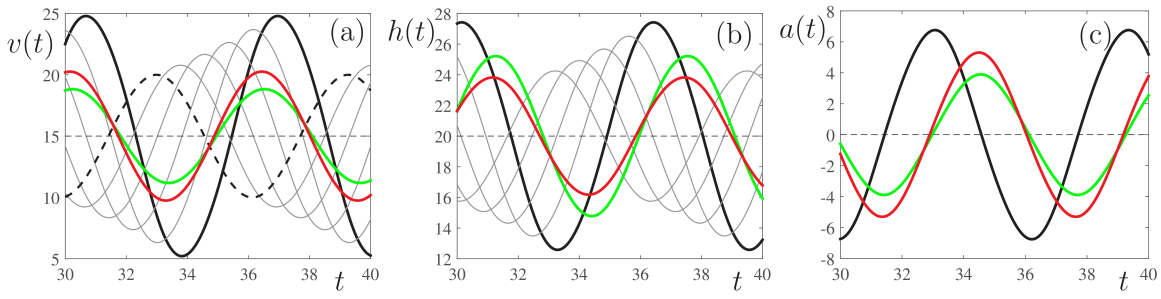

Figure 5.8: Velocity, headway, and acceleration responses of a $(5+1)$-car vehicle string with human parameters $\alpha = 0.6[1/\mathrm{s}]$, $\beta = 0.9\,[1/\mathrm{s}]$, $\kappa = \pi/2$ [1/s], $\tau = 0.4$ [s] and communication delay $\sigma = 0.4$ [s]. The black solid curves represent the case with no connectivity when the tail vehicle is also human-driven. The green solid curves correspond to the string stable design of the CCC vehicle ($\gamma_1 = 0.04\,[1/\mathrm{s}^2]$, $\gamma_2 = 0.30\,[1/\mathrm{s}^2]$, see point A in Fig. 5.5(b)). The red solid curves correspond to the string unstable design of the CCC vehicle ($\gamma_1 = 0.04\,[1/\mathrm{s}^2]$, $\gamma_2 = 0.60\,[1/\mathrm{s}^2]$, see point B in Fig. 5.5(b)). The thin grey curves are for non-CCC vehicles, and the black dashed curve is the velocity perturbation of the head vehicle.

the optimized feedback gains and distribution kernels. In particular, we can construct

$$
\begin{aligned}
\dot{h}_1(t) &= v_2(t) - v_1(t)\,, \\
\dot{v}_1(t) &= \sum_{i=1}^{n} \alpha_{1i}\big(V(h_i(t-\sigma)) - v_i(t-\sigma)\big) + \sum_{i=1}^{n} \beta_{1i}\big(v_{i+1}(t-\sigma) - v_i(t-\sigma)\big) \\
&\quad + \sum_{i=1}^{n} \int_{-\tau}^{0} f_i(\theta)\big(V(h_i(t+\theta-\sigma)) - v_i(t+\theta-\sigma)\big)\,\mathrm{d}\theta \\
&\quad + \sum_{i=1}^{n} \int_{-\tau}^{0} g_i(\theta)\big(v_{i+1}(t+\theta-\sigma) - v_i(t+\theta-\sigma)\big)\,\mathrm{d}\theta\,, \\
\dot{h}_i(t) &= v_{i+1}(t) - v_i(t)\,, \\
\dot{v}_i(t) &= \alpha\big(V(h_i(t-\tau)) - v_i(t-\tau)\big) + \beta\big(v_{i+1}(t-\tau) - v_i(t-\tau)\big),
\end{aligned}
\tag{5.56}
$$

for $i = 2, \ldots, n$, cf. (2.9), where the range policy function $V(h)$ is given by (2.3, 2.5). Linearizing (5.56) about the uniform flow equilibrium (2.6) indeed yields (5.41, 5.45).

To evaluate the performance at the nonlinear level, we consider a $(5+1)$-car system with human delay time $\tau = 0.4$ [s], communication delay $\sigma = 0.4$ [s] and simulate the propagation of headway and velocity perturbations along the connected vehicle system (5.56). The simulation is performed with Adam-Bashforth fourth-order method.

Fig. 5.8 compares the simulation results for the parameters corresponding to points A and B in Fig. 5.5(b) with the case where the CCC vehicle loses connectivity and has the same controller as the human-driven vehicles. The velocity profile of the head vehicle is

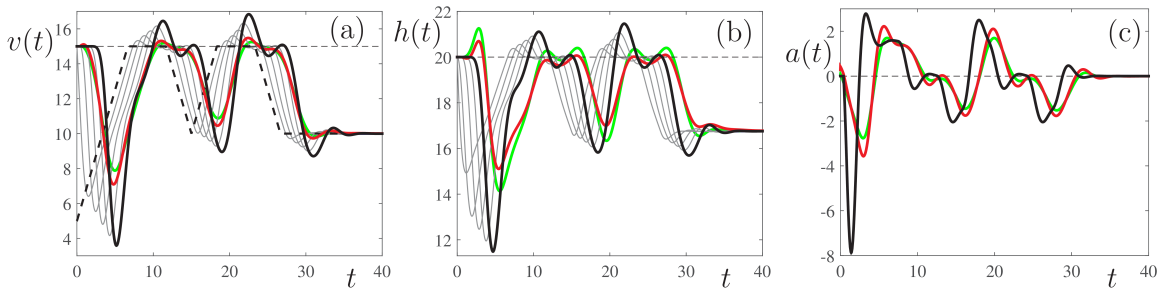

Figure 5.9: Velocity, headway, and acceleration responses of a $(5+1)$-car vehicle string in a real-traffic scenario. Notations and parameters are the same as in Fig. 5.8.

$v_{n+1}(t) = v^* + v_{n+1}^{\text{amp}} \sin(\omega t)$ with amplitude $v_{n+1}^{\text{amp}} = 5$ [m/s], frequency $\omega = 1$ [rad/s] and $v^* = 15$ [m/s].

Without connectivity, attenuation of velocity perturbation is not possible as the human reaction time $\tau > \tau_{\text{cr}}$. This is demonstrated by the black solid curve in Fig. 5.8(a). For the string unstable optimal design (point B in Fig. 5.5(b)), the velocity perturbation is attenuated as shown by the red solid curve in Fig. 5.8(a). However, the magnitude is still larger than that of the head vehicle (black dashed curve). On the other hand, for the string stable design corresponding to point A in Fig. 5.5(b), the CCC vehicle's velocity fluctuation (green solid curve) has smaller amplitude than the velocity input (black dashed curve), as depicted in Fig. 5.8(a). These results demonstrate that the linearized design can be used to predict the nonlinear behavior.

In Fig. 5.8(b), the headway fluctuations of the CCC vehicle (red and green solid curves) have smaller amplitude compared to the case without connectivity (black solid curve). This shows that although the CCC design is based on string stability in terms of velocity, the connectivity can also suppress headway errors. Notice that the headway fluctuation of the CCC vehicle in the string unstable case B (red solid curve) is slightly smaller than in the string stable case A (green solid curve), indicating a trade-off between attenuation of velocity and headway disturbances.

In Fig. 5.8(c) the accelerations of the CCC vehicle (red and green solid curves) are significantly smaller compared with the case with no connectivity (black solid curve), where the acceleration gets excessively large. As the road surface and the vehicle powertrain are often not able to provide such large acceleration/deceleration, the vehicle in general may not be able to remain safe.

To test the proposed CCC controller in a more realistic traffic setting, we consider a velocity profile of the leading vehicle that contains deviation from the uniform flow with constant acceleration and change of equilibrium points; see the black dashed curve in Fig. 5.9(a). Here we use the same parameters as in Fig. 5.8. Indeed, the velocity pertur-

bation of the CCC vehicle is larger when a string unstable design is adopted (compare the red and green solid curves). However, even with string unstable design, the performance of CCC vehicles is still significantly better than if there was no connectivity (compare the red and the black solid curves). Especially that the acceleration response of the tail vehicle without connectivity (black solid curve) may exceed the limit of friction the road could provide, as it has to engage emergency maneuver for active safety. By exploiting the information of multiple vehicles ahead, CCC can be used to avoid such safety-critical situation.

5.5 Conclusion

In this chapter, we proposed a connected cruise control design in a V2V-rich environment based on linear quadratic regulation. We analyzed the performance of the arising connected vehicle system where both automated and human-driven vehicles were allowed. By decomposing the optimization problem we showed that CCC can be designed sequentially as we incorporate signals from more and more vehicles ahead. Moreover, we showed that the gains decrease with the number of cars between the CCC vehicle and the signaling vehicle even when heterogeneity of human drivers is taken into account. This implies that a connected vehicle system using the proposed controller can gracefully degrade into smaller systems while maintaining certain optimality. Our analytical method significantly reduces the complexity of CCC design and is scalable for large connected vehicle systems.

We evaluated the head-to-tail string stability and summarized the results using stability charts. We showed that the optimized CCC is able to stabilize otherwise string unstable systems when the weights on the headway and velocity errors are chosen appropriately. This design was also shown to be robust against variations of human parameters and was extended to the nonlinear level. In the next chapter, we will extend the optimal CCC design to consider the stochasticity of human parameters in the non-CCC vehicles.

CHAPTER 6

Optimal design of connected cruise control considering stochastic human behavior

In this chapter we design a connected cruise controller that takes into consideration stochastic variations in human parameters. In Chapters 4 and 5 nominal values of human parameters α, β, κ, τ are used to demonstrate different design methods for a connected automated vehicle in V2V-sparse and V2V-rich environments, respectively. On the other hand, results from Chapter 3 show that human parameters vary in time stochastically (see Fig. 3.5) and follow certain distributions (see Fig. 3.6 and Fig. 3.7). Since the gains in a CCC controller in V2V-sparse environment are tuned directly as design parameters, the mean of human parameters can be set as the nominal values, and the variance can be taken into consideration via robustness analysis. However, the optimal CCC design in V2V-rich environment under stochastic human parameters may take different feedback gains and kernels, and robustness analysis may be more challenging. In this chapter, we design an optimal CCC controller while taking into account the distributions of human parameters, and test its performance based on the four-car experiment presented in Chapter 3.

6.1 Optimal control based on mean dynamics

Fig. 3.6 and Fig. 3.7 have shown that the feedback gains α_i, β_i, the inverse time headway κ_i and reaction time τ_i for human drivers vary stochastically. We consider the human car-following model with linear range policy function (3.1) and take the expected value

$$\begin{aligned}\mathbb{E}\big[\dot{h}_i(t)\big] &= \mathbb{E}[v_{i+1}(t)] - \mathbb{E}[v_i(t)]\,,\\ \mathbb{E}\big[\dot{v}_i(t)\big] &= \mathbb{E}\Big[\alpha_i(t)\Big(\kappa_i(t)h_i\big(t-\tau_i(t)\big) - v_i\big(t-\tau_i(t)\big)\Big)\Big]\\ &\quad + \mathbb{E}\Big[\beta_i(t)\Big(v_{i+1}\big(t-\tau_i(t)\big) - v_i\big(t-\tau_i(t)\big)\Big)\Big]\,.\end{aligned} \tag{6.1}$$

Denote the mean state variables and parameters

$$\begin{aligned} &\bar{h}_i(t) = \mathbb{E}[h_i(t)], \quad \bar{v}_i(t) = \mathbb{E}[v_i(t)], \\ &\bar{\alpha}_i = \mathbb{E}[\alpha_i(t)], \quad \bar{\beta}_i = \mathbb{E}[\beta_i(t)], \quad \bar{\kappa_i} = \mathbb{E}[\kappa_i(t)], \end{aligned} \tag{6.2}$$

and assume the gains α_i, β_i, the inverse time headway κ_i and reaction time τ_i are independent and identically distributed (IID). Then we have

$$\begin{aligned} \dot{\bar{h}}_i(t) &= \bar{v}_{i+1}(t) - \bar{v}_i(t)\,, \\ \dot{\bar{v}}_i(t) &= \bar{\alpha}_i\Big(\bar{\kappa}_i \mathbb{E}\big[h_i\big(t-\tau_i(t)\big)\big] - \mathbb{E}\big[v_i\big(t-\tau_i(t)\big)\big]\Big) \\ &\quad + \bar{\beta}_i\Big(\mathbb{E}\big[v_{i+1}\big(t-\tau_i(t)\big)\big] - \mathbb{E}\big[v_i\big(t-\tau_i(t)\big)\big]\Big)\,. \end{aligned} \tag{6.3}$$

Denote the realization of vehicle speed $v_i \in [0,\, v_{\max}]$ and reaction time $\tau_i \in [0, \tau_{\max}]$ as $\tilde{v}_i$ and $\tilde{\tau}_i$, where $\tau_{\max}$ is the maximum reaction time. Then due to the IID property of the reaction time

$$\begin{aligned} \mathbb{E}\big[v_i\big(t-\tau_i(t)\big)\big] &= \int_0^{\tau_{\max}} \int_0^{v_{\max}} \tilde{v}_i\, \mathbb{P}[v_i\big(t-\tilde{\tau}_i\big) = \tilde{v}_i,\, \tau_i(t) = \tilde{\tau}_i]\, \mathrm{d}\tilde{v}_i\, \mathrm{d}\tilde{\tau}_i \\ &= \int_0^{\tau_{\max}} \Big(\int_0^{v_{\max}} \tilde{v}_i\, \mathbb{P}[v_i\big(t-\tilde{\tau}_i\big) = \tilde{v}_i]\, \mathrm{d}\tilde{v}_i \Big) \mathbb{P}[\tau_i(t) = \tilde{\tau}_i]\, \mathrm{d}\tilde{\tau}_i \\ &= \int_0^{\tau_{\max}} \bar{v}_i\big(t-\tilde{\tau}_i\big)\, \mathbb{P}[\tau_i(t) = \tilde{\tau}_i]\, \mathrm{d}\tau_i\,, \end{aligned} \tag{6.4}$$

where $\mathbb{P}[\tau_i(t) = \tilde{\tau}_i]$ is the probability of reaction time $\tau_i(t)$, and $\mathbb{P}[v_i\big(t-\tilde{\tau}_i\big) = \tilde{v}_i,\, \tau_i(t) = \tilde{\tau}_i]$ is the joint probability of reaction time $\tau_i(t)$ and speed $v_i\big(t-\tilde{\tau}_i\big)$.

In this way we have the mean dynamics as

$$\begin{aligned} \dot{\bar{h}}_i(t) &= \bar{v}_{i+1}(t) - \bar{v}_i(t)\,, \\ \dot{\bar{v}}_i(t) &= \bar{\alpha}_i \int_{-\tau_{\max}}^{0} w_i(\theta)\big(\bar{\kappa}_i \bar{h}_i(t+\theta) - \bar{v}_i(t+\theta)\big)\, \mathrm{d}\theta \\ &\quad + \bar{\beta}_i \int_{-\tau_{\max}}^{0} w_i(\theta)\big(\bar{v}_{i+1}(t+\theta) - \bar{v}_i(t+\theta)\big)\, \mathrm{d}\theta\,. \end{aligned} \tag{6.5}$$

where the distribution $w_i(\theta)$ is the probability density function of the reaction time for $\theta \in [-\tau_{\max},\, 0]$. That is, when taking the expected value of (3.1) we obtain an expected value of the gains and the range policy slope while the delay distribution appears explicitly.

Similarly, the mean car-following dynamics of the CCC vehicle is given by

$$\begin{aligned} \dot{\bar{h}}_1(t) &= \bar{v}_2(t) - \bar{v}_1(t)\,, \\ \dot{\bar{v}}_1(t) &= u(t)\,, \end{aligned} \tag{6.6}$$

where $u(t)$ is the optimal CCC controller to be designed.

Similar to (5.5, 5.6), we define

$$x_i = \begin{bmatrix} \bar{\kappa}_i \bar{h}_i - \bar{v}_i \\ \bar{v}_{i+1} - \bar{v}_i \end{bmatrix}, \quad \phi_n = \begin{bmatrix} 0 \\ \dot{\bar{v}}_{n+1} \end{bmatrix}, \tag{6.7}$$

where $i = 1, \ldots, N$. Then we construct the vectors

$$X = \begin{bmatrix} x_1 \\ \vdots \\ x_n \end{bmatrix}, \quad \phi = \begin{bmatrix} 0 \\ \vdots \\ 0 \\ \phi_n \end{bmatrix}, \tag{6.8}$$

and rewrite the mean dynamics of the connected vehicle system (6.5, 6.6) as a system with distributed delay

$$\dot{X}(t) = \mathbf{A}X(t) + \int_{-\tau_{\max}}^{0} \mathbf{G}(\theta)X(t+\theta)\,\mathrm{d}\theta + \mathbf{D}u(t) + \phi(t)\,. \tag{6.9}$$

The coefficient matrices are given by

$$\mathbf{A} = \begin{bmatrix} \mathbf{A}_1 & & \\ & \ddots & \\ & & \mathbf{A}_n \end{bmatrix}, \quad \mathbf{D} = \begin{bmatrix} \mathbf{D}_1 \\ \mathbf{0} \\ \vdots \\ \mathbf{0} \end{bmatrix}, \quad \mathbf{G}(\theta) = \begin{bmatrix} \mathbf{0} & \mathbf{G}_{12}(\theta) & & & \\ & \mathbf{G}_{22}(\theta) & \mathbf{G}_{23}(\theta) & & \\ & & \ddots & \ddots & \\ & & & & \mathbf{G}_{nn}(\theta) \end{bmatrix}, \tag{6.10}$$

where the blocks are defined by

$$\begin{aligned} \mathbf{A}_i &= \begin{bmatrix} 0 & \bar{\kappa}_i \\ 0 & 0 \end{bmatrix}, \quad \mathbf{G}_{ii}(\theta) = -\begin{bmatrix} \bar{\alpha}_i & \bar{\beta}_i \\ \bar{\alpha}_i & \bar{\beta}_i \end{bmatrix} w_i(\theta), \\ \mathbf{D}_1 &= \begin{bmatrix} -1 \\ -1 \end{bmatrix}, \quad \mathbf{G}_{(i-1)i}(\theta) = \begin{bmatrix} 0 & 0 \\ \bar{\alpha}_i & \bar{\beta}_i \end{bmatrix} w_i(\theta)\,. \end{aligned} \tag{6.11}$$

Note that the coefficient matrices $G_{ij}(\theta)$ for the distributed delay has the same upper-triangular structure as the matrices (5.8) in the point delay, which indicates that the method used to solve the LQ problem with point delay in Chapter 5 may be applied here as well.

We recall the multi-objective cost function (5.10)

$$\begin{aligned} J_{t_{\mathrm{f}}}(u, X) &= \int_0^{t_{\mathrm{f}}} \Big(u^2 + \gamma_1 \big(\bar{\kappa}_1 \bar{h}_1 - \bar{v}_1 \big)^2 + \gamma_2 \big(\bar{v}_2 - \bar{v}_1 \big)^2 \Big) \, \mathrm{d}t \\ &= \int_0^{t_{\mathrm{f}}} \big(u^2 + X^{\mathrm{T}} \mathbf{\Gamma} X \big) \, \mathrm{d}t \,, \end{aligned} \tag{6.12}$$

where $\gamma_1 > 0$, $\gamma_2 > 0$ and

$$\mathbf{\Gamma} = \mathrm{diag}[\gamma_1, \gamma_2, 0, \ldots, 0] \in \mathbb{R}^{2n \times 2n}. \tag{6.13}$$

The optimal controller under this distributed time delay maintains the same form (5.19) as under the point delay [63], that is,

$$u(t) = -\mathbf{D}^{\mathrm{T}} \bigg(\mathbf{P}_1(t) X(t) + \int_{-\tau_{\max}}^{0} \mathbf{Q}_1(t, \theta) X(t+\theta) \, \mathrm{d}\theta + \mathbf{P}_2(t) + \int_{-\tau_{\max}}^{0} \mathbf{Q}_2(t, \theta) \, \mathrm{d}\theta \bigg) , \tag{6.14}$$

and similarly the state-feedback-control gain matrices $\mathbf{P}_1(t), \mathbf{Q}_1(t, \theta)$ are not influenced by the disturbance $\phi(t)$. We consider $\phi(t) = 0$ and set time horizon $t_{\mathrm{f}} \to \infty$ in the cost function (5.10). Then we also have the steady-state solution

$$\begin{aligned} &\mathbf{P}_1(t) \equiv \mathbf{P}_1, \quad \mathbf{Q}_1(t, \theta) \equiv \mathbf{Q}_1(\theta), \quad \mathbf{R}_1(t, \xi, \theta) \equiv \mathbf{R}_1(\xi, \theta) \,, \\ &\mathbf{P}_2(t) \equiv \mathbf{0}, \qquad \mathbf{Q}_2(t, \theta) \equiv \mathbf{0} \,. \end{aligned} \tag{6.15}$$

Substituting (6.15) into (6.14) also leads to the simplified controller as in (5.22)

$$u(t) = -\mathbf{D}^{\mathrm{T}} \bigg(\mathbf{P}_1 X(t) + \int_{-\tau_{\max}}^{0} \mathbf{Q}_1(\theta) X(t+\theta) \, \mathrm{d}\theta \bigg) , \tag{6.16}$$

where the matrices $\mathbf{P}_1,\ \mathbf{Q}_1(\theta)$ are given by

$$\begin{aligned} &\mathbf{A}^{\mathrm{T}} \mathbf{P}_1 + \mathbf{P}_1 \mathbf{A} - \mathbf{P}_1 \mathbf{D} \mathbf{D}^{\mathrm{T}} \mathbf{P}_1 + \mathbf{Q}_1(0) + \mathbf{Q}_1^{\mathrm{T}}(0) + \mathbf{\Gamma} = \mathbf{0} \,, \\ &\partial_\theta \mathbf{Q}_1(\theta) = \big(\mathbf{A}^{\mathrm{T}} - \mathbf{P}_1 \mathbf{D} \mathbf{D}^{\mathrm{T}} \big) \mathbf{Q}_1(\theta) + \mathbf{P}_1 \mathbf{G}(\theta) + \mathbf{R}_1(0, \theta) \,, \\ &(\partial_\xi + \partial_\theta) \mathbf{R}_1(\xi, \theta) = \mathbf{G}^{\mathrm{T}}(\xi) \mathbf{Q}_1(\theta) + \mathbf{Q}_1^{\mathrm{T}}(\xi) \mathbf{G}(\theta) - \mathbf{Q}_1^{\mathrm{T}}(\xi) \mathbf{D} \mathbf{D}^{\mathrm{T}} \mathbf{Q}_1(\theta) \,, \end{aligned} \tag{6.17}$$

with boundary conditions

$$\mathbf{Q}_1(-\tau_{\max}) = \mathbf{0}\,, \qquad \mathbf{R}_1(-\tau_{\max}, \theta) = \mathbf{0}\,. \tag{6.18}$$

Note that the Riccati equation (5.23) for the connected vehicle system with point delay (5.7) and the Riccati equation (6.17) for the connected vehicle system with distributed delay (6.9) share the same structure, while the later has extra terms corresponding to the probability density function of the delay time. Here we have trivial boundary condition (6.18) because the mean dynamics (6.9) does not have point delay any more.

We apply the notation (5.25)

$$\mathbf{P}_1 = \begin{bmatrix} \mathbf{P}_{11} & \cdots & \mathbf{P}_{1n} \\ \vdots & \ddots & \vdots \\ \mathbf{P}_{n1} & \cdots & \mathbf{P}_{nn} \end{bmatrix}, \quad \mathbf{Q}_1(\theta) = \begin{bmatrix} \mathbf{Q}_{11}(\theta) & \cdots & \mathbf{Q}_{1n}(\theta) \\ \vdots & \ddots & \vdots \\ \mathbf{Q}_{n1}(\theta) & \cdots & \mathbf{Q}_{nn}(\theta) \end{bmatrix}, \tag{6.19}$$

where $\mathbf{P}_{ij}, \mathbf{Q}_{ij}(\theta) \in \mathbb{R}^{2\times 2}$ for $i, j = 1, \ldots, n$, and the optimal controller takes the form (5.26)

$$u(t) = -\mathbf{D}_1^{\mathrm{T}} \sum_{i=1}^{n} \left(\mathbf{P}_{1i} x_i(t) + \int_{-\tau_{\max}}^{0} \mathbf{Q}_{1i}(\theta) x_i(t+\theta)\, \mathrm{d}\theta \right), \tag{6.20}$$

where $x_i(t)$ is defined in (6.7). Again, we only need to derive $\mathbf{P}_{1i}, \mathbf{Q}_{1i}(\theta)$ for $i = 1, \ldots, n$ to construct the controller. Substituting (5.25) into (6.17, 6.18), we obtain equations for each block $\mathbf{P}_{ij}, \mathbf{Q}_{ij}(\theta), \mathbf{R}_{ij}(\xi, \theta)$, $i, j = 1, \ldots, n$, which can be solved recursively.

Since $\mathbf{P}_{11}$, $\mathbf{Q}_{11}(\theta)$ and $\mathbf{R}_{11}(\xi, \theta)$ are not influenced by car-following dynamics of preceding vehicles, they remain the same as in the point delay case, cf. (5.30, 5.31). However, to obtain $\mathbf{P}_{1i}, \mathbf{Q}_{1i}(\theta), \mathbf{Q}_{i1}(\theta)$ for $i = 2, \ldots, n$, we need to solve

$$\begin{aligned}
&\hat{\mathbf{A}}_1 \mathbf{P}_{1i} + \mathbf{P}_{1i} \mathbf{A}_i + \mathbf{Q}_{1i}(0) + \mathbf{Q}_{i1}^{\mathrm{T}}(0) = \mathbf{0}\,, \\
&\partial_\theta \mathbf{Q}_{1i}(\theta) = \hat{\mathbf{A}}_1 \mathbf{Q}_{1i}(\theta) + \mathbf{P}_{1(i-1)} \mathbf{G}_{(i-1)i}(\theta) + \mathbf{P}_{1i} \mathbf{G}_{ii}(\theta) + \mathbf{R}_{1i}(0, \theta)\,, \\
&\partial_\theta \mathbf{Q}_{i1}(\theta) = \mathbf{A}_1^{\mathrm{T}} \mathbf{Q}_{i1}(\theta) - \mathbf{P}_{1i}^{\mathrm{T}} \mathbf{D}_1 \mathbf{D}_1^{\mathrm{T}} \mathbf{Q}_{11}(\theta) + \mathbf{R}_{1i}^{\mathrm{T}}(\theta, 0)\,, \\
&(\partial_\xi + \partial_\theta) \mathbf{R}_{1i}(\xi, \theta) = \mathbf{Q}_{(i-1)1}^{\mathrm{T}}(\theta) \mathbf{G}_{(i-1)i} + \mathbf{Q}_{i1}^{\mathrm{T}}(\theta) \mathbf{G}_{ii} - \mathbf{Q}_{11}^{\mathrm{T}}(\xi) \mathbf{D}_1 \mathbf{D}_1^{\mathrm{T}} \mathbf{Q}_{1i}(\theta)\,,
\end{aligned} \tag{6.21}$$

where $\hat{\mathbf{A}}_1 = \mathbf{A}_1^{\mathrm{T}} - \mathbf{P}_{11} \mathbf{D}_1 \mathbf{D}_1^{\mathrm{T}}$, cf. (5.29), and the boundary conditions are

$$\begin{aligned}
\mathbf{Q}_{1i}(-\tau_{\max}) = \mathbf{0}\,, \quad \mathbf{Q}_{i1}(-\tau_{\max}) = \mathbf{0}\,, \\
\mathbf{R}_{1i}(\theta, -\tau_{\max}) = \mathbf{0}\,, \quad \mathbf{R}_{1i}(-\tau_{\max}, \theta) = \mathbf{0}\,.
\end{aligned} \tag{6.22}$$

Now (6.21, 6.22) give the solution

$$\mathbf{Q}_{i1}(\theta) \equiv \mathbf{0}, \quad \mathbf{R}_{1i}(\xi, \theta) \equiv \mathbf{0}\,, \tag{6.23}$$

while the equations for $\mathbf{Q}_{1i}(\theta)$ simplify to

$$\begin{aligned} &\partial_\theta \mathbf{Q}_{1i}(\theta) = \hat{\mathbf{A}}_1 \mathbf{Q}_{1i}(\theta) + \mathbf{P}_{1(i-1)} \mathbf{G}_{(i-1)i}(\theta) + \mathbf{P}_{1i} \mathbf{G}_{ii}(\theta), \\ &\mathbf{Q}_{1i}(-\tau_{\max}) = \mathbf{0}\,, \end{aligned} \tag{6.24}$$

yielding the solution

$$\mathbf{Q}_{1i}(\theta) = \int_{-\tau_{\max}}^{\theta} \mathrm{e}^{\hat{\mathbf{A}}_1(\theta-\rho)} \big(\mathbf{P}_{1(i-1)} \mathbf{G}_{(i-1)i}(\rho) + \mathbf{P}_{1i} \mathbf{G}_{ii}(\rho) \big)\, \mathrm{d}\rho\,, \tag{6.25}$$

for $i = 2, \ldots, n$, cf. (5.36). Thus, the equation for $\mathbf{P}_{1i}$ becomes

$$\int_{-\tau_{\max}}^{0} \mathrm{e}^{-\rho \hat{\mathbf{A}}_1} (\mathbf{P}_{1(i-1)} \mathbf{G}_{(i-1)i}(\rho) + \mathbf{P}_{1i} \mathbf{G}_{ii}(\rho))\, \mathrm{d}\rho + \hat{\mathbf{A}}_1 \mathbf{P}_{1i} + \mathbf{P}_{1i} \mathbf{A}_i = \mathbf{0}\,, \tag{6.26}$$

cf. (5.37), yielding the solution

$$\mathrm{vec}(\mathbf{P}_{1i}) = \prod_{j=2}^{i} \mathbf{M}_j \mathrm{vec}(\mathbf{P}_{11})\,, \tag{6.27}$$

for $i = 2, \ldots, n$, cf. (5.38). Here $\mathrm{vec}(\cdot)$ gives a column vector by stacking the columns of the matrix on the top of each other, and $\mathbf{M}_i \in \mathbb{R}^{4\times 4}$ is given by

$$\mathbf{M}_i = -\left(\mathbf{I} \otimes \hat{\mathbf{A}}_1 + \mathbf{A}_i^{\mathrm{T}} \otimes \mathbf{I} + \int_{-\tau_{\max}}^{0} \mathbf{G}_{ii}^{\mathrm{T}}(\rho) \otimes \mathrm{e}^{-\rho \hat{\mathbf{A}}_1}\, \mathrm{d}\rho \right)^{-1} \left(\int_{-\tau_{\max}}^{0} \mathbf{G}_{(i-1)i}^{\mathrm{T}} \otimes \mathrm{e}^{-\rho \hat{\mathbf{A}}_1}\, \mathrm{d}\rho \right), \tag{6.28}$$

cf. (5.39).

6.2 Constructing the CCC controller

Recalling (6.10, 6.11), we denote

$$\mathbf{B}_{ii} = -\begin{bmatrix} \bar{\alpha}_i & \bar{\beta}_i \\ \bar{\alpha}_i & \bar{\beta}_i \end{bmatrix}, \quad \mathbf{B}_{(i-1)i} = \begin{bmatrix} 0 & 0 \\ \bar{\alpha}_i & \bar{\beta}_i \end{bmatrix}, \tag{6.29}$$

and recall (C.10)

$$\mathrm{e}^{-\rho\hat{\mathbf{A}}_1} = \mathbf{K}\mathrm{e}^{-\rho\hat{\mathbf{J}}_1}\mathbf{K}^{-1}\,, \tag{6.30}$$

where $\hat{\mathbf{J}}_1$ is the Jordan form of $\hat{\mathbf{A}}_1$ (see (C.11) for the eigenvalues).

Thus, here we have

$$\int_{-\tau_{\max}}^{0} \mathbf{G}_{ii}^{\mathrm{T}}(\rho) \otimes \mathrm{e}^{-\rho\hat{\mathbf{A}}_1}\,\mathrm{d}\rho = \mathbf{B}_{ii}^{\mathrm{T}} \otimes \left(\mathbf{K}\int_{-\tau_{\max}}^{0} w_i(\rho)\begin{bmatrix}\mathrm{e}^{-\rho\lambda_1} & 0\\ 0 & \mathrm{e}^{-\rho\lambda_2}\end{bmatrix}\mathrm{d}\rho\,\mathbf{K}^{-1}\right) \tag{6.31}$$

Denote

$$\mathbf{L}_i(\theta) = \begin{bmatrix} l_{i1}(\theta) & 0\\ 0 & l_{i2}(\theta)\end{bmatrix}, \quad l_{i1}(\theta) = \int_{-\tau_{\max}}^{\theta} w_i(\rho)\mathrm{e}^{-\rho\lambda_1}\,\mathrm{d}\rho\,, \quad l_{i2}(\theta) = \int_{-\tau_{\max}}^{\theta} w_i(\rho)\mathrm{e}^{-\rho\lambda_2}\,\mathrm{d}\rho\,, \tag{6.32}$$

then (6.28) becomes

$$\mathbf{M}_i = -\left(\mathbf{I}\otimes\hat{\mathbf{A}}_1 + \mathbf{A}_i^{\mathrm{T}}\otimes\mathbf{I} + \mathbf{B}_{ii}^{\mathrm{T}}\otimes\left(\mathbf{K}\mathbf{L}_i(0)\,\mathbf{K}^{-1}\right)\right)^{-1}\left(\mathbf{B}_{(i-1)i}^{\mathrm{T}}\otimes\left(\mathbf{K}\mathbf{L}_i(0)\,\mathbf{K}^{-1}\right)\right). \tag{6.33}$$

and (6.25) becomes

$$\mathbf{Q}_{1i}(\theta) = \mathbf{K}\mathrm{e}^{\theta\hat{\mathbf{J}}_1}\mathbf{L}_i(\theta)\mathbf{K}^{-1}\left(\mathbf{P}_{1(i-1)}\mathbf{B}_{(i-1)i} + \mathbf{P}_{1i}\mathbf{B}_{ii}\right). \tag{6.34}$$

Based on definitions (5.40, 6.7), the optimal controller (6.20) for the CCC vehicle is given by

$$\begin{aligned} u(t) = &\sum_{i=1}^{n}\Big(\alpha_{1i}\big(\bar{\kappa}_i\bar{h}_i(t) - \bar{v}_i(t)\big) + \beta_{1i}\big(\bar{v}_{i+1}(t) - \bar{v}_i(t)\big)\Big)\\ &+\sum_{i=1}^{n}\int_{-\tau_{\max}}^{0} f_i(\theta)\big(\bar{\kappa}_i\bar{h}_i(t+\theta) - \bar{v}_i(t+\theta)\big)\,\mathrm{d}\theta\\ &+\sum_{i=1}^{n}\int_{-\tau_{\max}}^{0} g_i(\theta)\big(\bar{v}_{i+1}(t+\theta) - \bar{v}_i(t+\theta)\big)\,\mathrm{d}\theta\,, \end{aligned} \tag{6.35}$$

where the distribution kernels take the form

$$\begin{aligned} f_i(\theta) &= \big(a_{i0} + a_{i1}\theta\big)\,\mathrm{e}^{\lambda_1\theta}l_{i1}(\theta) + a_{i2}\,\mathrm{e}^{\lambda_2\theta}l_{i2}(\theta)\,,\\ g_i(\theta) &= \big(b_{i0} + b_{i1}\theta\big)\,\mathrm{e}^{\lambda_1\theta}l_{i1}(\theta) + b_{i2}\,\mathrm{e}^{\lambda_2\theta}l_{i2}(\theta)\,, \end{aligned} \tag{6.36}$$

for $i = 1, \ldots, n$, $\theta \in [-\tau_{\max}, 0]$, where λ_1, λ_2 are the eigenvalues of $\hat{\mathbf{A}}_1$. The expressions for λ_1, λ_2, a_{i0}, a_{i1}, a_{i2}, and b_{i0}, b_{i1}, b_{i2} are given in Appendix B.

As the feedback kernels (6.32, 6.36) depend on the distribution $w_i(\rho)$ of the driver reaction time, and the histograms of estimated driver reaction time shown in Fig. 3.6 resembles a Gaussian distribution or a Gamma distribution, here we calculate and compare the feedback kernels when assuming Gaussian and Gamma distributions.

6.2.1 Gaussian Distribution

Consider scaled Gaussian distribution

$$w_i(\tau_i) = \frac{1}{W_i\sqrt{2\pi\sigma_i^2}} \mathrm{e}^{-\dfrac{(\tau_i - \bar{\tau}_i)^2}{2\sigma_i^2}}, \tag{6.37}$$

where $\tau_i \in [0,\ \tau_{\max}]$, the mean of the reaction time is $\bar{\tau}_i$, σ_i is the variance of the reaction time and the scaling factor

$$W_i = \int_0^{\tau_{\max}} \frac{\mathrm{e}^{-(\tau_i - \bar{\tau}_i)^2/(2\sigma_i^2)}}{\sqrt{2\pi\sigma_i^2}}\,\mathrm{d}\rho = \frac{1}{2}\mathrm{erf}\Big(\frac{\bar{\tau}_i}{\sqrt{2}\sigma_i}\Big) - \frac{1}{2}\mathrm{erf}\Big(\frac{\bar{\tau}_i - \tau_{\max}}{\sqrt{2}\sigma_i}\Big), \tag{6.38}$$

Thus, consider $\rho = -\tau_i$, then the function in (6.32) becomes

$$l_{ij}(\theta) = \frac{\mathrm{e}^{\lambda_j\bar{\tau}_i + \sigma_i^2\lambda_j^2/2}}{2W_i}\left(\mathrm{erf}\Big(\frac{\theta + \bar{\tau}_i + \lambda_j\sigma_i^2}{\sqrt{2}\sigma_i}\Big) - \mathrm{erf}\Big(\frac{-\tau_{\max} + \bar{\tau}_i + \lambda_j\sigma_i^2}{\sqrt{2}\sigma_i}\Big)\right), \tag{6.39}$$

where $j = 1, 2$.

6.2.2 Gamma distribution

Consider scaled Gamma distribution for $\tau_i \in [0, \tau_{\max}]$

$$w_i(\tau_i) = \frac{\tau_i^{a_i - 1}\,\mathrm{e}^{-\tau_i/b_i}}{\int_0^{\tau_{\max}} s^{a_i-1}\,\mathrm{e}^{-s/b_i}\,\mathrm{d}s} \tag{6.40}$$

where a_i is the shape parameter and b_i is the scale parameter. Consider $\rho = -\tau_i$, then the function in (6.32) becomes

$$l_{ij}(\theta) = \frac{\Gamma(a_i, \tau_{\max}/b_i - \lambda_j\tau_{\max}) - \Gamma(a_i, -\theta/b_i + \lambda_j\theta)}{(1 - \lambda_j b_i)^{a_i}\Gamma(a_i, \tau_{\max}/b_i)}. \tag{6.41}$$

where $\Gamma(a, b) = \int_0^b t^{a-1}\,\mathrm{e}^{-t}\,\mathrm{d}t$ is the lower incomplete gamma function.

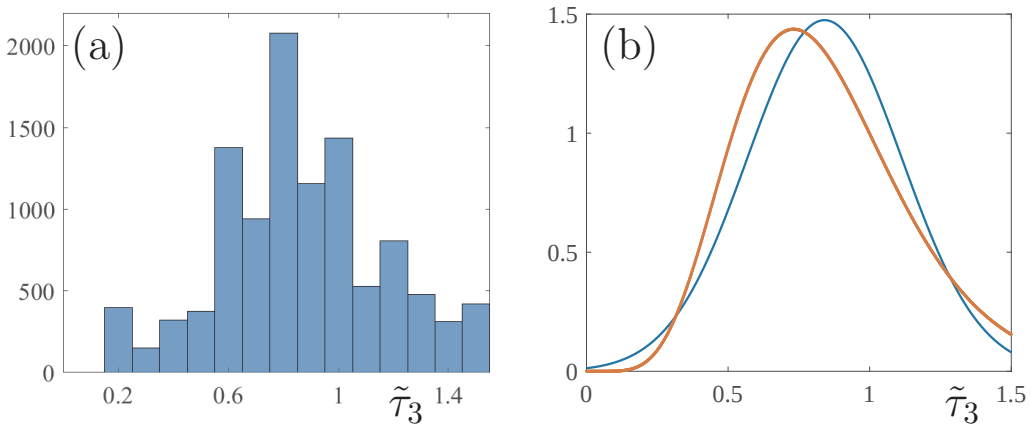

Figure 6.1: (a) Histogram of estimated driver reaction time $\tilde{\tau}_3$, cf. Fig. 3.6(b). (b) Probability density function of $\tilde{\tau}_3$. The blue curve is Gaussian distribution (6.37), while the red curve is for Gamma distribution (6.40).

Plugging the function (6.39) or (6.41) into (6.35, 6.36), we obtain the optimal CCC controller with consideration of stochastic human parameters.

6.3 Case study based on experimental data

In this section we apply the proposed CCC controller (6.35, 6.36) in the four-car experiment presented in Chapter 3. Since the last vehicle in the string has large velocity and headway fluctuations (cf. Fig. 3.3), we replace the human driver in the last car with the optimal controller (6.35, 6.36), and compare its performance with the human driver. While the controller gains and kernels (6.27, 6.34) allow heterogeneous human parameters $\bar{\alpha}_i$, $\bar{\beta}_i$, $\bar{\kappa}_i$ and delay distribution $w_i(\rho)$, for simplicity, here we assume the parameters and delay distribution for vehicle 2 are the same as vehicle 3, i.e., $\bar{\alpha}_3 = 0.2$ [1/s], $\bar{\beta}_3 = 0.4$ [1/s], $\bar{\kappa}_3 = 0.6$ [1/s]; cf. Fig. 3.7(b,d,f).

To obtain the delay distribution $w_3(\rho)$, $\rho \in [-\tau_{\max}, 0]$, we recall the histogram of estimated driver reaction time $\tilde{\tau}_3$ from Fig. 3.6(b). We consider the maximum delay time $\tau_{\max} = 1.5$ [s] and fit the histogram with a Gaussian distribution and a Gamma distribution, as shown in Fig. 6.1. The mean and standard deviation for the Gaussian distribution are $\bar{\tau}_3 = 0.86$ [s] and $\sigma_3 = 0.30$ [s]. The shape and scale parameters for the Gamma distribution are $a_3 = 6.79$ and $b_3 = 0.13$. The probability density function for both the Gaussian and Gamma distributions are plotted in Fig. 6.1(b). While the probability density function of the Gamma distribution (red curve) has smaller values as $\tilde{\tau}_3$ approaches zero, both distributions are fairly close to the histogram.

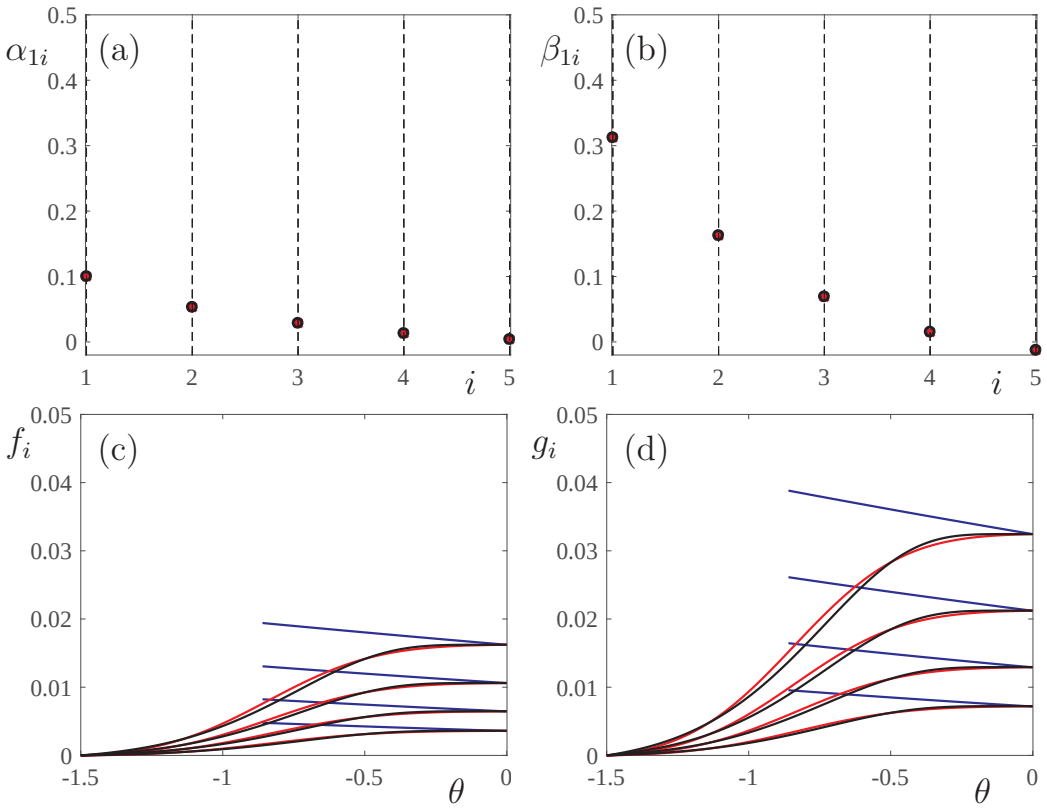

Figure 6.2: Optimal feedback gains α_{1i}, β_{1i} and kernels $f_i(\theta)$, $g_i(\theta)$ in the CCC controller when considering discrete delay time, Gaussian distribution and Gamma distribution. The blue dots and curves correspond to using the mean delay time $\bar{\tau}_3 = 0.86$ [s]. The red crosses and curves are for stochastic delay time under Gaussian distribution (6.37) with $\bar{\tau}_3 = 0.86$ [s] and $\sigma_3 = 0.30$ [s]. The black circle and curves are for stochastic delay time under Gamma distribution (6.40) with $a_3 = 6.79$ and $b_3 = 0.13$. The design parameters are $\gamma_1 = 0.01$, $\gamma_2 = 0.04$.

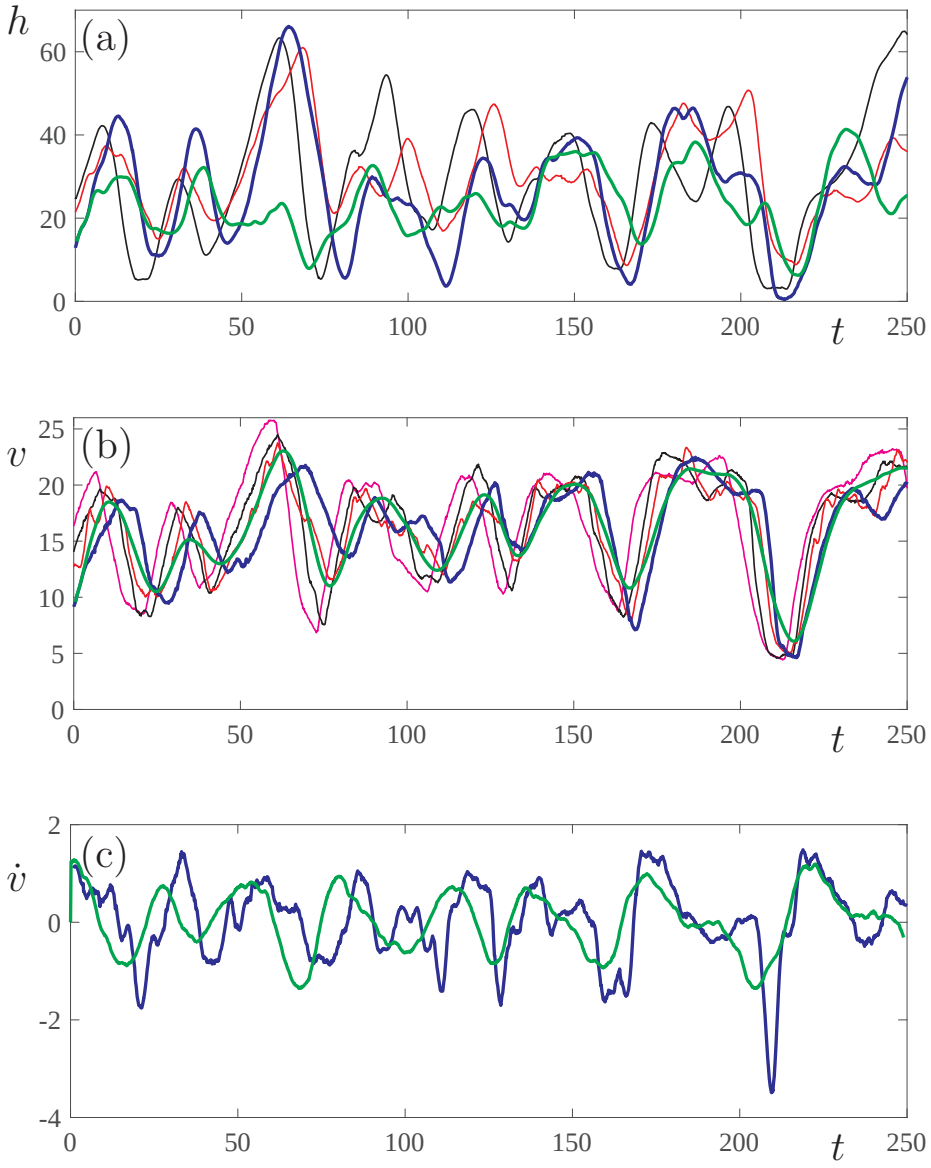

Figure 6.3: The headway, velocity, and acceleration profiles of a $(3+1)$-car vehicle string. The color scheme is the same as in Fig. 3.3. The green curves correspond to the response of the tail vehicle when it is driven by the CCC controller (6.35).

The optimal feedback gains and kernels are given by (5.38, 5.42) under nominal driver reaction delay τ and (6.27, 6.36) under distributed driver reaction delay. To demonstrate the influence of the distributed delay on the CCC controller, we first use the mean value of the estimated delay time $\bar{\tau}_3 = 0.86$ [s] as the nominal delay time to obtain a set of optimal gains and kernels, then consider the Gaussian and Gamma distribution in the controller design. The cost function (5.10) has design parameters $\gamma_1 = 0.01$, $\gamma_2 = 0.04$. In Fig. 6.2, the feedback gains α_{1i}, β_{1i} and kernels $f_i(\theta)$, $g_i(\theta)$ are plotted in blue, red, and black for point delay, Gaussian-distributed delay, and Gamma-distributed delay, respectively. Fig. 6.2(a,b) show that the feedback gains match well between three cases, i.e., if the mean value of driver reaction time remains the same, the feedback gains are not influenced by the variance of the delay time. However, Fig. 6.2(c,d) show that the kernels differ significantly under point delay (blue) and distributed delay (red, black). While kernels $f_i(\theta)$, $g_i(\theta)$ under the distributed delay cover the full range of possible delay values, kernels under the point delay only extend to the mean delay value. However, for a particular i, the area under a red, blue, or black kernel does not differ significantly, i.e., the 1-norm of $f_i(\theta)$ or $g_i(\theta)$ are similar for point delay or distributed delay. In particular, there seems to be little difference between kernels under Gamma distribution or Gaussian distribution. Therefore, we use kernels under Gaussian distribution (red curves) to evaluate the performance of the CCC controller.

In Fig. 6.3(a) the black, red, and blue curves are the headway h_3, h_2, h_1 observed in the experiment, while the green curve is the headway h_1 of the tail vehicle controlled by CCC. We find the CCC vehicle (green curve) has much smaller fluctuations in headway than any human-driven vehicle. While the real tail vehicle almost collided with vehicle 3 in the experiment (at $t \approx 210$ [s], $h_1(t) \approx 0$ [m]), such a safety hazard is avoided when the tail vehicle is driven by the CCC. In Fig. 6.3(b) the magenta curve is the velocity v_1 of the head vehicle, while the other curves have the same color scheme as in panel (a). Again, the tail vehicle will have smaller fluctuations in velocity compared with other vehicles when it is driven by a CCC controller. In Fig. 6.3(c) we compare the acceleration $\dot{v}_1$ of the tail vehicle (blue curve) and the acceleration u of the CCC vehicle (green curve). Notice that the CCC vehicle reduces harsh braking and acceleration maneuvers. In general the CCC controller demonstrates significant performance improvements compared with human-driven vehicles.

6.4 Conclusion

In this chapter we designed a connected cruise controller that considers human car-following with stochastic gains, range policy slope and reaction time delay. Under the assumption of IID, the mean dynamics of the car-following model is represented with distributed time delay. Compared with the CCC design under the point delay in Chapter 5, the feedback gains do not have recognizable changes, while the feedback kernels exhibit significant differences. The optimal CCC controller is tested using headway and velocity data collected in a 4-car experiment described in Chapter 3, and it is shown to reject traffic disturbances much better than a human driver.

CHAPTER 7

Optimal design of connected cruise control considering stochastic traffic disturbance and imperfect communication

In this chapter we include stochastic traffic disturbances and packet losses in V2V communication. In particular, we write the connected vehicle system as a Markov decision process with stochastic disturbances, and synthesize connected cruise controllers using probabilistic model checking [65], [66]. The synthesized CCC controller is collision-free and suppresses headway and velocity fluctuations based on ad-hoc V2V connectivity. While the CCC controllers proposed in Chapters 4, 5 and 6 are physically intuitive, computationally efficient, and robust to a certain degree, they cannot provide the CCC vehicle performance guarantees like the collision-free feature. Also, those controllers only contain static feedback terms, which might limit their response to disturbances in the traffic flow and V2V communication. Thus, probabilistic model checking is introduced as a new design method so that the controller can perform well in more realistic traffic scenarios.

The layout of this chapter is as follows. In Section 7.1 we introduce the car-following model used for human-driven vehicles and a class of connected cruise controllers with similar structure. In Section 7.2 we formulate the optimal connected cruise control design problem in terms of probabilistic model checking, and demonstrate how stochastic velocity disturbances can be included in this framework. In Section 7.3 we synthesize connected cruise controllers in a simple scenario and test their performance using numerical simulations. Finally, we conclude our findings in Section 7.4.

7.1 Modeling connected vehicle systems

In this section we model connected vehicle systems in discrete time under stochastic disturbances. We first describe the human car-following behavior using the optimal velocity

model (2.9), and then set up a class of connected cruise controllers which are structurally similar to the optimal velocity model. The predefined structure specifies certain dynamic properties the synthesized controller should exhibit, and thus reduces the emphasis on specifications formulated by linear temporal logic [67]. This setup may also give us more insights to the dynamics of the connected vehicle system and may scale well for connected vehicle systems consisting of a large number of vehicles.

7.1.1 Human car-following model

Recall the optimal velocity model for the human-driven vehicle i

$$\begin{aligned} \dot{h}_i(t) &= v_{i+1}(t) - v_i(t)\,, \\ \dot{v}_i(t) &= \alpha_i\big(V_i(h_i(t)) - v_i(t)\big) + \beta_i\big(v_{i+1}(t) - v_i(t)\big)\,, \end{aligned} \tag{7.1}$$

where the driver reaction time is neglected for simplicity and the range policy function is given by (2.3, 2.4)

$$V_i(h) = \begin{cases} 0 & \text{if} \quad h \le h_{\rm st}\,, \\ \kappa_i(h - h_{\rm st}) & \text{if} \quad h_{\rm st} < h < h_{\rm go}\,, \\ v_{\max} & \text{if} \quad h \ge h_{\rm go}\,. \end{cases} \tag{7.2}$$

Here we use $v_{\max} = 30$ [m/s], $h_{\rm st} = 5$ [m], $\kappa_i = 1$ [1/s] that corresponds to the time headway $t_{\rm h} = 1/\kappa_i = 1$ [s] in the region where $h_{\rm st} < h^* < h_{\rm go}$, $0 < v^* < v_{\max}$. In particular, we consider the system in the vicinity of the equilibrium $(h^*, v^*) = (20\,[\mathrm{m}], 15\,[\mathrm{m/s}])$.

7.1.2 Structured connected cruise controller

We recall the configuration shown in Fig. 5.1 where the vehicle at the tail is equipped with connected cruise control and it receives motion information from the n vehicles ahead through vehicle-to-vehicle communication (see dashed arrows terminating at vehicle 1). For simplicity, we assume that preceding vehicles are human-driven and can be described by (7.1).

Based on the dynamics of human-driven vehicles (7.1), we construct the connected

cruise controller in the form

$$\begin{aligned}\dot{h}_1(t) &= v_2(t) - v_1(t)\,,\\ \dot{v}_1(t) &= \alpha_{11}\big(V_1(h_1(t)) - v_1(t)\big) + \beta_{11}\big(w_2(t) - v_1(t)\big) + \sum_{j=2}^{n} \beta_{1j}\big(w_{j+1}(t) - w_j(t)\big)\,,\end{aligned} \tag{7.3}$$

where α_{11} and β_{1j}, $j = 1, \cdots, n$ are the feedback gains to be designed, and $w_j(t)$, $j = 2, \ldots, n+1$, are the velocity signals received by the connected cruise controller. We assume the headway h_1 and velocity v_1 of vehicle 1 are measured on-board, and thus are available to the controller. The received velocity signal $w_j(t)$ is equivalent to the actual velocity $v_j(t)$ without packet loss, but may differ when packet drops occur. Still, even for $w_j \neq v_j$ the equilibrium of the vehicle equipped with connected cruise control is given by (2.6).

In Chapter 5 we have shown that for a fixed group of preceding vehicles without packet loss, the optimal connected cruise control design gives β_{1j} that are constant in time but decrease with j. We can exploit this result later when synthesizing the optimal gains α_{11} and β_{1j}, $j = 1, \ldots, n$.

7.1.3 Implementing connected cruise control

Here we consider the human car-following model (2.2) and the connected cruise control (7.3) in the linear region and write them in discrete time to take into consideration the effect of sampling and zero-order hold in digital controllers. For simplicity we assume that the clocks used by the vehicles are synchronized.

We assume the dynamics of human-driven vehicles fluctuate around an equilibrium state (2.6), then we want the dynamics of the vehicle equipped with connected cruise control (7.1, 7.2) to be in the vicinity of that state as well. Because $v^* = 0$ describes the jammed state and $v^* = v_{\max}$ corresponds to free flow, we focus on the equilibrium states where the desired velocity increases with the headway linearly (i.e., $h_{\rm st} < h < h_{\rm go}$, $0 < v < v_{\max}$, see the middle part in Fig. 3.1(b)).

We define the headway perturbations $\tilde{h}_i(t) = h_i(t) - h^*$ and velocity perturbations $\tilde{v}_i(t) = v_i(t) - v^*$ and linearize (7.1) about the equilibrium (2.6):

$$\begin{aligned}\dot{\tilde{h}}_i(t) &= \tilde{v}_{i+1}(t) - \tilde{v}_i(t)\,,\\ \dot{\tilde{v}}_i(t) &= \alpha_i\Big(\kappa_1 \tilde{h}_i(t) - \tilde{v}_i(t)\Big) + \beta_i\big(\tilde{v}_{i+1}(t) - \tilde{v}_i(t)\big)\,.\end{aligned} \tag{7.4}$$

Similarly we linearize the connected cruise controller (7.3)

$$\dot{\tilde{v}}_1(t) = \alpha_{11}\Big(\kappa_1\tilde{h}_1(t) - \tilde{v}_1(t)\Big) + \beta_{11}\big(\tilde{w}_2(t) - \tilde{v}_1(t)\big) + \sum_{j=2}^{n}\beta_{1j}\big(\tilde{w}_{j+1}(t) - \tilde{w}_j(t)\big)\,, \quad (7.5)$$

where $\tilde{w}_j(t) = w_j(t) - v^*$.

When using vehicle-to-vehicle communication the human-driven vehicles transmit their kinematic data intermittently in every Δt. To represent this sampling we first discretize (B.1) with time step Δt:

$$\begin{aligned}\tilde{h}_i[k+1] &= \tilde{h}_i[k] + \Delta t\,(\tilde{v}_{i+1}[k] - \tilde{v}_i[k])\,,\\ \tilde{v}_i[k+1] &= \tilde{v}_i[k] + \Delta t\,\alpha_i\Big(\kappa_1\tilde{h}_i[k] - \tilde{v}_i[k]\Big) + \Delta t\,\beta_i\big(\tilde{v}_{i+1}[k] - \tilde{v}_i[k]\big)\,,\end{aligned} \quad (7.6)$$

which approximates the sampled dynamics of human-driven vehicle i. Here we introduced the notation $\tilde{h}_i[k] = \tilde{h}_i(k\Delta t)$, $\tilde{v}_i[k] = \tilde{v}_i(k\Delta t)$.

We then discretize (7.5) with the same time step in order to describe the dynamics of the vehicle equipped with digital connected cruise control. We assume the digital controller uses zero-order hold by utilizing $\tilde{h}_i[k]$ and $\tilde{v}_i[k]$ in the time interval $[k\Delta t, (k+1)\Delta t)$, but for simplicity we ignore the $\mathcal{O}(\Delta t^2)$ terms. In this case, the discretized dynamics of the connected cruise controller is given by

$$\begin{aligned}\tilde{h}_1[k+1] &= \tilde{h}_1[k] + \Delta t\,(\tilde{v}_2[k] - \tilde{v}_1[k])\,,\\ \tilde{v}_1[k+1] &= \tilde{v}_1[k] + \Delta t\,\alpha_{11}\Big(\kappa_1\tilde{h}_1[k] - \tilde{v}_1[k]\Big)\\ &\quad + \Delta t\,\beta_{11}\big(\tilde{w}_2[k] - \tilde{v}_1[k]\big) + \sum_{j=2}^{n}\Delta t\,\beta_{1j}\big(\tilde{w}_{j+1}[k] - \tilde{w}_j[k]\big)\,,\end{aligned} \quad (7.7)$$

Based on (7.6, 7.7), we formulate the controller synthesis problem in the next section.

7.2 Controller synthesis using probabilistic model checking

In this section we present the framework that uses probabilistic model checking to synthesize connected cruise controllers considering stochastic events. We express the dynamics of the connected vehicle system (7.6, 7.7) as a Markov decision process and formulate the optimization objective accordingly. In particular, we consider stochastic velocity disturbance from the leading vehicle and also model the packet losses.

7.2.1 Markov chain for human-driven vehicles

Here we rewrite the sampled dynamics (7.6) of a human-driven vehicle as a Markov chain. We first quantize a bounded region of the state space into a finite number of cells. We consider bounded headway and velocity disturbances

$$\begin{bmatrix} \tilde{h}_{\min} \\ \tilde{v}_{\min} \end{bmatrix} \leq \begin{bmatrix} \tilde{h} \\ \tilde{v} \end{bmatrix} \leq \begin{bmatrix} \tilde{h}_{\max} \\ \tilde{v}_{\max} \end{bmatrix}, \quad \tilde{v}_{\min} \leq \tilde{w}_i \leq \tilde{v}_{\max}, \tag{7.8}$$

for $i = 2, \ldots, n$. With quantization sizes

$$\Delta h = \frac{\tilde{h}_{\max} - \tilde{h}_{\min}}{N_{\mathrm{h}}}, \quad \Delta v = \frac{\tilde{v}_{\max} - \tilde{v}_{\min}}{N_{\mathrm{v}}}, \tag{7.9}$$

we define the quantized states and disturbances

$$x_i = \mathrm{floor}\big(\tilde{h}_i/\Delta h\big), \quad y_i = \mathrm{floor}(\tilde{w}_i/\Delta v), \quad z_i = \mathrm{floor}\big(\tilde{v}_i/\Delta v\big), \tag{7.10}$$

for $i = 2, \ldots, n$, with x_i evaluated among N_{h} cells, and y_i and z_i in the N_{v} cells.

When considering a connected vehicle system of $n+1$ vehicles with stochastic velocity disturbance from the leading vehicle, we assume that $\tilde{v}_{n+1}$ is bounded and the probability transition matrix $\mathcal{C}_{n+1}$ of the stochastic signal $\tilde{v}_{n+1}[k]$ is known, that is,

$$\mathbf{P}_{\mathrm{v}_{n+1}}[k+1] = \mathcal{C}_{n+1}\, \mathbf{P}_{\mathrm{v}_{n+1}}[k], \tag{7.11}$$

where $\mathbf{P}_{\mathrm{v}_{n+1}}[k]$ is the probability distribution of the quantized state $z_{n+1} = \mathrm{floor}(\tilde{v}_{n+1}/\Delta v)$ at time step k.

Then, based on the discretized car-following model (7.6) and (7.11), we are able to write the dynamics of human-driven vehicles (7.6) as a Markov chain

$$\mathbf{P}_{\mathrm{human}}[k+1] = \mathcal{C}_{\mathrm{human}}\, \mathbf{P}_{\mathrm{human}}[k], \tag{7.12}$$

where $\mathbf{P}_{\mathrm{human}}[k]$ denotes the probability distribution of the quantized state $\begin{bmatrix} x_2 & z_2 & \ldots & x_n & z_n & z_{n+1} \end{bmatrix}^{\mathrm{T}}$ at time step k, cf. (7.10).

7.2.2 Markov decision process for connected cruise control

We consider a finite set of feedback gains for the discretized linear connected cruise controller (7.7)

$$\alpha_{11} = K_{\mathrm{a}} \Delta\alpha \,, \qquad \beta_{1i} = K_{\mathrm{b}i} \Delta\beta \,, \tag{7.13}$$

where $K_{\mathrm{a}}, K_{\mathrm{b}i} \in \{0, \ldots, m\}$, $m \in \mathbb{N}^+$, and $i = 1, \ldots, n$. Now we are able to write the dynamics of the vehicle equipped with connected cruise controller as a Markov decision process

$$\mathbf{P}_1[k+1] = \mathcal{C}_{\mathrm{CCC}}(z_2, y_2, \ldots, y_{n+1}; K_{\mathrm{a}}, K_{\mathrm{b}1}, \ldots, K_{\mathrm{b}n})\, \mathbf{P}_1[k] \,, \tag{7.14}$$

where $\mathbf{P}_1[k]$ is the probability distribution of the state $\begin{bmatrix} x_1 & z_1 \end{bmatrix}^{\mathrm{T}}$, while the probability transition matrix $\mathcal{C}_{\mathrm{CCC}}$ depends on the actual velocity disturbance z_2, the received velocity signals y_i for $i = 2, \ldots, n+1$, and undetermined feedback gains $K_{\mathrm{a}}, K_{\mathrm{b}i}$ for $i = 2, \ldots, n$, at time step k.

Now we specify the relation between the received signal w_i and the actual velocity v_i in order to complete the description of the connected vehicle system. When there is no packet drop, the received signal corresponds to the actual motion of vehicle i

$$w_i[k] = v_i[k] \quad \Rightarrow \quad y_i[k] = z_i[k] \,, \tag{7.15}$$

for $i = 2, \ldots, n$, cf. (7.10). However, according to the vehicle-to-vehicle communication protocol, when a packet is dropped, it will not be resent at the next transmission, and the connected cruise controller uses the information received in the previous time step. Thus, we have

$$w_i[k] = v_i[k-1] \quad \Rightarrow \quad y_i[k] = z_i[k-1] \,. \tag{7.16}$$

In [58] it was found that the probability of more than one consecutive packet drops is relatively low. Thus, we only consider non-consecutive packet drops.

Therefore the dynamics of the connected vehicle system can be described by the Markov decision process (7.12, 7.14, 7.15) when there is no packet drop at time step k, while (7.12, 7.14, 7.16) is used when there is packet drop at time step k. The stochastic dynamics of packet drops can be integrated into the setup, but we only consider the scenario where every second packet is lost.

In order to synthesize the controller we set up the following stochastic optimization

problem:

$$\begin{aligned} &\min \sum_{k=1}^{N} \mathbb{E}\big[\, \gamma_1 x_1^2[k] + \gamma_2 z_1^2[k] + u_1^2[k] \,\big]\,, \\ &\begin{bmatrix} x_1[N] \\ z_1[N] \end{bmatrix} \in \mathbf{\Omega}_{\text{end}}\,, \quad \begin{bmatrix} x_1[k] \\ z_1[k] \end{bmatrix} \in \mathbf{\Omega}_{\text{safe}}\,, \end{aligned} \tag{7.17}$$

for $k = 1, \ldots, N$, where $\mathbb{E}$ denotes the expected value, γ_1 and γ_2 are the weighting factors for the headway and velocity fluctuations, respectively, while u_1 is the acceleration of vehicle 1 defined in (7.3, 7.7, 7.10). We also require the dynamics of the vehicle equipped with connected cruise control to stay within the safe region $\mathbf{\Omega}_{\text{safe}}$ in the quantized state space and to reach the desired region $\mathbf{\Omega}_{\text{end}}$ at the end of the optimization. Note that the time horizon N is not given but depends on when the trajectory hits $\mathbf{\Omega}_{\text{end}}$.

The optimization problem (7.12, 7.14, 7.15, 7.16, 7.17) can be solved using the stochastic model checking software PRISM [66]. The synthesized controller will be given as a map between the strategy $K_{\text{a}}, K_{\text{b}i}$ and the headway and velocity fluctuations:

$$\begin{aligned} \alpha_{11} &= K_{\text{a}}(x_1, z_1, z_2, y_2, \ldots, y_{n+1})\Delta\alpha\,, \\ \beta_{1i} &= K_{\text{b}i}(x_1, z_1, z_2, y_2, \ldots, y_{n+1})\Delta\beta\,, \end{aligned} \tag{7.18}$$

for $i = 1, \ldots, n$, cf. (7.13). Though such maps may not be deterministic for general stochastic optimization problems, for this particular problem we have a deterministic correspondence between the quantized states $(x_1, z_1, z_2, y_2, \ldots, y_{n+1})$ and the optimized feedback gains at each time step.

Note that due to the optimization setup, no feedback gains are specified for $(x_1,\, z_1) \in \mathbf{\Omega}_{\text{end}}$. One simple strategy in such cases is to set the feedback gains zero inside the end region, which we implement in this paper.

7.3 Simulation

In this section, we demonstrate the simplest results of probabilistic model checking by designing connected cruise control for a two-vehicle system (i.e., $n = 1$ in (7.3)). Here we only have two feedback gains:

$$\alpha_{11} = K_{\text{a}}(x_1, z_1, z_2, y_2)\Delta\alpha\,, \quad \beta_{11} = K_{\text{b1}}(x_1, z_1, z_2, y_2)\Delta\beta\,. \tag{7.19}$$

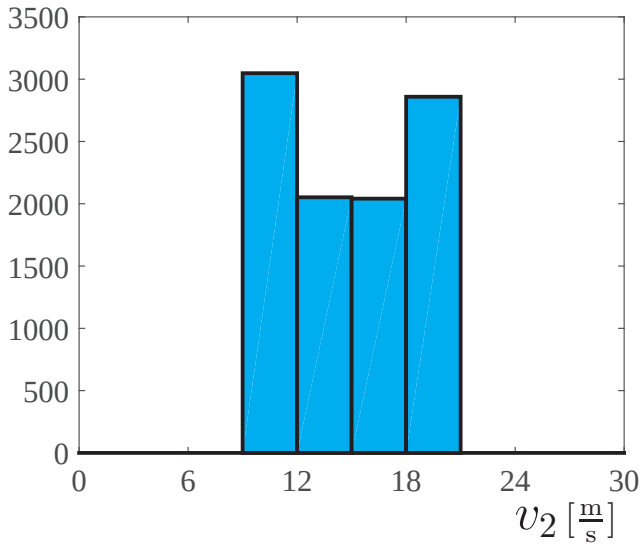

Figure 7.1: Histogram of 10000 velocity profiles $v_2(t)$ evaluated at $t = 50$ [s], where $v_2(t)$ is generated by (7.11, 7.23, 7.24).

We first synthesize the connected cruise controller using (7.14, 7.15, 7.16, 7.17) in discrete time and quantized space, and then simulate the continuous-time controller (7.3) with zero-order-hold assumption on the disturbance and feedback gains.

We consider the time step $\Delta t = 0.4$ [s] and the quantization size $\Delta h = 3$ [m], $\Delta v = 3$ [m/s], and we set the fluctuation bounds $\tilde{h}_{\max} = 12$ [m], $\tilde{h}_{\min} = -12$ [m], $\tilde{v}_{\max} = 12$ [m/s] and $\tilde{v}_{\min} = -12$ [m/s]. Thus, the number of headway and velocity cells are $N_{\mathrm{h}} = 8$ and $N_{\mathrm{v}} = 8$, respectively. For fluctuations with tighter bounds, the time step and quantization size can be proportionally reduced. We set the total number and increments for the quantized feedback gains as $m = 5$, $\Delta\alpha = 0.3$ [1/s], $\Delta\beta = 0.4$ [1/s]. The weighting factors are chosen to be $\gamma_1 = 1$ and $\gamma_2 = 1$.

We define the safety region and the end condition as

$$\begin{aligned} \mathbf{\Omega}_{\text{safe}} &= \left\{ \begin{bmatrix} x_1 \\ z_1 \end{bmatrix} \,\middle|\, \begin{bmatrix} 1 \\ 1 \end{bmatrix} \leq \begin{bmatrix} x_1 \\ z_1 \end{bmatrix} \leq \begin{bmatrix} 8 \\ 8 \end{bmatrix} \right\}, \\ \mathbf{\Omega}_{\text{end}} &= \left\{ \begin{bmatrix} x_1 \\ z_1 \end{bmatrix} \,\middle|\, \begin{bmatrix} 4 \\ 4 \end{bmatrix} \leq \begin{bmatrix} x_1 \\ z_1 \end{bmatrix} \leq \begin{bmatrix} 5 \\ 5 \end{bmatrix} \right\}. \end{aligned} \tag{7.20}$$

We consider bounded fluctuation of velocity v_2

$$v^* - 2\Delta v \leq v_2 \leq v^* + 2\Delta v\,, \tag{7.21}$$

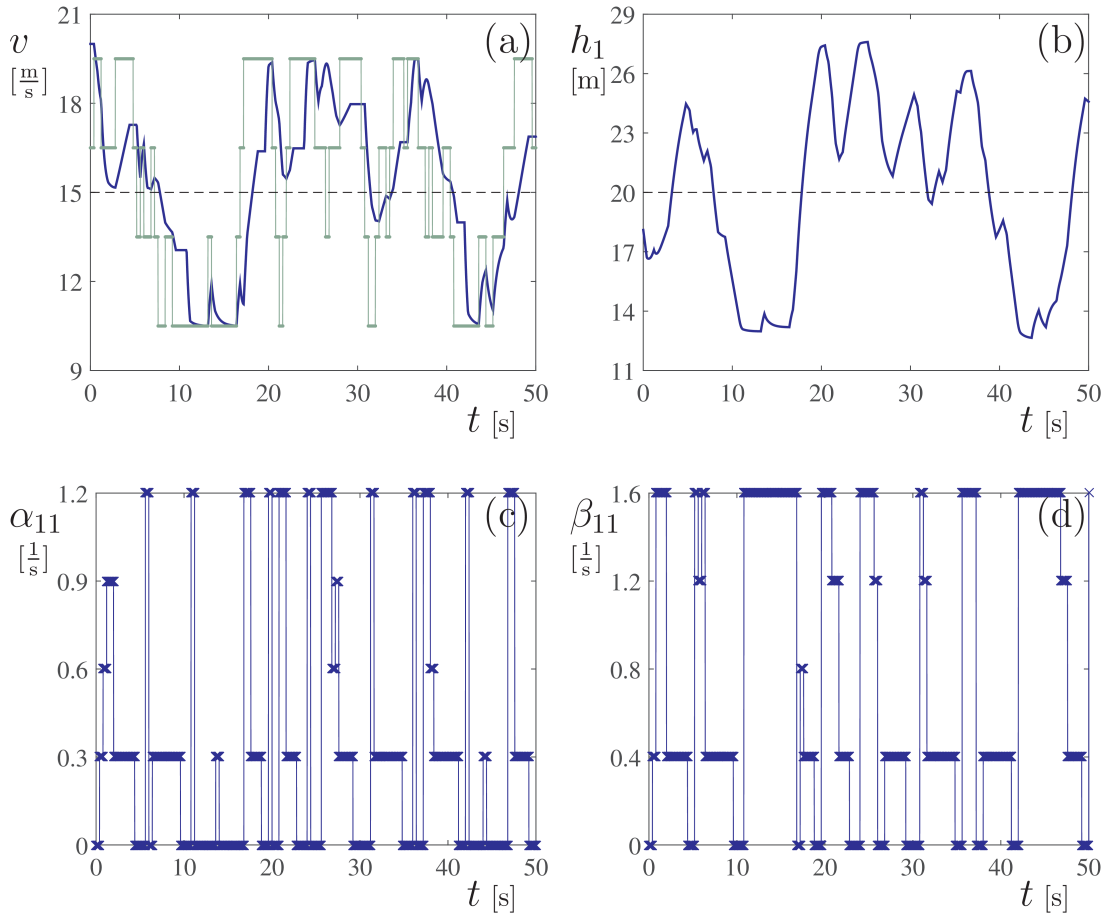

Figure 7.2: (a,b): Headway and velocity responses for a $(1+1)$-vehicle string as functions of time. The blue solid curves show the headway $h_1(t)$ and the velocity $v_1(t)$ for the vehicle equipped with connected cruise control. The green dots show the velocity $v_2(t)$ of the leading vehicle, which is the same as the received velocity signal $w_2(t)$. (c,d): The feedback gains α_{11} and β_{11} used by the controller.

that yields

$$3 \leq z_2 \leq 6\,, \tag{7.22}$$

and assume the probability transition matrix

$$\mathcal{C}_2 = \begin{bmatrix} 0.7840 & 0.3200 & 0 & 0 \\ 0.2160 & 0.3800 & 0.3080 & 0 \\ 0 & 0.3000 & 0.3840 & 0.2160 \\ 0 & 0 & 0.3080 & 0.7840 \end{bmatrix}, \tag{7.23}$$

cf. (7.11). This probability transition matrix has an eigenvalue at 1 and the corresponding eigenvector $\mathcal{K} = \begin{bmatrix} 0.3058 & 0.2064 & 0.2011 & 0.2867 \end{bmatrix}^{\mathrm{T}}$ gives the steady-state probability distribution of z_2. As an illustration, we generate 10000 discrete-time velocity profiles $\tilde{v}_2[k]$ based on (7.11, 7.23), and correspondingly define the continuous-time velocity profiles

$$v_2(t) = v^* + \tilde{v}_2[k]\,, \quad t \in [k\Delta t,\ (k+1)\Delta t)\,. \tag{7.24}$$

We sample each $v_2(t)$ at time $t = 50$ [s], and plot the histogram in Fig. 7.1. One can observe that the histogram corresponds to the steady-state distribution $\mathcal{K}$.

7.3.1 Controller synthesis with no packet loss

Here we synthesize the optimal connected cruise controller for the two-vehicle system (7.14, 7.15, 7.17) with no packet loss and test the nonlinear controller (7.3) with synthesized gains (7.18) in continuous time using zero-order hold.

We first demonstrate the performance of the connected cruise controller under a random velocity disturbance generated by (7.11, 7.23, 7.24). The headway and velocity responses and feedback gains of the vehicle equipped with connected cruise control are plotted in Fig. 7.2 as functions of time. We can see from Fig. 7.2(a) that the synthesized controller is able to follow the preceding vehicle's motion well, while maintaining reasonable headway as shown in Fig. 7.2(b). This simulation demonstrates that the connected cruise controller performs well under stochastic disturbances.

In order to evaluate the performance of the controller in the statistical sense, we repeat the simulation (7.3, 7.11, 7.23, 7.24) for 10000 different inputs, collect the value of headway, velocity, and feedback gains at $t = 50$ [s] in each run, and plot the corresponding histograms in Fig. 7.3. By comparing Fig. 7.1 and Fig. 7.3(a) we find that the probability of $z_1 \in \{4, 5\}$ is larger than $z_2 \in \{4, 5\}$, which show that the controller performs well in disturbance rejection. On the other hand, Fig. 7.3(b) shows that the headway fluctuation x_1

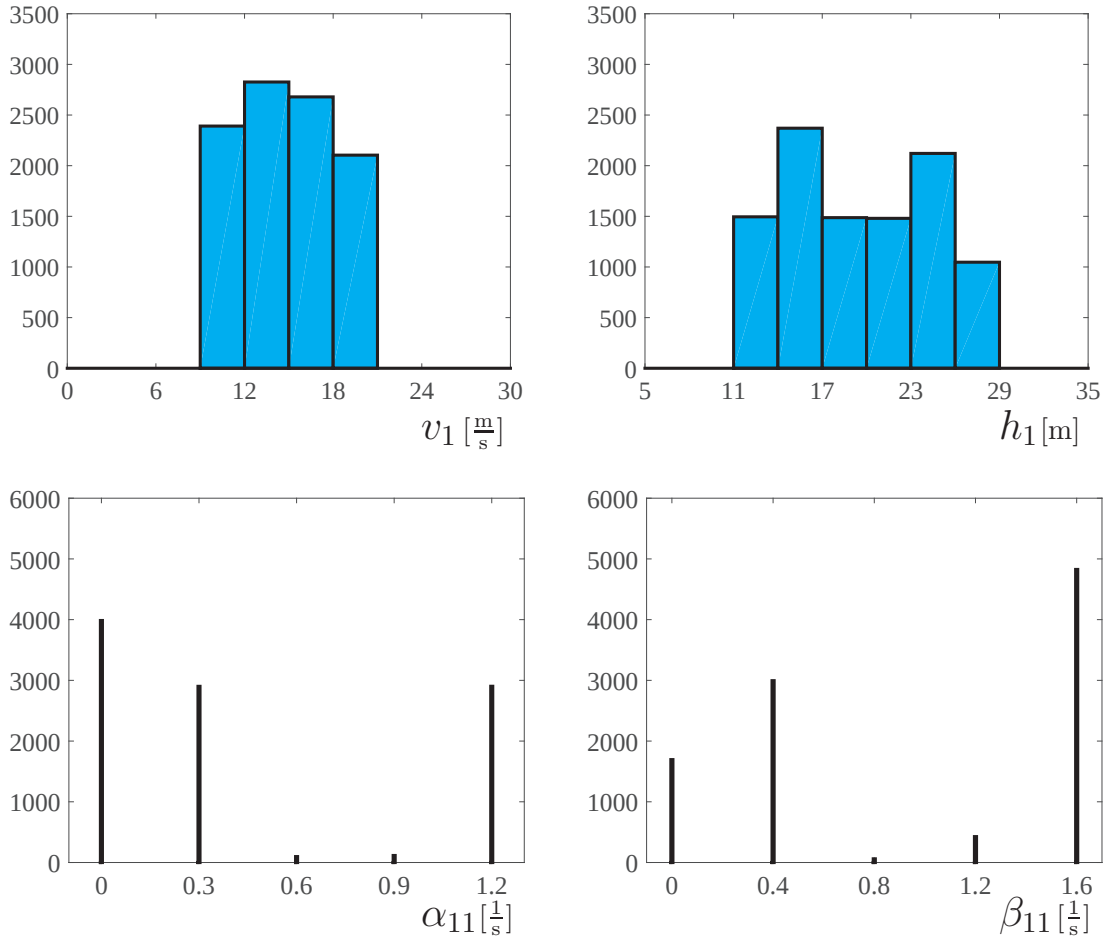

Figure 7.3: (a,b): Histograms of velocity and headway at $t = 50$ [s] in simulations of a $(1 + 1)$-vehicle string with stochastic velocity disturbance (7.3, 7.11, 7.23, 7.24). (c,d): The histogram of feedback gains α_{11} and β_{11} used by the connected cruise controller at $t = 50$ [s].

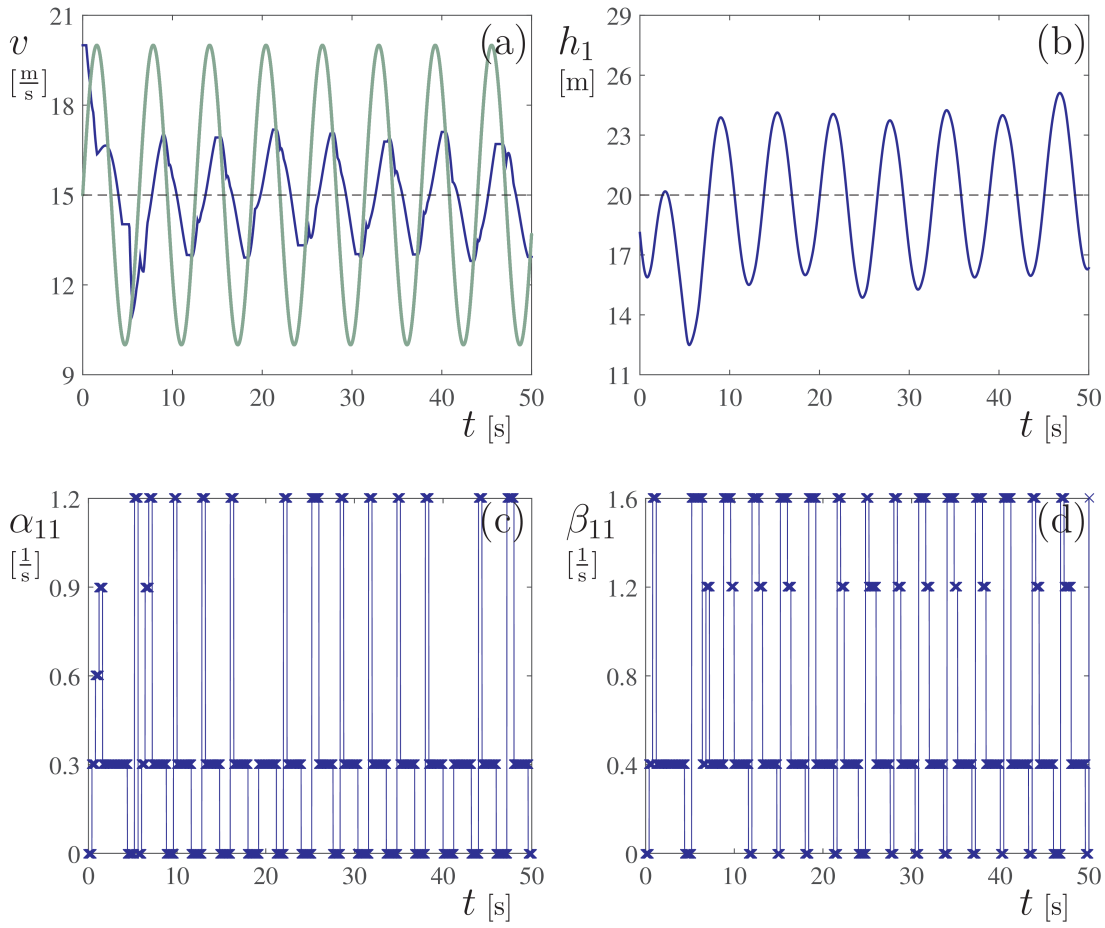

Figure 7.4: (a,b): Velocity and headway responses for a $(1 + 1)$-vehicle string under sinusoidal disturbance. (c,d): The feedback gains α_{11} and β_{11} used by the connected cruise controller. The notations are the same as in Fig. 7.2.

is well contained within the safe region, cf. (7.20).

To further evaluate the disturbance-rejection performance of the synthesized controller, we consider a sinusoidal velocity profile

$$v_2(t) = v^* + v^{\text{amp}} \cos(\omega t)\,, \tag{7.25}$$

where $v^{\text{amp}} = 5$ [m/s] and $\omega = 1$ [1/s]. The simulation results are shown in Fig. 7.4. In Fig. 7.4(a) we see that the velocity fluctuation of the vehicle equipped with connected cruise control (blue curve) has smaller amplitude than the preceding vehicle (green curve), and the headway fluctuations are also kept within safety region. Due to the periodicity of $v_2(t)$, the feedback gains α_{11} and β_{11} also exhibit certain periodic nature. We note that while static gains are also able to suppress the velocity fluctuations [5], dynamic gains may provide us more flexibility under stochastic influences from the traffic.

Finally, we test the synthesized controller using a triangular velocity signal that is more commonly seen in traffic flow, and plot the results in Fig. 7.5. In this case, the leading vehicle starts with a velocity below the equilibrium v^*, and then accelerates to v^* with constant acceleration, and after two dips its velocity settles down to v^*; see the green curve in Fig. 7.5(a). The controlled vehicle responds to the velocity fluctuations well, especially that v_1 (blue curve) has smaller local minima than v_2 (green curve), indicating successful attenuation of velocity perturbations. Moreover, the headway fluctuations are also kept within the safety region, see Fig. 7.5(b). Note that in Fig. 7.5(c,d) the feedback gains α_{11} and β_{11} settle down to their respective non-zero minimal value as the states of the controlled vehicle converge to the equilibrium.

7.3.2 Controller synthesis with packet loss

Here we still consider a two-vehicle system but assume the connected cruise controller fails to receive every second packet of the velocity signal sent by vehicle 2. We synthesize an optimal controller for (7.14, 7.15, 7.16, 7.17) similarly as in the previous subsection.

In Fig. 7.6 we test the synthesized controller using the same velocity signal v_2 as in Fig. 7.2(a), but in Fig. 7.6(a) the velocity profile w_2 received by vehicle 1 is plotted as green dots. We note that the dynamic gains in the no-packet-loss and packet-loss cases are clearly distinctive from each other, cf. Fig. 7.2(c,d) and Fig. 7.6(c,d). This demonstrates that the synthesized controller is able to adapt to the changes due to packet losses. Moreover, the generated car-following dynamics is robust against the packet losses, as shown by the similarities of the blue curves in Fig. 7.2(a,b) and Fig. 7.6(a,b). In both cases, the controlled vehicle is able to follow the preceding vehicle while maintaining the desired time headway.

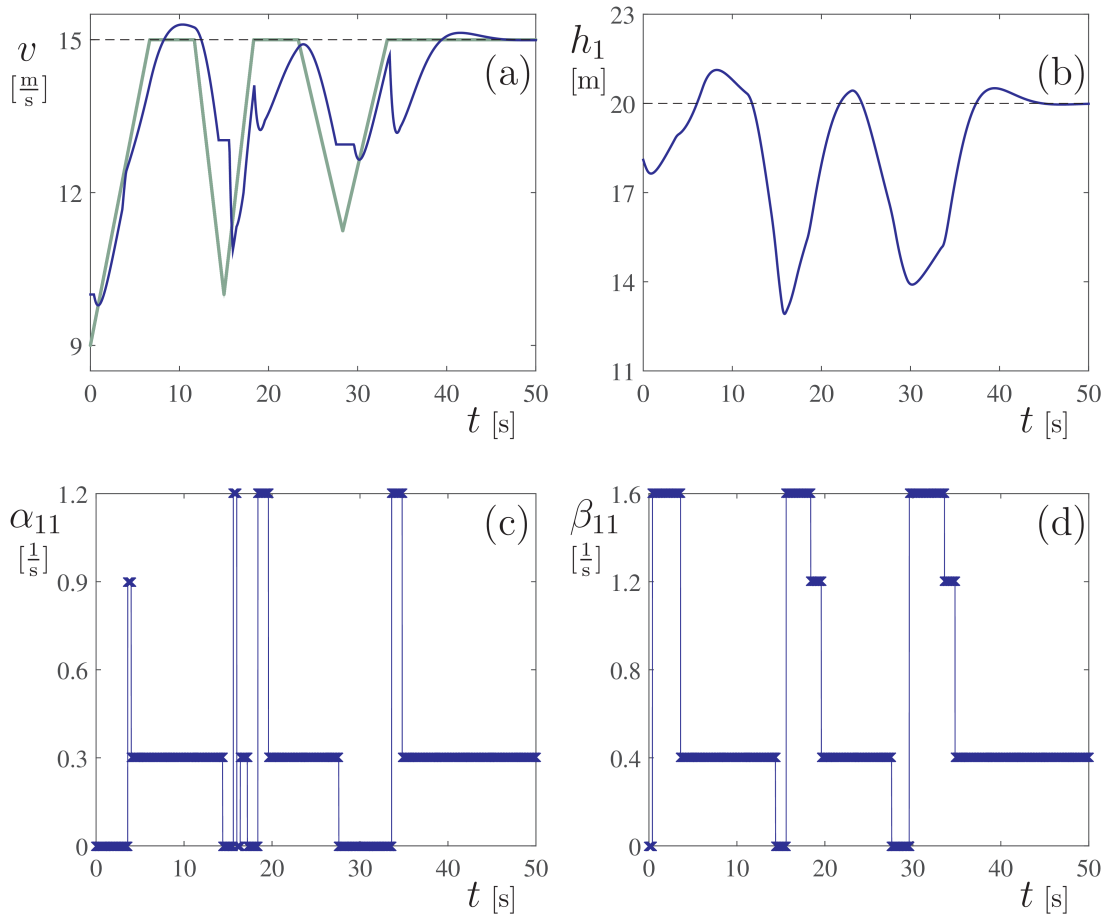

Figure 7.5: (a,b): Velocity and headway responses for a $(1+1)$-vehicle string under triangular velocity disturbance. (c,d): The feedback gains α_{11} and β_{11} used by the connected cruise controller. The notations are the same as in Fig. 7.2.

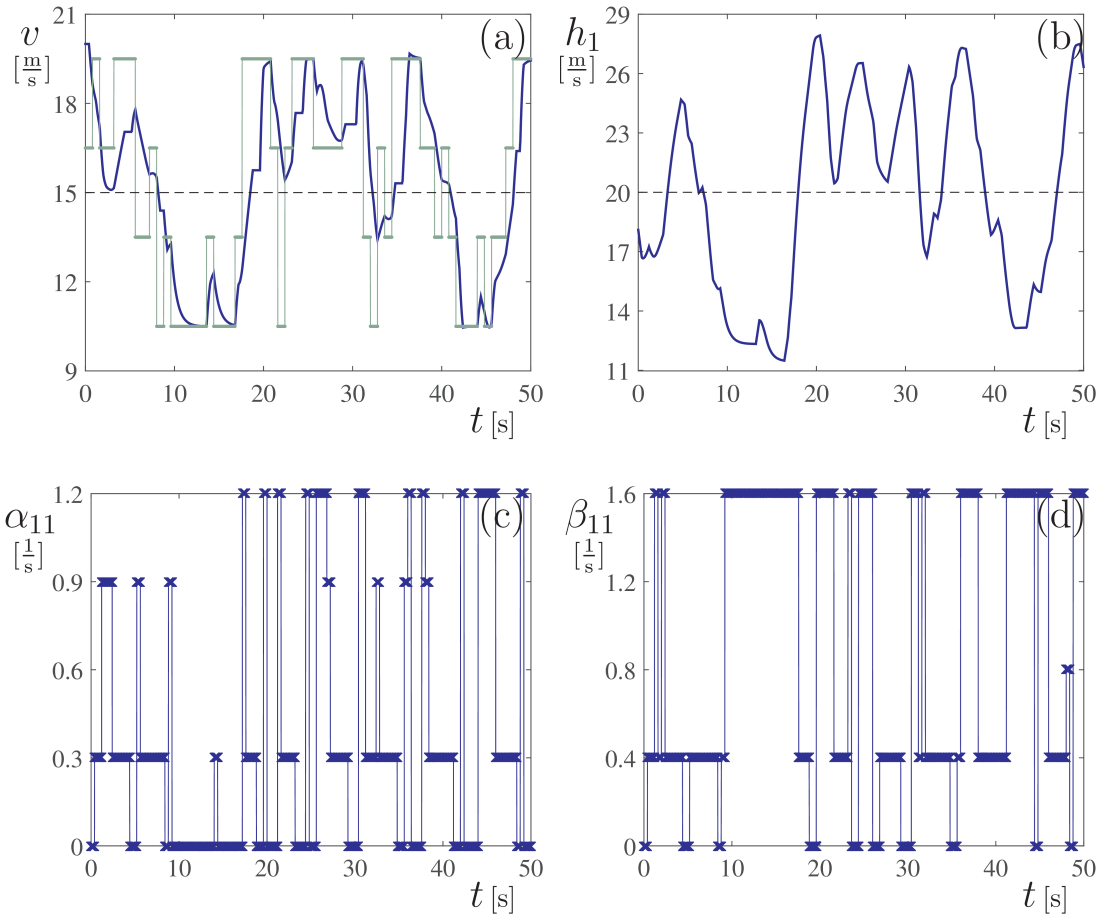

Figure 7.6: (a,b): Velocity and headway responses for a $(1+1)$-vehicle string under packet loss. The blue solid curves show the headway h_1 and the velocity v_1 for the CCC vehicle. The green dots show the observed velocity w_2 of the leading vehicle 2. (c,d): The feedback gains α_{11} and β_{11} used by the connected cruise controller.

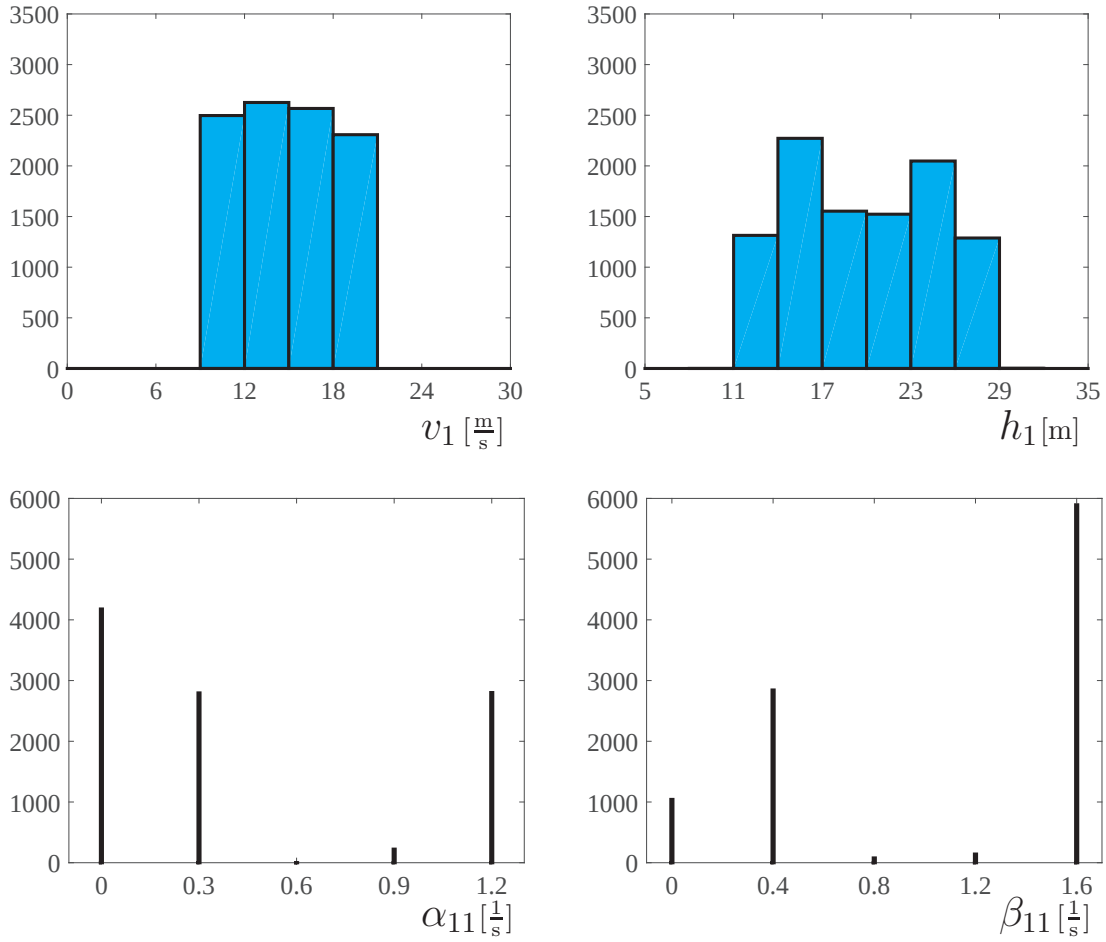

Figure 7.7: (a,b): Histograms of velocity and headway at $t = 50$ [s] in simulations of a $(1+1)$-vehicle string with stochastic velocity disturbance and packet losses. (c,d): Histogram of feedback gains α_{11} and β_{11} used by the connected cruise controller at $t = 50$ [s].

Similarly, to demonstrate the controller performance statistically, we perform 10000 runs and plot the histograms for the headway, velocity, and feedback gains at time $t = 50$ [s] in Fig. 7.7. We see that with packet losses, the connected cruise controller still maintains similar distributions for the velocity and headway fluctuations as in Fig. 7.3. However, we note that there are considerable differences in the distribution of feedback gain β_{11} between Fig. 7.3(d) and Fig. 7.7(d). This demonstrates the necessity of considering packet losses in the system.

7.4 Conclusion

In this chapter we demonstrated the design of connected cruise control using probabilistic model checking. Our method was based on stochastic optimal control and was able to accommodate stochastic events from the traffic flow and also react to packet drops in vehicle-to-vehicle communication. We showed through simulations that the synthesized controller is robust against imperfect communication and may be used in connected vehicle systems with a larger number of vehicles.

CHAPTER 8

Conclusion

In this research we designed connected cruise control in a mixed traffic system consisting of automated and human-driven vehicles. We proposed a class of connected cruise controllers based on a human car-following model, so that while the CCC vehicle exhibits similar behaviors as the surrounding human-driven vehicles, it actively mitigates undesired velocity fluctuations propagating through the traffic flow.

We found that while driver reaction time delay limits the string stability of a human-driven vehicle, eliminating delay from the car-following model using onboard sensors does not necessarily generate desired string stability for connected cruise control. Therefore, we designed CCC controllers by augmenting the human car-following model with headway/velocity/acceleration feedback terms from multiple vehicles ahead. We first proposed an online estimation algorithm to identify in real time both the human gains and driver reaction time of the vehicles ahead. We observed stochastic variations in both human gains and reaction time. Then we proposed a CCC algorithm using acceleration feedback when there are few DSRC-equipped vehicles nearby. We found that the connected vehicle system may benefit from larger delay time as the acceleration signals come from vehicles farther downstream. For V2V-rich environments, we proposed an optimal CCC design using linear quadratic regulation while considering driver reaction time delay. This setup exploits the uni-directional information flow in traffic systems, and enables us to decompose the large-dimensional optimization problem and obtain an analytical solution with small computational load. We found that, when a CCC vehicle receives motion information from n vehicles ahead, the optimal feedback gains decrease for signals from vehicles farther away, and the CCC controller degrades gracefully when the communication links fail.

In order to provide more robustness against human parameters in the connected vehicle system, we considered stochastic human parameters in the optimal CCC design using the mean dynamics. We found that the optimal CCC controller maintains the same structure and performs well when tested with experimental data. In the last part of this research, we included stochastic disturbances from the traffic flow and V2V communication in optimal

CCC design, and introduced the probabilistic model checking method so that in the future research the CCC vehicle can perform well in more realistic traffic scenarios.

APPENDIX A

String stability in ring configuration

Here we show that the necessary and sufficient conditions of string stability for a connected vehicle system are equivalent to the stability conditions of the system constructed by placing N vehicles on a ring and considering $N \to \infty$. That is, the string stability of a group of CCC and non-CCC vehicles (cf. Fig. 4.1) can be analyzed by repeating the configuration along a circular track. This setting introduces periodic boundary conditions and results in an autonomous system. Previous research has shown the equivalence of the ring and string configurations for predecessor-follower models based on headway and velocity feedback [68]. Here we give a brief demonstration of their equivalency for connected vehicle systems with delayed acceleration feedback. First, we analyze the simple scenario discussed in Section 4.3 where only the acceleration of the vehicle immediately ahead is used and then extend this analysis to the vehicle systems discussed in Sections 4.4 and 4.6.

Let us define $x_i = \begin{bmatrix} \tilde{v}_i & \tilde{h}_i \end{bmatrix}^{\mathrm{T}}$ and rewrite the linear model (4.2) into the state-space form

$$\dot{x}_1(t) = \mathbf{A}\, x_2(t) + \mathbf{B}\, x_1(t) + \mathbf{C}\, x_2(t-\tau) + \mathbf{D}\, x_1(t-\tau) + \mathbf{E}\, \dot{x}_2(t-\sigma_2)\,, \tag{A.1}$$

where the coefficient matrices are

$$\mathbf{A} = \begin{bmatrix} 0 & 0 \\ 1 & 0 \end{bmatrix}, \quad \mathbf{B} = \begin{bmatrix} 0 & 0 \\ -1 & 0 \end{bmatrix}, \quad \mathbf{C} = \begin{bmatrix} \beta & 0 \\ 0 & 0 \end{bmatrix}, \quad \mathbf{D} = \begin{bmatrix} -\alpha-\beta & \alpha\kappa \\ 0 & 0 \end{bmatrix}, \quad \mathbf{E} = \begin{bmatrix} \gamma_2 & 0 \\ 0 & 0 \end{bmatrix}. \tag{A.2}$$

Placing N vehicles on a ring and defining the state $X = \mathrm{col}[x_1 \ \cdots \ x_N]$ result in the

neutral delay differential equation (NDDE)

$$\dot{X} = \begin{bmatrix} \mathbf{B} & \mathbf{A} & & \\ & \ddots & \ddots & \\ & & \mathbf{B} & \mathbf{A} \\ \mathbf{A} & & & \mathbf{B} \end{bmatrix} X + \begin{bmatrix} \mathbf{D} & \mathbf{C} & & \\ & \ddots & \ddots & \\ & & \mathbf{D} & \mathbf{C} \\ \mathbf{C} & & & \mathbf{D} \end{bmatrix} X(t-\tau) + \begin{bmatrix} \mathbf{0} & \mathbf{E} & & \\ & \ddots & \ddots & \\ & & \mathbf{0} & \mathbf{E} \\ \mathbf{E} & & & \mathbf{0} \end{bmatrix} \dot{X}(t-\sigma_2)\,. \tag{A.3}$$

Block-diagonalizing (A.3), we can decompose it into N modal equations, which can be analyzed separately [3, 56]. The dynamics of the k^{th} mode is given by

$$\dot{z}_k(t) = (\mathbf{B} + \Lambda_k\,\mathbf{A})\,z_k(t) + (\mathbf{D} + \Lambda_k\,\mathbf{C})\,z_k(t-\tau) + \Lambda_k\,\mathbf{E}\,\dot{z}_k(t-\sigma_2)\,, \tag{A.4}$$

where $z_k \in \mathbb{R}^2$ is the modal coordinate for the k^{th} mode representing the amplitude of the corresponding traveling wave [42], while

$$\Lambda_k = \mathrm{e}^{2\,\mathrm{i}\theta_k}\,, \quad \theta_k = \frac{k\pi}{N}\,, \tag{A.5}$$

$k = 0, \ldots, N-1$ are the corresponding modal eigenvalues.

Using the trial solution $z_k = Z_k\,\mathrm{e}^{st}$, $Z_k \in \mathbb{C}^2$, $s \in \mathbb{C}$, we obtain the characteristic equation for the k^{th} mode as

$$s^2\big(1 - \gamma_2\,\mathrm{e}^{2\,\mathrm{i}\theta_k - s\sigma_2}\big) + s\Big(\alpha + \beta\big(1 - \mathrm{e}^{2\,\mathrm{i}\theta_k}\big)\Big)\,\mathrm{e}^{-s\tau} + \alpha\kappa\big(1 - \mathrm{e}^{2\,\mathrm{i}\theta_k}\big)\,\mathrm{e}^{-s\tau} = 0\,. \tag{A.6}$$

The necessary and sufficient condition of stability is that all modes are stable, that is, all eigenvalues s are in the left-half complex plane for all k [69]. The stability boundaries are located at the parameter values where eigenvalues cross the imaginary axis, i.e., $s = \mathrm{i}\omega$, $\omega \geq 0$.

Substituting this into (A.6) and separating the real and imaginary parts, we obtain

$$\begin{aligned} R(\omega) - \gamma_2\,\omega^2\cos(2\theta_k - \sigma_2\omega) &= 0\,, \\ T(\omega) - \gamma_2\,\omega^2\sin(2\theta_k - \sigma_2\omega) &= 0\,, \end{aligned} \tag{A.7}$$

where

$$\begin{aligned} R(\omega) &= \omega^2 - \alpha\omega\sin(\tau\omega) - 2\sin(\theta_k)\big(\beta\omega\cos(\theta_k - \tau\omega) + \alpha\kappa\sin(\theta_k - \tau\omega)\big)\,, \\ T(\omega) &= -\alpha\omega\cos(\tau\omega) - 2\sin(\theta_k)\big(\beta\omega\sin(\theta_k - \tau\omega) - \alpha\kappa\cos(\theta_k - \tau\omega)\big)\,. \end{aligned} \tag{A.8}$$

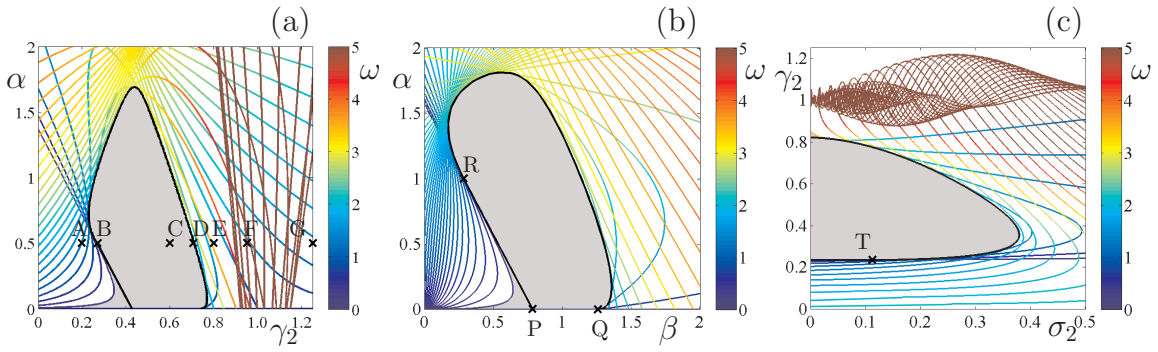

Figure A.1: (a): Stability chart in the (γ_2, α)-plane for the ring configuration using $N = 33$ vehicles and the same parameters as in Fig. 4.2(e). (b and c): Stability charts in the (β, α) and (σ_2, γ_2) planes for the ring configuration using $N = 33$ vehicles and the same parameters as in Fig. 4.4(a, b). Each colored curve represents a stability boundary for a mode (a traveling wave along the ring) and the color describes the frequency of arising oscillations at the boundaries. The black lines are the string stability boundaries obtained when analyzing string configuration.

Solving (A.7, A.8) for α and γ_2, we obtain the stability boundaries in the parametric form

$$\begin{aligned}
\alpha &= \frac{\omega^2 \sin(2\theta_k - \sigma_2\omega) - 2\beta\omega \sin(\theta_k) \sin\big(\theta_k + (\tau - \sigma_2)\omega\big)}{2\kappa \sin(\theta_k) \cos\big(\theta_k + (\tau - \sigma_2)\omega\big) - \omega \cos\big(2\theta_k + (\tau - \sigma_2)\omega\big)}\,, \\
\gamma_2 &= \frac{R(\omega)}{\omega^2 \cos(2\theta_k - \sigma_2\omega)}\,,
\end{aligned} \tag{A.9}$$

for $k = 0, \ldots, N-1$. Similarly one may solve (A.7, A.8) for α and β and obtain

$$\begin{aligned}
\alpha &= \frac{\omega^2 \sin(2\theta_k - \sigma_2\omega) - 2\beta\omega \sin(\theta_k) \sin\big(\theta_k + (\tau - \sigma_2)\omega\big)}{2\kappa \sin(\theta_k) \cos\big(\theta_k + (\tau - \sigma_2)\omega\big) - \omega \cos\big(2\theta_k + (\tau - \sigma_2)\omega\big)}\,, \\
\beta &= \frac{\omega \cos\big(2\theta_k + (\tau - \sigma_2)\omega\big) - 2\kappa \sin(\theta_k) \cos\big(\theta_k + (\tau - \sigma_2)\omega\big)}{2\sin(\theta_k)\big(2\kappa \sin(\theta_k) - \omega\cos(\theta_k)\big)/(\gamma_2\omega)} \\
&\quad + \frac{\omega\big(2\kappa \sin(\theta_k)\cos(\theta_k - \tau\omega) - \omega\cos(\tau\omega)\big)}{2\sin(\theta_k)\big(2\kappa\sin(\theta_k) - \omega\cos(\theta_k)\big)}\,,
\end{aligned} \tag{A.10}$$

for $k = 0, \ldots, N-1$. Finally, solving (A.7, A.8) for σ_2 and γ_2, we obtain

$$\begin{aligned}
\sigma_2 &= \frac{1}{\omega}\left(2\theta_k - \arctan\left(\frac{T(\omega)}{R(\omega)}\right)\right)\,, \\
\gamma_2 &= \frac{R(\omega)}{\omega^2 \cos(2\theta_k - \sigma_2\omega)}\,,
\end{aligned} \tag{A.11}$$

for $k = 0, \ldots, N-1$. The corresponding stability diagrams are shown in the (γ_2, α), (β, α), (σ_2, γ_2) planes in Fig. A.1(a, b, c), respectively. In all three panels, the gray areas are stable and each colored curve is a stability boundary for a mode number k. Black curves indicate the string stability boundaries obtained for the string configuration (cf. Figs. 4.2(e) and 4.4(b,c)). Clearly, the stability areas for the ring configuration match with those for the string configuration, except for a small corner in the low frequency part. Because there are only a finite number of vehicles on the ring ($N = 33$ is used here), the continuum of frequencies in the string unstable domain are "sampled" by a finite number of modes. This is demonstrated using similar coloring in Fig. A.1 as in Figs. 4.2(e) and 4.4(b,c). When the number of vehicles in the ring is increased, the discrepancy between string and the ring diminishes.

Figure A.2 shows the eigenvalue distribution for the points marked A–G in Fig. A.1(a) using the semi-discretization method [69]. They correspond to the Bode plots in Fig. 4.3. Since (A.3) is a neutral delayed differential equation (NDDE), there are infinitely many eigenvalues. We only plot the eigenvalues close to the imaginary axis, which dominate the dynamics. Case C is asymptotically stable, because all the eigenvalues are on the left-half complex plane. Cases B and D are marginally stable, with a pair of eigenvalues crossing the imaginary axis. The crossing frequencies are very close to the critical frequencies $\omega^{\rm cr}$ in Fig. 4.3(b) and (d). In case A, eigenvalues with small imaginary values are on the right-half complex plane, indicating instabilities for low frequencies, while in case E, eigenvalues with larger imaginary parts crossed the imaginary axis, resulting in instabilities with higher frequencies. In case F, both low frequency and high frequency instabilities occur and in case G, there are infinitely many eigenvalues on the right-half complex plane. We remark that the appearance of such 'hyperbolic-like' spectrum in a dissipative system may reconcile the conflict that arose for the continuum traffic models, regarding whether the model should be fundamentally hyperbolic [70] or parabolic [71].

Stability analysis for more general connectivity structures can be done by placing the connected vehicle systems on a ring road repetitively. Here we show that the intersection of acceleration links for the ring configuration generates similar results as for the string configuration. Fig. A.3 compares the stability in the (β, α)-plane between two 32-vehicle rings. Panel (a) depicts the stability chart when 16 CCC vehicles are evenly distributed in the ring of 32 vehicles and acceleration links do not intersect, see configuration F in Fig. 4.10(a). Panel (b) shows the stability chart when 32 vehicles are all equipped with CCC, and the connectivity is similar to configuration H in Fig. 4.10(a). Even though the number of acceleration links in panel (a) is half the number in panel (b), the stable area is significantly larger. The stable domain in Fig. A.3(a) matches the string stability boundary

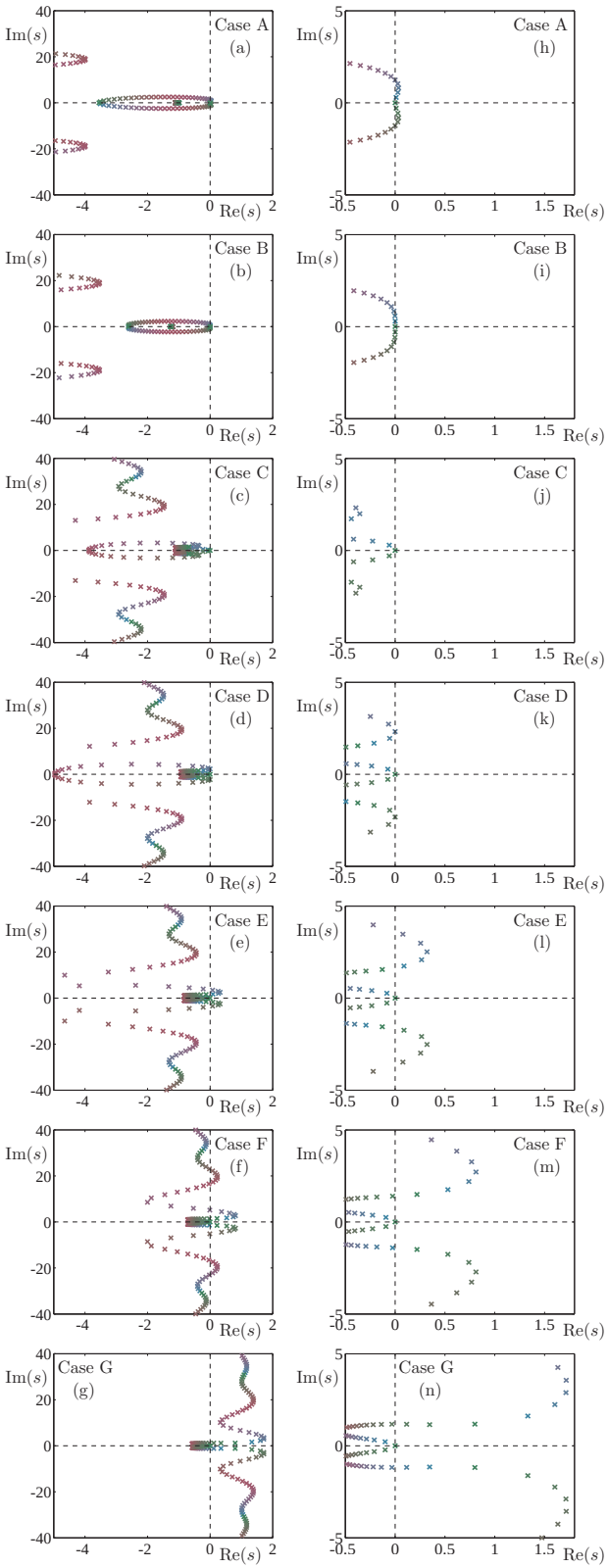

Figure A.2: (a-g): Eigenvalue distributions for the ring configuration for the points A–G in Fig. A.1(c) . (h-n): The zoom-ins for panels (a-g). The color of eigenvalues changes from blue through purple to green as the mode number $k = 0, \ldots, 32$ increases.

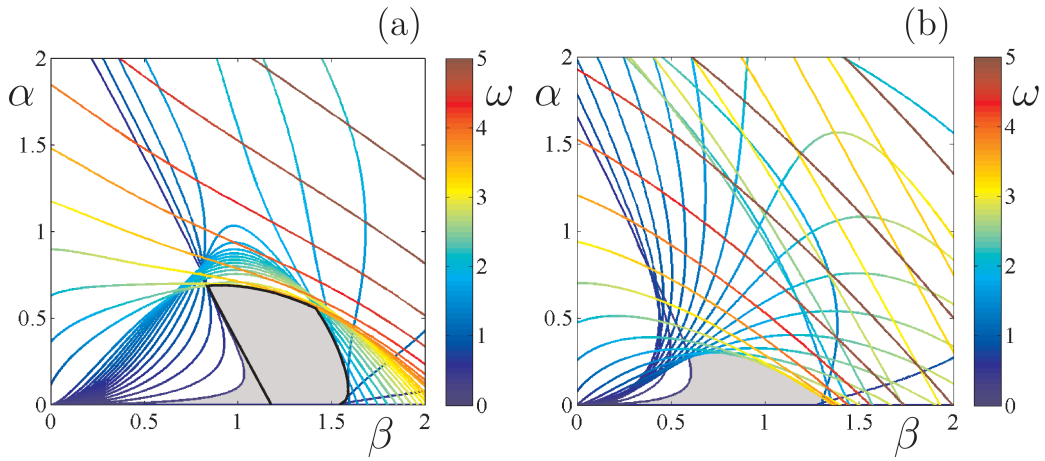

Figure A.3: Stability diagrams in the (β, α)-plane for the ring configuration using $N = 32$ vehicles. (a): Every second vehicle is equipped with acceleration-based CCC, cf. Fig. 4.6(a) and configuration F in Fig. 4.10(a). The black lines are the string stability boundaries obtained when analyzing the string configuration. (b): Every vehicle is CCC and all acceleration links intersect, cf. Fig. 4.6(a) and configuration H in Fig. 4.10(a).

obtained for the string configuration in Fig. 4.6(c), except a corner in the low-frequency area; see black curves for comparison. Such difference diminishes when increasing the number of vehicles on the ring. Also, the stability chart in Fig. A.3(b) resembles the chart in Fig. 4.10(e). Again, by increasing the number of vehicles in the string as well as on the ring, better match can be obtained.

APPENDIX B

Parameter estimation in linear time-delayed systems

In Chapter 3 we have shown how to estimate in real time parameters in human car-following models using a sweeping least squares method. The data-based method is robust against human parameter variations and can be readily applied in connected automated vehicles. However, for applications where the gains and delay time are fixed, or vary at a slower time scale, Lyapunov-based methods may require smaller computational load and provide more intuition. Thus, we demonstrate three algorithms for simultaneous identification of the feedback gains and delay in linear time-invariant systems. The first method is first proposed by [53] and used in many following studies. Its idea is to convert the problem of estimating delay time into estimating feedback gains on a finite set of discrete delay time candidates. To overcome the large computational need and poor convergence performance seen in the first method, we propose the second algorithm which explicitly estimates the delay time parallel to the feedback gains. The idea for this algorithm comes from [54], where the authors estimate multiple discrete delay time with known feedback gains. The third algorithm is proposed to further improve the convergence rate by introducing additional nonlinearities. Then, numerical simulations are used to compare the performance of the three methods.

B.1 Parametric model for identification

Consider the configuration in Fig. 3.1 where the tail vehicle receives motion signals from vehicles i and $i+1$. We describe the dynamics of the human-driven vehicle i with car-following model (3.1) and assume the dynamics of the vehicle to be in the vicinity of the uniform flow (2.6). Here we denote the headway perturbations $\delta h_i(t) = h_i(t) - h^*$ and velocity perturbations $\delta v_i(t) = v_i(t) - v^*$, and rewrite the linearized car-following model

in term of delay differential equations

$$\begin{aligned} \delta\dot{h}_i(t) &= \delta v_{i+1}(t) - \delta v_i(t)\,, \\ \delta\dot{v}_i(t) &= -(\alpha+\beta)\delta v_i(t-\tau) + \alpha\kappa\delta h_i(t-\tau) + \beta\,\delta v_{i+1}(t-\tau)\,, \end{aligned} \tag{B.1}$$

where $i = 2, \ldots, N-1$. To simplify the notation in this chapter, we dropped the vehicle index i in parameters $\alpha\,, \beta\,, \kappa\,, \tau$.

Let us introduce the notation

$$x(t) = \delta v_i(t), \quad u_1(t) = \delta h_i(t), \quad u_2(t) = \delta v_{i+1}(t)\,. \tag{B.2}$$

Based on the dynamics (B.1) of vehicle i, we write out the parametric model

$$\dot{x}(t) = ax(t-\tau) + bu_1(t-\tau) + cu_2(t-\tau)\,, \tag{B.3}$$

where the delay time τ and the feedback gains

$$a = -\alpha - \beta, \quad b = \alpha\kappa, \quad c = \beta \tag{B.4}$$

are unknown a priori and to be determined through parameter identification. In the next three sections, we present three parameter estimation methods that may be used to identify the feedback gains and delay time simultaneously in the linearized car-following model (B.1). We compare the algorithms in terms of convergence rate and estimation accuracy, and present a systematic way to improve both performance measures.

B.2 Direct Lyapunov method of approximated delay

This method was originally proposed in [53]. It bypasses the estimation of delay time by introducing multiple fictitious delays whose corresponding gains are zero, i.e., the parametric model (B.3) is rewritten as

$$\dot{x}(t) = \sum_{i=1}^{n} \left(a_i x(t-\tau_i) + b_i u_1(t-\tau_i) + c_i u_2(t-\tau_i) \right), \tag{B.5}$$

where $0 \le \tau_1 < \tau_2 < \cdots < \tau_n$, and there exists $j \in \{1, \ldots, n\}$ such that the real delay $\tau = \tau_j$. Thus,

$$a_j = -\alpha - \beta, \quad b_j = \alpha\kappa, \quad c_j = \beta\,, \tag{B.6}$$

and

$$a_i = b_i = c_i = 0\,, \tag{B.7}$$

for $i \neq j$. Then by identifying the zero gains we are able to "weed out" the "fake" delays and obtain the real delay time and corresponding feedback gains. Based on [53], the estimation algorithm for (B.5) is given by

$$\begin{aligned}
\dot{\tilde{x}}(t) &= \sum_{i=1}^{n} \left(\tilde{a}_i x(t-\tau_i) + \tilde{b}_i u_1(t-\tau_i) + \tilde{c}_i u_2(t-\tau_i)\right) + r\hat{x}(t)\,,\\
\dot{\tilde{a}}_i(t) &= \gamma_{0i}\hat{x}(t)x(t-\tau_i)\,,\\
\dot{\tilde{b}}_i(t) &= \gamma_{1i}\hat{x}(t)u_1(t-\tau_i)\,,\\
\dot{\tilde{c}}_i(t) &= \gamma_{2i}\hat{x}(t)u_2(t-\tau_i)\,,
\end{aligned} \tag{B.8}$$

where tildes are used to denote estimated state and parameters, the state error is $\hat{x} = x - \tilde{x}$, and the estimation gains are $r > 0$, $\gamma_{ki} > 0$, $k = 0, 1, 2$, $i = 1, \ldots, n$.

Define the vectors

$$Z = \begin{bmatrix} \hat{x} \\ \hat{A} \\ \hat{B} \\ \hat{C} \end{bmatrix}, \quad \hat{A} = \begin{bmatrix} \hat{a}_1 \\ \vdots \\ \hat{a}_n \end{bmatrix}, \quad \hat{B} = \begin{bmatrix} \hat{b}_1 \\ \vdots \\ \hat{b}_n \end{bmatrix}, \quad \hat{C} = \begin{bmatrix} \hat{c}_1 \\ \vdots \\ \hat{c}_n \end{bmatrix}, \tag{B.9}$$

that contain the estimation errors $\hat{a}_i = \tilde{a}_i - a_i$, $\hat{b}_i = \tilde{b}_i - b_i$, $\hat{c}_i = \tilde{c}_i - c_i$, $i = 1, \ldots, n$. Using (B.5, B.8), we can write the estimation model as a linear time-varying system:

$$\dot{Z} = \begin{bmatrix} -r & X_\tau^{\mathrm{T}}(t) & U_{1\tau}^{\mathrm{T}}(t) & U_{2\tau}^{\mathrm{T}}(t) \\ \Gamma_0 X_\tau(t) & 0 & 0 & 0 \\ \Gamma_1 U_{1\tau}(t) & 0 & 0 & 0 \\ \Gamma_2 U_{2\tau}(t) & 0 & 0 & 0 \end{bmatrix} Z\,, \tag{B.10}$$

where

$$\begin{aligned}
\Gamma_k &= \operatorname{diag}\begin{bmatrix} \gamma_{k1} & \cdots & \gamma_{kn} \end{bmatrix}, \quad k = 0, 1, 2\,,\\
X_\tau(t) &= \begin{bmatrix} x(t-\tau_1) & \cdots & x(t-\tau_n) \end{bmatrix}^{\mathrm{T}},\\
U_{1\tau}(t) &= \begin{bmatrix} u_1(t-\tau_1) & \cdots & u_1(t-\tau_n) \end{bmatrix}^{\mathrm{T}},\\
U_{2\tau}(t) &= \begin{bmatrix} u_2(t-\tau_1) & \cdots & u_2(t-\tau_n) \end{bmatrix}^{\mathrm{T}}.
\end{aligned} \tag{B.11}$$

We would like the fixed point $Z(t) \equiv 0$ of (B.10) to be (at least) Lyapunov stable. Thus, we define the Lyapunov function candidate

$$V = \frac{1}{2} Z^{\mathrm{T}} \begin{bmatrix} 1 & & & \\ & \Gamma_0 & & \\ & & \Gamma_1 & \\ & & & \Gamma_2 \end{bmatrix}^{-1} Z = \frac{1}{2}\hat{x}^2 + \sum_{i=1}^{n} \frac{1}{2}\Big(\frac{1}{\gamma_{0i}}\hat{a}_i^2 + \frac{1}{\gamma_{1i}}\hat{b}_i^2 + \frac{1}{\gamma_{2i}}\hat{c}_i^2\Big)\,, \tag{B.12}$$

and using (B.10), the Lie derivative becomes

$$\dot{V} = -r\hat{x}^2\,. \tag{B.13}$$

Since (B.12) is positive definite and (B.13) is negative semi-definite, $Z(t) \equiv 0$ is stable in the sense of Lyapunov, and the system (B.10) converges to the manifold of $\hat{x}(t) \equiv 0$ asymptotically.

On the other hand, the convergence of the estimated parameters ($\lim_{t\to\infty} \hat{A}(t) = 0$, $\lim_{t\to\infty} \hat{B}(t) = 0$, $\lim_{t\to\infty} \hat{C}(t) = 0$) results from the convergence of $\hat{x}$ given sufficiently rich signals $x(t), u_1(t), u_2(t)$, i.e., the persistent excitation condition. Here this condition requires piecewise continuous signals with a sufficient number of discontinuities at non-commensurable points [53], and in each continuous subinterval it also requires a sufficient number of Fourier components. Such "jumps" may be common in electronic signals, but they are seldom observed in mechanical systems such as the velocity of a car. Thus, it may not be easy to implement this method to estimate the parameters of a car-following model.

We also note that to obtain a more accurate estimation on the actual delay time τ, finer meshes of fictitious delay τ_i are required, which increases the dimension of the adaptive law (B.8). This would not only require more computational power, but also significantly slow down the convergence rate. If the identification becomes slower than the variation of driver behavior this method would eventually fail.

B.3 Method of state-dependent delay

To obtain a more accurate estimation of the delay time without relying on a high-dimensional parametric model, we consider an adaptive law where both the delay time and the feedback

gains in (B.3) are identified simultaneously. In particular, we propose

$$\begin{aligned}
\dot{\tilde{x}}(t) &= \tilde{a}x(t-\tilde{\tau}) + \tilde{b}u_1(t-\tilde{\tau}) + \tilde{c}u_2(t-\tilde{\tau}) + r\hat{x}\,,\\
\dot{\tilde{a}}(t) &= \gamma_1\hat{x}x(t-\tilde{\tau})\,,\\
\dot{\tilde{b}}(t) &= \gamma_2\hat{x}u_1(t-\tilde{\tau})\,,\\
\dot{\tilde{c}}(t) &= \gamma_3\hat{x}u_2(t-\tilde{\tau})\,,\\
\dot{\tilde{\tau}}(t) &= -\gamma_4\hat{x}\tilde{\zeta}\,,
\end{aligned} \tag{B.14}$$

where we use tildes to denote estimated state and parameters, the state error is defined as $\hat{x} = x - \tilde{x}$, and

$$\tilde{\zeta}(t) = \tilde{a}\dot{x}(t-\tilde{\tau}) + \tilde{b}\dot{u}_1(t-\tilde{\tau}) + \tilde{c}\dot{u}_2(t-\tilde{\tau})\,. \tag{B.15}$$

Due to the adaptive law of $\tilde{\tau}$, (B.14) is a nonlinear system with state-dependent delay. To discuss the convergence of the algorithm, we denote the parameter errors by

$$\hat{a} = \tilde{a} - a, \quad \hat{b} = \tilde{b} - b, \quad \hat{c} = \tilde{c} - c, \quad \hat{\tau} = \tilde{\tau} - \tau\,, \tag{B.16}$$

and formulate the dynamics of $\hat{x}$ using (B.3, B.14)

$$\begin{aligned}
\dot{\hat{x}}(t) &= -r\hat{x}(t) + ax(t-\tau) - \tilde{a}x(t-\tilde{\tau}) + bu_1(t-\tau) - \tilde{b}u_1(t-\tilde{\tau}) + cu_2(t-\tau) - \tilde{c}u_2(t-\tilde{\tau})\\
&= -r\hat{x}(t) - \hat{a}x(t-\tau) - \hat{b}u_1(t-\tau) - \hat{c}u_2(t-\tau)\\
&\quad + \tilde{a}(x(t-\tau) - x(t-\tilde{\tau})) + \tilde{b}(u_1(t-\tau) - u_1(t-\tilde{\tau})) + \tilde{c}(u_2(t-\tau) - u_2(t-\tilde{\tau}))\,.
\end{aligned} \tag{B.17}$$

Assuming constant feedback gains in the parametric model (B.3) we obtain

$$\dot{\hat{a}} = \dot{\tilde{a}}\,, \quad \dot{\hat{b}} = \dot{\tilde{b}}\,, \quad \dot{\hat{c}} = \dot{\tilde{c}}\,, \quad \dot{\hat{\tau}} = \dot{\tilde{\tau}}\,. \tag{B.18}$$

While the convergence of approximated delay method (B.8) can be proven with negative semi-definiteness of the Lie derivative of a quadratic Lyapunov function (B.13), here we could not establish the negative semi-definiteness directly using similar quadratic Lyapunov functions, due to the estimated delay $\tilde{\tau}$. Thus we resort to the indirect Lyapunov method by first isolating the nonlinearity due to the time-varying delay $\tilde{\tau}$ and establishing convergence for the linearized dynamics.

We assume $x(t)$, $u_1(t)$ and $u_2(t)$ are bounded and have bounded derivatives up to the

third order, and perform Taylor expansion to extract $\hat{\tau}$ from terms with time-varying delay

$$\begin{aligned}
x(t-\tau) - x(t-\tilde{\tau}) &= \hat{\tau}\dot{x}(t-\tau) - \frac{1}{2}\hat{\tau}^2\ddot{x}(t-\tau) + \mathcal{O}(3)\,, \\
u_1(t-\tau) - u_1(t-\tilde{\tau}) &= \hat{\tau}\dot{u}_1(t-\tau) - \frac{1}{2}\hat{\tau}^2\ddot{u}_1(t-\tau) + \mathcal{O}(3)\,, \\
u_2(t-\tau) - u_2(t-\tilde{\tau}) &= \hat{\tau}\dot{u}_2(t-\tau) - \frac{1}{2}\hat{\tau}^2\ddot{u}_2(t-\tau) + \mathcal{O}(3)\,,
\end{aligned} \tag{B.19}$$

where $\mathcal{O}(n)$ denotes n-th order terms in the state error $\hat{x}$ and the parameter errors $\hat{a}, \hat{b}, \hat{c}, \hat{\tau}$. Assuming constant gains and delay time in the parametric model (B.3), we have

$$\ddot{x}(t) = a\dot{x}(t-\tau) + b\dot{u}_1(t-\tau) + c\dot{u}_2(t-\tau)\,, \tag{B.20}$$

and (B.17) is rewritten as

$$\dot{\hat{x}}(t) = -r\hat{x}(t) - x(t-\tau)\hat{a} - u_1(t-\tau)\hat{b} - u_2(t-\tau)\hat{c} + \ddot{x}(t)\hat{\tau} + g_0(\hat{a}, \hat{b}, \hat{c}, \hat{\tau})\,, \tag{B.21}$$

where the higher-order terms are given by

$$g_0 = \dot{x}(t-\tau)\hat{a}\hat{\tau} + \dot{u}_1(t-\tau)\hat{b}\hat{\tau} + \dot{u}_2(t-\tau)\hat{c}\hat{\tau} - \frac{\dddot{x}(t)}{2}\hat{\tau}^2 + \mathcal{O}(3). \tag{B.22}$$

Similarly, we rewrite (B.14, B.18) as

$$\begin{aligned}
\dot{\hat{a}}(t) &= \gamma_1 x(t-\tau)\hat{x}(t) + g_1(\hat{x}, \hat{\tau})\,, \\
\dot{\hat{b}}(t) &= \gamma_2 u_1(t-\tau)\hat{x}(t) + g_2(\hat{x}, \hat{\tau})\,, \\
\dot{\hat{c}}(t) &= \gamma_3 u_2(t-\tau)\hat{x}(t) + g_3(\hat{x}, \hat{\tau})\,, \\
\dot{\hat{\tau}}(t) &= -\gamma_4\ddot{x}(t)\hat{x}(t) + g_4(\hat{x}, \hat{a}, \hat{b}, \hat{c}, \hat{\tau})\,,
\end{aligned} \tag{B.23}$$

where the higher-order terms are

$$\begin{aligned}
g_1 &= -\gamma_1\dot{x}(t-\tau)\hat{x}(t)\hat{\tau}(t) + \mathcal{O}(3)\,, \\
g_2 &= -\gamma_2\dot{u}_1(t-\tau)\hat{x}(t)\hat{\tau}(t) + \mathcal{O}(3)\,, \\
g_3 &= -\gamma_3\dot{u}_2(t-\tau)\hat{x}(t)\hat{\tau}(t) + \mathcal{O}(3)\,, \\
g_4 &= -\gamma_4\big(\dot{x}(t-\tau)\hat{a}(t) + \dot{u}_1(t-\tau)\hat{b}(t) + \dot{u}_2(t-\tau)\hat{c}(t) - \dddot{x}(t)\hat{\tau}(t)\big)\hat{x}(t) + \mathcal{O}(3).
\end{aligned} \tag{B.24}$$

We define the state variable $Y = \begin{bmatrix} \hat{x} & \hat{a} & \hat{b} & \hat{c} & \hat{\tau} \end{bmatrix}^{\mathrm{T}}$ and then write (B.21, B.23) into

state space form

$$\dot{Y} = \mathbf{M}(t)Y + \mathbf{N}(Y,t)\,, \tag{B.25}$$

where the coefficient matrix is given by

$$\begin{aligned}
\mathbf{M}(t) &= \begin{bmatrix} -r & -v(t) \\ \Gamma v^{\mathrm{T}}(t) & 0 \end{bmatrix}, \\
\Gamma &= \operatorname{diag}\begin{bmatrix} \gamma_1 & \gamma_2 & \gamma_3 & \gamma_4 \end{bmatrix}, \\
v(t) &= \begin{bmatrix} x(t-\tau) & u_1(t-\tau) & u_2(t-\tau) & -\ddot{x}(t) \end{bmatrix},
\end{aligned} \tag{B.26}$$

and the higher-order terms are collected in

$$\mathbf{N}(Y,t) = \begin{bmatrix} g_0 & g_1 & g_2 & g_3 & g_4 \end{bmatrix}^{\mathrm{T}}. \tag{B.27}$$

When the fixed point $Y(t) \equiv 0$ of (B.25) is uniformly asymptotically stable, both the state error $\hat{x}$ and the parameter errors $\hat{a}, \hat{b}, \hat{c}, \hat{\tau}$ are guaranteed to decay to zero. It has been found that given $r > 0$, the uniform asymptotic stability of $\dot{Y} = \mathbf{M}(t)Y$ is equivalent to the persistent excitation condition of the signal $v(t)$ [72]. That is, there exist positive constants T_0, δ_0, and ϵ_0 such that for all $t_1 \geq 0$ and a unit vector w with the same dimension as $v(t)$, there is a $t_2 \in [t_1, t_1 + T_0]$ such that

$$\left| \int_{t_2}^{t_2+\delta_0} v(\theta) w^{\mathrm{T}} \,\mathrm{d}\theta \right| \geq \epsilon_0\,. \tag{B.28}$$

This establishes the local convergence of this algorithm.

However, the size of the basin of attraction depends on the nonlinear term $\mathbf{N}(Y,t)$. While we assume the input signals $x(t), u_1(t), u_2(t)$ are bounded, the bounds in general depend on the magnitude of different frequency components in $u_2(t)$. These bounds, together with the choice of adaptation gains $\gamma_1, \gamma_2, \gamma_3, \gamma_4$, determine the basin of attraction. We believe that the size of the basin of attraction can be estimated through bifurcation analysis. Here, we simply point out that the algorithm is observed to perform well even for initial guesses with relatively large parameter errors, when considering properly chosen adaptation gains and sufficiently rich signals based on experiences from parameter estimation in non-delayed systems.

Meanwhile, having an adaptive law for the delay time instead of a grid approximation has been found to be important to ensure the performance of the parameter estimation.

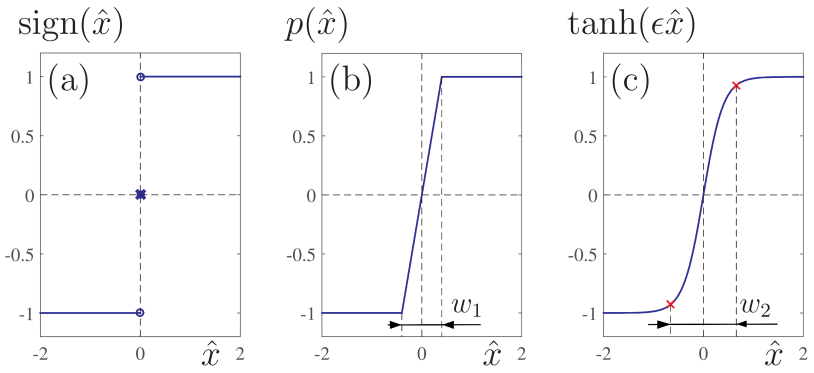

Figure B.1: (a): The non-continuous sign function (B.30). (b): The non-smooth piecewise linear function (B.31) with the width of boundary layer $w_1 = 2\epsilon$. (c): The infinitely smooth hyperbolic tangent function (B.32) with the width of boundary layer $w_2 = \epsilon \ln(2+\sqrt{3})$. We set $\epsilon = 0.4$ in (b,c).

Consequently, this method is more practical for applications like connected vehicle systems. It may be used to identify parameters in the car-following dynamics of an automated vehicle.

B.4 Modified method of state-dependent delay

It is noted in sliding mode control that the switching between different control laws in different regions of the state space may increase the convergence rate [73]. Motivated by the estimator proposed in [54], we consider introducing the sign function into our adaptive law and rewrite it as

$$\begin{aligned}
\dot{\hat{x}}(t) &= \tilde{a}x(t-\tilde{\tau}) + \tilde{b}u_1(t-\tilde{\tau}) + \tilde{c}u_2(t-\tilde{\tau}) + r\hat{x}\,,\\
\dot{\tilde{a}}(t) &= \gamma_1 f(\hat{x})x(t-\tilde{\tau})\,,\\
\dot{\tilde{b}}(t) &= \gamma_2 f(\hat{x})u_1(t-\tilde{\tau})\,,\\
\dot{\tilde{c}}(t) &= \gamma_3 f(\hat{x})u_2(t-\tilde{\tau})\,,\\
\dot{\tilde{\tau}}(t) &= -\gamma_4 f(\hat{x})\tilde{\zeta}\,,
\end{aligned} \tag{B.29}$$

where $\tilde{\zeta}$ is given by (B.15) and we may use the switching function

$$f(\hat{x}) = \operatorname{sign}(\hat{x}) = \begin{cases} -1 & \text{if} \quad \hat{x} < 0\,,\\ 0 & \text{if} \quad \hat{x} = 0\,,\\ 1 & \text{if} \quad \hat{x} > 0\,, \end{cases} \tag{B.30}$$

that is plotted in Fig. B.1(a).

However, the sign function cannot be perfectly implemented numerically, which typically leads to high-frequency oscillation (called chattering) in the vicinity of the sliding surface. To eliminate chattering, we define a boundary layer $|\hat{x}| \leq \epsilon$, $\epsilon > 0$ and define the switching function as

$$f(\hat{x}) = p(\hat{x}) = \begin{cases} 1 & \text{if} \quad \hat{x} > \epsilon\,, \\ \hat{x}/\epsilon & \text{if} \quad -\epsilon \leq \hat{x} \leq \epsilon\,, \\ -1 & \text{if} \quad \hat{x} < -\epsilon\,, \end{cases} \tag{B.31}$$

as shown in Fig. B.1(b). Here ϵ is used to adjust the gradient of the switching function, and consequently the width $w_1 = 2\epsilon$ of the boundary layer. Note that inside the boundary layer, (B.31) is linear and the estimator (B.29, B.31) is equivalent to (B.14).

In order to avoid non-smoothness when entering the boundary layer, we may use a hyperbolic tangent function

$$f(\hat{x}) = \tanh\big(\hat{x}/\epsilon\big)\,, \tag{B.32}$$

as shown in Fig. B.1(c). Again, ϵ determines the gradient, and by calculating the third-order inflection points ($\partial_{\hat{x}}^3 \tanh\big(\hat{x}/\epsilon\big) = 0$) we obtain the width of the boundary layer as $w_2 = \epsilon \ln(2+\sqrt{3})$. Indeed, as ϵ decreases, the width of both boundary layers in (B.31) and (B.32) tend to zero, and (B.31) and (B.32) converge to (B.30).

We note that when implementing algorithms that contain the dynamics of $\tilde{\tau}$, a lower bound and an upper bound on the estimation $\tilde{\tau}$ are needed. We set $\tilde{\tau} \in [0, \tau_{\max}]$, where $\tau_{\max}$ is the maximum delay time known a priori.

B.5 Simulations

In this section, we implement the method of approximated delay (B.8), and two methods of state-dependent delay (B.14, B.29) to estimate the delay time and feedback gains in the parametric car-following model (B.3), and compare their performances.

We use $v_{\max} = 30$ [m/s], $h_{\rm st} = 5$ [m], $h_{\rm go} = 35$ [m] that corresponds to realistic traffic data [42] in the range policy (2.3), which results in the constant slope $\kappa = 1$ [1/s]. Moreover, we set the equilibrium at $(h^*, v^*) = (20\,[\mathrm{m}], 15\,[\mathrm{m/s}])$ and use the gains $\alpha = 0.6$ [1/s], $\beta = 0.9$ [1/s] and reaction time $\tau = 0.5$ [s]. Then the real parameter values in the parametric model (B.3) are $a = -1.5$ [1/s], $b = 0.6$ [1/s], $c = 0.9$ [1/s]; see (B.4).

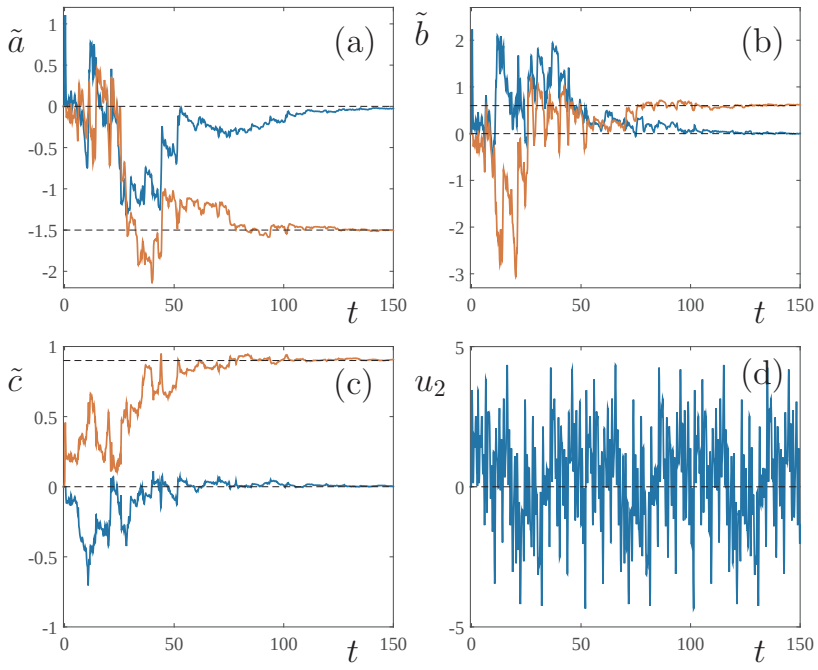

Figure B.2: (a,b,c): Estimated feedback gains using (B.8). The blue curves are gains corresponding to $\tau_1 = 0$ [s], and the red curves corresponds to $\tau_2 = 0.5$ [s]. The dashed lines mark the real value of a, b, and c, respectively. (d): The input signal $u_2(t) = \delta v_{i+1}(t)$ used by the estimator (B.5) is discontinuous at $t \approx 2.7,\ 52.1,\ 101.5$ [s]. In each continuous subinterval $u_2(t) = \sum_{j=1}^{6} \sin(\omega_j t + \rho_j)$ with frequency components $\omega_j \in \{0.2, 0.6, 1.5, 3.8, 5.3, 7\}$ [rad/s].

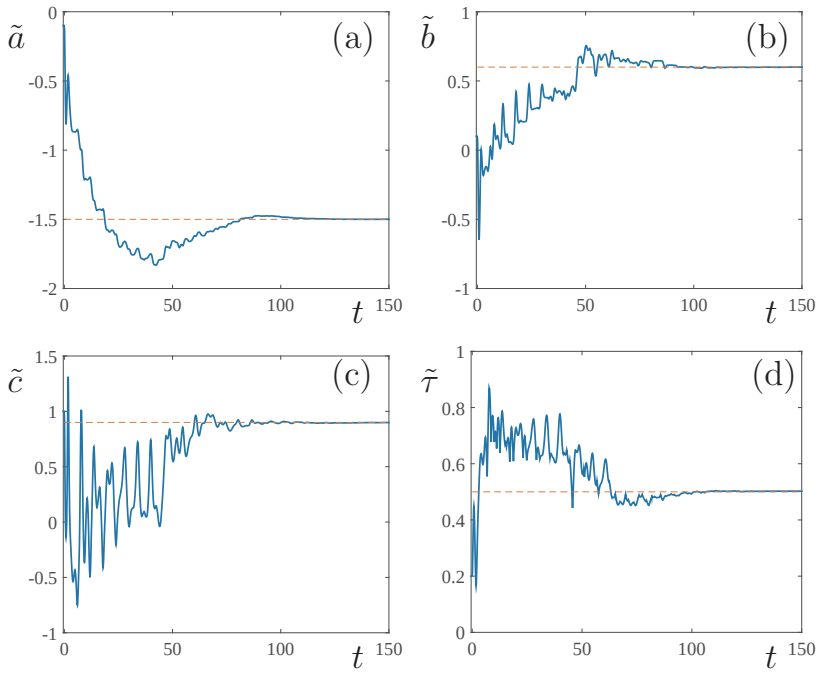

Figure B.3: Estimated feedback gains and delay time using the estimator (B.14). The dashed lines mark the real parameter values. The signals are generated using (B.1, B.2) with $u_2(t) = \delta v_{i+1}(t) = \frac{2}{3}\big(\cos(t) + \cos(2.1t) + \cos(7t)\big)$. The estimator gains are $\gamma_1 = 1.5$, $\gamma_2 = 1.5$, $\gamma_3 = 6.0$, $\gamma_4 = 1.0$.

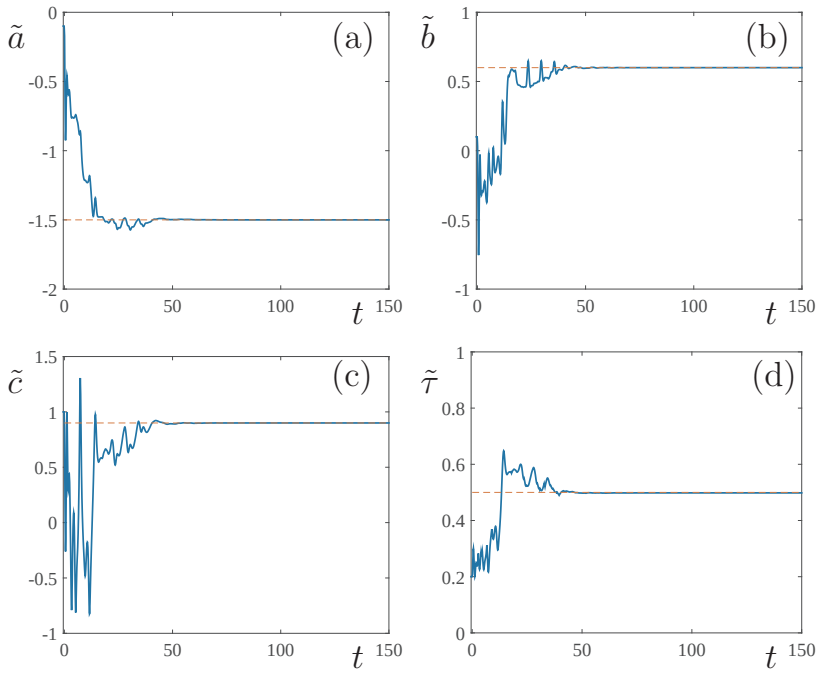

Figure B.4: Estimated feedback gains and delay time using the estimator (B.29, B.32). The notations and input signals are the same as in Fig. B.3. The estimator gains are $\gamma_1 = 1.5$, $\gamma_2 = 1.5$, $\gamma_3 = 4.0$, $\gamma_4 = 0.35$, and we set $\epsilon = 0.4$.

For the first method (B.8), we assume one fictitious delay time $\tau_1 = 0$ [s] aside from the real delay time $\tau_2 = 0.5$ [s]. The signals $x(t)$, $u_1(t)$, $u_2(t)$ are generated by the linearized car-following model (B.1, B.2) with non-smooth velocity perturbation $u_2(t)$ with frequency components $\omega_j \in \{0.2, 0.6, 1.5, 3.8, 5.3, 7\}$ [rad/s]. The trajectory of estimated parameters are shown in Fig. B.2(a,b,c). Note that while the parameters converge within 150 [s], the velocity profile of vehicle $i+1$ contains 6 frequency components and 3 discontinuities to meet the persistent excitation condition (see the caption of Fig. B.2). Such non-smooth velocity profile is not commonly observed in cars on road, as vehicles can be viewed as low-pass filters. Thus, the convergence rate of this estimator may be significantly slower in real-world implementation. Also, the number of estimated parameters ($3n$) increases with the number of fictitious delays (n), leading to observed deterioration of convergence rate in simulations. Meanwhile, as the mesh for delay time becomes finer, the time interval between mesh points shortens. As a result, the numerical algorithm will have increasing difficulty in correctly identifying gains corresponding to each mesh point. Thus, it is difficult to preserve the convergence rate in Fig. B.2 when we do not start with the exact guess of $\tau_2 = 0.5$ [s].

Fig. B.3 and Fig. B.4 show the performance of the estimators (B.14) and (B.29, B.32), respectively. Signals $x(t)$, $u_1(t)$, $u_2(t)$ are generated by the linearized car-following model (B.1, B.2) with a sinusoidal velocity perturbation $u_2(t) = \delta v_{i+1}(t) = \frac{2}{3}\big(\cos(t) + \cos(2.1t) + \cos(7t)\big)$. In both figures, the feedback gains and delay converge to the real values within reasonable amount of time, producing more accurate estimations than in Fig. B.2. However, the convergence rate is faster in Fig. B.4, which illustrates the potential benefits of the modified estimator (B.29, B.32).

B.6 Conclusion

Int his chapter we presented three estimators for parameter estimation in linear time-invariant systems, and applied them to a car-following model with driver reaction time. The method of multiple delays is a direct extension of parameter estimation in systems without delay. However, it required non-continuous signals for persistent excitation and the convergence rate deteriorated rapidly as the number of fictitious delays were increased. The method of state-dependent delay is able to provide accurate estimation of delay time and feedback gains without sacrificing the convergence rate. We further modified this method in order to improve the convergence rate.

APPENDIX C

Solving time-delayed LQ problem in connected vehicle design

C.1 The solution of LQR problem with delay

Here we present a detailed solution to the LQR problem with time delay. Since (5.12, 5.13) is constructed to include disturbance $\phi(t)$ in the LQR format, and the optimal controller (5.19) is given using partitioned matrices (5.18), we write (5.16, 5.17) into four groups, where $\mathbf{P}_1(t)$, $\mathbf{Q}_1(t,\theta)$, $\mathbf{R}_1(t,\xi,\theta)$ are independent from the disturbance and can be solved using only the coefficient matrices $\mathbf{A}, \mathbf{B}, \mathbf{D}$ and the weighting factor $\mathbf{\Gamma}$. That is, for the first group we obtain the PDE

$$\begin{aligned}
&-\dot{\mathbf{P}}_1(t) = \mathbf{A}^{\mathrm{T}}\mathbf{P}_1(t) + \mathbf{P}_1(t)\mathbf{A} - \mathbf{P}_1(t)\mathbf{D}\mathbf{D}^{\mathrm{T}}\mathbf{P}_1(t) + \mathbf{Q}_1(t,0) + \mathbf{Q}_1^{\mathrm{T}}(t,0) + \mathbf{\Gamma}\,,\\
&(\partial_\theta - \partial_t)\mathbf{Q}_1(t,\theta) = \big(\mathbf{A}^{\mathrm{T}} - \mathbf{P}_1(t)\mathbf{D}\mathbf{D}^{\mathrm{T}}\big)\mathbf{Q}_1(t,\theta) + \mathbf{R}_1(t,0,\theta),\\
&(\partial_\xi + \partial_\theta - \partial_t)\mathbf{R}_1(t,\xi,\theta) = -\mathbf{Q}_1^{\mathrm{T}}(t,\xi)\mathbf{D}\mathbf{D}^{\mathrm{T}}\mathbf{Q}_1(t,\theta)\,,
\end{aligned} \tag{C.1}$$

with boundary conditions

$$\begin{aligned}
&\mathbf{P}_1(t_{\mathrm{f}}) = \mathbf{0}\,,\\
&\mathbf{Q}_1(t_{\mathrm{f}},\theta) = \mathbf{0}\,, \qquad \mathbf{Q}_1(t,-\tau) = \mathbf{P}_1(t)\mathbf{B}\,,\\
&\mathbf{R}_1(t_{\mathrm{f}},\xi,\theta) = \mathbf{0}\,, \qquad \mathbf{R}_1(t,-\tau,\theta) = \mathbf{B}^{\mathrm{T}}\mathbf{Q}_1(t,\theta)\,.
\end{aligned} \tag{C.2}$$

Using $\mathbf{P}_1(t)$ and $\mathbf{Q}_1(t,\theta)$ obtained from (C.1, C.2), we can calculate $\mathbf{Q}_2(t,\theta)$ and $\mathbf{R}_2(t,\xi,\theta)$ by solving

$$\begin{aligned}
&(\partial_\theta - \partial_t)\mathbf{Q}_2(t,\theta) = \big(\mathbf{A}^{\mathrm{T}} - \mathbf{P}_1(t)\mathbf{D}\mathbf{D}^{\mathrm{T}}\big)\mathbf{Q}_2(t,\theta) + \mathbf{R}_2(t,0,\theta),\\
&(\partial_t - \partial_\xi - \partial_\theta)\mathbf{R}_2(t,\xi,\theta) = \mathbf{Q}_1^{\mathrm{T}}(t,\xi)\mathbf{D}\mathbf{D}^{\mathrm{T}}\mathbf{Q}_2(t,\theta)\,,
\end{aligned} \tag{C.3}$$

with boundary conditions

$$\begin{aligned} &\mathbf{Q}_2(t_{\mathrm{f}},\theta)=\mathbf{0}\,, \qquad &&\mathbf{Q}_2(t,-\tau)=\mathbf{0}\,,\\ &\mathbf{R}_2(t_{\mathrm{f}},\xi,\theta)=\mathbf{0}\,, \qquad &&\mathbf{R}_2(t,-\tau,\theta)=\mathbf{B}^{\mathrm{T}}\mathbf{Q}_2(t,\theta)\,. \end{aligned} \tag{C.4}$$

Note that the disturbance $\phi(t)$ does not appear in (C.3) either. As a matter of fact, (C.3, C.4) result in $\mathbf{Q}_2(t,\theta)\equiv\mathbf{0}$ and $\mathbf{R}_2(t,\xi,\theta)\equiv\mathbf{0}$.

The dynamics of $\mathbf{P}_2(t)$ and $\mathbf{Q}_3(t,\theta)$ are driven by the disturbance $\phi(t)$:

$$\begin{aligned} -\dot{\mathbf{P}}_2(t)&=\big(\mathbf{A}^{\mathrm{T}}-\mathbf{P}_1(t)\mathbf{D}\mathbf{D}^{\mathrm{T}}\big)\mathbf{P}_2(t)+\mathbf{P}_1(t)\phi(t)+\mathbf{Q}_2(t,0)+\mathbf{Q}_3^{\mathrm{T}}(t,0)\,,\\ (\partial_\theta-\partial_t)\mathbf{Q}_3(t,\theta)&=\big(\phi^{\mathrm{T}}(t)-\mathbf{P}_2^{\mathrm{T}}(t)\mathbf{D}\mathbf{D}^{\mathrm{T}}\big)\mathbf{Q}_1(t,\theta)+\mathbf{R}_2^{\mathrm{T}}(t,\theta,0), \end{aligned} \tag{C.5}$$

with boundary conditions

$$\begin{aligned} &\mathbf{P}_2(t_{\mathrm{f}})=\mathbf{0}\,,\\ &\mathbf{Q}_3(t_{\mathrm{f}},\theta)=\mathbf{0}\,, \qquad &&\mathbf{Q}_3(t,-\tau)=\mathbf{P}_2^{\mathrm{T}}(t)\mathbf{B}\,. \end{aligned} \tag{C.6}$$

Although $\mathbf{P}_4(t)$, $\mathbf{Q}_4(t,\theta)$, $\mathbf{R}_4(t,\xi,\theta)$ do not appear in the optimal control (5.19), they appear in the minimal cost function, and are given by the PDE

$$\begin{aligned} -\dot{\mathbf{P}}_4(t)&=\phi^{\mathrm{T}}(t)\mathbf{P}_2(t)+\mathbf{P}_3(t)\phi(t)-\mathbf{P}_3(t)\mathbf{D}\mathbf{D}^{\mathrm{T}}\mathbf{P}_2(t)+\mathbf{Q}_4(t,0)+\mathbf{Q}_4^{\mathrm{T}}(t,0)\,,\\ (\partial_\theta-\partial_t)\mathbf{Q}_4(t,\theta)&=\big(\phi^{\mathrm{T}}(t)-\mathbf{P}_3(t)\mathbf{D}\mathbf{D}^{\mathrm{T}}\big)\mathbf{Q}_2(t,\theta)+\mathbf{R}_4(t,0,\theta),\\ (\partial_\xi+\partial_\theta-\partial_t)\mathbf{R}_4(t,\xi,\theta)&=-\mathbf{Q}_2^{\mathrm{T}}(t,\xi)\mathbf{D}\mathbf{D}^{\mathrm{T}}\mathbf{Q}_2(t,\theta)\,, \end{aligned} \tag{C.7}$$

with boundary conditions

$$\begin{aligned} &\mathbf{P}_4(t_{\mathrm{f}})=\mathbf{0}\,,\\ &\mathbf{Q}_4(t_{\mathrm{f}},\theta)=\mathbf{0}\,, \qquad &&\mathbf{Q}_4(t,-\tau)=\mathbf{0}\,,\\ &\mathbf{R}_4(t_{\mathrm{f}},\xi,\theta)=\mathbf{0}\,, \qquad &&\mathbf{R}_4(t,-\tau,\theta)=\mathbf{0}\,. \end{aligned} \tag{C.8}$$

C.2 The distribution kernels

Here we provide the constants that appear in the expression of $f_i(\theta), g_i(\theta), i=1,\ldots,n$ in (5.42) using (5.36, 5.40, 5.44). For $i=1$ (5.44) corresponds to

$$a_{10}=a_{11}=a_{12}=0, \quad b_{10}=b_{11}=b_{12}=0\,. \tag{C.9}$$

For $i = 2, \ldots, n$ we write in (5.36) that

$$\mathrm{e}^{\hat{\mathbf{A}}_1(\theta+\tau)} = \mathbf{K}\mathrm{e}^{\hat{\mathbf{J}}_1(\theta+\tau)}\mathbf{K}^{-1}\,, \tag{C.10}$$

where the Jordan form $\hat{\mathbf{J}}_1$ contains the eigenvalues of $\hat{\mathbf{A}}_1$:

$$\lambda_{1,2} = \frac{1}{2}\Big(- \sqrt{\gamma_1 + \gamma_2 + 2\kappa\sqrt{\gamma_1}} \pm \sqrt{\gamma_1 + \gamma_2 - 2\kappa\sqrt{\gamma_1}}\Big)\,, \tag{C.11}$$

and the real part of λ_1, λ_2 are smaller than zero (which is ensured by the closed-loop plant stability of LQ design). In most cases $\hat{\mathbf{A}}_1$ is diagonalizable, that is, $\hat{\mathbf{J}}_1 = \mathrm{diag}([\lambda_1, \lambda_2])$. In the special case $\gamma_2 = 2\kappa\sqrt{\gamma_1} - \gamma_1$, we have $\lambda_1 = \lambda_2$ and $\hat{\mathbf{A}}_1$ may not be diagonalizable, yielding the nontrivial Jordan form $\hat{\mathbf{J}}_1 = \begin{bmatrix} \lambda_1 & 1 \\ 0 & \lambda_1 \end{bmatrix}$.

Denote $\mathbf{K} = \begin{bmatrix} k_{11} & k_{12} \\ k_{21} & k_{22} \end{bmatrix}$, $\mathbf{K}^{-1} = \begin{bmatrix} i_{11} & i_{12} \\ i_{21} & i_{22} \end{bmatrix}$, then from (5.36, 5.40) we obtain

$$\begin{bmatrix} f_i(\theta) & g_i(\theta) \end{bmatrix} = \begin{bmatrix} f_{\mathrm{c}}(\theta) & g_{\mathrm{c}}(\theta) \end{bmatrix} \big(\mathbf{P}_{1i}\mathbf{B}_1 + \mathbf{P}_{1(i-1)}\mathbf{B}_2\big), \tag{C.12}$$

where

$$\begin{aligned} f_{\mathrm{c}}(\theta) &= \big(t_{\mathrm{ca}} + t_{\mathrm{cc}}(\theta+\tau)\big)\mathrm{e}^{\lambda_1(\theta+\tau)} + t_{\mathrm{cb}}\mathrm{e}^{\lambda_2(\theta+\tau)}\,, \\ g_{\mathrm{c}}(\theta) &= \big(s_{\mathrm{ca}} + s_{\mathrm{cc}}(\theta+\tau)\big)\mathrm{e}^{\lambda_1(\theta+\tau)} + s_{\mathrm{cb}}\mathrm{e}^{\lambda_2(\theta+\tau)}\,, \end{aligned} \tag{C.13}$$

such that we have

$$\begin{aligned} t_{\mathrm{ca}} &= (k_{11}+k_{21})i_{11}\,, \qquad t_{\mathrm{cb}} = (k_{12}+k_{22})i_{21}\,, \\ s_{\mathrm{ca}} &= (k_{11}+k_{21})i_{12}\,, \qquad s_{\mathrm{cb}} = (k_{12}+k_{22})i_{22}\,, \\ t_{\mathrm{cc}} &= \begin{cases} 0\,, & \text{if } \hat{\mathbf{A}}_1 \text{ is diagonalizable}\,, \\ (k_{11}+k_{21})i_{21}\,, & \text{if } \hat{\mathbf{A}}_1 \text{ is not diagonalizable}\,, \end{cases} \\ s_{\mathrm{cc}} &= \begin{cases} 0\,, & \text{if } \hat{\mathbf{A}}_1 \text{ is diagonalizable}\,, \\ (k_{11}+k_{21})i_{22}\,, & \text{if } \hat{\mathbf{A}}_1 \text{ is not diagonalizable}\,. \end{cases} \end{aligned} \tag{C.14}$$

Substituting (5.9, C.13) into (C.12), we obtain (5.42) with the coefficients

$$\begin{aligned} a_{i0} &= \alpha(t_{\rm ca} l_{i1} + s_{\rm ca} l_{i2})\,, \quad b_{i0} = \beta(t_{\rm ca} l_{i1} + s_{\rm ca} l_{i2})\,, \\ a_{i1} &= \alpha(t_{\rm cc} l_{i1} + s_{\rm cc} l_{i2})\,, \quad b_{i1} = \beta(t_{\rm cc} l_{i1} + s_{\rm cc} l_{i2})\,, \\ a_{i2} &= \alpha(t_{\rm cb} l_{i1} + s_{\rm cb} l_{i2})\,, \quad b_{i2} = \beta(t_{\rm cb} l_{i1} + s_{\rm cb} l_{i2})\,, \end{aligned} \tag{C.15}$$

where

$$\begin{aligned} l_{i1} &= -\mathbf{P}_{1i}[1,1] - \mathbf{P}_{1i}[1,2] + \mathbf{P}_{1(i-1)}[1,2]\,, \\ l_{i2} &= -\mathbf{P}_{1i}[2,1] - \mathbf{P}_{1i}[2,2] + \mathbf{P}_{1(i-1)}[2,2]\,, \end{aligned} \tag{C.16}$$

for $i = 2, \ldots, n$, and $\mathbf{C}[i,j]$ stands for the element of $\mathbf{C}$ at the $i^{\rm th}$ row and $j^{\rm th}$ column.

C.3 The contracting map

To show that the feedback gains and distribution functions decay exponentially with the car number, all eigenvalues of $\mathbf{M}$ must be smaller than 1 in magnitude, cf. (5.38, 5.39).

We assume diagonalizable $\hat{\mathbf{A}}_1$ and plug (C.10) into (5.39) to obtain

$$\mathbf{M} = (\mathbf{I} \otimes \mathbf{K})\tilde{\mathbf{M}}(\mathbf{I} \otimes \mathbf{K}^{-1})\,, \tag{C.17}$$

where

$$\tilde{\mathbf{M}} = -\begin{bmatrix} \hat{\mathbf{J}}_1 - \alpha\, \mathrm{e}^{\tau \hat{\mathbf{J}}_1} & -\alpha\, \mathrm{e}^{\tau \hat{\mathbf{J}}_1} \\ \kappa \mathbf{I} - \beta\, \mathrm{e}^{\tau \hat{\mathbf{J}}_1} & \hat{\mathbf{J}}_1 - \beta\, \mathrm{e}^{\tau \hat{\mathbf{J}}_1} \end{bmatrix}^{-1} \begin{bmatrix} \mathbf{0} & \alpha\, \mathrm{e}^{\tau \hat{\mathbf{J}}_1} \\ \mathbf{0} & \beta\, \mathrm{e}^{\tau \hat{\mathbf{J}}_1} \end{bmatrix}. \tag{C.18}$$

Indeed, the eigenvalues of $\mathbf{M}$ are the same as the eigenvalues of $\tilde{\mathbf{M}}$. It is evident that $\tilde{\mathbf{M}}$ has two zero eigenvalues, while the other two non-zero eigenvalues are

$$\mu_{1,2} = -\frac{\alpha\kappa - \beta\lambda_{1,2}}{\lambda_{1,2}^2\, \mathrm{e}^{-\tau\lambda_{1,2}} - (\alpha+\beta)\lambda_{1,2} + \alpha\kappa}\,, \tag{C.19}$$

where $\lambda_{1,2}$ are given in (C.11). That is, the recursive map (5.38, 5.39) is contracting if

$$|\mu_1| < 1, \quad |\mu_2| < 1\,. \tag{C.20}$$

Consider plant stable human-driven vehicles where κ and α, β are positive. We found that (C.20) holds in the string stable region in the parameter space. Note that (C.19) bears an interesting resemblance to $H_0(s)$ in (5.47), and still holds when $\hat{\mathbf{A}}_1$ is not diagonalizable.

C.4 Robustness of CCC against other CCC vehicles

Here we consider the scenario where vehicles $2-n$ in Fig. 5.1 are no longer homogeneous, that is, some of them may have different human parameters or even become CCC vehicles. To demonstrate the general influence of heterogeneity among preceding vehicles on the CCC design, we assume the dynamics of vehicle i is

$$\begin{aligned}\dot{h}_i(t) &= v_{i+1}(t) - v_i(t)\,,\\ \dot{v}_i(t) &= \sum_{j=i}^{n} \Big(\alpha_{ij}\big(V_j(h_j(t-\tau)) - v_j(t-\tau)\big) + \beta_{ij}\,\dot{h}_j(t-\tau)\Big)\,,\end{aligned} \tag{C.21}$$

for $i = 2,\dots,n$, where α_{ij}, β_{ij} are vehicle i's feedback gains on motion signals from vehicle j, cf. (2.2, 5.56).

Thus, the dynamics of the connected vehicle system is still described by (5.7), with a new coefficient matrix

$$\mathbf{B} = \begin{bmatrix} \mathbf{0} & \mathbf{B}_{12} & \mathbf{B}_{13} & \cdots & \mathbf{B}_{1n} \\ & \mathbf{B}_{22} & \mathbf{B}_{23} & \cdots & \mathbf{B}_{2n} \\ & & \ddots & & \vdots \\ & & & \mathbf{B}_{(n-1)(n-1)} & \mathbf{B}_{(n-1)n} \\ & & & & \mathbf{B}_{nn} \end{bmatrix}, \tag{C.22}$$

where

$$\begin{aligned}\mathbf{B}_{1i} &= \begin{bmatrix} 0 & 0 \\ \alpha_{2i} & \beta_{2i} \end{bmatrix}, \quad \mathbf{B}_{ii} = -\begin{bmatrix} \alpha_{ii} & \beta_{ii} \\ \alpha_{ii} & \beta_{ii} \end{bmatrix}, \quad i = 2,\cdots,n,\\ \mathbf{B}_{ij} &= \begin{bmatrix} -\alpha_{ij} & -\beta_{ij} \\ \alpha_{(i+1)j} - \alpha_{ij} & \beta_{(i+1)j} - \beta_{ij} \end{bmatrix}, \quad j = i+1,\cdots,n\,,\end{aligned} \tag{C.23}$$

cf. (5.8, 5.9).

Since the matrix $\mathbf{B}$ is still upper-triangular, the optimal control design (5.23, 5.24, 5.26) can be decomposed as before. Now instead of (5.36, 5.38, 5.39), we have

$$\mathbf{Q}_{1i}(\theta) = \sum_{k=1}^{i} e^{\hat{\mathbf{A}}_1(\theta+\tau)}\mathbf{P}_{1k}\mathbf{B}_{ki}\,, \tag{C.24}$$

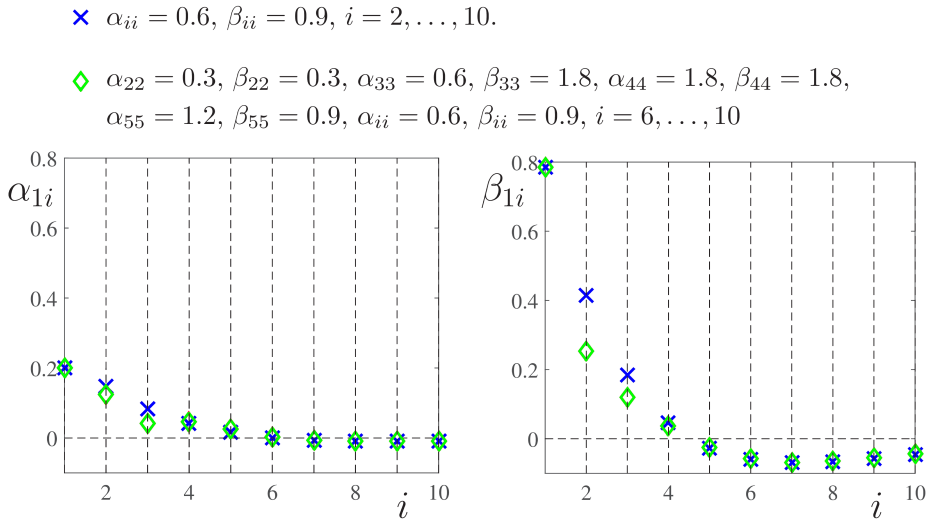

Figure C.1: The optimized headway and velocity gains $\alpha_{1i}, \beta_{1i}, i = 1, \ldots, n$ of the CCC vehicle in a $(10+1)$-car system for homogeneous (blue crosses) and heterogeneous (green diamonds) human gains as indicated. The other parameters are the same as in Fig. 5.2.

and

$$\mathrm{vec}(\mathbf{P}_{1i}) = \sum_{k=1}^{i-1} \mathbf{M}_{ik} \mathrm{vec}(\mathbf{P}_{1k}), \tag{C.25}$$

for $i = 2, \ldots, n$, where

$$\mathbf{M}_{ik} = -(\mathbf{I} \otimes \hat{\mathbf{A}}_1 + \mathbf{A}_1^{\mathrm{T}} \otimes \mathbf{I} + \mathbf{B}_{ii}^{\mathrm{T}} \otimes \mathrm{e}^{\tau \hat{\mathbf{A}}_1})^{-1} (\mathbf{B}_{ki}^{\mathrm{T}} \otimes e^{\tau \hat{\mathbf{A}}_1}). \tag{C.26}$$

This means that the maps between $\mathrm{vec}(\mathbf{P}_{1i})$, $i = 2, \ldots, n$, and $\mathrm{vec}(\mathbf{P}_{11})$ are determined by $\mathbf{B}_{ki}$, $k = 2, \ldots, i-1$, i.e., by the connectivity structure between vehicle 1 and vehicle i. Thus, the connectivity structure among vehicles farther downstream still does not influence feedback gains on existing feedback terms of the CCC controller.

We first demonstrate only the influence of heterogeneous human parameters. In this case, the coefficient matrix $\mathbf{B}$ still has the same structure is in (5.8), i.e., $\mathbf{B}_{ij} \neq \mathbf{0}$ only for $j = i+1$. Thus, there is only one term $\mathbf{M}_{i(i-1)}$ left in the right-hand side of (C.25), and it still defines a recursively contracting map given plant stable human parameters in (C.26).

As an example, we take a $(10+1)$-car connected system, keep the design parameters $\gamma_1 = 0.04\,[1/\mathrm{s}^2]$, $\gamma_2 = 0.30\,[1/\mathrm{s}^2]$ and human reaction time $\tau = 0.4$ [s] as in Fig. 5.2, but increase/decrease the human gains for vehicles $2, 3, 4, 5$ as indicated in Fig. C.1. The blue crosses correspond to the homogeneous system (cf. Fig. 5.2), while the green diamonds correspond to the heterogeneous system. The gains α_{11}, β_{11} are the same for both cases, because they do not depend on parameters of preceding vehicles. Although α_{1i}, β_{1i} , $i =$

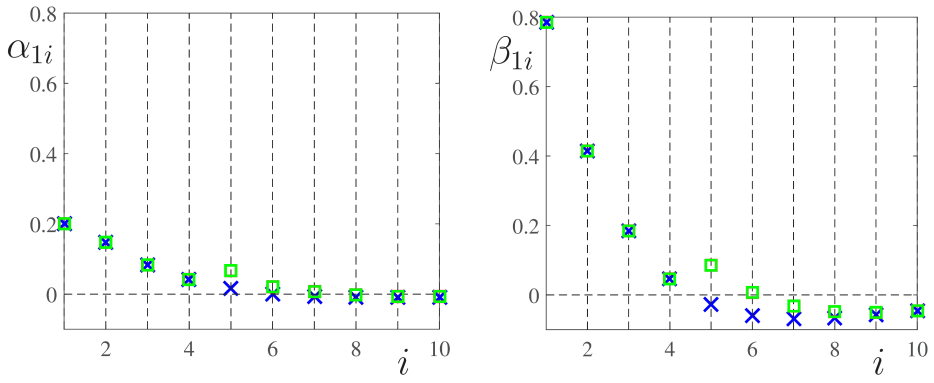

Figure C.2: The optimized headway and velocity gains $\alpha_{1i}, \beta_{1i}, i = 2, \ldots, n$ of the CCC vehicle in a $(10+1)$-car connected vehicle system. The blue crosses denote gains obtained with homogeneous human-driven vehicles, while the green squares denote the case when vehicle 3 uses additional feedback from vehicle 5, with gains $\alpha_{35} = 0.9\,[1/\mathrm{s}]$ and $\beta_{35} = 0.9\,[1/\mathrm{s}]$. The other parameters are the same as in Fig. 5.2.

$2, \ldots, n$ differ between the homogeneous and heterogeneous cases, the difference is only noticeable for $i = 2, 3$, even though α_{44}, β_{44}, α_{55}, β_{55} differ significantly. This is because the contracting map (C.25, C.26) forces the gains to decrease for signals coming from farther downstream, and then heterogeneity of vehicles further away has less significant impact on the CCC vehicle.

We then consider the robustness of the CCC design against extra connectivity links among preceding vehicles. In Fig. C.2, the blue crosses still show the gains in a $(10+1)$-car system with homogeneous human-driven vehicles (cf. Fig. 5.2), while the green squares depict the case when vehicle 3 is also using motion information of vehicle 5, with feedback gains $\alpha_{35} = 0.6\,[1/\mathrm{s}]$ and $\beta_{35} = 0.9\,[1/\mathrm{s}]$. Notice that the gains α_{1i}, β_{1i} of the CCC controller do not change for $i = 1, \ldots, 4$. While α_{15} and β_{15} change considerably, as i increases further the changes in α_{1i}, β_{1i} decay exponentially.

These case studies demonstrate that our proposed algorithm is robust against heterogeneity among preceding vehicles.

BIBLIOGRAPHY

[1] J. I. Ge, G. Orosz, D. Hajdu, T. Insperger, and J. Moehlis, "To delay or not to delay - stability of connected cruise control," in *Time Delay Systems - Theory, Numerics, Applications and Experiments, Advances in Delays and Dynamics*, G. Orosz, T. Ersal, and T. Insperger, Eds., vol. 7. Springer, 2016, pp. 263–282.

[2] J. I. Ge and G. Orosz, "Estimation of feedback gains and delays in connected vehicle systems," in *Proceedings of the American Control Conference*. IEEE, 2016, pp. 6000–6005.

[3] J. I. Ge, S. S. Avedisov, and G. Orosz, "Stability of connected vehicle platoons with delayed acceleration feedback," in *Proceedings of the ASME Dynamical Systems and Control Conference*. ASME, 2013, p. V003T30A006, paper no. DSCC2013-4040.

[4] J. I. Ge and G. Orosz, "Dynamics of connected vehicle systems with delayed acceleration feedback," *Transportation Research Part C*, vol. 46, pp. 46–64, 2014.

[5] ——, "Optimal control of connected vehicle systems," in *Proceedings of the 53rd IEEE Conference on Decision and Control*. IEEE, 2014, pp. 4107–4112.

[6] ——, "Optimized connected cruise control with time delay," in *Proceedings of the 12th IFAC Workshop on Time-Delay Systems*. IFAC, 2015, pp. 468–473.

[7] ——, "Optimal control of connected vehicle systems with communication delay and driver reaction time," *IEEE Transactions on Intelligent Transportation Systems*, p. submitted, 2015.

[8] S. E. Shladover, "PATH at 20 History and Major Milestones," The University of California PATH Program, Richmond, CA 94804, Progressreport 8, 2006.

[9] K. Li and P. Ioannou, "Modeling of traffic flow of automated vehicles," *IEEE Transactions on Intelligent Transportation Systems*, vol. 5, no. 2, pp. 99–113, 2004.

[10] L. C. Davis, "Effect of adaptive cruise control systems on traffic flow," *Physical Review E*, vol. 69, no. 6, p. 066110, 2004.

[11] "Nissan Disengagement Report," 2016, https://www.dmv.ca.gov/portal/wcm/connect/0170b0e7-7992-45f6-918d-8d3cc5bce9ee/nissan_disengagement_report.pdf?MOD=AJPERES.

[12] "Delphi Disengagement Report," 2016, https://www.dmv.ca.gov/portal/wcm/connect/851838fb-da8b-45da-bd95-0ae0451de988/delphi_disengagement_report.pdf?MOD=AJPERES.

[13] "Dedicated Short Range Communications (DSRC) Service," 2016, https://www.fcc.gov/dedicated-short-range-communications-dsrc-service.

[14] "Dedicated Short Range Communications (DSRC) Message Set Dictionary Set," SAE International," SAE J2735SET_201603, 2016.

[15] "Taxonomy and Definitions for Terms Related to On-Road Motor Vehicle Automated Driving Systems," SAE International," SAE J3016_201609.

[16] "On-Board System Requirements for V2V Safety Communications," SAE International," SAE J2945/1_201603, 2016.

[17] X. Cheng, L. Yang, and X. Shen, "D2D for intelligent transportation systems: A feasibility study," *IEEE Transactions on Intelligent Transportation Systems*, vol. 16, no. 4, pp. 1784–1793, 2015.

[18] X. Cheng, X. Hu, L. Yang, I. Husain, K. Inoue, P. Krein, R. Lefevre, Y. Li, H. Nishi, J. Taiber, F. Wang, Y. Cha, W. Gao, and Z. Li, "Electrified vehicles and the smart grid: the its perspective," *IEEE Transactions on Intelligent Transportation Systems*, vol. 15, no. 4, pp. 1388–1404, 2015.

[19] E. van Nunen, R. J. A. E. Kwakkernaat, J. Ploeg, and B. D. Netten, "Cooperative competition for future mobility," *IEEE Transactions on Intelligent Transportation Systems*, vol. 13, no. 3, pp. 1018–1025, 2012.

[20] E. Chan, P. Gilhead, P. Jelinek, P. Krejci, and T. Robinson, "Cooperative control of SARTRE automated platoon vehicles," in *Proceedings of the 19th ITS World Congress*, 2012.

[21] B. van Arem, C. J. G. van Driel, and R. Visser, "The impact of cooperative adaptive cruise control on traffic-flow characteristics," *IEEE Transactions on Intelligent Transportation Systems*, vol. 7, no. 4, pp. 429–436, 2006.

[22] M. di Bernardo, A. Salvi, and S. Santini, "Distributed consensus strategy for platooning of vehicles in the presence of time varying heterogeneous communication delays," *IEEE Transaction on Intelligent Transportation Systems*, vol. 16, no. 1, pp. 102–112, 2015.

[23] V. Milanes, J. Alonso, L. Bouraoui, and J. Ploeg, "Cooperative maneuvering in close environments among cybercars and dual-mode cars," *IEEE Transactions on Intelligent Transportation Systems*, vol. 12, no. 1, pp. 15–24, 2011.

[24] J. Ploeg, N. van de Wouw, and H. Nijmeijer, "$\mathcal{L}_{\mathrm{p}}$ string stability of cascaded systems: application to vehicle platooning," *IEEE Transactions on Control Systems Technology*, vol. 22, no. 2, pp. 786–793, 2014.

[25] J. Ploeg, E. Semsar-Kazerooni, G. Lijster, N. van de Wouw, and H. Nijmeijer, "Graceful degradation of cooperative adaptive cruise control," *IEEE Transactions on Intelligent Transportation Systems*, vol. 16, no. 1, pp. 488–497, 2015.

[26] J. Ploeg, D. Shukla, N. van de Wouw, and H. Nijmeijer, "Controller synthesis for string stability of vehicle platoons," *IEEE Transactions on Intelligent Transportation Systems*, vol. 15, no. 2, pp. 845–865, 2014.

[27] M. Wang, W. Daamen, S. P. Hoogendoorn, and B. van Arem, "Rolling horizon control framework for driver assistance systems. part II: Cooperative sensing and cooperative control," *Transportation Research Part C*, vol. 40, pp. 290–311, 2014.

[28] Y. Zheng, S. E. Li, J. Wang, D. Cao, and K. Li, "Stability and scalability of homogeneous vehicular platoon: Study on the influence of information flow topologies," *IEEE Transactions on Intelligent Transportation Systems*, vol. 17, no. 1, pp. 14–26, 2016.

[29] D. Helbing, "Traffic and related self-driven many-particle systems," *Reviews of Modern Physics*, vol. 73, pp. 1067 – 1141, 2001.

[30] K. Nagel, P. Wagner, and R. Woesler, "Still flowing: Approaches to traffic flow and traffic jam modeling," *Operations Research*, vol. 51, no. 5, pp. 681–710, 2003.

[31] M. Treiber, A. Hennecke, and D. Helbing, "Congested traffic states in empirical observations and microscopic simulations," *Physical Review E*, vol. 62, pp. 1805–1824, 2000.

[32] M. Bando, K. Hasebe, A. Nakayama, A. Shibata, and Y. Sugiyama, "Dynamical model of traffic congestion and numerical simulation," *Physical Review E*, vol. 51, pp. 1035–1042, 1995.

[33] R. Herman, E. W. Montroll, R. B. Potts, and R. W. Rothery, "Traffic dynamics: Analysis of stability in car following," *Operations Research*, vol. 7, no. 1, pp. 86–106, 1959.

[34] D. C. Gazis, R. Herman, and R. W. Rothery, "Nonlinear follow-the-leader models of traffic flow," *Operations Research*, vol. 9, no. 4, pp. 545 – 567, 1961.

[35] P. A. Ioannou and M. Stefanovic, "Evaluation of ACC vehicles in mixed traffic: lane change effects and sensitivity analysis," *IEEE Transactions on Intelligent Transportation Systems*, vol. 6, no. 1, pp. 79–89, 2005.

[36] S. Krauss, P. Wagner, and C. Gawron, "Metastable states in a microscopic model of traffic flow," *Physical Review E*, vol. 55, pp. 5597–5602, 1997.

[37] R. Wiedemann, *Simulation des Strassenverkehrsflusses*. Institut Fur Verkehrswesen Der Universitat Karlsruhe, 1973.

[38] D. Krajzewicz, J. Erdmann, M. Behrisch, and L. Bieker, "Recent development and applications of SUMO simulation of urban mobility," *International Journal on Advances in Systems and Measurements*, vol. 5, no. 3&4, pp. 128–138, 2012.

[39] Q. Yang and H. N. Koutsopoulos, "A microscopic traffic simulator for evaluation of dynamic traffic management systems," *Transportation Research Part C: Emerging Technologies*, vol. 4, no. 3, pp. 113–129, 1996.

[40] S. Hoogendoorn and R. Hoogendoorn, "Calibration of microscopic traffic-flow models using multiple data sources," *Philosophical Transactions of the Royal Society of London A*, vol. 368, no. 1928, pp. 4497–4517, 2010.

[41] P. Wagner, "Fluid-dynamical and microscopic description of traffic flow: a data-driven comparison," *Philosophical Transactions of the Royal Society of London A*, vol. 368, no. 1928, pp. 4481–4495, 2010.

[42] G. Orosz, R. E. Wilson, and G. Stépán, "Traffic jams: dynamics and control," *Philosophical Transactions of the Royal Society A*, vol. 368, no. 1928, pp. 4455–4479, 2010.

[43] G. Orosz, "Connected cruise control: modeling, delay effects, and nonlinear behavior," *Vehicle System Dynamics*, vol. 54, no. 8, pp. 1147–1176, 2016.

[44] P. Seiler, A. Pant, and K. Hedrick, "Disturbance propagation in vehicle strings," *IEEE Transactions on Automatic Control*, vol. 49, no. 10, pp. 1835–1842, 2004.

[45] G. Stépán, *Retarded Dynamical Systems: Stability and Characteristic Functions*, ser. Pitman Research Notes in Mathematics. Longman, 1989, vol. 210.

[46] W. B. Qin, M. M. Gomez, and G. Orosz, "Stability and frequency response under stochastic communication delays with applications to connected cruise control design," *IEEE Transactions on Intelligent Transportation Systems*, vol. 18, no. 2, pp. 388–403, 2017.

[47] M. Wang, W. Daamen, S. P. Hoogendoorn, and B. van Arem, "Rolling horizon control framework for driver assistance systems. part I: Mathematical formulation and non-cooperative systems," *Transportation Research Part C: Emerging Technologies*, vol. 40, pp. 271 – 289, 2014.

[48] L. Zhang and G. Orosz, "Motif-based analysis of connected vehicle systems: delay effects and stability," *IEEE Transactions on Intelligent Transportation Systems*, vol. 17, no. 6, pp. 1638–1651, 2016.

[49] R. Pandita and D. Caveney, "Preceding vehicle state prediction," in *2013 IEEE Intelligent Vehicles Symposium*, 2013, pp. 1000–1006.

[50] P. A. Ioannou and J. Sun, *Robust Adaptive Control*. Dover Publications, 2012.

[51] S. Diop, I. Kolmanovsky, P. Moraal, and M. V. Nieuwstadt, "Preserving stability/performance when facing an unknown time-delay," *Control Engineering Practice*, vol. 9, no. 12, pp. 1319–1325, 2001.

[52] O. Gomez, Y. Orlov, and I. V. Kolmanovsky, "On-line identification of SISO linear time-invariant delay systems from output measurements," *Automatica*, vol. 43, no. 12, pp. 2060 – 2069, 2007.

[53] Y. Orlov, L. Belkoura, J.-P. Richard, and M. Dambrine, "Adaptive identification of linear time-delay systems," *International Journal of Robust and Nonlinear Control*, vol. 13, pp. 857–872, 2003.

[54] S. Drakunov, W. Perruquetti, J.-P. Richard, and L. Belkoura, "Delay identification in time-delay systems using variable structure observers," *Annual Reviews in Control*, vol. 30, no. 2, pp. 143–158, 2006.

[55] J. Inman, *Navigation and Nautical Astronomy: For the Use of British Seamen*. C. W. Woodward and J. Rivington, 1835.

[56] S. S. Avedisov and G. Orosz, "Nonlinear network modes in cyclic systems with applications to connected vehicles," *Journal of Nonlinear Science*, vol. 25, no. 4, pp. 1015–1049, 2015.

[57] T. Insperger, J. Milton, and G. Stépán, "Acceleration feedback improves balancing against reflex delay," *Journal of The Royal Society Interface*, vol. 10, no. 79, p. 20120763, 2013.

[58] F. Bai and H. Krishnan, "Reliability analysis of DSRC wireless communication for vehicle safety applications," in *Intelligent Transportation Systems Conference, IEEE*, 2006, pp. 355–362.

[59] T. K. Engelborghs and G. Samaey, "DDE-BIFTOOL v. 2.00: a Matlab package for bifurcation analysis of delay differential equations," Department of Computer Science, K.U.Leuven, Leuven, Belgium, Technical Report TW-330, 2001.

[60] W. B. Qin and G. Orosz, "Digital effects and delays in connected vehicles: linear stability and simulations," in *Proceedings of the ASME Dynamical Systems and Control Conference*. ASME, 2013, p. V003T30A001, paper no. DSCC2013-3830.

[61] L. Zhang and G. Orosz, "Designing network motifs in connected vehicle systems: delay effects and stability," in *Proceedings of the ASME Dynamical Systems and Control Conference*. ASME, 2013, p. V003T42A006, paper no. DSCC2013-4081.

[62] C. R. He, H. Maurer, and G. Orosz, "Fuel consumption optimization of heavy-duty vehicles with grade, wind, and traffic information," *ASME Journal of Computational and Nonlinear Dynamics*, vol. 11, no. 6, pp. 061 011–1–12, 2016.

[63] V. Kolmanovskii and A. Myshkis, *Applied Theory of Functional Differential Equations*. Kluwer Academic Publisher, 1992.

[64] D. Ross and I. Flugge-Lotz, "An optimal control problem for systems with differential-difference equation dynamics," *SIAM Journal on Control*, vol. 7, no. 4, pp. 609–623, 1969.

[65] V. Forejt, M. Kwiatkowska, G. Norman, and D. Parker, *Automated Verification Techniques for Probabilistic Systems*. Springer, 2011, pp. 53–113.

[66] M. Kwiatkowska, G. Norman, and D. Parker, "Prism 4.0: Verification of probabilistic real-time systems," in *Proceedings of the 23rd International Conference on Computer Aided Verification*, ser. CAV'11. Springer, 2011, pp. 585–591.

[67] D. Han, Y. Mo, and R. M. Murray, "Synthesis of distributed longitudinal control protocols for a platoon of autonomous vehicles," in *Proceedings of the 54th IEEE Conference on Decision and Control*. IEEE, 2015.

[68] G. Orosz, J. Moehlis, and F. Bullo, "Delayed car-following dynamics for human and robotic drivers," in *Proceedings of the ASME IDETC/CIE Conference*. ASME, 2011, pp. 529–538, paper no. DETC2011-48829.

[69] T. Insperger and G. Stépán, *Semi-Discretization for Time Delay Systems*. Springer, 2011.

[70] A. Aw and M. Rascle, "Resurrection of "second order" models of traffic flow?" *SIAM Journal on Applied Mathematics*, vol. 60, no. 3, pp. 916–938, 1999.

[71] C. F. Daganzo, "Requiem for second-order fluid approximations of traffic flow," *Transportation Research Part B: Methodological*, vol. 29, no. 4, pp. 277 – 286, 1995.

[72] A. P. Morgan and K. S. Narendra, "On the stability of nonautonomous differential equations $\dot{x} = [\mathbf{A} + \mathbf{B}(t)]x$ with skew symmetric matrix $\mathbf{B}(t)$," *SIAM Journal of Control and Optimization*, vol. 15, no. 1, pp. 163–175, 1977.

[73] J.-J. E. Slotine and W. Li, *Applied Nonlinear Control*. Prenice Hall, 1991.